CBM

Compressed Baryonic Matter experiment at FAIR

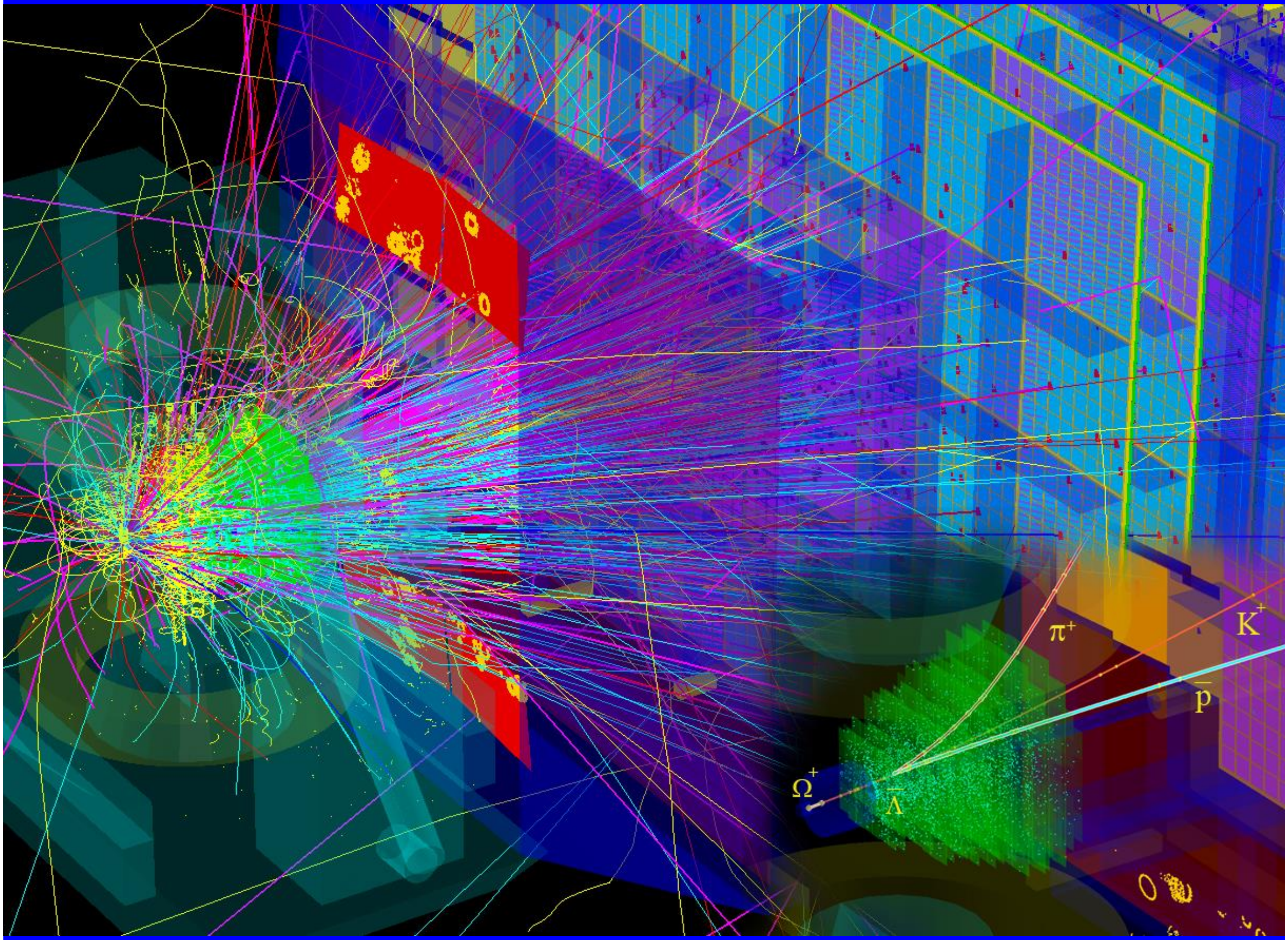

PROGRESS REPORT

2014

CBM Progress Report 2014

ISBN 978-3-9815227-2-3

Editors: Volker Friese and Christian Sturm
v.friese@gsi.de c.sturm@gsi.de

Reviewers: C. Blume, S. Chattopadhyay, V. Friese, N. Herrmann, J. Heuser, C. Höhne, I. Korolko, W. Müller, C. Müntz, I. Selyuzhenkov, P. Senger, C. Sturm

`http://www.gsi.de`

Printed in Darmstadt by GSI

Several of the contributions to this volume also appear in the GSI Scientific Report 2014.

Preface

Dear colleagues,

by now, the CBM Progress Report already looks back at a considerable history. Its first issue dates back to the year 2006, when we decided to collect all CBM-related contributions to the GSI Scientific Report, which at that time ceased to appear in print, in a separate, printed volume, and augment it with numerous CBM reports from outside GSI. Since then, the CBM Progress Report annually documents the manifold activities towards the realisation of the CBM project, and its ever increasing size demonstrates the steady growth of efforts.

Browsing through the past volumes, it is possible to trace some of the CBM history, from first conceptual considerations and rather basic feasibility studies, over thorough detector and electronics R&D to a close-to-final detector design and physics performance studies with detailed and realistic detector response. Now, the year 2014 marks the beginning of a new phase of the CBM project. Most of the Technical Design Reports are submitted and approved, the basic technological and design decisions are made, and the physics programme is being shaped for the first years of operation at the SIS-100 accelerator. The next years will be devoted to the building of the detectors, the actual realisation of what has been developed and planned over the past years.

The FAIR project itself enters a new phase. The managements of both FAIR and GSI are being restructured, and construction plans, priorities and time lines are under renewed discussions. Whatever the outcome will be, CBM continues to be one of the most important scientific pillars of the FAIR, and our efforts remain directed to have our experiment ready for taking data when the FAIR accelerators will start to deliver beams.

Our thanks go to all who contributed to this report.

Darmstadt, April 2015

Volker Friese and Christian Sturm

Contents

The Compressed Baryonic Matter Experiment at FAIR

The CBM Collaboration, January 2015

Substantial experimental and theoretical efforts worldwide are devoted to explore the phase diagram of strongly interacting matter. At top RHIC and LHC energies, QCD matter is studied at very high temperatures and very low net-baryon densities. For larger net-baryon densities and lower temperatures, it is expected that the QCD phase diagram exhibits a rich structure such as a critical point, a first order phase transition between hadronic and partonic matter, or new phases like quarkyonic matter. The discovery of these landmarks would be a breakthrough in our understanding of the strong interaction, and, therefore, is in the focus of various high-energy heavy-ion research programs. The Compressed Baryonic Matter (CBM) experiment at FAIR will play a unique role in the exploration of the QCD phase diagram in the region of neutron star core densities, because it is designed to run at unprecedented interaction rates. High rate operation is the key prerequisite to measure rare diagnostic probes which are sensitive to the dense phase of the nuclear fireball, such as multi-strange hyperons, lepton pairs, and particles containing charm quarks, with high precision and statistics. Most of these observables will be studied for the first time in the FAIR energy range. The start version of the CBM setup is very well suited to perform an internationally unrivaled nuclear-matter research programme with a substantial discovery potential using beams from SIS100. The experimental exploration of strongly interacting matter at ultra-high baryon densities will be extended towards higher beam energies with the full version of the CBM detector system using high-intensity beams from SIS300.

I. PROBING QCD MATTER WITH HEAVY-ION COLLISIONS

High-energy heavy-ion collision experiments provide the possibility to create and investigate extreme states of strongly-interacting matter in the laboratory. Figure 1 illustrates the conjectured phases of nuclear matter and their boundaries in a diagram of temperature versus baryon chemical potential [1]. In experiments at LHC and top RHIC energies, matter is produced at very high energy densities with equal numbers of particles and antiparticles, i.e. at almost zero baryon chemical potential. After hadronization, the fireball finally freezes out chemically at a temperature of 155 - 165 MeV [2]. This temperature coincides with the critical temperature predicted by Lattice QCD calculations for a chiral phase transition [3, 4] which is found to be a smooth crossover from partonic to hadronic matter [5]. Lattice QCD calculations for finite baryon chemical potential are still in their infancy, and are not yet able to make firm predictions on possible phase transitions at high net-baryon densities. On the other hand, model calculations predict structures in the QCD phase diagram at large baryon chemical potentials, like a critical endpoint followed by a first order phase transition [6]. Moreover, new phases are predicted, such as quarkyonic matter which can be considered as a Fermi gas of free quarks, with all thermal and Fermi surface excitations permanently confined [7]. The experimental discovery of these landmarks and regions in the QCD phase diagram would be a major breakthrough in our understanding of the properties of strongly interacting matter at extreme conditions, with fundamental consequences for our knowledge on the structure of neutron stars, chiral symmetry restoration, and the origin of hadron masses.

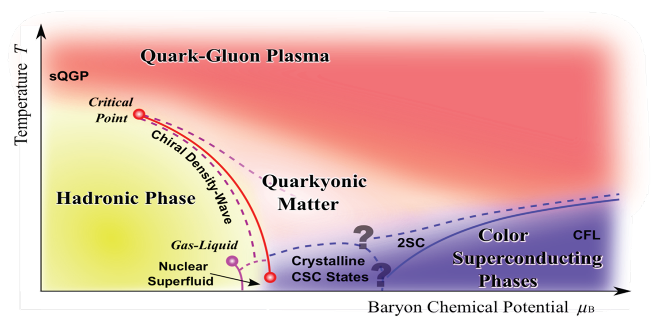

FIG. 1. Sketch of the phase diagram for nuclear matter. Taken from [1].

II. EXPERIMENTS EXPLORING HIGH NET-BARYON DENSITIES

Pioneering heavy-ion experiments have been performed at AGS in Brookhaven [8] and at low CERN-SPS beam energies [9] in order to explore the QCD phase diagram at large baryon-chemical potentials. Due to the available detector technologies at that time these measurements were restricted to abundantly produced hadrons. At the CERN-SPS, the NA61/SHINE experiment continues to search for the first-order phase transition using light and medium size beams [10]. This detector setup is limited to reaction rates of about 80 Hz. The STAR collaboration at RHIC plans a second beam energy scan to improve the statistical significance of the data taken in the first series of measurements [11]. However, the reaction rates at RHIC drop down to a few Hz when decreasing the beam energies below $\sqrt{s_{NN}}$=8 GeV. Neither STAR at RHIC nor NA61 at SPS will be able to run at beam energies of 10 A GeV and less. At the Joint

Institute for Nuclear Research (JINR) in Dubna, a fixed target experiment is being developed at the Nuclotron to study heavy-ion collisions at gold-beam energies up to about 4 A GeV. Moreover, the collider facility NICA together with a multi-purpose detector is planned at JINR [12]. The luminosity limitations of these existing and future facilities constrain the research programs to the investigation of bulk observables, and prevent high precision measurements of rare diagnostic probes. In contrast, the Compressed Baryonic Matter (CBM) experiment at the Facility for Antiproton and Ion Research (FAIR) is designed to run at extremely high interaction rates (up to 10 MHz). This feature is the key requirement for the measurement of both bulk and rare probes with unprecedented precision. The combination of high-intensity beams with a high-rate detector system and sufficient beam time provides worldwide unique conditions for the study of nuclear matter at neutron star core densities. In the FAIR Modularized Start Version only the SIS100 ring will be available. In order to close the gap between SIS100 and low RHIC and SPS energies, SIS300 will be required. In addition, SIS300 will be used as a stretcher ring offering the opportunity to run several experimental programs in parallel.

III. THE CBM PHYSICS PROGRAM AT SIS100

FAIR will provide heavy-ion beam energies from 2 - 11 (14) A GeV for Q = 0.4 A (0.5 A) nuclei with the SIS100 synchrotron, and 11 - 35 (45) A GeV with the SIS300 synchrotron. Already in central Au+Au collisions at top SIS100 energies the nuclear fireball will be compressed - according to transport model calculations - to more than 8 times saturation density ρ_0. Even at moderate SIS100 energies, for example at 5 A GeV, a density above 6 ρ_0 is reached as illustrated in figure 2 [13]. At such densities, the nucleons will start to melt and to dissolve into their constituents. The calculations predict that the dense fireball spends a relatively long time within the phase coexistence region. Those conditions appear to be sufficient to allow for a phase transition. For example, according to a non-local 3-flavor Nambu Jona-Lasinio model calculation, which predicts a deconfinement phase transition in the core of a 2 solar mass neutron star [14], a mixed phase of hadrons and quarks develops at densities between 5 ρ_0 and 8 ρ_0, above which pure quark matter is formed. In conclusion, the beam energies available at SIS100 appear to be especially well suited for generating signals of the phase transition, and offer the opportunity to address fundamental scientific questions:

- What is the equation of state of nuclear matter at neutron star densities, and what are the relevant degrees of freedom at these densities? Is there a phase transition from hadronic to quark-gluon matter, or a region of phase coexistence? Do exotic QCD phases like quarkyonic matter exist?
- To what extent are the properties of hadrons modified in dense baryonic matter? Are we able to find indications of chiral symmetry restoration?
- How far can we extend the chart of nuclei towards the third (strange) dimension by producing single and double hypernuclei? Does strange matter exist in the form of heavy multi-strange objects?
- What is the production mechanism of charm quarks at threshold beam energies, how does open and hidden charm propagate in cold and in hot nuclear matter?

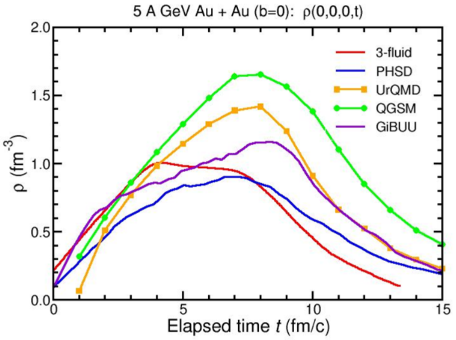

FIG. 2. Evolution of the central net baryon density $\rho(t)$ as function of elapsed time reached in a central Au+Au collision at 5 A GeV as calculated with different transport models and with a 3-fluid hydrodynamics code. [13].

The experimental challenge is to identify diagnostic probes of the dense phase of the fireball which is transiently formed in the collision. In experiments performed so far at AGS, at low SPS energies, or at very low RHIC energies, mainly such particles have been measured which are created at freeze-out where the density already has dropped below saturation density. The focus of the CBM experiment at FAIR is to study messengers from the dense fireball such as multiple strange hyperons, lepton pairs, and hadrons containing charm quarks in order to find answers to the questions raised above. A survey of the theoretical concepts and the experimental programs devoted to the exploration of the QCD phase diagram with focus on high baryon densities is given in the CBM Physics Book [15]. The CBM research program at SIS100 includes the following observables.

Strangeness
At top SPS energies it was found that the production of hyperons is enhanced in heavy ion collisions, i.e. the multiplicity of hyperons per participating nucleon increases with the mass of the collision system [16]. The enhancement increases with the number of strange quarks in the hyperon. According to transport models, multi-strange (anti-)hyperons are produced in sequential collisions involving kaons and Λs, and, therefore, are sensitive to the

density in the fireball. This sensitivity is expected to increase towards lower beam energies close to or even below the production threshold. SIS100 beam energies will be ideally suited to perform such experiments which require a systematic measurement of multi-(anti-)strange hyperons at different energies and for different colliding nuclei. Up to date, only about 300 Ξ^- hyperons have been measured in Au+Au collisions at 6 A GeV [17]. The excitation functions of multi-strange hyperons ($\Xi^-(dss)$ and $\Omega^-(sss)$) and anti-hyperons ($\Xi^+(\bar{d}\bar{s}\bar{s})$ and Ω^+ ($\bar{s}\bar{s}\bar{s}$)) in A+A collisions with different A values at SIS100 beam energies are very promising observables which will shed light on the compressibility of nuclear matter at neutron star core densities.

Lepton pairs

Lepton pairs will be measured over a wide range of invariant masses covering low-mass vector mesons including their Dalitz decays and charmonium. The precise measurement of lepton pairs at low invariant masses will allow to analyze modifications of vector meson properties in dense baryonic matter. This observable is expected to be sensitive to chiral symmetry restoration [18]. The slope of the dilepton invariant mass distribution between 1 and 2 GeV/c^2 directly reflects the average temperature of the fireball. The study of the energy dependence of this slope opens the unique possibility to measure the caloric curve which would be a signature for phase coexistence [19]. This measurement would also provide indications for the onset of deconfinement and the location of the critical endpoint. The flow of lepton pairs as function of their invariant mass would allow to disentangle radiation from the early partonic phase from the late hadronic phase. No dilepton data are available at FAIR energies.

Collective flow, correlations and fluctuations

The collective flow of hadrons is driven by the pressure created in the early fireball. For example, the observed difference between the elliptic flow of particles and their antiparticles has been explained by mean-field potential effects in both the partonic and the hadronic phase [20]. A direct proof for a first order phase transition would be the discovery of phase coexistence by observing an enhanced production of composite particles or multi-particle correlations caused by the spinodal amplification of density fluctuations [21]. Higher moments of the net-baryon and the net-charge multiplicity distributions, which are related to the thermodynamical susceptibilities, have been measured by the STAR collaboration in order to search for the QCD critical point [22]. Most of these observables will be measured for the first time at SIS100 energies. Up to now, only the proton flow excitation function has been measured at the AGS [8], and was used to extract the compressibility of nuclear matter [23].

Hypernuclei and hypermatter

Theoretical models predict that single and double hypernuclei, and heavy multi-strange short-lived objects are produced via coalescence in heavy-ion collisions with the maximum yield in the region of SIS100 energies [24, 25]. The discovery and investigation of new hypernuclei and of hypermatter will shed light on the hyperon-nucleon and hyperon-hyperon interactions which are essential ingredients for the nuclear equation-of-state at high densities and low temperatures [26].

Charm

Charm-anticharm quark pairs are produced in primary hard scattering processes and then propagate through the nuclear or partonic medium as it is produced in high-energy heavy-ion collisions. Depending on their interaction with the medium, the charm and anticharm quarks hadronize into D mesons, charmed baryons, or charmonium. The suppression of charmonium due to color screening of the heavy quark potential in the deconfined phase is the first predicted signature for quark-gluon plasma formation [27]. Charmonium suppression was first observed in central Pb+Pb collisions at 158 A GeV [28], and then also found in experiments at RHIC [29] and LHC [30]. At SIS100 energies, the charm production mechanism will be studied for the first time at beam energies close to production threshold. Moreover, exploratory experiments of charm production in collisions of medium size nuclei will be possible. In addition, the propagation of open and hidden charm in cold nuclear matter will be systematically investigated in proton-nucleus collisions. Measurements of (open and hidden) charm in collisions of heavy nuclei can only be performed at SIS300 energies.

IV. THE COMPRESSED BARYONIC MATTER (CBM) EXPERIMENT

The CBM detector is designed as a multi-purpose device which will be able to measure hadrons, electrons and muons in heavy-ion collisions over the full SIS100/SIS300 beam energy range. Therefore, no major adjustments have to be made to optimize the experiment for SIS100 beams, only some of the detectors and the DAQ system will be realized in phases (see below). In order to extract the dilepton signals, the physical and combinatorial background of lepton pairs has to be precisely determined, which is notoriously difficult. Measuring both electrons and muons will dramatically reduce the systematical error of the data, because the background sources of electrons and muons are completely different. In order to perform high-precision multi-differential measurements of rare probes the experiment should run at event rates of 100 kHz up to 10 MHz for several months per year. Because of the complicated decay topology of particles like Ω hyperons or D mesons, no simple trigger signal can be generated, so the events have to be reconstructed and selected online by fast algorithms running on a high-performance computing farm. Therefore, the data readout chain is based on a free streaming frontend electronics which delivers time-stamped signals from each detector channel without event correlation. The reconstruction algorithms are tuned to run at high speed on modern many-core CPU architectures.

The detector system features a fixed target geometry accepting polar emission angles between 2.5 and 25 degrees in order to cover midrapidity for symmetric collision systems at beam energies between 2 and about 40 A GeV. The setup comprises the following components:

- A large aperture superconducting dipole magnet,
- a Silicon Tracking System (STS) based on double-sided silicon microstrip sensors arranged in 8 stations inside the magnetic field,
- a Micro Vertex Detector (MVD) consisting of 4 layers of silicon monolithic active pixel sensors,
- a time-of flight wall (TOF) based on multigap resistive plate chambers with low-resistivity glass for high-rate operation,
- a Ring Imaging Cherenkov (RICH) detector comprising a CO_2 radiator, a glass-mirror system and a photon detector based on multianode photomultipliers for electron identification,
- a Transition Radiation Detector (TRD) for pion suppression particle tracking,
- a forward hadron calorimeter (Projectile Spectator Detector) for event characterization,
- a Muon chamber (MuCh) system for muon identification consisting of a set of gaseous micro-pattern chambers sandwiched between iron plates as hadron absorbers,
- a First-Level-Event-Selection (FLES) system for online event reconstruction and selection.

For SIS100, only start versions of the TRD, the MuCh, and the FLES will be built. The TRD comprises only 4 out of 12 layers, the number of absorber and detector stations of the MuCh is reduced, and the FLES has less computing power as compared to the full version required for SIS300. The Technical Design Reports (TDR) on the magnet, on the STS, on the RICH, on the PSD, and on the MuCh have been approved, the TDR on the TOF detector is in evaluation. The TDRs on the DAQ/FLES system, on the MVD, on the TRD and on the Electromagnetic Calorimeter will be submitted in 2015.

Until the start of FAIR, the nuclear matter research program at GSI will be pursued with the HADES experiment at SIS18. At the SIS100 accelerator, the HADES detector can be used to perform di-electron and hadron reference measurements in collision systems with moderate particle multiplicities, such as proton-proton, proton-nucleus and nucleus-nucleus collisions with light nuclei.

V. SUMMARY

The goal of the CBM research program at SIS100 is to explore the QCD phase diagram in the region of neutron star core densities. This includes the study of the equation-of-state of nuclear matter and the search for new phases. The start version of the CBM detector will be able to measure rare diagnostic probes such as multi-strange hyperons and lepton pairs with unprecedented precision and statistics. Most of these probes will be studied for the first time in the FAIR energy range. In order to achieve the required precision for multi-differential observables, the measurements will be performed at reaction rates between 100 kHz and 10 MHz. The search and exploration of new phases of strongly interacting matter will be extended to higher energies with a completed detector setup once SIS300 will come into operation.

Acknowledgment

The design and development of the CBM detection systems and read-out electronics is performed by the CBM Collaboration which currently consists of more than 500 persons from 59 institutions and 12 countries. The CBM project is supported by the Helmholtz Association, by the EU FP7 Hadronphysics3 programme, and by national funds of the CBM member institutions.

---

[1] K. Fukushima and T. Hatsuda: Rept. Prog. Phys. **74** (2011) 014001

[2] F. Becattini et al., Phys. Rev. Lett. **111** (2013) 082302

[3] S. Borsanyi et al., JHEP **1009** (2010) 073

[4] A. Basavov et al.: Phys. Rev. **D85** (2012) 054503

[5] Y. Aoki et al., Nature **443** (2006) 675

[6] J. Luecker et al., arXiv:1308.4509v1 [hep-ph]

[7] L. McLerran and R. D. Pisarski, Nucl. Phys. **A796**, 83-100 (2007),

[8] C. Pinkenburg et al., Phys. Rev. Lett. **83** (1999) 1295

[9] C. Alt et al., Phys. Rev. **C77** (2008)024903

[10] A. Laszlo, Pos(CPOD07)054 (2007)

[11] https://drupal.star.bnl.gov/STAR/starnotes/public/sn0598

[12] http://nica.jinr.ru/

[13] I.C. Arsene et al.: Phys. Rev. **C75** (2007) 24902

[14] M. Orsaria et al., Phys. Rev. **C89** (2014)015806

[15] The CBM Physics Book, B. Friman et al.(eds): Series: Lecture Notes in Physics, Vol. **814** (2011)

[16] F. Antinori et al., Nucl. Phys. **A661** (1999) 130c

[17] P. Chung et al., Phys. Rev. Lett. **91** (2003) 202301

[18] P. Hohler and R. Rapp, Phys. Lett. **B731** (2014) 103-109

[19] R. Rapp and H. van Hees, arXiv:1411.4612

[20] J. Xu et al., Phys. Rev. Lett. **112** (2014) 012301

[21] J. Steinheimer and J. Randrup, Phys. Rev. Lett. **109** (2012) 212301

[22] L. Adamczyk et al., Phys. Rev. Lett. **113** (2014) 092301

[23] P. Danielewicz et al., Science **298** (2002) 1592

[24] A. Andronic et al., Phys. Lett. **B697** (2011) 203

[25] H. Stoecker et al., Nucl. Phys. **A827** (2009)

[26] A.S. Botvina et al., 1412.6665v1 [nucl-th]

[27] T. Matsui and H. Satz, Phys. Lett. **B178** (1986) 416.

[28] M. Abreu et al., Phys. Lett. **B410** (1997) 337.

[29] A. Adare et al., Phys. Rev. **C84** (2011) 054912

[30] B. Abelev et al., Phys. Rev. Lett. **109** (2012) 072301

The CBM experiment in the international context

The CBM Collaboration, January 2015

The exploration of the QCD phase diagram at large baryon-chemical potentials addresses funda-mental scientific questions, and, therefore, is in the focus of heavy-ion experiments worldwide. Key observables which probe the dense phase of the collision include multi-strange baryons, electro-magnetic radiation (dileptons), and particles containing charm quarks. Important information can be extracted from the particle multiplicities, the phase-space distributions, from particle correlations and fluctuations. In order to measure these multi-differential observables with a very good statistical significance, the experiments have to be operated at very high reaction rates over a sufficient amount of time. According to model calculations, the SIS100 beam energy range is very well suited to study the properties of strongly interacting matter at neutron star core densities.

I. PIONEERING EXPERIMENTS

First systematic experiments on hadron production in heavy-ion collisions have been performed at the Bevalac in Berkeley and at the AGS in Brookhaven. At the CERN-SPS, the NA49 collaboration measured excitation functions of hadrons with limited statistics, in particular for multi-strange baryons at low SPS energies. Dimuon measurements have been performed by NA60 at top SPS energies only. Low-statistics data on di-electrons were taken by the CERES collaboration at a beam energy of 40 A GeV ($\sqrt{s_{NN}}$= 8.8 GeV).

II. RUNNING EXPERIMENTS

At the CERN-SPS the NA61/SHINE experiment continues to search for the first-order phase transi-tion using light and medium size beams with limited reaction rates (see figure 1). The STAR collaboration at RHIC plans a second beam energy scan. However, the reaction rates at RHIC drop down to a few Hz when decreasing the collision energies below $\sqrt{s_{NN}}$= 8 GeV (see figure 1). Neither STAR at RHIC nor NA61 at SPS will be able to run at energies of $\sqrt{s_{NN}}$= 5 GeV and below, i.e. in the SIS100 energy range. A first complete measurement of rare and penetrating probes in Au+Au collisions at low beam energies ($\sqrt{s_{NN}}$= 2.4 GeV) has recently been accomplished by HADES at SIS18. At SIS100, HADES is very well suited to perform reference measurements (p+p, p+A) and A+A with low multiplicities because of its large acceptance and low material budget.

III. PLANNED EXPERIMENTS

At the Joint Institute for Nuclear Research (JINR) in Dubna, the collider facility NICA together with a multipurpose detector (MPD) is under design. The luminosity limitation of NICA will constrain the research program to the investigation of bulk observables (see figure 1). The Compressed Baryonic Matter (CBM) experiment at the Facility for Antiproton and Ion Research (FAIR) is designed to run at extremely high interaction rates (see figure 1). This feature is the key requirement for the measurement of bulk and rare probes, and of multi-differential observables with unprecedented precision. The combination of high-intensity beams with a high-rate detector system and sufficient beam time provides worldwide unique conditions for the study of nuclear matter at neutron star core densities.

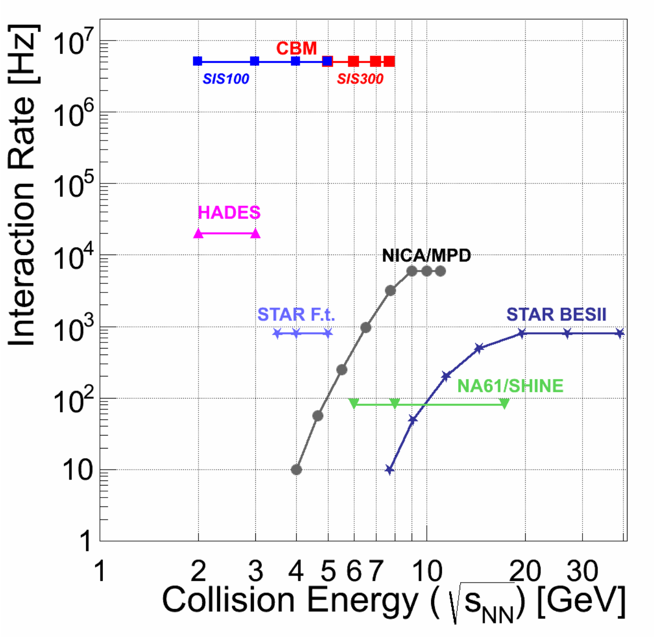

FIG. 1. Interaction rates of existing experiments and experiments under construction.

Common Activities

Test of prototype CBM detector components with proton beams at COSY[*]

J. Heuser[1], *R. Adak*[2], *T. Balog*[1], *S. Chattopadhyay*[2], *D. Dementyev*[7], *A. Dubey*[2], *D. Emschermann*[1], *J. Eschke*[3], *V. Friese*[1], *P. Ghosh*[4,1], *T. Heinz*[1], *V. Khomyakov*[5], *P. Koczon*[1], *P. Larionov*[4,1], *J. Lehnert*[1], *Ie. Momot*[4,1], *W.F.J. Müller*[1], *W. Niebur*[1], *A. Oancea*[4], *F. Uhlig*[1], *J. Saini*[2], *S. Samanta*[2], *M. Singla*[1], *I. Sorokin*[1,6], *C. Sturm*[1], *C. Stüllein*[4], *D. Varga*[8], *A. Wolf*[1], *and P. Zumbruch*[1]

[1]GSI, Darmstadt, Germany; [2]VECC, Kolkata, India; [3]FAIR, Darmstadt, Germany; [4]Goethe-Universität, Frankfurt, Germany; [5]ITEP, Moscow, Russia; [6]KINR, Kiev, Ukraine; [7]JINR, Dubna, Russia; [8]Wigner RCP, Budapest, Hungary

Teams of the CBM collaboration performed several in-beam tests of prototype detectors and electronics in 2014. In April at GSI, TOF and TRD detectors were examined in a parasitic ion beam steered onto a target. Prototypes of the TRD, RICH and TOF detectors were under test in a mixed electron-pion beam in November at the CERN-PS. Two campaigns of beamtime took place at COSY, Research Center Jülich, within beam time blocks provided to support FAIR related detector developments. In August, a team spent one week with testing prototype electronics under intense proton irradiation. In December, a week of beam time focused on studies of neutron-irradiated silicon microstrip sensors for the STS detector system, response measurements of a full-size triple-GEM sector for the MUCH detector system, and further studies of radiation effects in FPGA and LDO electronics. We report here on the December test at COSY.

The CBM test bench, 3 m long, is installed in the JESSICA cave into which the proton beam of COSY is extracted. Intensities from minimum 10^4 to maximum 10^9 protons per seconds can serve testing different objects. While detector systems are preferrably tested at lower impinging particle rates, and only for load tests at higher rates, electronics is required to be tested in high beam intensity conditions. The beam can be focused down to about 0.5 cm r.m.s diameter at the objects under test. Beam defocusing to areas of a few cm^2 is possible.

The aim of the beam time campaign was to study the performance of two full-size CBM prototype components, double-sided silicon microstrip sensors for the Silicon Tracking System and a full-size GEM sector for the Muon Chambers, as well as several electronics components for the read-out chains. The double-sided silicon microstrip sensors were produced in two technical versions which were to compare. Prior to the experiment, the sensors had been irradiated at the KIT irradiation facility to 2×10^{14} 1 MeV neutron equivalent fluence matching the integrated "lifetime" exposure expected in CBM running conditions. The detectors were operated in a thermally insulated station at a temperature of -8 °C, achieved with a flow of chilled nitrogen gas. The station was part of a telescope shown in Fig. 1 (top) comprising also two reference stations to define the proton tracks, and one further station with a STS prototype module under test. The full-size prototype GEM sector seen in Fig. 1 (bottom) was produced at CERN from 500 by 471 mm GEM foils in a three-foil stack, segmented into several areas, altogether having 1200 read-out pads with progressively increasing size.

The read-out of both the silicon and the GEM detectors was achieved with n-XYTER based front-end electronics and the DABC data acquisition system. The data collected allowed studying the detector response including charge collection properties.

At the downstream end of the test stand, boards with prototype electronics were placed on the beam. Already during detector operation, tests of FPGA electronics at moderate beam intensities allowed investigating single-event upsets. Dedicated runs at highest intensities were done with analog power regulating electronics (LDO) and memory components, after the conclusion of the detector tests.

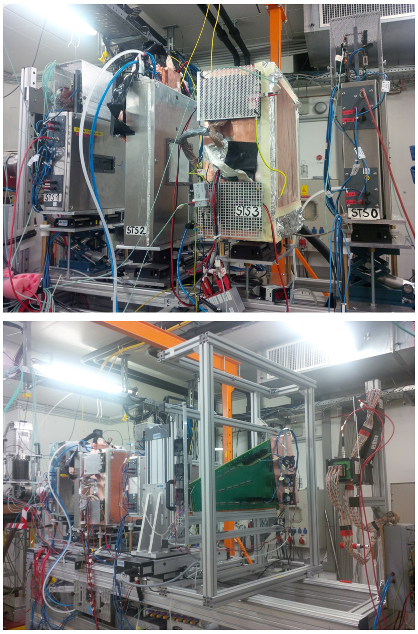

Figure 1: (Top) Telescope with four silicon detector stations. The second to the right operates the irradiated sensors. (Bottom) A full-size prototype GEM sector was installed further downstream comprising a triple-GEM foil stack.

---

[*] Work supported by EU-FP7 HadronPhysics3, HIC-for-FAIR, H-QM and HGS-HIRe. We acknowledge various support by IKP, FZ Jülich.

Common CBM beam test of the RICH, TRD and TOF subsystems at the CERN PS T9 beam line in 2014*

C. Bergmann[1], *D. Emschermann*[2], *W. Amend*[3], *A. Bercuci*[6], *R. Berendes*[1], *C. Blume*[3], *P. Dillenseger*[3], *C. Garcia*[4], *S. Gläßel*[3], *N. Heine*[1], *D. Hutter*[8], *B. Kardan*[3], *M. Kohn*[1], *M. Krieger*[7], *T. Morhardt*[2], *C. Pauly*[5], *M. Petriş*[6], *M. Petrovici*[6], *F. Roether*[3], *M. Tanha*[3], *W. Verhoeven*[1], *and J. P. Wessels*[1]

[1]Institut für Kernphysik, Münster, Germany; [2]GSI, Darmstadt, Germany; [3]Goethe-Universität, Frankfurt, Germany; [4]IRI, Frankfurt, Germany; [5]Bergische Universität, Wuppertal, Germany; [6]NIPNE, Bucharest, Romania; [7]ZITI, Universität Heidelberg, Mannheim, Germany; [8]FIAS, Frankfurt, Germany

A common beam test of the CBM Ring Imaging CHerenkov (RICH), Transition Radiation Detector (TRD) and Time Of Flight (TOF) subsystems was performed at the CERN Proton Synchrotron (PS) accelerator in October/November 2014. The measurements were carried out at the T9 beam line in a mixed beam of electrons and pions with momenta from 0.5 to 6 GeV/*c*. In addition to the above mentioned detectors, the setup consisted of: two Cherenkov detectors, two fiber-hodoscopes, beam trigger scintillators and a lead-glass calorimeter. The first fiber-hodoscope was placed at the upstream end of the setup, followed by a large volume RICH prototype, five real-size TRD prototypes and one small chamber, two TOF detectors and finally the second fiber-hodoscope at the downstream end, see Fig. 1.

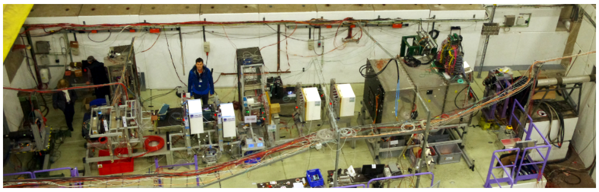

Figure 1: Setup of CBM in the PS/T9 beam line in 2014

The RICH prototype [1] was based on a mirror focusing setup with CO_2 gas as radiator. The photon camera was modified with respect to the previous year: the 2014 version was composed of 4×4 Hamamatsu multi-anode photomultipliers (MAPMTs). The RICH camera were tested using a free streaming approach based on the HADES Trigger and Readout Board (TRB3) [2].

The TRD laboratories in Münster [3], Bucharest [4] and Frankfurt [5] have built real-size (57×57 cm^2) detector modules based on MWPC technology with cathode pad readout. The signal processing on the TRD modules from Münster and Frankfurt was performed with the Self-triggered Pulse Amplification and Digitization asIC (SPADIC) v1.0 from 2013 [7, 9]. The latter reads out 32 channels in self-triggered mode and implements the CBM-net protocol on the ASIC. The readout of the Bucharest prototypes was based on the Fast Analog Signal Processor (FASP) ASIC, either digitized in a VME-based MADC32, or using the free streaming MAXIM front-end. The TRD test program consisted of a systematic study of different radiator prototypes with a Xe(80%)+CO_2(20%) gas mixture in the detection volume, as well as beam momentum and impact angle scan.

Bucharest completed the setup with a segmented TOF prototype, consisting of four partially overlapping RPC cells, combined with a single RPC cell reference TOF prototype from 2011 [6]. These two TOF modules were again tested using a $C_2F_4H_2$(90%)+SF_6(5%)+C_4H_{10}(5%) gas mixture allowing for fast signal generation. All prototypes under test as well as the the beam monitoring detectors were read out in two parallel hybrid data acquisition systems based on FLIB DAQ [8], DABC and DABC. It was the first successful in beam test of the FLES DAQ system. The CbmRoot based online monitoring was extended to incorporate all new front-end devices.

References

[1] J. Förtsch *et al.*, *The CBM RICH camera and readout chain for the 2014 CERN PS beam test*, this report

[2] M. Penschuk *et al.*, *A CBMNet bridge for the TRB3*, this report

[3] C. Bergmann *et al.*, *Test of Münster CBM-TRD real-size detector and radiator prototypes at the CERN PS/T9 beam line*, this report

[4] A. Bercuci *et al.*, *Two-dimensional MWPC prototype for CBM TRD*, this report

[5] M. Tanha *et al.*, *Construction and test of a new CBM-TRD prototype in Frankfurt*, this report

[6] M. Petris *et al.*, *Cosmic-ray and in-beam tests of 100 Ohm transmission line MGMSRPC prototype developed for the inner zone of CBM-TOF*, this report

[7] M. Krieger and P. Fischer, *Progress in TRD readout using SPADIC 1.0*, this report

[8] D. Hutter, J. de Cuveland and V. Lindenstruth, *CBM FLES input interface developments*, this report

[9] C. Garcia *et al.*, CBM Progress Report 2012, Darmstadt 2013, p. 59

---

* Work supported by BMBF and the HadronPhysics3 project financed by EU-FP7

A monitoring system for radiation hardness tests of electronic components for future FAIR experiments

S. Löchner and P. Koczoń
GSI, Darmstadt, Germany

Electronic components installed in the field of reaction products in future experiments at FAIR have to be radiation hard. At present, selected parts undergo exhaustive tests with use of intense minimum ionising particles' beams, mostly 3 GeV protons at Jülich sychrotron facility. A control system based on ARDUINO processor has been developed to monitor the components status in situ.

For components like DC/DC converters or LDO voltage stabilisers the output voltage level as well as expected transient voltage spikes rate has to be monitored during irradiation. Voltage level monitoring (input and output) requires relatively low readout frequency below 1 Hz and can be implemented on inexpensive ARDUINO-Nano system (Fig.1). It is programmed to control an optocoupler based set of relays to govern applied input voltages (for each of 12 channels separately) and reading an ADC values of output voltages for each channel. System supervises the output voltage level and - if needed - switches off the malfunctioning channels to avoid its influence on other DUTs. Measurement status is logged on a local memory and displayed via implemented web server on connected clients. The control electronics has to be placed far away from the device under test in order to avoid spurious effects due to the irradiation.

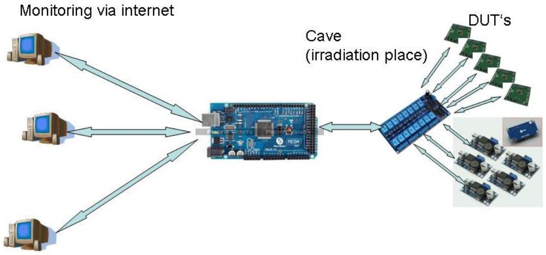

Figure 1: Block diagram of the system testing a set of DC/DC converters controlled by the ARDUINO processor

A base plate equipped with two sets of clamps and a PCB-holder has been prepared to accomodate different devices under test (DUTs) (Fig. 2). They have to be placed in a row such that the irradiating beam punches through all of them. A small scintillator placed on the beam axis behind tested chips and read out by a photomultiplier monitors the beam intensity. Its signals are also registered by ARDUINO system on separate counter and stored with time stamps spill by spill. This information helps to estimate precisely beam intensity integral. One raw of electrical clamps is supplied with input voltage (controlled by ARDUINO via set of relays) for the DUTs. Their outputs are wired via second clamps raw to the multiplexer and ADC on controller board to supervise output voltage levels.

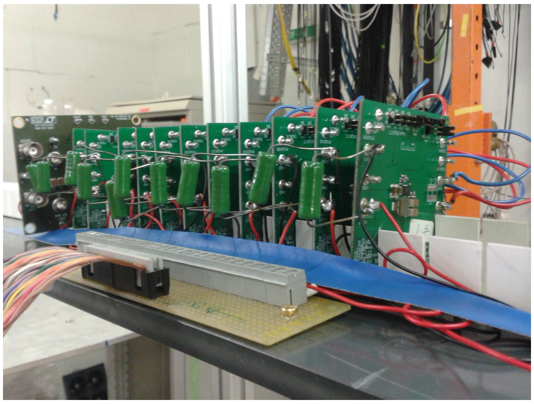

Figure 2: Base plate with PCB card holder and wiring

The processor itself can be programmed in a C-like programing language with use of different libraries to serve standard functionality (time server, SD-card I/O, internet I/O). The main loop of the program consists of output voltage check channel by channel, input voltage check, counter readout, internet service, timer service. The voltage read out values are compared to the upper and lower threshold values which can be defined for each channel. In case of over- or under voltage in three consecutive readout steps the affected channel is switched off (Fig. 3).

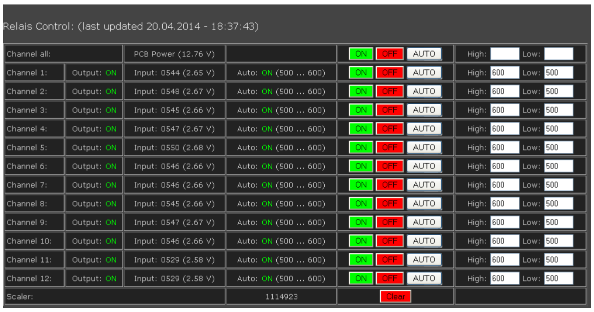

Relais Control: (last updated 20.04.2014 - 18:37:43)

Channel all:		PCB Power (12.76 V)		ON OFF AUTO	High:	Low:
Channel 1:	Output: ON	Input: 0544 (2.65 V)	Auto: ON (500 ... 600)	ON OFF AUTO	High: 600	Low: 500
Channel 2:	Output: ON	Input: 0548 (2.67 V)	Auto: ON (500 ... 600)	ON OFF AUTO	High: 600	Low: 500
Channel 3:	Output: ON	Input: 0545 (2.66 V)	Auto: ON (500 ... 600)	ON OFF AUTO	High: 600	Low: 500
Channel 4:	Output: ON	Input: 0547 (2.67 V)	Auto: ON (500 ... 600)	ON OFF AUTO	High: 600	Low: 500
Channel 5:	Output: ON	Input: 0550 (2.68 V)	Auto: ON (500 ... 600)	ON OFF AUTO	High: 600	Low: 500
Channel 6:	Output: ON	Input: 0546 (2.66 V)	Auto: ON (500 ... 600)	ON OFF AUTO	High: 600	Low: 500
Channel 7:	Output: ON	Input: 0546 (2.66 V)	Auto: ON (500 ... 600)	ON OFF AUTO	High: 600	Low: 500
Channel 8:	Output: ON	Input: 0545 (2.66 V)	Auto: ON (500 ... 600)	ON OFF AUTO	High: 600	Low: 500
Channel 9:	Output: ON	Input: 0547 (2.67 V)	Auto: ON (500 ... 600)	ON OFF AUTO	High: 600	Low: 500
Channel 10:	Output: ON	Input: 0546 (2.66 V)	Auto: ON (500 ... 600)	ON OFF AUTO	High: 600	Low: 500
Channel 11:	Output: ON	Input: 0529 (2.58 V)	Auto: ON (500 ... 600)	ON OFF AUTO	High: 600	Low: 500
Channel 12:	Output: ON	Input: 0529 (2.58 V)	Auto: ON (500 ... 600)	ON OFF AUTO	High: 600	Low: 500
Scaler:			1114923	Clear		

Figure 3: Control output of the monitoring system

References

[1] http://www.arduino.cc/

Superconducting Dipole Magnet

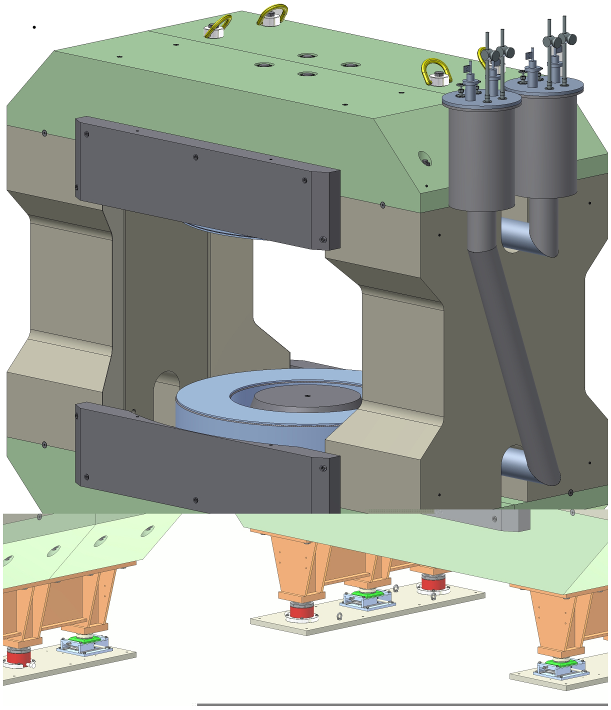

The SC dipole magnet for the CBM experiment at FAIR

A. V. Bychkov[1], *Yu. V. Gusakov*[1], *P. K. Kurilkin*[1], *V. P. Ladygin*[1], *A. I. Malakhov*[1], *G. Moritz*[2],
P. Senger[2], *and A. V. Shabunov*[1]
[1]LHEP-JINR, Dubna, Russia; [2]GSI, Darmstadt, Germany

The superconducting dipole magnet is a central part of the CBM detector system. The magnet has to provide a vertical magnetic field with a bending power of 1 Tm over a length of 1 m from the target. The magnet gap has a height of 140 cm and a width of 250 cm in order to accommodate the target station, the Micro-Vertex Detector and the Silicon Tracking System providing a polar angle acceptance of ±25° in vertical and ±30° in horizontal direction.

The CBM superconducting dipole magnet [1] is of H-type with a warm iron yoke/pole and cylindrical superconducting coils in two separate cryostats. The potted coil has 1749 turns. The wire, similar to the CMS wire, has Nb-Ti filaments embedded in a copper matrix and is soldered in a copper stabilizer with a total Cu/SC ratio of about 13 in the conductor. The operating current and the maximal magnetic field in the coils are 686 A and 3.25 T, respectively. The coil case made of stainless steel contains 20 liters of liquid helium for one coil. The vertical force in the coils is about 250 t. The cold mass is suspended from the room-temperature vacuum vessel by six suspension links. Six cylindrical support struts compensate the vertical forces.

Design calculations for the CBM superconducting dipole magnet [2] were performed using the code TOSCA for calculating the electromagnetic forces exerted on the coil, while the structural analysis for the coil case, the coil vessel and the support links was made using the code ANSYS.

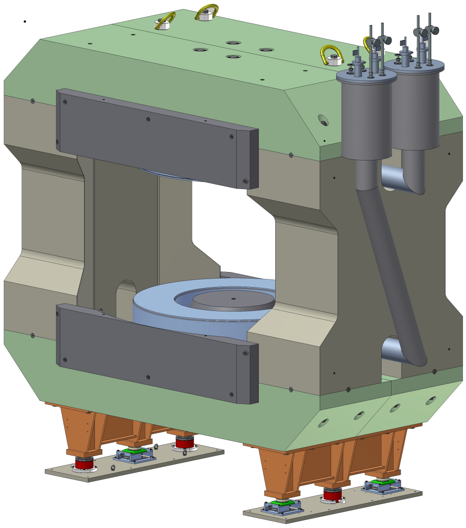

Figure 1: CBM dipole magnet with the support

The energy stored in the magnet is about 5 MJ. The magnet will be self-protecting. However, in order to limit the temperature rise to 100 K in case of a quench, the energy will be dumped in an external resistor [3].

One of the purposes of the magnet support is the vertical and horizontal adjustment of the CBM magnet. A perspective view of the CBM magnet with the support is shown in Fig.1. The magnet support consists of two support beams, each of which is placed on the base plate. The vertical adjustment of the magnet is provided by 3 hydraulic jacks. 3 roller skids are used for the adjustment in the horizontal plane. They allow to adjust the magnet position along and transversely to the beam direction as well as provide the rotation in the horizontal plane. 6 sets of the magnetic base with digital indicators are used for displacement control. The results of the stress calculation for the beam support using the ANSYS code is shown in Fig. 2. The design of the support system satisfies the CBM magnet requirements [1].

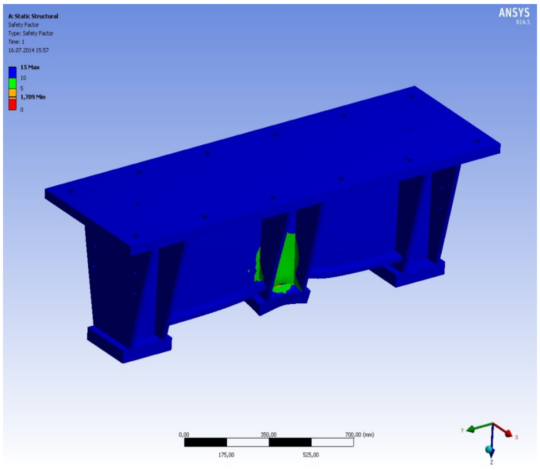

Figure 2: Results of the stress calculations for the support beam using the ANSYS code

References

[1] The CBM Collaboration, *Technical Design Report for the CBM Superconducting Dipole Magnet*, Darmstadt 2014

[2] P. Akishin *et al.*, CBM Progress Report 2013, Darmstadt 2014, p. 7

[3] P. Kurilkin *et al.*, CBM Progress Report 2013, Darmstadt 2014, p 10

3D CIEMAT code optimization for the CBM magnet quench calculation

P. Kurilkin[1]*, P. Szwangruber*[2]*, E. Floch*[2]*, F. Toral*[3]*, A. Malakhow*[1]*, and V. Ladygin*[1]
[1]LHEP-JINR, Dubna, Russia; [2]GSI, Darmstadt, Germany; [3]CIEMAT, Madrid, Spain

A superconducting dipole magnet for the CBM experiment will be constructed and installed in the CBM cave at GSI Darmstadt, Germany. The important feature of this magnet is a large gap (height of 1.4 m and width of 2.5 m) in order to accommodate the target and the Silicon Tracking System. The magnet is a H-type dipole, having circular superconducting coils. It will store about 5.15 MJ at its nominal current of 686 A. The coil design of the CBM magnet is based on the design of the FAIR Super-FRS dipole. It has 1749 turns (53 layers with 33 turns per layer). The conductor insulation consist of 2 × 0.05 mm polyimide tape and 2 × 0.1 mm glassfiber material (tape or braid), in total 0.3 mm. Detailed information about coil and conductor structure can be found in [1].

When designing the quench protection system for the magnet, it is important to perform the simulation of the quench process in the coil at different operation conditions. This note presents the results of 3D calculations done with the use of two programs. One of them is currently used at GSI [2]. The other one is based on the 3D CIEMAT code [3] modified for CBM dipole magnet calculations [1].

The calculation presented here was done for the case when no dump resistor was used for the quench protection. Both calculations take into account the inductance function $L_d(I)$ [1]. The 3D GSI calculation is performed for a uniform field distribution in the coil using the maximal values $B_m(I)$ and also for a conductor insulation (G10 tape) of 0.3 mm thickness. The modified 3D CIEMAT program takes into account the real field distribution in the coil and two layers of conductor insulation (0.1 mm Kapton, 0.2 mm G10). The additional 3D CIEMAT calculations were performed to investigate the influence of the coil field distribution and insulation properties on the simulation results.

Figs. 1 and 2 present the time dependence of the hot-spot temperature and quench voltage during the quench, respectively. The blue solid and dashed-dotted curves are the results of 3D CIEMAT and GSI computations for uniform coil field distribution and G10 conductor insulation, respectively. They give a maximum hot-spot temperature and quench voltage on the level of 130 K and 1240 V, respectively. The difference between the results calculated with the GSI and CIEMAT models is related to the different material data bases used in those programs.

The red curves present the result of 3D calculations for two layers of conductor insulation (0.1 mm Kapton, 0.2 mm G10) and a real field distribution in the coil. The maximum hot-spot temperature and quench voltage in this case are 170 K and 1200 V, respectively.

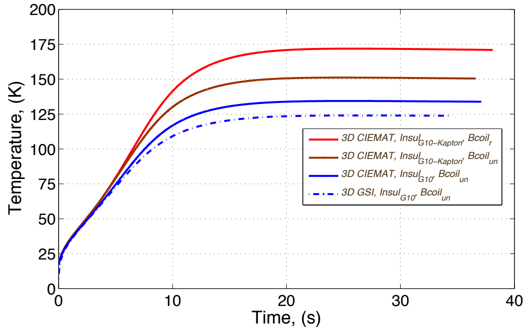

Figure 1: 3D quench calculation of the CBM dipole magnet: the hot-spot temperature

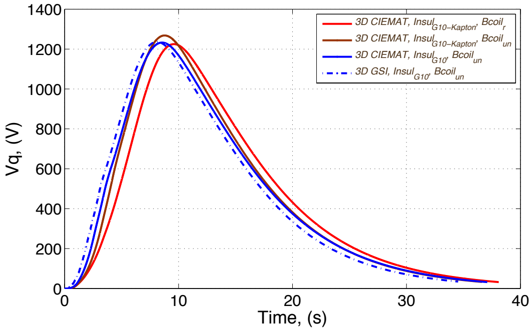

Figure 2: 3D quench calculation of the CBM dipole magnet: the quench voltage

The modification of the 3D CIEMAT program was done to perform the CBM magnet quench calculations for the case of two-layer conductor insulation of different type and real field distribution in the coil. The presented results show that the CBM dipole magnet is self-protecting.

References

[1] The CBM Collaboration, *Technical Design Report for the CBM Superconducting Dipole Magnet*, Darmstadt 2014

[2] P. Szwangruber *et al.*, IEEE Trans. Appl. Supercond. **23** (2013) 4701704

[3] F. Toral, *Design and Calculation Procedure for Particle Accelerator Superconducting Magnets: Application to an LHC Superconducting Quadrupole*, Ph. D. Thesis, Madrid 2001

[4] P. Kurilkin *et al.*, CBM Progress Report 2013, Darmstadt 2014, p. 10

A 3D model of the SC dipole magnetic field for the muon option of the CBM experiment

P. G. Akishin[1], *V. V. Ivanov*[1,2], *V. P. Ladygin*[3], *and A. I. Malakhov*[3]
[1]LIT-JINR, Dubna, Russia; [2]National Research Nuclear University ”MEPhi”, Moscow, Russia; [3]LHEP-JINR, Dubna, Russia

The superconducting dipole magnet is a central part of the CBM detector system [1]. The target station, the Micro-Vertex Detector (MVD) and the Silicon Tracking System (STS) are placed in the magnet gap, which has a height of 140 cm and a width of 250 cm in order to cover a polar angle acceptance of $\pm 25^\circ$ in vertical and $\pm 30^\circ$ in horizontal direction. The magnet has to provide a vertical magnetic field with a bending power of $\sim$1 Tm over a length of 1 m from the target. One of the options of the CBM detector includes a muon detection system (MuCH), which consists of 6 hadron absorber blocks and 6 tracking detector triplets placed downstream of the magnet [2]. This report presents calculations of the magnitude of the magnetic field and of the acting forces on the MuCH detector.

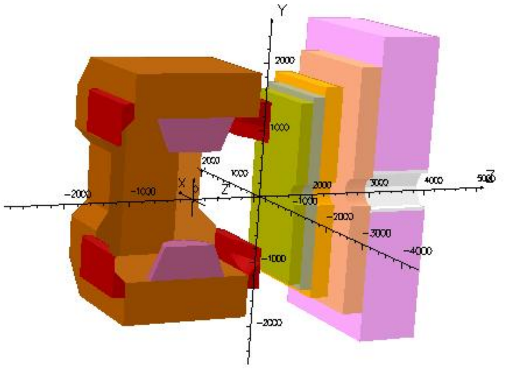

Figure 1: 3D model for the CBM SC dipole magnet with MuCH system

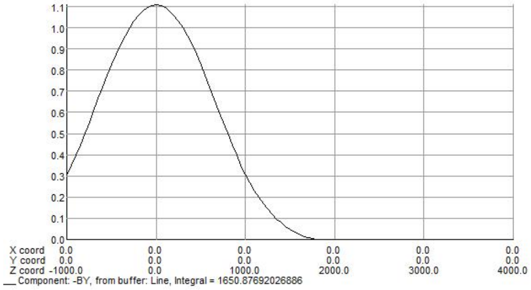

Figure 2: Distribution of the vertical magnetic field component B_y (in T) along the beam direction

One half of a simplified 3D model of the CBM SC dipole magnet with MuCH system is shown in Fig. 1. It is assumed that the first absorber and the supporting structure of the MuCH system are made from non-magnetic materials. The magnetic field calculations were performed using the 3D TOSCA code [3]. Two planar symmetries of the magnetic field were used in the modeling. The current density was taken as 43.93 $\mathrm{A/mm^2}$, which provides a total current through one coil of 1.121 MA. The calculated stored energy is 4.592 MJ. The distribution of the vertical magnetic field component B_y along the beam direction is presented in Fig. 2. The maximal value of B_y is $\sim$1.1 T with a field integral of $\sim$1 Tm.

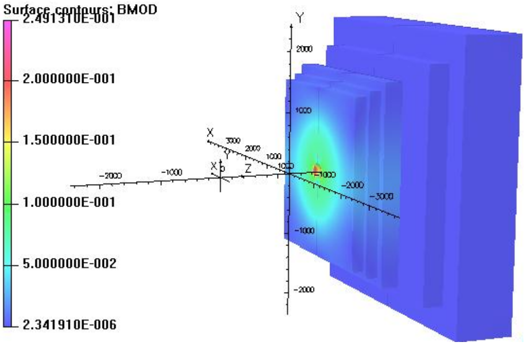

Figure 3: Magnetic field in the MuCH absorber

Fig. 3 shows the distribution of the magnetic field in the MuCH absorber. The maximal value of the magnetic field of $\sim$0.25 T is in the center of the first absorber.

The results of the calculations for the forces acting on the MuCH absorbers are presented in Table 1. These forces are negligible for the last two absorbers.

Table 1: Forces acting on the MuCH absorbers

No. of absorber	2	3	4	5	6
Force $[N]$	1358	459	174	0.06	0.1

References

[1] The CBM Collaboration, *Technical Design Report for the CBM Superconducting Dipole Magnet*, Darmstadt 2014

[2] S. Ahmad *et al.*, Nucl. Instrum. Methods **A 775** (2014) 139

[3] OPERA-3d User Guide, http://www.lepp.cornell.edu/critten/opera/user-3d.pdf

Micro-Vertex Detector

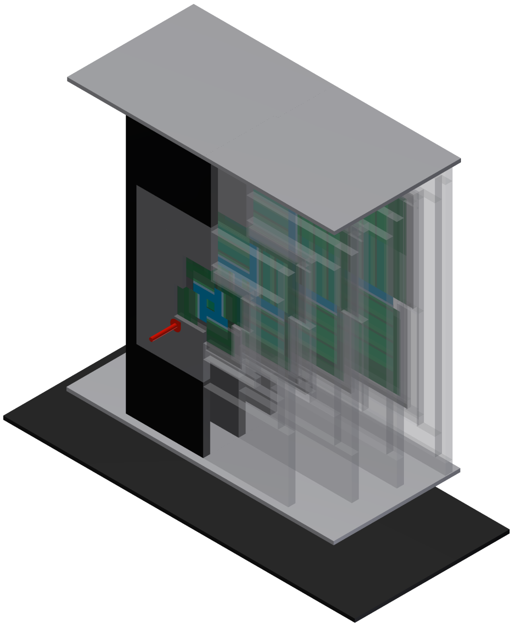

Non-ionizing radiation hardness of CMOS Monolithic Active Pixel Sensors manufactured in a 0.18 μm CMOS process*

D. Doering[1], *M. Deveaux*[1], *B. Linnik*[1], *and J. Stroth*[1,2] *for the CBM-MVD collaboration*
[1]Goethe-Universität, Frankfurt, Germany; [2]GSI Darmstadt, Germany

Modern 0.18 μm CMOS processes provide numerous features which may allow for decisive progresses in the read-out speed and the radiation tolerance of the CMOS Monolithic Active Pixel Sensors (MAPS) to be used in the Micro-Vertex-Detector of CBM. Together with the PICSEL group of IPHC Strasbourg, we aim to exploit those features by migrating the successful architecture of our sensors toward this novel technology. This work reports about our findings on the first prototypes manufactured with the new technology.

A weak point of CMOS sensors is the slow diffusion of signal charge in the undepleted active medium. A sufficient radiation hardness was only achievable with very small pixels, which do not provide the required readout speed. A few years ago, this obstacle was alleviated by the upcoming availability of CMOS processes providing a high-resistivity epitaxial layer of 1 $\mathrm{k\Omega cm}$. It could be demonstrated that this increases the non-ionizing radiation hardness by more than one order of magnitude. Therefore pixels of this high-resistivity AMS-0.35-process having a pitch of $20-30$ μm achieved the design goal of a non-ionizing radiation hardness in the order of $10^{13}\ \mathrm{n_{eq}/cm^2}$ [1]. Using this technology, a first vertex detector based on CMOS sensors is taking data in the heavy-ion experiment STAR since 2014.

While achieving the required non-ionizing radiation hardness, the ionizing radiation hardness and read-out speed of sensors in the AMS-0.35-process were not sufficient for the application in modern vertex detectors, e.g. in ALICE and CBM. Therefore, a novel $TOWER-0.18$ μm process was exploited and found to provide a higher tolerance to ionizing radiation [2]. Moreover, the smaller feature size allows for the integration of a more complex logic into the pixel, providing a faster read-out. An additional feature of this process is the use of very high-resistivity epitaxial layers up to 6 $\mathrm{k\Omega cm}$. It was expected that this would improve the non-ionizing hardness further, which would allow for larger pixels and therefore for a faster sensor readout.

To test this assumption, the prototype sensor MIMOSA-34 was designed, irradiated to $10^{13}\ \mathrm{n_{eq}/cm^2}$ and tested hereafter. The sensor provides elongated pixels with a pixel pitch between 22 μm × 33 μm and 33 μm × 66 μm. Figure 1 shows the response of the largest pixel to photons from a Fe-55 source. The charge collection efficiency is reduced by radiation damage from 34% to 25% for the seed pixel and from close to 100% to 62% for the charge of the full cluster. The signal to noise ratio, as measured with a Sr-90-β-source, decreases from 49 to 35. According to our experience with other sensors, this signal to noise ratio is sufficient to provide an excellent detection efficiency.

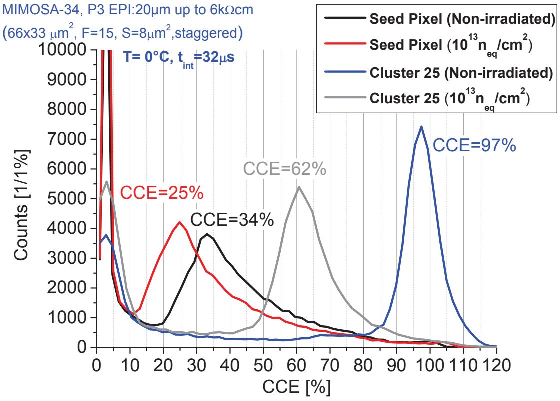

Figure 1: Signal response to photons after a radiation dose of $10^{13}\ \mathrm{n_{eq}/cm^2}$.

In conclusion, the novel process is likely to provide a tolerance to $10^{13}\ \mathrm{n_{eq}/cm^2}$ as needed for CBM even in combination with a 33 μm × 66 μm pixel pitch. Consequently, this pitch seems now limited by the need for matching a spatial resolution of 5 μm rather than by the radiation tolerance. The latter allows for increasing the pixel pitch of the vertex detector, which comes with significant advantages in terms of readout speed and reduced power consumption.

References

[1] D. Doering *et al.*, Nucl. Instrum. Methods **A 739** (2013) 111

[2] D. Doering *et al.*, JINST **9** (2014) C0551

---

* Work supported by BMBF (05P12RFFC7), HIC for FAIR and GSI

Yield studies on a fully integrated sensor for the CBM-MVD*

B. Linnik[1], *D. Doering*[1], *M. Deveaux*[1], *and J. Stroth*[1,2] *for the CBM-MVD collaboration*
[1]Goethe-Universität, Frankfurt, Germany; [2]GSI Darmstadt, Germany

The CBM experiment will study the phase diagram of hadronic matter in the region of highest baryon densities by means of rare probes like open charm particles. Reconstructing those particles calls for a vertex detector providing a unique combination of excellent spatial resolution, light material budget and high rate capability. To match those requirements, we intend to use CMOS Monolithic Active Pixel Sensors, which are developed by the PICSEL group of IPHC Strasbourg and evaluated at the IKF Frankfurt within a common R&D project.

A first fully integrated sensor, MIMOSA-28, was developed in the AMS $0.35\ \mu\mathrm{m}$ CMOS process and is used in the STAR-HFT since 2014. However, this sensor does not match the requirements of CBM regarding radiation tolerance and readout speed. Therefore, the sensor architecture was migrated to a novel $0.18\ \mu\mathrm{m}$ process. This process was found to provide a higher tolerance to ionizing radiation [1]. Moreover, its higher packing density allows for reading two lines in parallel, which accelerates the readout by a factor of two with respect to the older design.

In 2014, a first fully integrated prototype sensor (FSBB-M0) was realized in the new process [2]. The sensor was realized in two flavors (FSBB-M0a and FSBB-M0b), which differ slightly in the dimensions of some transistors. It features 416×416 pixels of $22 \times 33\ \mu\mathrm{m}^2$ pitch and is read out within $40\ \mu\mathrm{s}$ via a pair of discriminators at the end of each column. Hereafter, the digital data is zero-suppressed and sent out via two 320 Mbps digital links. The sensitive surface of the FSBB is $13.7 \times 9.2\ \mathrm{mm}^2$. The final sensor of the CBM-MVD will presumably consist of three FSBBs. The FSBB-M0 was tested at the CERN-SPS and provided a detection efficiency for minimum ionizing particles of $\gtrsim 99,5\%$, a noise occupancy of $\lesssim 10^{-5}$ and a spatial resolution of $< 5\ \mu\mathrm{m}$ in both dimensions [3], which matches the requirements of CBM.

To test the robustness of the design and to assess the production costs for the CBM-MVD, we measured the production yield of the FSBB. In accordance with our experience, we assumed that flaws due to production mistakes would turn into a measurable deterioration of the noise of the sensors. A total of 25 (17 FSBB-M0a and 8 FSBB-M0b) sensors was bonded on PCB and operated with a suited readout system. By measuring the transfer functions we revealed the temporal noise (TN) of the individual pixels and the fixed pattern noise (FPN), which is caused by the offset of the dark signal of the pixels.

The results of the study on the FSBB-M0a are shown in Fig. 1. We found all tested sensors to be operational, and they provided a $\mathrm{TN} = (0.70 \pm 0.05)\ \mathrm{mV}$ and $\mathrm{FPN} = (0.73 \pm 0.14)\ \mathrm{mV}$. Only one of the tested sensors showed a higher FPN of $\sim 1.2\ \mathrm{mV}$, which might still be acceptable. Similarly good results (not shown) were obtained with the eight tested FSBB-M0b, all found to be operational.

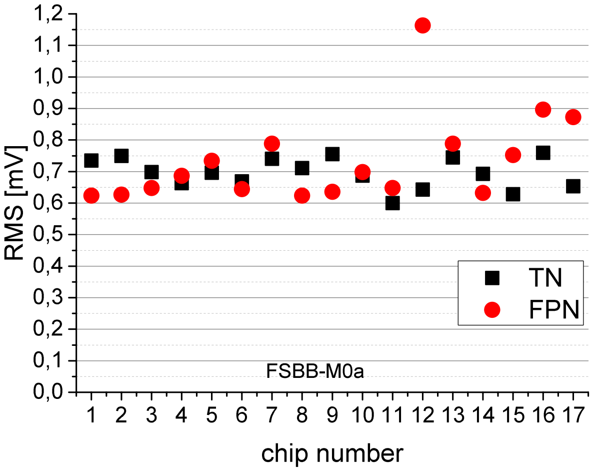

Figure 1: Temporal noise and fixed pattern noise measurement of all 17 FSBB-M0a chips.

We conclude that a first full-size sensor meets the requirements of CBM with respect to surface size, data rate and spatial resolution. Moreover, the design mostly meets the specification in terms of readout speed. Measurements demonstrated that the sensor provides a good detection of minimum-ionizing particles, and the production yield was found to exceed 95%.

References

[1] D. Doering *et al.*, JINST **9** (2014) C0551
[2] F. Morel *et al.*, JINST **9** (2014) C01026
[3] M. Winter, private communication

---

* Work supported by BMBF (05P12RFFC7), HIC for FAIR, HGS-HIRe and GSI

An ultra-low material budget Cu-based flexible cable for the CBM-MVD*

P. Klaus[1], *J. Michel*[1], *M. Wiebusch*[1], *M. Koziel*[1], *T. Tischler*[1], *S. Schreiber*[1], *C. Müntz*[1], *and J. Stroth*[1,2] *for the CBM-MVD collaboration*
[1]Goethe-Universität Frankfurt; [2]GSI, Darmstadt, Germany

The CBM Micro-Vertex Detector (MVD) relies on employing a material budget x/X_0 per detector station of 0.3% (first station) to 0.5% (following stations) to allow for a secondary vertex resolution of better than 70 μm with typical pixel pitches of about 20 μm. To reach this ambitious goal, all components in the acceptance of the detector have to be challenged w.r.t. their impact on the material budget, while at the same time maintaining their cutting-edge performance regarding mechanical and electrical properties as well as radiation hardness. In addtion, the sensor readout has to be robust with low noise occupancy, which puts strong constraints on the electrical properties of the rather long cables connecting the sensors with the front-end electronics (FEE) being outside the acceptance of the detector. Especially in the outer stations, substantial parts of those cables are placed inside the acceptance and hence contribute to multiple scattering. Those cables are flexible printed circuits (FPC) and provide power to the CMOS Pixel Sensors (CPS), allow to control them, and to read out the hits. The previous-generation cable was not specifically optimized for ultra-low material budget, being a two-layer copper-based cable with a layer thickness of about 25 μm. It was successfully tested in a beamtime with the CBM-MVD prototype [1].

Reducing the dominant factor of the material budget meant reducing the thickness of the copper layer, see Tab. 1. The cable was redesigned with a readout to the side (see Fig. 1), a smaller feature size (80 μm) and thus a reduced total cable width, and copper traces with a thickness of only 12 μm. The cables were manufactured using a commercial technology offered by ILFA [2].

Table 1: Material budget of the new cable.

Layer	d [μm]	x/X_0	Si-equiv [μm]
Coverlay	26	0.009 %	8.6
Copper	40% · 12	0.033 %	31.3
Polyimide	25	0.009 %	8.2
Sum	63	0.051 %	48.1

Some problems may arise from the ultra-thin layout though: Without an accompanying ground layer, the traces will not have an excellently controlled impedance. In addition, the resistance of the power supply lines becomes substantial. To compensate for this, their width was increased to 360 μm resulting in visible areas of higher material budget in Fig. 1. Dedicated tests with a new sensor test stand will evaluate the effect of the missing shielding and possible impedance mismatch of signal lines as well as the higher resistance of the power supply lines. This test stand comprises a compact, Peltier-based temperature control unit, and a readout chain using a special test mode of the sensor which makes it possible to measure transfer functions. This allows to deduce the temporal and fixed pattern noise of a reference sensor to conduct extensive systematic tests of flex cable generations.

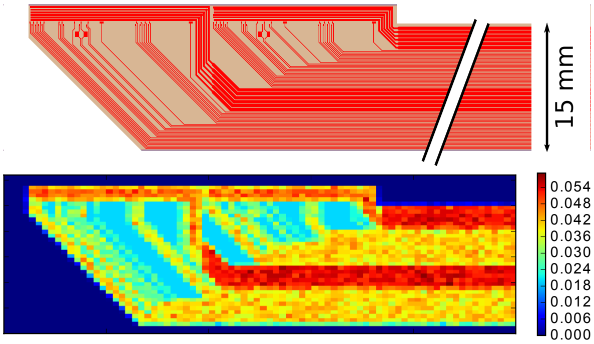

Figure 1: CAD layout of the new ultra-thin FPC showing the bonding zone and the part of the cable situated in the acceptance of the detector (top); an analysis of its material budget in % of x/X_0 (bottom).

Another possible approach to reach an even smaller material budget employs Aluminium instead of Copper for the conductive layer. Aluminium has a smaller conductivity (3.5010^7 S/m vs. $5.96 \cdot 10^7$ S/m) but at the same time a much larger radiation length (88.97 mm vs. 14.36 mm), suggesting an improvement in the material budget by a factor of 3.6. The downside of this non-standard Aluminium-based technology is the lower production reliablity, and thus higher cost and production times.

To summarize, a new ultra-thin design of the FPC for the CBM Micro-Vertex Detector was created and the cables produced. Its suitability will be analyzed including its electrical performance and integration stability. Further technologies to reduce the material budget even more are being evaluated.

References

[1] M. Koziel *et al.*, Nucl. Instrum. Methods **A 732** (2013) 515

[2] ILFA Industrieelektronik und Leiterplattenfertigung aller Art GmbH, Hannover, Germany

---

* Work supported by BMBF (05P12RFFC7), HIC for FAIR and GSI

PRESTO: PREcursor of the Second sTatiOn of the CBM-MVD[*]

M. Koziel[1], *T. Tischler*[1], *C. Müntz*[1], *and J. Stroth*[1,2] *for the CBM-MVD collaboration*
[1]Goethe-Universität, Frankfurt, Germany; [2]GSI Darmstadt, Germany

This report summarizes the activities undertaken to construct a precursor of a quadrant of the second MVD station.

The PRESTO (PREcursor of the Second sTatiOn) project of the CBM-MVD addresses the double-sided integration of 15 MIMOSA-26 sensors (dummies and working sensors, 9 of these on the front in a 3×3 and 6 sensors on the back in a 2×3 arrangement) onto a 8×8 cm^2 CVD diamond carrier [1] featuring a thickness of 150 μm. The PRESTO module will employ new flex cables (FPC) [2] providing all signals needed to operate and read out the sensors (10 FPCs in total), see Fig. 1.

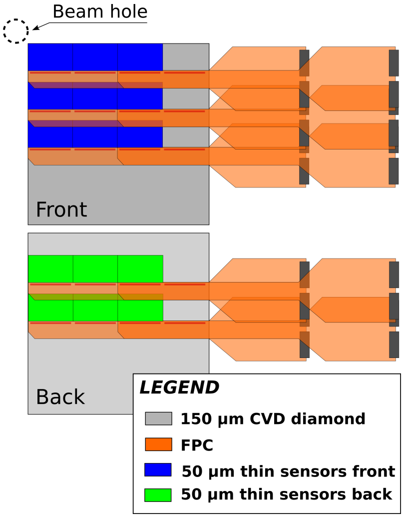

Figure 1: Sketch of the arrangement of the sensors and the FPCs with respect to the support carrier within the PRESTO module.

For the assembly of this module, new sensor positioning jigs aiming for a sensor positioning precision with respect to the support and the neighboring sensors of below 100 μm were manufactured. To evaluate the integration concept, the RAL-247 adhesive [3] and the new jigs, a dummy PRESTO module was assembled employing 50 μm thin MIMOSA-26 dummies and a 200 μm thin glass plate which serves as sensor carrier (Fig. 2).

In the process of gluing, the inclusion of air bubbles should be avoided because of the vacuum operation of the MVD and the use of thinned sensors. This triggered a study focusing on optimizing the preparation of the glue, its dispensing and the quality assurance of the results. The number of air bubbles introduced into the glue during its mixing process was significantly reduced by degassing it in an exicator at about $4 \cdot 10^{-1}$ mbar for about one hour. However, this did not prevent the air bubbles to appear after the gluing of the sensors onto the carrier. The introduced air bubbles featured a size of about $100 - 300$ μm diameter. To verify their impact on the 50 μm thin sensor dummies, the cured module was placed inside a small vacuum chamber which had been evacuated for about 48 hours to a level of $4 \cdot 10^{-1}$ mbar. The visual inspection of the sensor dummies using a high-precision microscope did not reveal any mechanical damage. Further studies will be addressed with working sensors to check on-the-fly any possible correlation between sensor performance, pressure and bubble sizes.

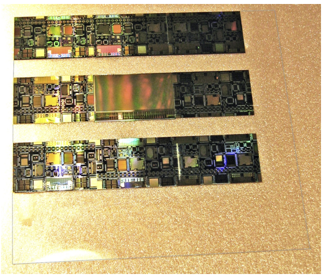

Figure 2: Assembled dummy module of PRESTO.

The gluing of the dummy sensors onto the glass carrier demonstrated that a glue volume of $3 - 5$ μl (different glue volume used for each row of sensors) is sufficient to dispense a uniform and thin (about $10 - 17$ μm) layer underneath the sensors. The horizontal sensor-to-sensor distances were measured to be below 5 μm. The vertical variation in the distances between the sensor edges were measured to be of about 20 μm. The achieved precision is significantly below the envisioned one. Next steps comprise the establishing of procedures for the integration of the FPCs, the exercise of double-sided bonding and the verification of the vacuum compatibility.

References

[1] Diamond Materials GmbH, Germany

[2] P. Klaus *et al.*, *An ultra-low material budget Cu-based flexible cable for the CBM-MVD*, this report

[3] Private communication, Simon Canfer Rutherford Appleton Laboratory, Composites and Materials Testing Group, UK

---

[*] Work supported by BMBF (05P12RFFC7), EU-FP7 Hadron-Physics3, HGS-HIRe, GSI and HIC for FAIR

Assessing the vacuum compatibility of the CBM Micro-Vertex Detector*

G. Kretzschmar[1], *M. Koziel*[1], *C. Müntz*[1], *T. Tischler*[1], *M. Deveaux*[1], *and J. Stroth*[1,2]
[1]Goethe-Universität, Frankfurt, Germany; [2]GSI, Darmstadt, Germany

The CBM Micro Vertex Detector (MVD) will operate in a moderate vacuum of about 10^{-4} mbar to minimize multiple scattering. The vacuum compatibility of the detector needs to be validated with respect to thermal management of the MVD stations and their mechanical integrity during the design and prototyping phase. A dedicated large-volume vacuum vessel, located at IKF Frankfurt, allows for systematic studies on the selection of material, the detector operation and thermal management in vacuum.

The setup comprises a 260 liter stainless steel vacuum chamber with multiple flanges providing a flexible access setup inside. Full-size MVD modules can be housed and operated, see Fig. 1 (right). The chamber is supplied with a combination of rotary and turbomolecular pumps to routinely reach pressures of $2 \cdot 10^{-6}$ mbar, despite of the chamber volume and the variety of feedthroughs for signals and cooling media. The pressure is measured with a penning/pirani sensor system. Special emphasis is put on operating the detector at temperatures below room temperature and hence, providing active cooling inside the vessel is mandatory.

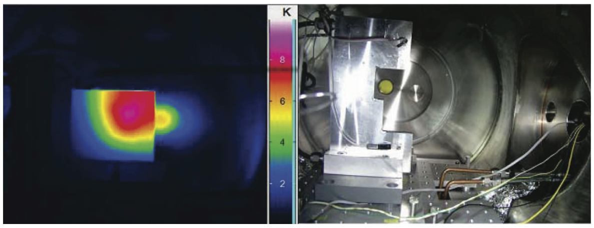

Figure 1: Left: IR picture, taken at 10^{-4} mbar, of a dedicated heater featuring 1.12 W/cm^2 attached to a copper carrier and heat sink, used to characterize the setup. Right: Full-size half-station heat sink of the first MVD station located in the vacuum chamber.

To characterize cooling media and to select a reliable concept of piping inside the vacuum, a dedicated setup was constructed, based on copper pipes and Swagelok fittings. The circuit inside the vacuum chamber was connected to a commercial cooling system (HUBER). With standard silicone oil as cooling liquid, circulated at atmospheric pressure, no leak was observed. However, at pressure of 10^{-2} mbar and after one week of pumping, residues of the coolant were spotted on the pipe connectors inside the vacuum. Finally, the coolant was changed to glycol, and no leaks were observed any longer, neither when replacing the copper pipes bypolyurethane pipes. These studies underline the need of a careful preparation of reliable pipe interconnections and suggest not to employ coolants which feature strong creeping, like silicone oil.

Outgassing of materials has to be kept at a minimum, both to not spoil the vacuum close to the target and to avoid contamination of surfaces. The setup allows to characterize coarse outgassing of detector components, like (flex) cables, adhesives or electronic components, by employing the so-called throughput method or the gas accumulation method [2]. However, outgassing measurements with higher accuracy request a large probe area compared to the setup area, and hence a dedicated setup.

Evaluating the thermal management of the MVD modules in vacuum is one of the most pressing tasks to be assessed with the setup presented here. Emphasis is put on heat sinks and sensor carriers based on high-performance materials like chemical vapor deposition (CVD) diamond and thermal pyrolitic graphite[1] (TPG). The evaluation is carried out by contact temperature sensors (DS1820) in combination with a high-resolution infrared camera positioned outside of the chamber, observing through a dedicated zincselenide window transparent for infrared. The contact sensors serve as a reference for the infrared-based characterization of the detector setup, and they allow at the same time for a proper calibration of IR camera with respect to the reflectivity of materials and reference measurements. To emulate the expected MVD-sensor heat dissipation, Kapton flexible heaters from OMEGA [3] are glued on materials under evaluation, see Fig. 1.

It is planned to characterize in vacuum full-size detector prototypes like PRESTO (PREcursor of the Second sTatiOn) [1], with a focus on the long-term operation of MVD modules in vacuum.

References

[1] M. Koziel *et al.*, *PRESTO: PREcursor of the Second sTatiOn of the CBM-MVD*, this report

[2] P. A. Redhead, *Recommended practices for measuring and reporting outgassing data*, National Research Council, p. 4, Ottawa ON K1A 0R6, Canada

[3] OMEGA Engineering, INC., `www.omega.com`

---

* Work supported by BMBF (05P12RFFC7), HIC for FAIR and GSI

[1] These materials are selected due to their outstanding heat conductivity, allowing at the same time a minimum material budget, which represents another important constraint for the MVD.

The CBM-MVD: Progress in mechanical integration*

M. Koziel[1], *T. Tischler*[1], *C. Müntz*[1], *M. Deveaux*[1], *and J. Stroth*[1,2] *for the CBM-MVD collaboration*
[1]Goethe-Universität, Frankfurt, Germany; [2]GSI Darmstadt, Germany

This report summarizes the activities undertaken towards the construction of the Micro Vertex Detector (MVD) of the Compressed Baryonic Matter (CBM) experiment.

Quality assurance of 50 µm thin PRESTO sensors. Thinned MIMOSA-26 sensors will be used for assembling the so called PRESTO module. PRESTO addresses the double-sided integration of 15 MIMOSA-26 sensors (dummies and working sensors) onto a 8×8 cm^2 CVD diamond support (see [1] for more details). Sensors will be connected with the R/O system by means of a newly designed ultra-low material budget flex cable employing commercially available processes based on copper traces [2]. Constructing the PRESTO allows to estimate the integration yield providing that the employed sensors are tested prior to assembly. Up to now, 18 MIMOSA-26 AHR sensors thinned to 50 µm were probe tested using the setup described in [3]. The setup allows to test the standard operation modes of the sensor as well as to measure the fixed pattern and temporal noise by the means of so called s-curves. 12 sensors were found without a significant number of dead/noisy pixels; they were qualified as fully operational. Four sensors exhibiting some dead rows/columns were marked as faulty. The two remaining sensors were not operational because of a power supply short (one sensor) and problems while powering one out of the four MIMOSA-26 sub-matrices. The estimated yield was then of about 65%, which is in agreement with expectations for this type of sensors [4]. The temporal noise was found to be about 1.6-1.8 mV and the fixed pattern noise about 0.5-1.0 mV, which is by a factor of 2-3 higher than the noise specified by the sensor provider. This was nevertheless as expected since the sensor power signals were generated outside the probe card. The addressed probe tests allowed also to establish test procedures required for non-destructive tests of thinned CMOS sensors and can be applied for testing the final MVD sensors.

Development of a custom made glue. An "ideal" adhesive for the integration of the sensors onto their supports should be easy to dispense in a thin and uniform layer – calling for a low viscosity –, radiation hard as well as flexible (to compensate for the thermal expansion mismatches between the sensor and their support material) within the temperature range foreseen for the operation of the MVD sensors. Since there are none "on-shelf" products that meet these requirements, a custom-made, two compound adhesive with the working name RAL-247 was manufactured at the Rutherford Appleton Laboratory (RAL), Composites and Materials Testing Group, UK. The glue features a glass temperature of -45 °C, a viscosity of below 100 mPa·s and a curing time of 48 h at +50 °C. To investigate its radiation hardness, RAL-247 samples were irradiated with X-rays to 100 Mrad and to a proton dose of about 10^{15} n_{eq}/cm^2. The irradiated samples were sent to RAL for further Dynamic Mechanical Analysis tests which unraveled no significant change of properties [5], confirming the expected radiation hardness in the range of radiation doses expected for the MVD.

Development of the heat sinks for the MVD. The operation of the MVD in vacuum requires a continuous cooling of the sensors to limit radiation-induced defects as well as noise. To keep the material budget of the individual MVD station as low as possible, the cooling approach of the MVD employs highly thermal conductive sensor support materials (CVD diamond [6] and encapsulated high performance graphite) in the acceptance of the MVD and actively cooled aluminum-based heat sinks outside of this area. To evaluate the cooling concept and its vacuum compatibility, half-station heat sinks of the first three MVD stations were manufactured at COOLTEK GmbH. The heat sinks incorporate a buried cooling pipe and were thermally simulated prior their manufacturing, using a worst case scenario for the sensor power dissipation plus an additional safety factor of four. These heat sinks are currently being evaluated under laboratory conditions focusing on their vacuum compatibility [7]. The heat dissipation of the MVD sensors is provided by Kapton-insulated flexible heaters from OMEGA Engineering, INC.

References

[1] M. Koziel *et al.*, *PRESTO: PREcursor of the Second sTatiOn of the CBM-MVD*, this report

[2] P. Klaus *et al.*, *An ultra-low material budget Cu-based flexible cable for the CBM-MVD*, this report

[3] M. Koziel *et al.*, CBM Progress Report 2014, Darmstadt 2013, p. 14

[4] L. Greiner *et al.*, CPIX 2014, Bonn, Germany

[5] Private communication, Simon Canfer Rutherford Appleton Laboratory, Composites and Materials Testing Group, UK

[6] Diamond Materials GmbH, Germany

[7] G. Kretzschmar *et al.*, *Assessing the vacuum compatibility of the CBM Micro-Vertex Detector*, this report

---

* Work supported by BMBF (05P12RFFC7), EU-FP7 HadronPhysics3, HGS-HIRe, GSI and HIC for FAIR

The CBM MVD read-out electronics*

M. Wiebusch[1], *J. Michel*[1], *M. Koziel*[1], *B. Milanovic*[1], *S. Amar-Youcef*[1], *P. Klaus*[1], *and J. Stroth*[1,2] *for the CBM-MVD collaboration*

[1]Goethe-Universität Frankfurt; [2]GSI, Darmstadt, Germany

Electronics

The CBM Micro-Vertex-Detector (MVD) front-end electronics serve as an intermediating device between the Monolithic Active Pixel Sensors (MAPS) and the DAQ system (based on the TRB3 system developed by HADES). In the current connection scheme, one TRB3 FPGA board can support up to 16 sensors of type "MIMOSA-26" in parallel. The front-end electronics are necessary to supply the sensors with electrical power and to convert between different digital signal standards. The central element of these custom-built PCBs is the converter board. In addition to remotely controlled power supplies, signal switches and drivers, it features an ADC section to monitor the sensor's momentary electrical parameters. The sensors have to be supplied with a sensitive external biasing voltage, the so-called clamping voltage, which gets distributed to all sensor pixels. Several generation and distribution schemes were implemented to investigate which setup results in the best noise performance.

Measurements

The MIMOSA-26 provides a test mode to measure the discriminator transfer function[1] of all pixels. The slope steepness is directly related to the temporal noise of the sensor. The read-out sytem was extended to operate and read out the sensor in this test mode. The recorded data is evaluated by a dedicated ROOT-based analysis software. Noise tests with MIMOSA-26 are ongoing. However, preliminary results concerning the influence of the clamping voltage suggest that it is beneficial to generate this reference voltage as close to the sensor as possible and to use decoupling capacitors, if possible, next to the bonding pads on the flex print cable. These results are in particular important for the development of the next generation of cables [2]. Furthermore, the ADC section on the converter board can be used to perform systematic scans in order to characterize the sensors. As an example of such an automatic scan, Figure 1 shows the dependence of the sensor's current consumption on the discriminator threshold setting.

Laboratory instrumentation

When characterizing sensors, it is desirable to investigate the temperature dependence of certain sensor parameters. Until recently, such tests were conducted using a large cooling system which circulates coolant through a cooling block to which the sensors under test are attached. The sensors are now operated on a small copper platform which is cooled with a peltier element. A PID controller implemented on a micro-controller senses the temperature of the platform by means of a onewire temperature sensor and regulates the current through the peltier element. The device features a small display and a simple user interface; alternatively it can be remotely controlled via a USB connection. The platform can be cooled down to circa $-10\,^{\circ}\mathrm{C}$ within few minutes while consuming $50\,\mathrm{W}$. Overall, the set-up was greatly reduced in size, while at the same time improved in usability.

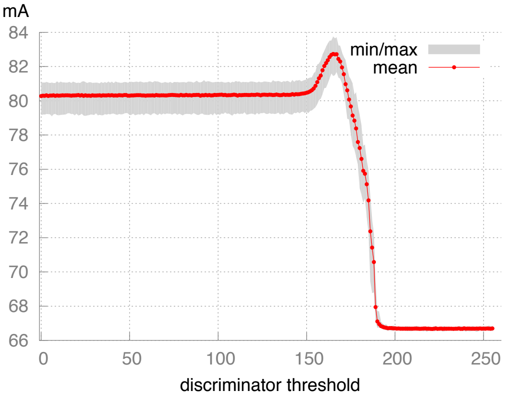

Figure 1: The current consumption (digital VCC) of a MIMOSA-26 sensor as a function of the discriminator threshold. The data were acquired with front-end electronics on-board monitoring devices.

PRESTO

Current activities focus on building a prototype [1] of a quadrant of the second station of the MVD. For now, MIMOSA-26 sensors are used in this project though they do not qualify to be used in the final detector. Parts of the front-end electronics are currently redesigned to fit the spacial constraints of the set-up.

References

[1] M. Koziel *et al.*, *PRESTO: PREcursor of the Second sTatiOn of the CBM-MVD*, this report

[2] P. Klaus *et al.*, *An ultra-low material budget Cu-based flexible cable for the CBM-MVD*, this report

---

* Work supported by BMBF (05P12RFFC7), HIC for FAIR and GSI

[1] The firing probability of a binary pixel as a function of discriminator threshold; it usually has the form of a sigmoid function.

Silicon Tracking System

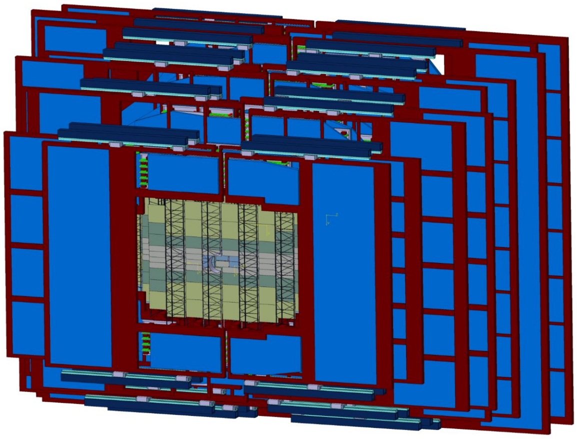

Charge collection in STS silicon microstrip sensors at their surface layer*

I. Panasenko[1], *V. Dobishuk*[1], *J. Heuser*[2], *V. Kyva*[1], *V. Militsiya*[1], *Ie. Momot*[1,3], *V. Pugatch*[1], *and M. Teklishyn*[1]

[1]KINR, Kiev, Ukraine; [2]GSI, Darmstadt, Germany; [3]Goethe-Universität, Frankfurt, Germany

To provide radiation tolerant devices for the CBM experiment (Silicon Tracker Station) prototypes of silicon microstrip sensors have been produced in two technologies. For the short-long stereo-strips connection, either double-metallization lines ("double metal" sensor) or a single-metallization design with an external microcable ("single metal" sensor) have been manufactured. We report here the results of studies performed for those sensors with the Pu (triplet) alpha-source and laser (640 nm wavelength). Both methods provide test of the charge collection at the sensor surface layer where double metallization is laid out. Measurements were carried out exploring discrete electronics and the fast-slow coincidences setup at KINR. This allows studying a charge sharing between adjacent strips of the silicon sensor hit by alphas or laser pulses. The degradation of the cluster finding efficiency in the vicinity to the double-metal connecting lines in heavily irradiated microstrip silicon sensors has been observed [1].

The CBM05H4 'double metal' and 'single metal' (HAMAMATSU) sensors were full depleted at 80 V. In a two-dimensional (E_i x E_{i+1}) energy distribution of events in adjacent strips 'i' and '(i+1)' three loci for ^{239}Pu, ^{238}Pu and ^{233}U alpha-particles source are shifted by $\sim$ 20 % to lower energies for the double metallization sensor in comparison with the single metal one. Also the widths of loci are larger. The evaluation shows that this could be explained by the alpha-particles energy loss and straggling in the SiO_2 isolation layer present only in the sensor with a second metallization layer. Biasing voltage scan has demonstrated expected performance for these sensor types, while CBM06C6 (CiS production) have shown appearance of the dead layer ($\sim$ 25 μm) in the interstrip gap at full depletion voltage.

Also measurements with a 640 nm laser beam (7 μm spot) scanned over the sensor area were performed for sensors irradiated at the KINR isochronous cyclotron up to the $2{*}10^{14}$ 1 MeV n_{eq}/cm^2. Figure 1 shows two dimensional distribution of amplitude of charges originated in the interstrip gap of the CBM05 non-irradiated sensor illuminated by the scanning laser beam. It demonstrates excellent position resolution achieved: beam spot position is indicated by figures of 15 μm, 18 μm, 21 μm etc. Figure 2 illustrates degradation of the charge collection by 30% in the irradiated sensor (the locus of laser events is shifted to lower amplitudes region). Analysis of data for other sensors is in progress. Tests with the ^{90}Sr β-source will be made soon exploring the 'ALIBAVA' microelectronics readout system.

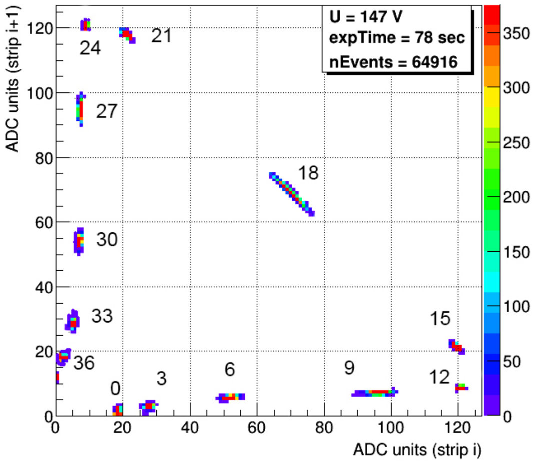

Figure 1: CBM05 – non-irradiated sensor: Laser scan in the interstrip gap

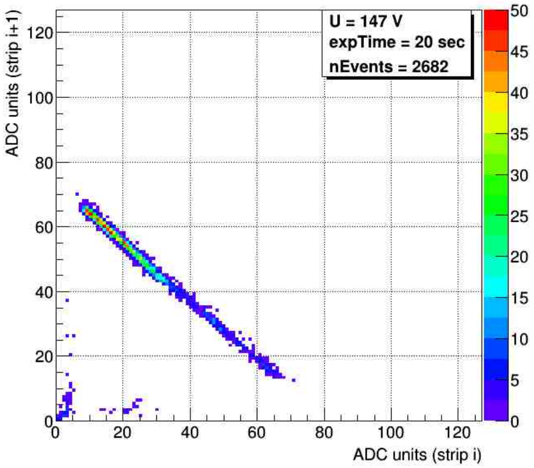

Figure 2: CBM05 – irradiated sensor: Laser scan in the interstrip gap

References

[1] A. Affolder *et al.*, JINST **8** (2013) P08002, arXiv:1302.5259

---

* Work supported by HIC-for-FAIR

Studies of correlated signals in CBM STS silicon microstrip sensors*

V. Pugatch[1], *J. Heuser*[3], *P. Larionov*[1], *M. Pugach*[1,2], *I. Sorokin*[1,3], *and C. Sturm*[3]
[1]KINR, Kiev, Ukraine; [2]Goethe-Universität, Frankfurt, Germany; [3]GSI, Darmstadt, Germany

Physically correlated signals in adjacent strips of a microstrip detector appear due to charge sharing. A significant fraction of tracks is reconstructed from two- and three-strip cluster events where analogue read-out improves the position resolution. Non-physically correlated signals originated by cross-talk, pick-up or common mode fluctuations may also occur in read-out channels. Measurements of charge sharing between adjacent strips of the CBM05 and CBM06 prototype silicon sensors designed for the CBM Silicon Tracking System were performed at KINR [1]. In a two-dimensional (E$_i$ x E$_{i+1}$) energy distribution of physically correlated events loci from an alpha-particle source were clearly observed in adjacent strips i and (i+1) (Fig. 1).

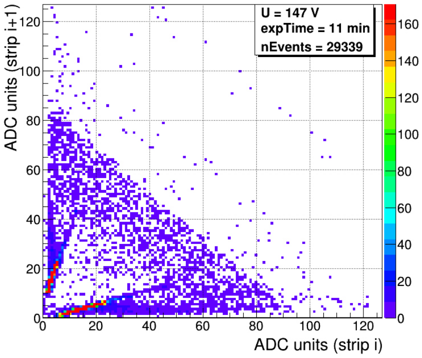

Figure 1: Two-dimensional (E$_i$ x E$_{i+1}$) energy distribution in adjacent strips i and (i+1) obtained with alpha-particles

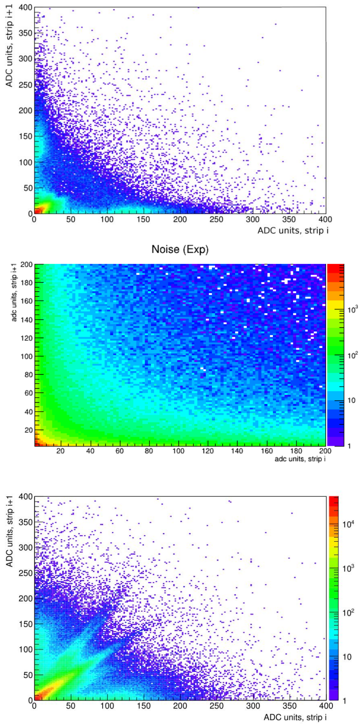

Figure 2: Two-dimensional (E$_i$ x E$_{i+1}$) amplitude distribution of events in adjacent strips 'i' and '(i+1)' of the CBM05 sensor. Data taken with ^{90}Sr source (upper: p-side; lower: n-side). A simulated noise distribution is shown in the middle panel.

Detailed studies revealed also non-physical correlated events populating loci from the very low amplitudes along the straight lines and reaching the positions of the alpha particle contribution. Among possible explanations we considered a cross-talk with the channels (i-1) and (i+2) located in close vicinity to the ones under the test. Correlated event studies were carried out recently with n-XYTER readout electronics at GSI. Examples of data obtained are shown in Fig. 2.

In the upper panel physically correlated events at the p-side triggered by MIP β-particles from ^{90}Sr are observed along the expected line (most probable value) with a sum of amplitudes around 140 ADC counts. The simulated noise distribution is shown in the middle part of Fig. 2. The events populating the loci alongside the straight lines originating from the (0.0 $\times$ 0.0) coordinate are apparently correlated non-physical events (see lower Fig. 2). These signals simultaneously appearing at adjacent strips i and (i+1) are initiated either by the digital part of the n-XYTER chip and/or by external powerful electromagnetic sources. It is worthwhile to notice that such events were also observed at n-XYTER channels not connected to the microstrip detector at all though with a low, yet significant amplitude of up to 40 ADC counts. The results of these studies have to be taken into account in the test measurements with a newly designed STS-XYTER microchip as well as in building the infrastructure for power lines, shielding and grounding of the STS detector. Further studies with the ALIBAVA readout system [2] are planned to clarify the origin of the non-physical correlated events.

References

[1] I. Panasenko *et. al.*, *Charge collection in STS silicon micros trips sensors at their surface layers*, this report

[2] https://www.alibavasystems.com

---

* Work supported by HIC-for-FAIR, H-QM and HGS-HIRe

Charge sharing in micro-strip sensors: experiment and simulation*

H. Malygina[1,2], *V. Friese*[3], *J. M. Heuser*[3], *A. Senger*[3], *and I. Sorokin*[2,3]
[1]Goethe-Universität, Frankfurt, Germany; [2]KINR, Kiev, Ukraine; [3]GSI, Darmstadt, Germany

In December 2013 [1] and December 2014 [2] a prototype setup of the Silicon Tracking Systerm (STS) for the CBM Experiment was tested in a 2.4 GeV/c proton beam at the COSY synchrotron (Jülich, Germany). In the middle station, which could be rotated around its vertical axis, CBM05 prototype sensors (n-side with 0^0 stereo-angle, p-side with 7.5^0, 285 ± 15 μm thick) were under a test aiming at studying charge sharing. The n-XYTER read-out chips were triggered by a hodoscope. The equivalent noise charge of about 8 ADC promoted adapting the threshold of 20 ADC in the cluster finder to cut off the noise.

Charge sharing between two fired strips is described by $\eta = S_R/(S_R + S_L)$ with $S_{R(L)}$ being the signals on the right (left) strip of the cluster [3]. The left panel in Fig. 1 shows the measured distribution of η. Positions and widths of the peaks depend on characteristics of the sensor and the readout electronics (e.g. strip pitch, signal-to-noise ratio, coupling capacitance, threshold, etc.). For inclined tracks the η-distribution is essentially asymmetric. The position of the cluster with respect to the left strip can be calculated as $x_\eta = p\left(\int_0^\eta \frac{dN}{d\eta'}d\eta'\right)\left(\int_0^1 \frac{dN}{d\eta'}d\eta'\right)^{-1} = pf(\eta)$, where p is the strip pitch and $f(\eta)$ is obtained from measurements (see the right panel of Fig. 1).

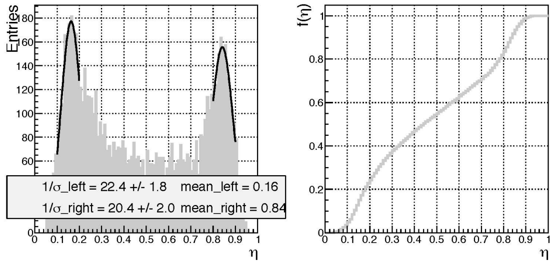

Figure 1: *Left:* η measured for p-side of CBM05 with Gaussians fitting the peaks. *Right:* $f(\eta)$. Perpendicular tracks.

Investigating cluster size distribution at different beam incidence angles is a good tool to verify the simulations of charge sharing in a silicon strip detector (implemented in the advanced model of the digitizer in CbmRoot). Figure 2 presents a typical distribution at one angle. Assuming the n-XYTER calibration [4] to be accurate, we get the reconstructed charge (Fig. 3) smaller than the one modelled. This indicates additional effects. Imposing 20% less charge from the sensor than expected from its thickness alone (on top of the 5% loss due to the trigger signal delay affecting the signal sampling in the ASIC) yields a better agreement. This is still to be explained.

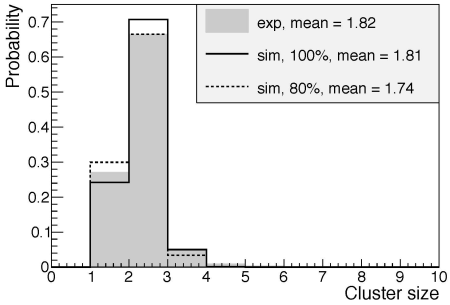

Figure 2: Cluster size distribution for slightly inclined tracks (10^0). Experimental data for n-side (the gray filled histogram), simulations with no (the solid line) and 20% (dashed) additional charge loosing.

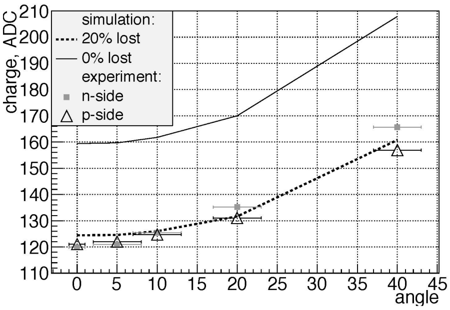

Figure 3: Most probable registered charge in dependence of track angles. The points show the experimental data from beamtime 2013 (the open triangles – p-side, the filled squares – n-side, the uncertainties in the angle measurements are drawn with bars) and the modelled data are represented by the lines (the solid line – no charge losses in the sensor, the dashed – 20% losses).

References

[1] T. Balog *et al.*, CBM Progress Report 2013, Darmstadt 2014, p. 32

[2] J. M. Heuser et al., *Test of prototype CBM detector components with proton beams at COSY*, this report

[3] R. Turchetta, Nucl. Instrum. Methods **A 335** (1993) 44

[4] I. Sorokin *et al.*, CBM Progress Report 2012, Darmstadt 2013, p. 14

---

* Work supported by HIC-for-FAIR, H-QM and HGS-HIRe

Neutron irradiated prototype CBM-STS microstrip sensors tested for double metal or cable interconnections of the end strips*

M. Singla[1], *P. Larionov*[2], *I. Momot*[2,3], *T. Balog*[1], *J. Heuser*[1], *I. Sorokin*[1,3], *and C. Sturm*[1]
[1]GSI, Darmstadt, Germany; [2]Goethe-Universität, Frankfurt, Germany; [3]KINR, Kiev, Ukraine

The Silicon Tracking System (STS), the core detector of the CBM experiment, is located in the dipole magnet to provide track reconstruction and momentum determination of charged particles from beam-target interactions. The STS will have double-sided silicon microstrip sensors mounted onto a low-mass carbon fibre support structure. The strips on one side of the double sided silicon microstrip sensors are tilted to have 7.5^0 stereo angle. This allows to reconstruct multiple hits from the same sensor at the expense of a poorer spatial resolution in vertical direction [1]. To have read out only from one sensor side, the end strips from one edge of the sensor were connected to the end strips on the other end as shown in Fig. 1. This interconnection can be provided via double metallization (DM) or by using external interstrip cables (SMwC). However, the central strips were the full strips without any kind of interconnections (region II in Fig. 1).

Test results of these prototype sensors before and after their exposure to neutron equivalent fluences of $2{\times}10^{14}$ $n_{eq}cm^{-2}$, as they are expected for the worst case scenario in the CBM experiment, will be disucssed. The sensors were irradiated at Karlsruhe Institute of Technology (KIT), Germany.

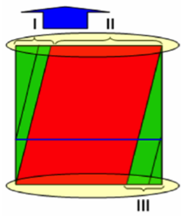

Figure 1: Sensor topology to read out inclined sensor strips

All the measurements were performed in a refrigrator at temperatures between -5^0 C to -10^0 C to limit the radiation-induced effects on detector current and to prevent thermal runaway [2]. Four sensors were selected for the measurement of variation of leakage current with bias voltage (IV), bulk capacitance versus bias voltage (CV), and for charge collection tests for the central strips (region II in Fig. 1) and for the end strips (with these special interconnection scheme, region I in Fig. 1) with a ^{90}Sr source. In this report only the results from central strips will be discussed. The list of the sensors under test is given in Table 1 along with their sizes, thickness, types of the connections and full depletion voltage before irradiations (extracted from the capacitance-voltage measurements). These sensors were mounted in the printed circuit boards and were wire bonded to read out about 10 strips for each sensor side using self-triggered n-XYTER chip.

Table 1: Specifications for the sensors under tests. The naming convention in the left column encodes the prototype generation (5 or 6), the manufacturer (H = Hamamatsu, C = CiS), the sensor height/strip length in cm (4 or 6), and the wafer number.

name CBM0-	size cm × cm	thickness μm	inter-connection	V_{fd} ±5 V
5H4-W18	6 × 4	327	SMwC	68
5H4-W10	6 × 4	331	DM	75
6C6-W14	6 × 6	293	SMwC	94
5C6-W6	6 × 6	291	DM	98

Charge collection studies were performed with ^{90}Sr for the sensors under test by applying suffieciently high reverse bias. Results are shown in Fig. 2 for all the sensors with either double metal interconnection scheme or single metal with external microcable bonded on its top p-side. As can be seen in Fig. 2, the charge collection efficiency degrades after the irradations. These sensors were also tested in-beam at COSY, Research Center Jülich, in December 2014. Before concluding on the type of the p-strip interconnection scheme, one should also consider the beamtime results about charge collection and detection efficiency of these sensors. This work is still in progress.

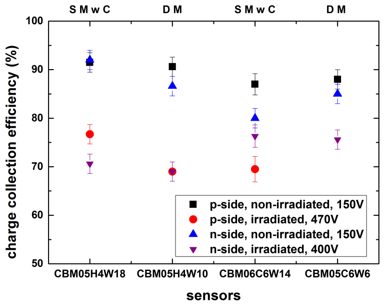

Figure 2: Charge collection results with ^{90}Sr, comparing the sensors before and after irradiation

References

[1] J. Heuser *et al.*, *Technical Design Report for the CBM Silicon Tracking System*, GSI Report 2013-4

[2] M. Moll *et al.*, Nucl. Instrum. Methods. **A 439** (2000) 282

---

* Work supported by HIC-for-FAIR, H-QM and HGS-HIRe

Long-term operation stability of neutron-irradiated STS prototype sensors[*]

P. Larionov[1] *and J. Heuser*[2]
[1]Goethe-Universität, Frankfurt, Germany; [2]GSI, Darmstadt, Germany

The Silicon Tracking System (STS) is the core tracking detector of the Compressed Baryonic Matter (CBM) experiment. The STS silicon sensors [1] will be operated during long periods of time continuously. During the operation a high level of radiation damage is expected to impact on the sensors. The exposure of 1×10^{14} 1 MeV neuton equivalent per cm^2 is the harshest scenario for sensors in the innermost areas of the STS stations, close to the beam axis, after several years of running. In this work, the long-term stability of the leakage current of highly irradiated prototype sensors has been investigated.

Table 1: Prototype sensors used for tests

Prototype sensor	Vendor	Sensor size, cm	Interconnection technology
CBM05H4	Hamamatsu	6.2×4.2	Double-Metal
CBM05H4	Hamamatsu	6.2×4.2	External cable
CBM05C6	CiS	6.2×6.2	Double-Metal
CBM06C6	CiS	6.2×6.2	External cable

To study the impact of irradiation on the properties of the sensors, the latest STS prototype sensors have been irradiated to 2×10^{14} n_{eq} cm^{-2} at KIT, Karlsruhe. The following prototype sensors with two different strip interconnection technologies [1], indicated in Table 1, were used for the tests. All the measurements were performed at -5°C to reproduce the real operating conditions of the CBM experiment. The sensors were placed inside the shielded box with connected N_2 supply to keep the humidity at the lowest possible level.

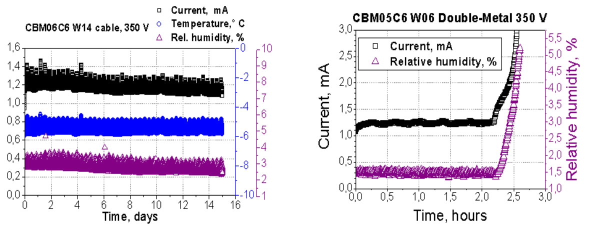

(a) (b)

Figure 1: a) Long-term stability of the leakage current of the CBM06C6 prototype sensor; b) Measurement results of the humidity impact test.

During a single measurement, the leakage current of the sensor at 350 V reverse bias voltage, and the temperature and humidity of the surrounding air were monitored in steps of 30 seconds. Figure 1a indicates the measurement result of the CBM06C6 sensor prototype during 15 days of continuous operation. The temperature of the air fluctuated within 1°C periodically during the measurement because of the cooling device's operating principle, keeping the mean value of -5.5° C. This resulted in a leakage current fluctuation due to its temperature dependence

$$I(T) \propto T^2 exp(-E_g/2k_BT)\ . \tag{1}$$

Moreover, it was observed that the leakage current is also sensitive to the humidity variation. The correlation between leakage current and the relative humidity curves are shown in Fig. 1 a, b. This can be explained by the introduction and rearrangement of negative charges in a humid air on the oxide surface which leads to surface depletion and consequent increase in the leakage current, as the surface generation becomes added to the bulk leakage current [2], [3].

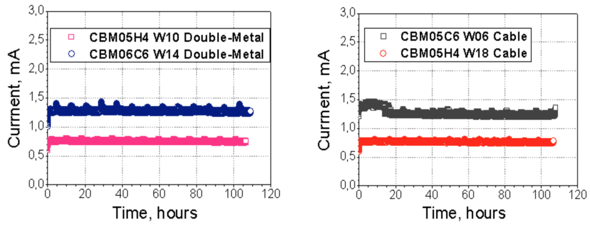

Figure 2: Leakage current stablity: sensors with double-metal (left) and external microcable (right) technologies

Figure 2 shows the results obtained for all prototype sensors for a 110 hours time period. All the presented data points have been normalized to the values at the reference temperature (-5°C) to exclude the temperature variation impact using Equiation 1. The humidity variation for the selected time period was considered to be negligible. The measurement results show stable behaviour of the leakage current for the sensors with both double-metal and external microcable interconnection technologies.

References

[1] J. Heuser *et al.*, *Technical Design report for the CBM Silicon Tracking System*, GSI Report 2013-4.

[2] M. Laakso, P. Singh and P. F. Shepard, Nucl. Instrum. Methods **A 327** (1993) 517

[3] F.G. Hartjes, Nucl. Instrum. Methods **A 552** (2005) 168

---

[*] Work supported by HIC-for-FAIR, H-QM and HGS-HIRe

A scalable neutron source for radiation hardness tests of STS sensors

E. Friske[1], *T. Jammer*[1], *and H. R. Schmidt*[1,2]
[1]Universität Tübingen, Tübingen, Germany; [2]GSI, Darmstadt, Germany

During operation of the STS, the silicon strip detectors are expected to be irradiated with large numbers of neutrons, some sectors in excess of 10^{12} $\mathrm{n_{eq}/cm^2/month}$ [1], with an accumulated dose of 10^{14} $\mathrm{n_{eq}/cm^2}$ [2].

To test detector performance and particularly neutron induced changes in the semiconducting properties, a neutron source with high flux is necessary. Unfortunately, reactors with sufficient neutron flux are heavily occupied. This leads to irradiation campaigns with very short irradiation times (in the order of minutes) in which the desired neutron dose is achieved.

To get a more realistic representation of the irradiation process, an exposure of days or weeks with defined annealing phases is more desirable. To fulfill these goals a scalable neutron source with good accessibility is required.

Present neutron source

The current neutron source consists of a gas cell filled with deuterium gas under a pressure of a few bar. A 2 MeV deuteron beam from the University of Tübingen's Rosenau accelerator passes an entrance window of a few microns thickness to induce deuterium fusion. However, even at this thickness the heat load on the entrance window reduced its mechanical stability, limiting both the beam current and the pressure of the gas cell.

Because of the limitations of both the accelerator and the window currently the neutron production is limited to a rate of $\approx 10^{12}\mathrm{n_{eq}/cm^2/week}$. As this rate is about two orders of magnitude below the required total dose, it would take way too long to accumulate with the current setup. To solve these issues, a new gas cell is currently being manufactured, based on [3].

New cryogenic source

The new neutron source currently in production consists of a steel endcap for the accelerator beam pipe. Mounted inside the endcap is the actual cell, cooled by liquid nitrogen. In contrast to [3], the gas cell is cooled by a copper finger reaching into a liquid nitrogen dewar. The entrance window is fixed to a thick copper disk sealing off the gas cell. A technical sketch is shown in Fig. 1. This setup has several advantages over the present cell: The enclosed deuterium gas is more dense by a factor of 4 compared to room temperature, and the lower ambient temperature should increase the durability of the entrance window, allowing higher beam currents.

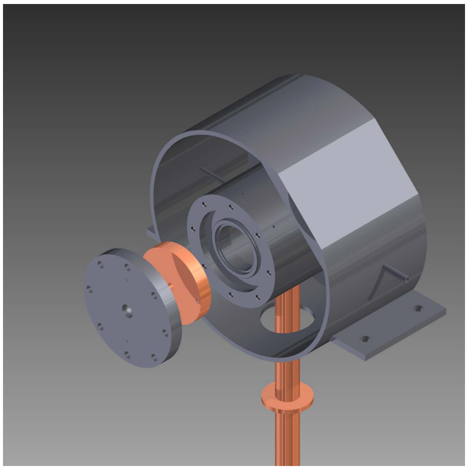

Figure 1: Schematic view of the cryogenic source

Combining these effects, it should be possible to increase both beam current and beam energy (to the accelerator's limit), which both significantly increases the neutron yield. In addition, the detector can be positioned within a few centimeters of the gas cell, providing maximum solid angle coverage. These improvements should increase the neutron flux by at least one order of magnitude, but the actual gain has to be determined once the cryogenic source is operational.

Before the new source can be put into operation additional tasks have to be performed, including tests of possible window materials and the cooling system.

References

[1] J. Heuser *et al.*, CBM Progress Report 2013, Darmstadt 2014, p. 25

[2] I. Sorokin, PhD thesis, Universität Frankfurt 2014

[3] W. von Witsch and J. G. Willaschek, Nucl. Instrum. Methods **138** (1976) 13

Optical quality assurance procedures for STS silicon sensors

E. Lavrik[1], *A. Lymanets*[1,2], *and H.-R. Schmidt*[1]
[1]Universität Tübingen, Tübingen, Germany; [2]KINR, Kiev, Ukraine

The CBM Silicon Tracking System (STS) is a compact array of silicon microstrip sensors [1]. The total number of sensors is about 1300 and they will be delivered from different manufacturers and in different form factors [2]. Thus the operation of the detector requires all sensors to be optically quality assured in order to meet the requirements with respect to surface conditions (scratches, durst grains, photo-resist residues, etc) and geometry (wafer thickness and warp, edge parallelity etc.)

For this purpose a clean area was established in a laboratory at the University of Tübingen and an optical inspection setup was built [3]. The setup consists of a XY-inspection object table based on closed-loop Movtec SMC-300 linear servomotors with a 5 MP Moticam microscope camera combined with 12× magnification lens from Navitar company. The setup allows to scan in X-Y-Z range of 200/75/75 mm with a micrometer precision and taking pictures with a resolution of 2592 × 1944 pixels.

Optical inspection workflow

A typical inspection workflow consists of several steps: preparation for inspection, inspection procedures, inspection report (Fig. 1).

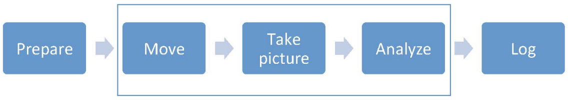

Figure 1: Typical workflow of inspection procedure

First, a sensor is laid on the inspection chuck, camera parameters are adjusted followed by a self-calibration cycle of the system. In the main part of the program the sensor is moved below the camera to scan the regions of interest, pictures are taken and analyzed to detect various defects and features on the sensor's surface. Lastly, a report that summarize the inspection results is produced. In this report all the technical data are comprised about sensor defects and features with corresponding images containing these defects and features. The report is then stored to disk and uploaded to the STS sensor database.

Method implementation

First, the motors and camera parameters are adjusted if needed (gamma, brightness, color gain, other parameters). Geometrical self-calibration begins with a spiraling pattern search for the nearest alignment mark which is an 120×120 µm^2 object (Fig. 2). The alignment mark is detected by pattern matching algorithms. Information extracted at this step gives a rough estimate of the sensor misalignment with respect to the XY motor axes. This in turn allows to optimize the amount of steps needed to detect all 8 alignment marks of a sensor.

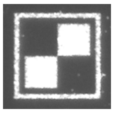

Figure 2: Sample alignment mark image to use in pattern matching algorithms

After detecting all of 8 alignment marks and determining their respective coordinates in step motor space, one can solve the minimization problem (1).

$$\vec{x}_m = \mathbf{S}\,\mathbf{R}\,\vec{x}_s \qquad (1)$$

Having a stretching matrix S and rotation matrix R from problem solution, coordinates from sensor coordinate space (s) could be translated to motor coordinate space (m), thus enabling us to precisely scan along sensor axes. Specific scans are performed for various geometries (e.g. normal, ”baby”, daisy-chained sensors) and different manufacturers (CiS, Hamamatsu) of a sensor.

After each step of a moving sequence the picture in the camera's field of view is taken. This image is then analyzed with the NI Vision® package to detect various defects and features on the sensors' surface, such as photo-resist residues, scratches, or dust grains. OCR algorithms from the Vision package enable us to read text parts written on the sensor to extract information about sensor's part number and include it later in the report.

When the scan is finished, the quality of the sensor is classified based on a given set of criteria. Lastly a human readable report containing the information on the sensor is produced. The report contains pictures of possible defects and their coordinates in sensor coordinate space.

References

[1] J. Heuser *et al.*, Nucl. Instrum. Methods **A 568** (2006) 258

[2] J. Heuser *et al.*, *Technical Design Report for the CBM Silicon Tracking System*, GSI Report 2013-4, p. 28

[3] E. Lavrik *et al.*, CBM Progress Report 2013, Darmstadt 2014, p. 28

A custom made wafer prober for quality assurance of CBM-STS sensors

A. Lymanets[1,2], *I. Panasenko*[1,2], *and H.-R. Schmidt*[1]
[1]Universität Tübingen, Tübingen, Germany; [2]KINR, Kiev, Ukraine

The CBM Silicon Tracking System will be constructed from about 1300 double-sided silicon microstrip sensors with a total area of $\sim 4\ m^2$. It will have about 2.1 million readout channels. The double-sided microstrip sensors with strips of 58 μm pitch have double metalization connecting the short corner strips resulting from the stereo angle of 7.5°. Due to its complex structure, all sensors have to be tested before they are assembled into detector modules. Large volume tests of the sensors require a suitable probe station and automatisation. Due to the relatively large size of 62×62 mm^2, the CBM microstrip sensors are not well suited for the characterization at conventional probe stations. Therefore, a custom probe station is beeing developed at Tübingen University (see Fig. 1). It consists of optical, mechanical and vacuum systems placed in a shielding box. Components of our probe station set-up are (see schematic view in Fig. 2):

- SourceMeter Keithley 2410
- Picoammeter Keithley 6487
- LCR-Meter QuadTech 7600
- Switching matrix Keithley 708B
- Aerotech linear and rotary motors with NPAQ-MR controller
- Vacuum pump (200 mbar abs.) and shielding box
- NAVITAR optical system with TheImagingSource camera (5 MP resolution)

One of the main requirements is a position repeatability better than 1 μm to allow an automatic succesive positioning on all 1024 pads of a sensor. It will be fulfilled with Aerotech linear motors providing a precision of $\sim 0.4\ \mu$m. The sensors will be fixed on a custom made vacuum chuck mounted on the motors.

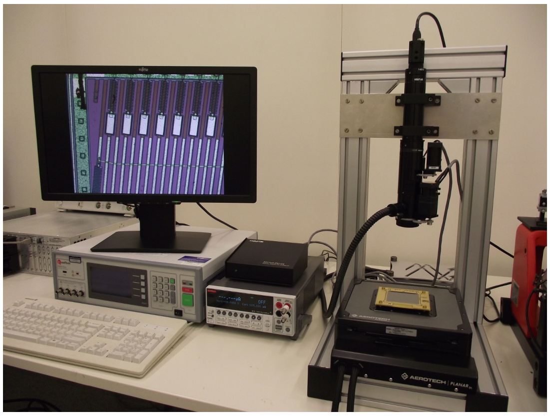

Figure 1: QA infrastructure in the clean room

The probe station allows to investigate the electrical characteristics of the sensors (full depletion voltage) as well as characteristics of individual strips (leakage current, interstrip capacitance, etc). The switching matrix allows to use all connected needles in any combination by any of the measuring devices. It leads to strongly reduced measurement time due to fast reconfiguration of the setup.

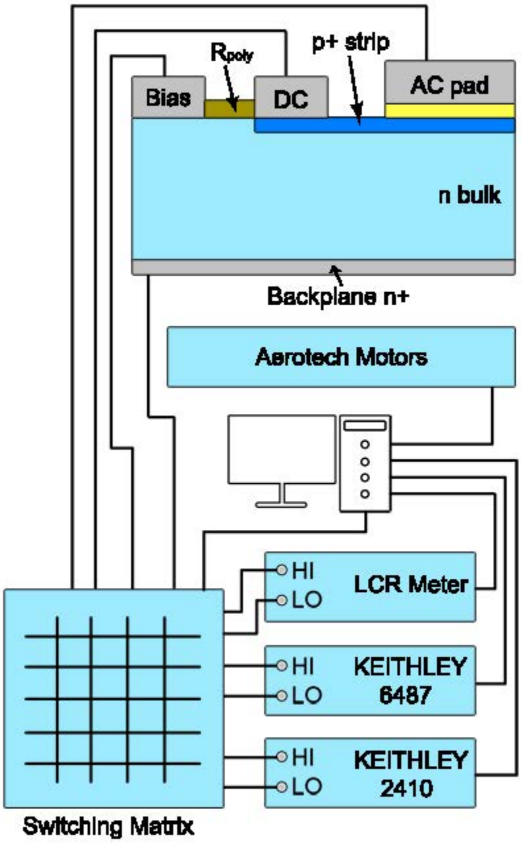

Figure 2: Schematic view of the probe station set-up

It is foresees that all system components will be controlled via LabVIEW. A dedicated software development to automate repetitive measurement steps is in progress.

References

[1] J. Heuser *et al.*, *Technical Design Report for the CBM Silicon Tracking System*, GSI Report 2013-14, http://repository.gsi.de/record/54798

[2] J. Heuser *et al.*, CBM Progress Report 2012, Darmstadt 2013, p. 8

Fixtures for quality assurance of STS silicon sensors and STS-XYTER ASIC

C. Simons[1], *C. J. Schmidt*[1], *V. Kleipa*[1], *and K. Kasiński*[2]
[1]GSI, Darmstadt, Germany; [2]AGH University of Science and Technology, Cracow, Poland

To assure the functionality of the silicon microstrip sensors and the quality of bond contacts of the microcables on the STS-XYTER-chip, fixtures are needed, that preferably allow on one hand for non-destructive handling and measurements as well as easy and fast procedures on the other. Several companies were asked for proposals and aps Solutions GmbH had the most promising one: test sockets with Pogo Pins for contacting. *Pogo Pin* is a registered trademark of a US company, they are also called spring loaded contacts. Formed like a cylinder, it contains two peaked, spring-loaded pins that make secure contacts with two electronic circuits. For the Pogo Pins different combinations on tip shapes, structures, materials and plating are available so that the particular application may be optimized.

Test socket for the silicon sensors

The challenge for the different quality measurements of the double-sided sensors is the need for simultaneous biasing contacts from bottom and top side. This problem can be solved with a fixture that consists of a bottom and a top socket. Both sockets include a Pogo Pin to which the bias voltage is applied via a small pcb. The bias pads on the sensor have a comfortable size of 400 μm × 150 μm to facilitate contacting. With the help of a wafer prober equipped with a movable chuck, the strips may then be stepped through for investigation by means of a probe card. The schematical layout of the fixture and its installation on a wafer prober are shown in Figs. 1 and 2.

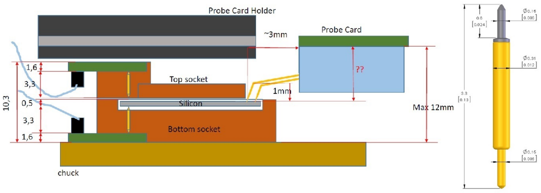

Figure 1: Draft design of the sensor test socket by WinWay Technology

Test socket for the STS-XYTER-chip

Each traceline of the microcables that connect the silicon microstrip sensor to the STS-XYTER-readout-chips has to be TAB-bonded onto the pads of the sensors on one side and on the chip on the other. These contacts should be checked before applying the protective glob-top because TAB-bonds without contact may be rebonded. The quality check can be put into practice by taking the chip into operation, a minimal set of essential connectivity has been elaborated with the chip designers towards this end. A probe card, that is typically chosen as a good solution for operating a chip without wirebonding, cannot be used for this test because it only works in combination with a wafer prober that assures alignment and positioning. The STS-module (STS-XYTER + microcable + sensor) would need to be placed on the chuck of the prober, inhibitive because of the module size and the fragility of the module. Therefore working with a test socket with Pogo Pins is an appropriate solution. The chip by itself is placed into the socket that will have an opening for the microcable. Several requirements regarding the test pad size, pitch and general arrangement and balance of connections across the chip have to be taken into account. Proposals for the pad layout of the STS-XYTER are under development with consultation of *aps Solutions GmbH*. Continuative tasks for the execution of tests are the development of a modified STS-XYTER board and suitable software.

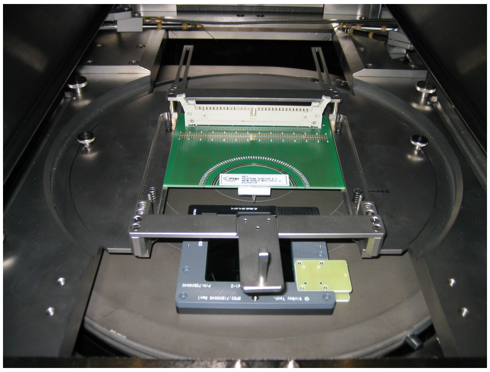

Figure 2: Test socket and probe card on wafer prober

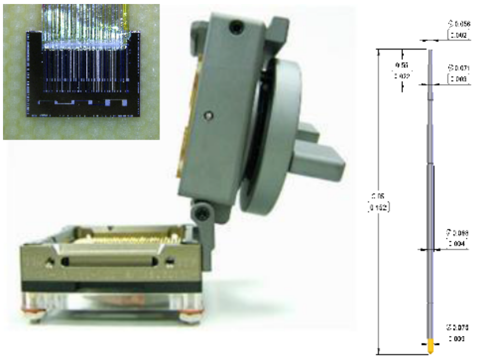

Figure 3: Test socket for ASICs by WinWay Technology

Development of a laser test system for the characterization of prototype silicon micro-strip sensors*

P. Ghosh[1], *J. Eschke*[3], *W. Niebur*[2], *P. Zumbruch*[2], *and J. Heuser*[2]
[1]Goethe-Universität, Frankfurt, Germany; [2]GSI, Darmstadt, Germany; [3]FAIR, Darmstadt, Germany

For the characterization and quality assurance of prototype micro-strip sensors produced for the CBM Silicon Tracking System (STS), a semi-automated infra-red pulsed laser test system has been developed [1]. The amount of energy deposited by the laser light is chosen such, that it is equivalent to charge created by a minimum ionizing particle. The purpose of this investigation is to understand the charge sharing and uniformity of sensor performance in the inter-strip regions. Two prototype sensor, namely CBM02 (double-sided, 256 strips/side, pitch = 50 μm, full read-out) and CBM05 (double-sided, 1024 strips/side, pitch = 58 μm, one-eighth read-out) have been investigated [2]. The strips on the sensors are read-out via self-triggering n-XYTER based front-end electronics.

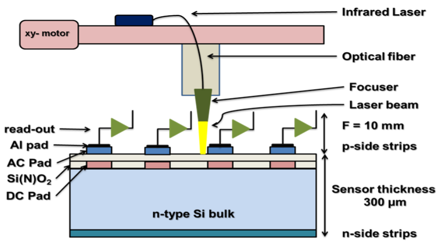

Figure 1: Schematic representation of the laser set-up

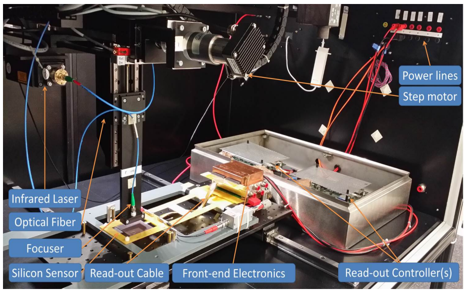

Figure 2: Components of Laser Test Stand

The automated tests are performed at several positions across the sensor. The laser beam is focused to a spot-size of $(\sigma_{spot}) \approx 12$ μm. The duration (~ 5 ns) and power (few mW) of the laser pulses are selected such that the absorption of the laser light in the 300 μm thick silicon sensors produces about 24 000 electrons, which is similar to the charge created by minimum ionizing particles (MIP). The wavelength of the laser is chosen to be 1060 nm because of the absorption depth being of the order of the thickness of the silicon sensors [3]. Figure 1 shows the measurement set up in a schematic view. Figure 2 shows various components installed in the laser test stand. The laser beam is transmitted through a 6 μm thick optical fibre to a single focusing system, which focuses the light to a spot of about 12 μm diameter. The working distance is about 10 mm [1]. The laser focuser is calibrated to a focused position on the sensor surface as a function of the number of strips fired with a signal just above threshold. At this reading the proper focal distance has been achieved. Figure 3 shows a measurement of the charge sharing function (η) in the inter-strip region. The η function is defined as the ratio of charge collected by either strip divided by the sum of both. The EPICS device control is used to control the step motor. A special program with a user interface has been developed to operate and move with the laser over the active area of the sensor to perform several measurements automatically. The data acquisition software DABC accesses the motor position information from EPICS. The on-line and off-line analysis is performed using the Go4 analysis tool.

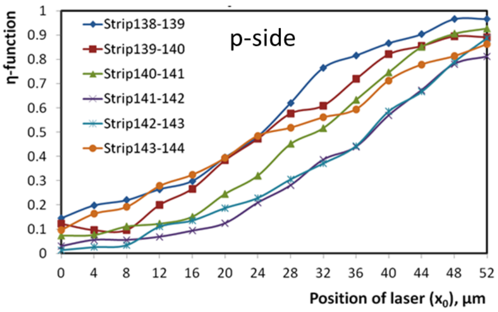

Figure 3: Charge sharing function (η) as a function of the position of the laser spot on one side of the sensor

References

[1] P. Ghosh, PoS(Bormio 2013)018 (2013)
[2] P. Ghosh, J. Phys. Conf. Ser. **503** (2014) 012028
[3] P. O'Connor *et al.*, Proc. SPIE **62761W-1**, p. 2

---

* Work supported by HIC-for-FAIR, H-QM and HGS-HIRe

Quality assurance of CBM-STS silicon micro-strip sensors using pulsed infra-red laser*

P. Ghosh[1], *J. Eschke*[2], *and J. Heuser*[3]

[1]Goethe-Universität, Frankfurt, Germany; [2]FAIR, Darmstadt, Germany; [3]GSI, Darmstadt, Germany

The Silicon tracking system (STS) of the CBM experiment is aimed to reconstruct the trajectories of the hundreds of charged particles created in heavy-ion collision, and to determine their momenta with a resolution of around $\Delta p/p \approx 1\%$. This precision is prerequisite for high-resolution mass measurements of e.g. rare probes and implies a thin detection system, with high-resolution space-point measurement and capable of interaction rates up to 10 MHz. The STS will comprise 1220 silicon microstrip sensors from which 896 detector modules will be constructed [1]. Quality assurance of the sensors is an important pre-requisite for the detector module production as the assembly steps are non-reworkable to a good extend. These tests can be either invasive or non-invasive as explained below. From the results entered into a database, one can identify sensors or detector modules with certain characteristics and grade them according to their performance.

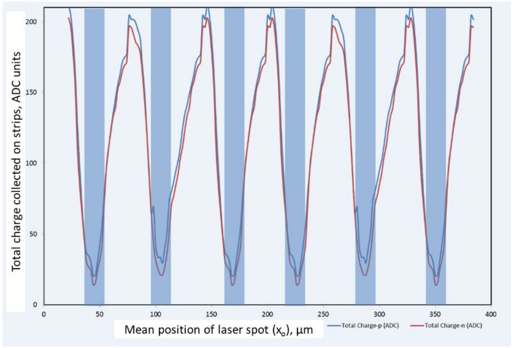

Figure 1: Amplitude response of a few strips from a detector module scanned with a laser spot

Invasive methods are the characterization with methods that require physical contact of probes to the objects. The important features are: (i) this allows detailed analyses of the device under test (DUT), (ii) this leaves scratches or marks on the surface, (iii) this is limited to sensors, not to detector modules, (iv) this method involves passive electrical measurements using a wafer prober and micro-probing needles [2].

Non-invasive methods are the characterization with methods that do not require physical contact of probes. The important features are: (i) a few significant parameters of the DUT can be investigated, (ii) this leaves no scratches or marks on the surface, (iii) this is not limited to bare sensors but can be applied to detector modules, (iv) this method involves injection of localized charge using a pulsed infra-red laser [3].

The laser test stand (LTS) is developed with the idea to perform key quality assurance tests on silicon detector modules. The significant parameters that can be analysed or investigated using the LTS are: (i) Uniformity of charge collection (or strip integrity) from scanning the strips. An example of such laser scan is shown in Fig. 1. (ii) Operation voltage from the bias scan. An example of charge collection as function of the bias voltage is shown in Fig. 2 (a). (iii) Charge coupling to neighbour and next-neighbour strips from bias scan. An example is shown in Fig. 2 (a). (iv) Ratio of AC-coupling to inter-strip capacitance from amplitude response at specific positions. An example is shown in Fig. 2 (b). (v) Charge sharing function (η) in the inter-strip region can be determined. Figure 3 shows η-function dependence with the position of the laser spot.

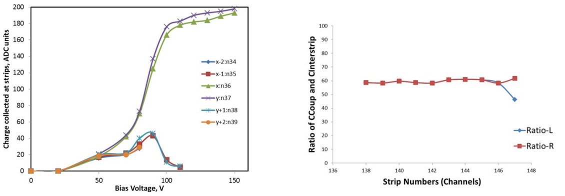

(a) (b)

Figure 2: a) Operating voltage determination and charge sharing between neighbouring and next to neighbouring strips and b) Ratio of coupling to inter-capacitance.

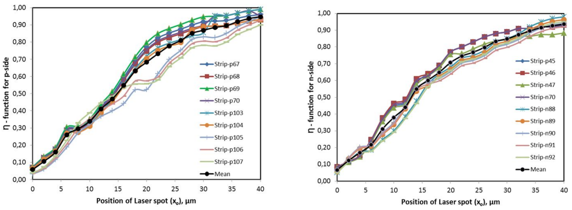

(a) (b)

Figure 3: Charge sharing measurements in the inter-strip region of a silicon detector module: a) p-side and b) n-side.

References

[1] P. Ghosh, J. Phys. Conf. Ser. **503** (2014) 012028

[2] P. Ghosh, PoS(Bormio 2013)018 (2013)

[3] P. Ghosh, CBM Progress Report 2013, Darmstadt 2014, p. 29

---

* Work supported by HIC-for-FAIR, H-QM and HGS-HIRe

Development of a 124 mm long silicon strip sensor for the CBM STS

D. Soyk and C.J. Schmidt
GSI, Darmstadt, Germany

The new segmentation of the CBM STS ladders [1] requires to design and produce a silicon strip sensor with 62 mm width and 124 mm height. This new long sensor will replace the 2 daisy-chained 62 mm sensors.

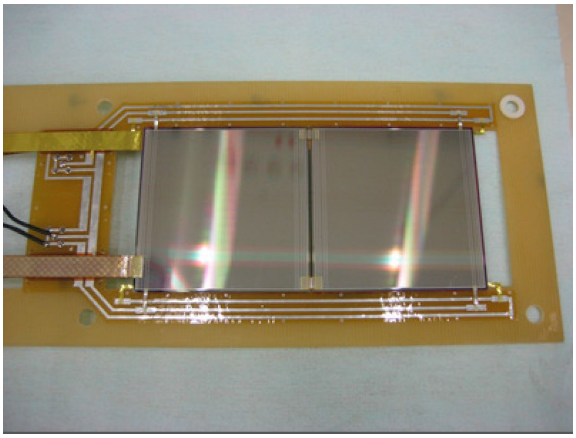

Figure 1: Two daisy-chained 62 mm sensors

In Fig. 1 a functional prototype module with read-out of 1/8 of its channels is shown, produced by LED Technologies of Ukraine (LTU) Ltd, Kharkov, Ukraine, using two sensors 6.2 cm by 6.2 cm large compatible with 4 inch wafer technology. Between the two sensors two short daisy-chain-cables are shown. That serve to connect the strips from one sensor to the next. In the final version, all strips of the sensors must be connected. Therefore a daisy-chain-cable with the full width must be produced and bonded onto the sensors. Every sensor also needs a cross connection on the p-side that links inclined strips ending on one lateral side to a corresponding strip on the other lateral side. It is not jet finally resolved, whether such connection should be realised on an additional metal layer or with a seperate microcable. If the sensor is single-metal, additionally for each sensor a interstrip-connection-cable must be bonded on the p-side of the sensor. Together with the CiS Forschungsinstitut für Mikrosensorik und Photovoltaik GmbH, Jena, Germany the plan was developed to produce a single 124 mm × 62 mm sensor in double-side and double-metal technology on a 6 inch wafer. If it is possible to solve all technological challenges, the production of a module with 124 mm sensorheight would become much simpler. The production and assembly of two interstrip cables and the production and assembly of one daisy-chain-cable could be made unnecessary. Also the bonding process of these three cables will be avoided. This reduction of fabrication and manufacturing steps will increase reliability and yield. Additionally the replacement of the daisy-chained sensor by one sensor will reduce the assembly effort because the daisy-chained module must be installed on a special frame before it is mounted on the ladder. In Fig. 2 the layout of the wafer is shown.

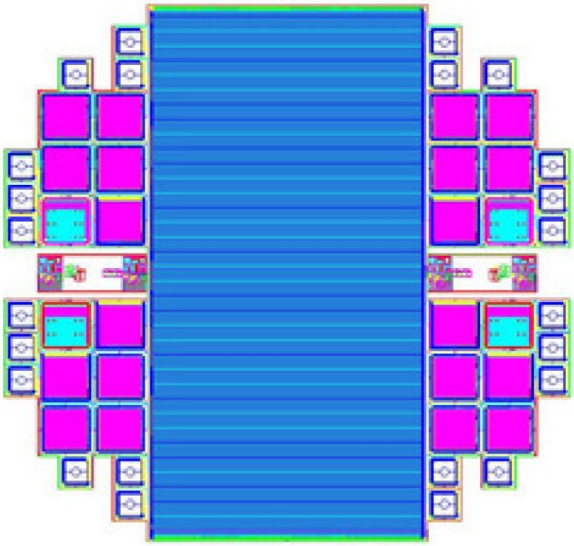

Figure 2: Layout of the 6 inch wafer with the 124 mm × 62 mm STS sensor in the middle, around the sensor CBM baby sensors and test features

At the moment the design of the 124 mm sensor is finished and the production of masks has already started. The design of the AC- pads will follow the classification of pad layout, described in [2].

References

[1] J. Heuser *et al.*, *Technical Design Report for the CBM Silicon Tracking System*, GSI Report 2013-4

[2] D. Soyk *et al.*, CBM Progress Report 2013, Darmstadt 2014, p. 24

Towards the STS-XYTERv2, a silicon strip detector readout chip for the STS

K. Kasiński, R. Kłeczek, R. Szczygieł, P. Gryboś, and P. Otfinowski
AGH University of Science and Technology, Cracow, Poland

The STS-XYTER as a 128+2 channel full-size prototype IC dedicated for silicon strip detector readout in the CBM Silicon Tracking System was fabricated in 2013 [1]. Figure 1 presents the test PCB developed at AGH used for functional verification. It provides on-board 5 separate power domains with dedicated low-noise LDO regulators, an ERNI connector for sensor attachment, interconnects for test interface, test points and the AC-coupled CBMnet interface (HDMI connector). The board is controlled by SysCore V3 (CBMnet) and NI FPGA (test interface) cards.

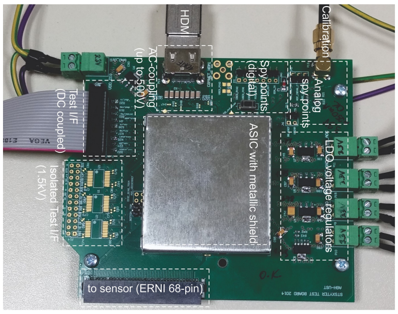

Figure 1: Test PCB for the STS-XYTER ASIC

The architecture details of the chip and test results were presented and published in [2]. Detailed tests using silicon sensors (e.g. CBM05) are currently being prepared. Using the same setup it was possible to further evaluate the chip. Figure 2 shows a thermal image of the STS-XYTER chip on the test PCB. The thermal resistance was estimated to be approx. 52 °C/W, but it needs to be verified on the final FEB board in an environment similar to the final application as well. The temperature coefficients measured for various biasing points of of the ASIC evaluated for ambient temperatures of 7–85 °C are:

ADC_vdiscr_ref = -0.622 mV/°C,
ADC_ibias_corr = -0.312 mV/°C,
BG_iref = +0.154 mV/°C,
ADC_vref_n = -0.366 mV/°C,
ADC_vref_p = +0.286 mV/°C,
DISCR_bias_t = -0.435 mV/°C.

The STS-XYTERv2 which will be an evolution of the STS-XYTER prototype ASIC among the small fixes the changes includes:

- a new concept of the digital back-end (focused on the use of GBTx chip as a data concentrator), reaching hit bandwidths 9.4–47 MHit/s/chip,
- definition of the new communication protocol optimized for the conditions and requirements of the CBM experiment. The preliminary protocol was published [3] and is currently a subject of fine-tuning,
- a configurable front-end (gain, bandwidth) for possible support of gas detectors (MUCH),
- a new pad layout supporting quality test with pogo-probes and reduced connectivity required for regular operation,
- testability and temperature stability improvements of the in-channel ADC,
- further optimization of the analog front-end towards lower noise and better stability.

The STS-XYTERv2 ASIC is currently being under development. It is expected to be taped-out in Q2 of 2015 via Europractice services.

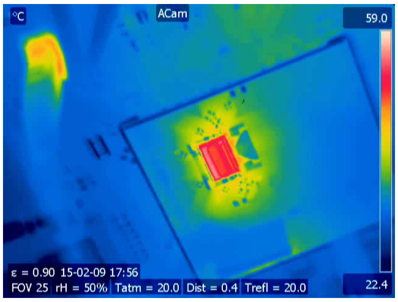

Figure 2: Thermal imaging of the operating ASIC on the test board

Acknowledgment

We would like to thank the colleagues from GSI and WUT Warsaw for the efforts towards verification and specification of the new requirements.

References

[1] P. Gryboś *et al.*, CBM Progress Report 2012, Darmstadt 2013, p. 17

[2] K. Kasiński *et al.*, “STS-XYTER, a High Count-Rate Self-Triggering Silicon Strip Detector Readout IC for High Resolution Time and Energy Measurements”, to appear in IEEE NSS/MIC, 2014

[3] K. Kasiński, W. Zabołotny and R. Szczygieł, Proc. SPIE Int. Soc. Opt. Eng. **9290** (2014) 929028

Data throttling procedures for the STS-XYTER based read-out of the CBM Silicon Tracking System

T. Balog, W.F.J. Müller, J. Lehnert, and C.J. Schmidt
GSI, Darmstadt, Germany

In high interaction rate experiments using a continuous beam such as the Compressed Baryonic Matter experiment CBM at FAIR, beam intensity fluctuations are a critical issue. When such fluctuations occur, they will lead to a sudden increase in occupancy in the detector. For detector systems closest to the target such as the Silicon Tracking System STS, this may result in a local or even global overload situation, where the read-out bandwidth cannot cope with the incoming data load. In consequence, incomplete event information may be transmitted.

In conventional, triggered systems overload situations are handled by common dead time mechanisms which discard the affected fraction of events. In continuous beam experiments with freely streaming readout, however, no such trigger is available and overload would lead to uncontrolled data losses that might yield the collected data overall as none analyzable. Apart from event overlap and local pile-up, the fundamental question may be stated as: ”How can one register all the data of most of the events rather than most of the data of all the events.” In order to prevent complete clogging of the data chain, a throtteling mechanism is needed, that allows to inhibit acquisition of data from scrambled, not interpretable events in favour of clearing the data path for uncompromized sets of event data, once the overload condition has cleared.

In the STS the STS-XYTER read-out ASIC will be used [1]. This read-out chip is a dedicated custom design for the STS. Each readout channel is equipped with a 5 bit flash ADC. The statistically incoming hits are buffered in a per channel fifo eight levels deep and subsequently read out using a token ring scheme that is set-up to have oldest data read-out first.

Clearly, every single channel may, by pure statistical fluctuations, suffer signal pile-up or even a fifo overflow. This situation will be marked to the adjacent data elements but is not the key issue demanding throtteling. It is rather the situation of a sudden, potentially regularly appearing intensity increase that yields the average data load to be higher than the readout bandwidth. In such a situation, good data in the queue should still be read-out, but data belonging to potentially incomplete events should not cause an uncontrollable system deadtime before new data may be taken upon recovery. Further, the system should resume operation coherently.

To this end various measures have been foreseen in the design of the readout ASIC:

- Pile-up and fifo-overflow are indicated on the data elements of the particular channel.
- Channel fifo overflow conditions are counted on the chip and will realease a response report when beyond some configurable level.
- Fifos may be cleared coherently through a command.

The protocol for communication with the ASIC [2] was designed to ensure fast transfer of both the fill status reports from the ASICs and of the required responses (commands to stop -for emptying fifos- and to restart acquisition or for fast clearing of fifos).

The above provisions in the ASIC will allow to identify a problematic situation, realize throtteling as well as a coherent DAQ restart from a global control point such as the data processing board (DPB) layer through various mechanisms. No further complicated logic is needed nor foreseen in the radiation exposed front-end electronics. All further steps in the evaluation of throttling conditions can be flexibly implemented in the FGPA based DPB layer [3] based on the dedicated throttling information provided by the ASICs and on information gained directly from monitoring the ASIC hit data stream, for example indications on the ASIC fifo fill state from the difference between readout time and creation time of individual hits.

A simulation model was developed using the hardware description language SystemC [4] and some simulative pre-studies have been carried out. The model currently implements a simplified structure of an STS-XYTER ASIC and allows to investigate throttling by variation of parameters like event rate, channel fifo overflow thresholds and timing of global throttling decisions. Additional simulations need to be realized to verify adequate system performance through such throttelling strategies.

References

[1] K. Kasiński *et al.*, *Towards the STS-XYTERv2, a silicon strip detector readout chip for the STS*, this report

[2] K. Kasiński *et al.*, *STS-HCTSP, an STS Hit & Control Transfer Synchronous Protocol*, this report

[3] W. Zabołotny *et al.*, *Towards the Data Processing Boards for the CBM experiment*, this report

[4] `http://www.systemc.org`

Testing of n-XYTER 2.0 front-end boards from JINR

D. Dementyev[1], *V. Kleipa*[2], *C.J. Schmidt*[2], *Yu. Murin*[1], *V. Tugulbaev*[1], *and A. Salivon*[1]
[1]JINR, Dubna, Russia; [2]GSI, Darmstadt, Germany

Sixteen front-end boards (FEBs) each with a n-XYTER 2.0 ASIC were produced with the aim to assemble the first setup for the in-beam tests at JINR's Nuclotron. The PCBs were developed at JINR for the new version of the n-XYTER ASIC. Specialists of LTU Ltd. mounted the ASICs on FEBs using double-layer micro-cables [1]. The power consumption of one chip is about 5 W so every ASIC was mounted on metal radiator plate.

Previous tests of the first prototype of the n-XYTER chip have shown that there is a high temperature coefficient for the DC signal level of about 4%/K. The version 2.0 of the ASIC was designed with the aim to decrease the temperature coefficient. Several output biased potentials were added and finally the ability to change gain by factor of 4 was implemented with the aim to extend the dynamic range. The n-XYTER 2.0 was previously tested on the FEB already available from operating the first prototype of the chip; a mezzanine PCB for the adjustments of new bias potentials was added. Tests had shown that n-XYTER 2.0 is functional and the temperature coefficient was improved by a factor of 200 [2].

Previously two separate interfaces were used to configure the FEB revision D. The first is an I^2C interface for the n-XYTER and the second is an SPI interface for the ADC. The JINR FEBs were suggested to support the new generation of SysCore3 boards, so there is one control interface based on the SPI LVDS protocol. However, it was necessary to operate the FEBs with SysCore2 boards since SysCore3s were not available. So additional adapter boards based on the ATtiny-88 MCU were developed at GSI [3]. It translates the SPI and I^2C interfaces from SysCore2 to the SPI interface emulating SysCore3 (see Fig. 1). To adjust external biased potentials of n-XYTER 2.0 a new DAC is employed. With the aim to control DAC, ADC and n-XYTER the ATtiny-88 MCU was implemented on the FEB. To set values of bias potentials one needs to send write commands to the I^2C registers 0x31-0x38. These registers are not used by the n-XYTER chip and the MCU on the FEB redirects those commands to the DAC.

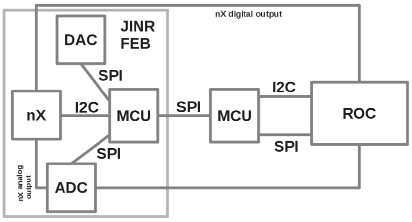

Figure 1: Data transmission scheme SysCore2 – FEB

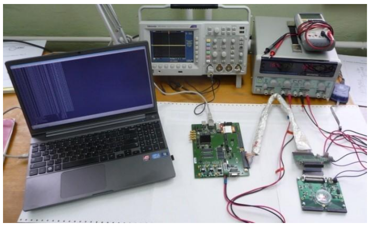

Figure 2: FEB under testing

The strategy of adjusting external biases was very simple. The bias for the per-amplifier should be set such that the input potential is equal to the output. Three other biases for the slow and fast shapers should be set such the output DC levels are on adequate level. Another bias is used to set the value of the gain of the slow shaper. Unfortunately, this feature turned out to be useless. The dynamic range remains on the same value independently of the gain. Indeed, the gain could be changed by the factor of 3. The FEBs were tested and calibrated with external and internal calibration circuit. The maximum gain was found on the level of 18 mV/fQ which is about 15% less than for the first prototype of n-XYTER. It could be explained by the manufacturing variation for the different bunches of ASICs (see Fig. 3).

The ASICs on four FEBs were replaced after tests. Since the chips were not tested before mounting it is difficult to conclude whether the problem was in ASICs or in micro-cables. Indeed, micro-cable mounting turned out to be a good solution. There were no broken connections on the other tested FEBs. The tests showed that the FEBs are fully operative and compatible with the readout system based on the SysCore board.

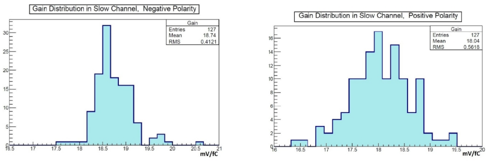

Figure 3: Histograms for measured gain for negative (left) and positive (right) polarity

References

[1] V. M. Borshchov *et al.*, CBM Progress Report 2013, p. 34

[2] D. Dementyev *et al.*, CBM Progress Report 2012, p. 15

[3] P. Gudge and V. Kleipa, Basic Reference for Atmel Tiny 88 Board, private communication

A front-end electronics test board for the CBM Silicon Tracking System*

V. Kleipa, C. Simons, D. Soyk, J. Carpenter, and C. J. Schmidt
GSI, Darmstadt, Germany

The 896 modules of the CBM Silicon Tracking System will be equipped with two front-end electronics boards (FEBs) each, carrying per board eight STS-XYTER ASICs that read out the silicon micro-strip sensors of the modules [1]. The boards will be stacked at the top and bottom layers of the detector, mounted in a shelf structure that is in contact with a cooling plate to remove the power dissipated by the electronics. Due to the spatial contstraints there, the board dimensions are restricted to the limited size, as shown in Fig. 1. At the same time, the board has to provide the infrastructure for achieving the full output band width needed to read out the detector. This translates to realizing up to 5 LVDS pairs per final ASIC, a high-density challenge for the FEB design and prototyping.

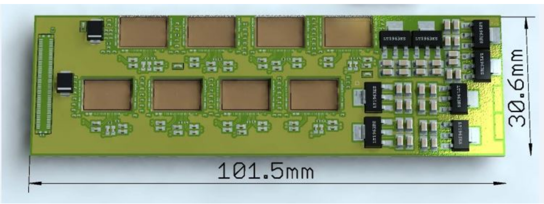

Figure 1: Rendering of the STS front-end electronics board comprising 8 STS-XYTER ASICs arranged in a fixed pattern on two double-rows of 4 ASICs each. Power supply section with LDOs on the right. The small components are decoupling capacitors to common and communication ground.

For assembly test purposes, a PCB was produced onto which 8 STS-XYTERv1 ASICs can be mounted but not having any electrical functionality. Only the top and bottom layers are covered with a gold layer for test bonding of ASICs and cables. During its layout, it turned out that only one of the four readout channels of each ASIC could be routed to the digital I/O connector, limited due to the available space in between the ASICs. This technological problem is the subject of current work.

In order to prepare a test equipment for a complete readout chain from sensor to GBTx boards, an intermediate FEB board has been designed that is not constrained to the small dimensions. The PCB, called FEB4, hosts only four ASICs. Its layout is shown in Fig. 2. This PCB comprises the required power supply LDOs. All I/O channels of each ASIC are linked to a connector. In addition, the required high-voltage capacitors (rated 250 V) for bias decoupling have been added to the differential LVDS connections. In Fig. 3(a) the board's assembly pads for passive devices are visible. For the devices' case size, the norm *0201[m]* had to be chosen in order to fit them between the ASICs. This board is currently being used for testing of the STS-XYTERv1 chips. One ASIC wire-bonded to the board is shown in Fig. 3(b).

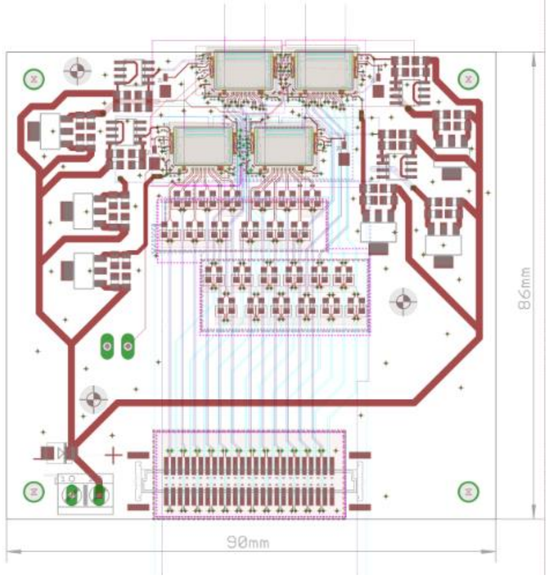

Figure 2: Layout of a front-end board comprising four read-out ASICs and all outgoing LVDS data lines on a somewhat relaxed geometrical footprint (FEB4)

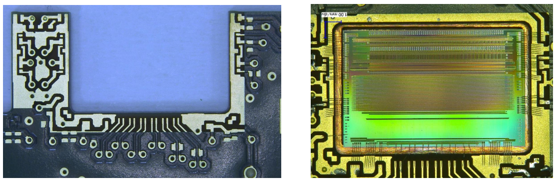

(a) (b)

Figure 3: (a) High-density region in between the openings for the STS-XYTER ASICs on FEB4, filled with the full set of LVDS lines, micro-vias and connecting pads for high-voltage decoupling capacitors. (b) STS-XYTERv1 ASIC installed into FEB4 and wire-bonded to its power supply, control and outgoing data lines.

References

[1] V. Kleipa et al., CBM Progress Report 2013, Darmstadt 2014, p. 36

---

* supported by EU-FP7 HadronPhysics3

The GBT based readout concept for the CBM Silicon Tracking System

J. Lehnert[1], *W. Müller*[2], *and C.J. Schmidt*[1]
[1]GSI, Darmstadt, Germany; [2]FAIR, Darmstadt, Germany

The sensors of the CBM Silicon Tracking System (STS) are read out by frontend boards (FEB) with 8 STS-XYTER ASICs for 128 channels each implementing the analog frontend, analog-to-digital conversion and the readout of buffered hits via multiple serial links. A subsequent stage with data aggregation from several ASIC links and an electrical-to-optical interface is required before transfering the data to the FPGA based data processing boards (DPBs) located in some distance at the detector site where preprocessing and further data transfer occur. The aggregation stage is located in the cooled STS detector box inside the CBM magnet, which implies that the hardware must fulfill conditions in terms of radiation hardness, magnetic field, space contraints and thermal environment.

GBT Devices

A concept was devised for the STS readout to implement the aggregation and optical readout functionality on a separate readout board (ROB) using the GBTX, SCA and Versatile link devices [1] developed at CERN. The devices of the GBT project are mainly designed as interface between on-detector and off-detector electronics for future LHC experiment upgrades in a radiation environment up to tens of Mrad. The GBTX ASIC implements up to 56 SLVS links (E-Links) as electrical frontend interface with link speeds of 80, 160 or 320 Mb/s and a total bidirectional user bandwidth up to 4.48 Gb/s on the high speed serial link. Latencies of data throughput in the GBTX are fully deterministic. The Versatile Link devices are radiation hard optical transceivers and (twin) transmitters in SFP formfactor modules.

The STS Readout Chain

The ROBs for the STS will contain 1 GBTX device as master connected to an optical transceiver (VTRx), 2 GBTX devices connected to an optical twin transmitter (VTTx) and a GBT-SCA (Slow Control Adapter) device for I^2C based control of the 2 GBTX without optical downlink (see Fig.1). The GBTX uplinks will be operated in the widebus mode (without forward error correction) and therefore provide 3x14 frontend links at 320 Mb/s each. Fourty of these links are used to connect to the FEBs. Three types of FEBs will be used with either 1, 2 or 5 readout E-Links per ASIC depending on the local data load, resulting in a maximum of 5, 2.5 or 1 FEBs of the different types connected to a single ROB. With additional spatial contraints from system integration (no connections across quarter stations, no cable crossings) the total number of ROBs for the STS amounts to approx. 1000, with 3000 optical readout links and 1000 control links. For ASIC timing and control, one single E-Link output and one phase adjustable 160 MHz clock are connected from the master GBTX to each FEB; the control responses use any of the readout uplinks. All E-Links between FEBs and ROBs will be AC-coupled in order to allow the connection of a single ROB to multiple FEBs operated at different potentials together with their connected sensors. The ROBs will be located at the sides of the STS detector box outside the detector acceptance. Flexible flat cables of approximately 0.6 m length will connect the stacks of FEBs for a given quarter station of the detector to the corresponding stack of ROBs.

The version 2 of the STS-XYTER ASIC [2] will implement the GBTX E-Link interface with a configurable number of 1 to 5 readout links and a synchronous readout and control protocol that was specifically developed for the STS-XYTER readout via GBTX [3]. A demonstrator board with a single GBTX and Versatile Link components will be available from CERN for initial tests in early 2015 and a CBM ROB prototype with full functionality is currently being prepared. Larger quantities of the devices from the sole production run are expected end of 2015.

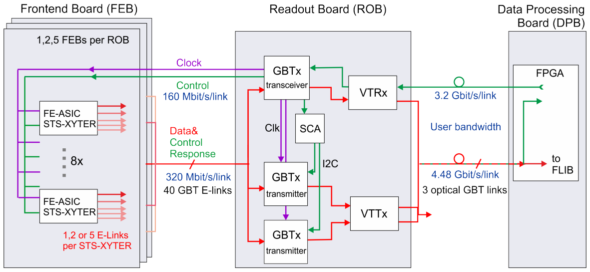

Figure 1: The STS readout chain with the readout board based on GBTX and Versatile Link components

References

[1] P. Moreira *et al.*, CERN-2009-006.342

[2] K. Kasinski *et al.*, *Towards the STS-XYTERv2, a silicon strip detector readout chip for the CBM STS*, this report

[3] K. Kasinski *et al.*, Proc. SPIE Int. Soc. Opt. Eng. **9290** (2014) 929028

Development of software tools for the prototype readout chains of the CBM Silicon Tracking System

I. Sorokin[1,2]*, M. Krieger*[3]*, J. Lehnert*[1]*, W. Müller*[1]*, E. Ovcharenko*[4,5]*, and F. Uhlig*[1]

[1]GSI, Darmstadt, Germany; [2]KINR, Kiev, Ukraine; [3]ZITI, Universität Heidelberg, Mannheim, Germany; [4]ITEP, Moscow, Russia; [5]JINR, Dubna, Russia

Development and characterization of detector prototypes requires powerful, flexible, and reliable software tools, such as data acquisition, slow control and on-line/off-line monitoring systems. The present STS prototype readout chain includes the n-XYTER 1.0 and STS-XYTER 1.0 front-end ASICs, the SysCore versions 2 and 3 (SCV2, SCV3) readout boards, and the FLIB interface board [3]. Whereas the FLIB-based data acquisition system is covered in [4], the present report covers the controls and monitoring tools for the front-end ASICs and readout boards, as well as the USB-based readout system.

Controls

A control server library, which provides a high-level interface to various CBMNet [2] devices, such as the front-end ASICs and the SCV2 and SCV3 readout boards, has been developed. Having in mind its usage for the final experiment, the control server enables sending command sequences to a large numbers of CBMNet slaves in parallel.

Client libraries with device-specific macro commands were also developed. For the systems, based on SCV2s and n-XYTERs, these commands include transactions over the I^2C interface (which is needed for n-XYTER configuration), as well as over the SPI interface (which is used for controlling the ADC). Additionally, the possibilities to switch n-XYTER between the self-triggering and externally-triggered operation modes was provided. A possibility to configure the AUX block of the SCV2 was provided as well. For the systems, based on the STS-XYTER ASIC and SCV3 readout boards, only simple configuration scripts with hard-coded default settings are currently available.

In future it is planned to connect the data acquisition system to the control libraries. This will enable to receive the feedback from the system immediately after changing a setting, and to use this information for taking decisions on further adjustments. Thus, for example automatic trimming of the thresholds will be possible. This will also simplify performing various parameter scans and calibrations.

Both the server and the client libraries are provided together with the dictionaries for the CERN ROOT interpreter. This enables to use the ROOT interpreter as convenient environment for interactive system configuration.

On-line and off-line monitoring

The development of the on-line/off-line monitoring tools is still in progress. Unpackers for the n-XYTER and STS-XYTER raw data were implemented in CbmRoot [5]. For the STS-XYTER, basic checks of the self-consistency of the data is performed. Thus, it is checked whether the epoch numbers within an individual epoch message are consistent, and whether the epoch messages from each data link are coming in the right sequence. For the hit messages the bit parity check is performed. Also the correctness of the detector transport message (DTM) number is checked at the stage of microslice unpacking.

An analysis library, evaluating the hit rates per channel, hit amplitude distributions, total data rate, etc. was implemented. It is a simple, but essential system diagnostic tool.

Particular care was taken to optimize the code for high performance, in order to achieve maximum analysis throughput.

USB-based readout for SCV3 and STS-XYTER 1.0

Along with the FLIB-based data acquisition system, a data acquisition system operating over USB has been developed. This enables external R&D groups to quickly deploy the SCV3-based setups, and operate them without the need of using the FLIB board. Same control and on-line analysis tools can be used with systems, read out over USB. Transporting up to 27 MB/s of data was achieved, and it is limited by the USB bus.

References

[1] A. S. Brogna *et al.*, *n-XYTER reference manual*, unpublished. http://hipex.phys.pusan.ac.kr/drupal/sites/default/files/nXYTER.pdf

[2] F. Lemke, S. Schatral and U. Brüning, CBM Progress Report 2013, Darmstadt 2014, p. 86

[3] J. de Cuveland, D. Hutter and V. Lindenstruth, CBM Progress Report 2012, Darmstadt 2013, p. 89

[4] D. Hutter, J. de Cuveland and V. Lindenstruth, *CBM FLES input interface developments*, this report

[5] M. Al-Turany and D. Bertini, CBM Progress Report 2006, Darmstadt 2007, p. 3

Radiation hardness tests on electronic components for low voltage power supply of the CBM Silicon Tracking System

S. Löchner, P. Koczoń, and A. Rost
GSI, Darmstadt, Germany

Electronic components installed in the field of reaction products in future experiments at FAIR have to be radiation hard. At present, selected parts like DC/DC converters and LDO voltage stabilisers undergo exhaustive tests with use of intense minimum ionising particles' beams, mostly 3 GeV protons at Research Center Jülich's sychrotron facility COSY.

Testing setup

For components like DC/DC converters or LDO voltage stabilisers the output voltage level as well as expected transient voltage spikes rate due to the Single Event Upsets has to be monitored during irradiation. Voltage level monitoring (input and output) requires relatively low readout frequency below 1 Hz and can be implemented on inexpensive ARDUINO-Nano system [1]. Fast transients have been investigated on 4 trace digital oscilloscope Rhode-Schwarz RTO1044 [2] (triggering threshold has been setup to 15 mV). Measurement results have been recorded in nonvolatile memory and analysed.

Selected ASICs

For the radiation hardness tests several DC/DC converters have been chosen. Selection criteria like circuit efficiency, chip size, low coil inductivity, apropriate output voltage and sufficient output power as well as voltage setting flexibility have been applied. Only one model of the LDO stabilizer produced in rad hard technology has been examined until now. Alltogether 10 test boards with LTC3605 and 3 Boards with LTC3610 (Linear Technology) and 4 boards containing LM2596S (Texas Instruments) have been tested in two beam times. A GaN based ISL75051SRH has been abandoned according to producer information on radiation hardness of only 100 krad. All tested ASICs have been powered on during irradiation runs.

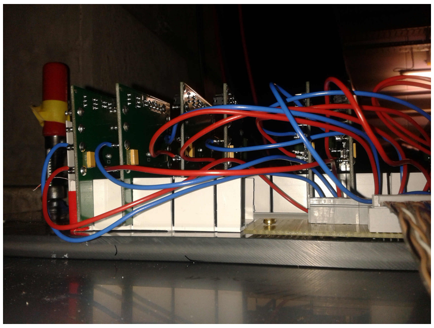

Figure 1: Base plate with PCB card holder and wiring

Test results

PCBs with tested chips have been placed in a row along the beam axis such that the irradiating beam punched through all of them. A small ionisation chamber placed on the beam axis behind tested chips has been used to monitor the beam intensity, corresponding to the shape of the proton beam with optical density corresponding to the integrated beam intensity. The total dose is known from the measurement with the ionisation chamber and position of irradiated chips is marked on the film. By optical scanning a fractional dose can be estimated for each point on the film. This allows to estimate precisely beam intensity integral and - consequenty - the dose at ASIC chips.

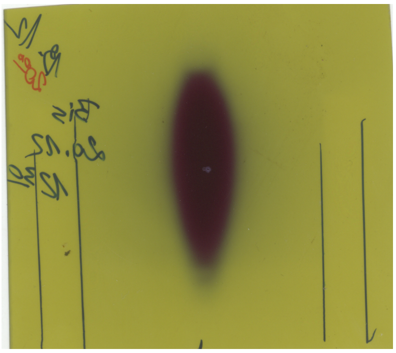

Figure 2: Beam spot on Gafchromic self-developing dosimetric film

Neither of tested DC/DC converters survived more than 4.3*10^9 protons.

No fast transients have been observed on LDO voltage stabilisers which have absorbed only 10^8 protons (measurement was stopped for technical reasons before planned dose was reached).

References

[1] S. Löchner and P. Koczoń, *A monitoring system for radiation hardness tests of electronic components for future FAIR experiments*, this report

[2] http://www.rohde-schwarz.de/de/Produkte/messtechnik-testsysteme/aerospace-and-defense/messtechnik/oszilloskope-fuer-ad/RTO.html

[3] http://www.ashland.com/products/gafchromic-radiotherapy-films

Low and high voltage powering concept for the CBM Silicon Tracking System

C. J. Schmidt and P. Koczoń
GSI, Darmstadt, Germany

Due to the radiation damage to the silicon sensors in the CBM-STS detector their performance will deteriorate in course of experimental activity. Gradually increasing their depletion voltage will improve the efficiency again and prolong their life time. This procedure will be applied to each of almost 1300 sensors separtely what motivates the powering architecture described in this report.

Requirements for powering

The Silicon Tracking Systen of CBM will be operated together with the Micro Vertex Detector inside the 1 T dipole magnet, in a rather small volume of about 2 m^3 [1]. To minimize the scattering of the reaction products tracked by the system only silicon sensors, their supporting structure and signal cables will be installed in the detector acceptance. The readout and converting electronics and its cooling as well as power converter will be installed on the detector's perimeter. Altogether almost 40 kW of heat has to be removed from the STS box to reach working conditions of -5 ^{o}C for the silicon sensors. Moreover, a very restricted amount of surface is available for connectivity with the outside infrastructure: all the cooling system's tubing, low and high voltage cabeling, data transmission and control link sockets have to be connected on 1.5 m^2 surface of the upstream wall of the detector. At least two different voltages are necessary for the STS-XYTER read-out ASIC [3, 4] and additional two for the GBTx [5] and optical converter.

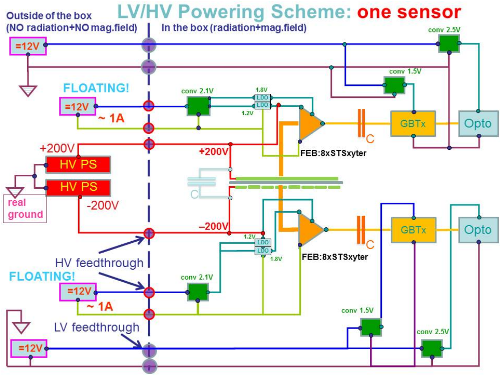

Figure 1: Low and high voltage powering scheme for one silicon sensor

Each sensor will be operated in a floating manner, i.e. the p- and n-sides will sense one half of the depletion potential (positive and negative); the read-out ASICs (and their powering) operate "on top" of the sensors' depletion voltage. The distance between the last component shaping low voltage should be as close as possible to the front end ASIC in order to minimize the amount of noise irradiated into the system. High depletion voltage (low current) can be generated and controlled from the outside of the STS volume. All electronics parts inside the STS box should be radiation hard and stand a magnetic field of at least 1 T.

Proposed powering scheme

The schematics in Fig. 1 shows the proposed power distribution. Both sides of the sensor (central part in the figure) are supplied with positive and negative depletion voltage generated outside of the magnetic field (+200 V and -200 V in this case, red lines) with a common ground. The sensors' strips are connected to the STS-XYTER read-out ASIC on the Front Electronic Board (FEB) with microcables (orange elements). The ASIC's powering of 2.2 V and ca. 4 A (per FEB) will be generated by a FEAST DC/DC converter placed on the side part of the cooling plate [2]. It supplies two LDOs converting the input voltage to 1.8 V (digital) and 1.2 V (analog part) of the ASIC. The latter has to be grounded in the vicinity of the sensor to +200 V or -200 V respectively. Input power of 12 V and about 1 A is delivered from outside for each detector module separately. This construction minimizes grounding loops and assures separation of strong and weak current flow. A GBTx chip is equipped with many e-links and can communicate with more than one FEB simultaneously so GBTx circuitry has to be galvanically isolated from the STS-XYTER chips. GBTx and optical interface require their own power which will be generated from dedicated 12 V lines and additional FEAST converters (uppermost and lowermost parts in Fig. 1 in green). STS-XYTER as well as GBTx power stabilisation will be realised by LDO components placed directly on the corresponding PCB boards. The vertical dashed line in Fig. 1 depicts the border of the high irradiation and magnetic field region (front wall of the STS detector box) and the little circles the electrical connectors to the high (in red) and low (in blue) voltage DC generators.

References

[1] J. Heuser *et al.*, Technical Design Report for the CBM Silicon Tracking System, GSI Report 2013-4

[2] http://project-dcdc.web.cern.ch/project-dcdc/

[3] http://repository.gsi.de/record/51956/files/PHN-NQM-EXP-22.pdf

[4] R. Kleczek et a., IEEE NSS/MIC 2013, doi:10.1109/NSS-MIC.2013.6829538

[5] GBTx Project: https://indico.cern.ch/event/113796/session/7/contribution/37/material/slides/0.pdf

Modification of the CBM-STS micro-cable stack-up

D. Soyk, C. J. Schmidt, V. Kleipa, and I. Sorokin
GSI, Darmstadt, Germany

During several years of development of the CBM modules, the STS sensors and the CBM STS-XYTER chips were carefully studied and designed. Despite this careful evolution, the design and study of the connecting part between the sensor and the chip had not been addressed in such intensity. Some studies on the electrical behavior were performed, while all questions of cable stockage were addressed this year. In [1] the cross section of the cable - like it was used for the electrical simulation - is described. Figure 1 shows the modified cable stack-up.

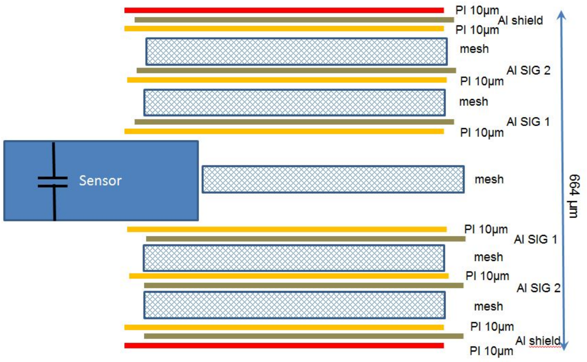

Figure 1: Schematic side view of the micro cable stack up for one CBM module. The red layer on the top and the bottom of the cable is the newly introduced insulation layer. In the middle, at the side of the sensor, the meshed layer to reduce crosstalk between the two sensor sides was newly introduced.

The geometry of the signal strands with a height of 14 μm and a width of 46 μm is kept, also the pitch between the strands remains 116 μm on each signal layer. As substrate for the strands 10 μm thick polyimide will be used. The thickness of the mesh will be kept at 100 μm, but a study is beeing done to find a mesh material with a lower mean dielectric constant. Also a additional layer of meshed material will be inserted between the microcable for the n- and p-side of the sensor. With this layer the crosstalk between the signals of both sensor sides should be minimized. The shielding layer will be modified. The thickness of the aluminum will be reduced to 14 μm (instead of 30 μm) and the polyimide will have a thickness of 10 μm (instead of 20 μm). With these changes the same aluminium polyimide film may be used for the signal layers, as well as for the shielding layers. Due to the fact that the sensors of different modules of a ladder are on different potentials, it could be an advantage to introduce a additional layer of polyimide insulation on the outside of the shielding. This allows us to keep the shielding potential for each sensor side and for each sensor in a ladder on a defined and independent level, namely the reference level of the pre-amplifier input stage. With these additional two insulating layers of 10 μm and the meshed layer in between, the total thickness of the stack is 664 μm per module.

The modified stack-up of the micro cable was already presented at the 24th CBM Collaboration Meeting in September 2014. The research for a mesh material with lower dielectric constant is ongoing. This cable stack-up will now be realized for the next module prototype.

References

[1] J. Heuser *et al.*, *Technical Design Report for the CBM Silicon Tracking System*, GSI Report 2013-4, Darmstadt, Fig. 4.10

Improvement of ultra-light microcables production at LTU for the CBM Silicon Tracking System

V. M. Borshchov[1], *I. T. Tymchuk*[1], *C. J. Schmidt*[2], *V. G. Kucherenko*[1], *G. I. Nikitskiy*[1], *J. M. Heuser*[2], *M. A. Protsenko*[1], *J. Eschke*[2,3], *R. A. Kushniruk*[1], *L. V. Klimova*[1], *and K. M. Liholitova*[1]

[1]LED Technologies of Ukraine (LTU) Ltd, Kharkov, Ukraine; [2]GSI, Darmstadt, Germany; [3]FAIR, Darmstadt, Germany

Ultra-light micro-cables are the key component for the CBM-STS. They are employed to realize the analogue signal interconnection between detector and readout for the STS at minimized material budget. Taking into account the complexity of micro-cables and their required quantity a few "bottlenecks" in the production line have been identified and improvements were realized on the production line. Additionally the preliminary technological regimes were defined and a test batch of micro-cables (100 pieces) was manufactured within the framework of the STCU partner project P635.

For the detector modules two kinds of interconnection components will be employed [1-2]:

- ultra-light interconnection microcables based on aluminium-polyimide adhesiveless dielectrics (connecting microcables, interstrip cables, daisy-chain cables, shielding layers).
- meshed spacers based on Kapton or polyimide (narrow and wide meshed spacers).

The typical technological process of micro-cable and spacer manufacturing includes the following main technological operations based on photolithography and chemical wet etching processes: chemical cleaning of the substrate, photoresist coating on the substrate, photoresist exposure, photoresist development, aluminium etching (for interconnecting micro-cables), polyimide etching and finally photoresist removal.

Taking into account that large numbers of components in a considerable design variety need to be produced for the CBM STS (about 58 thousand micro-cables and spacers) the available technological equipment and the production line were analyzed with the aim to identify possible production "bottlenecks" which might result in production yield issues or even a suspension of production. The available equipment allows to produce the required components but two "bottlenecks" were identified:

- equipment for photoresist coating needed duplication,
- an exposure unit for photoresist exposing needed to be duplicated.

The following equipment was in consequence supplied by GSI to LTU Ltd within the STCU partner project, both from Bungard Elektronik, Germany:

- a Dip Coater RDC 21-K type,
- a parallel beam exposure unit EXP8000.

The equipment was installed and tuned in the clean room at the cable production site in Kharkov (Fig. 1). Process parameters for the operation of these machines for the different types of components were investigated and preliminary regimes were chosen.

Based on these parameters, a first pilot batch of microcables was produced and delivered to GSI so that the module assembly processes could be elaborated (48 laminated and 52 non-laminated test microcables 11 cm and 21 cm long). Samples of test cables are depicted in Fig. 2. The cable production line at LTU has been strengthened towards the large scale serial production of micro-cables for the CBM-STS. Technological regimes on the newly installed equipment were investigated and a batch of test microcables produced. This is a starting point for further production process optimization towards yield.

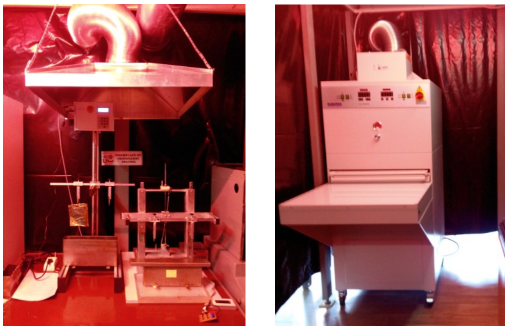

Figure 1: Dip coater RDC 21-K (left) and exposure unit EXP8000 (right) installed at LTU

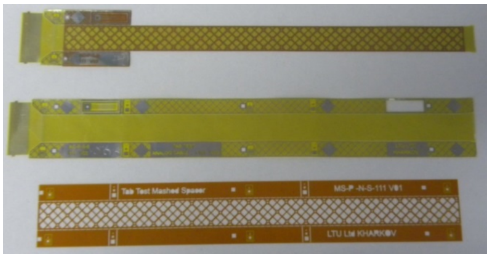

Figure 2: Experimental micro-cables for the development of the TAB-bonding assembly steps at GSI

References

[1] V. M. Borshchov *et al.*, CBM Progress Report 2013, p. 41
[2] C. J. Schmidt *et al.*, CBM Progress Report 2012, p. 18

Tooling for CBM STS module assembly

D. Soyk, C. Simons, and R. Visinka
GSI, Darmstadt, Germany

The CBM STS module assembly needs tooling to simplify and speed up fabrication [1]. For several assembly steps specialized assembly tools are needed. Assembly will comprise the following steps: First, two layers of microcables need to be bonded on to the STS-XYTER chip to form a "chip-cable". Second, 8 chip-cables must be bonded to the CBM STS sensors side by side for readout of the full 1024 channels for every sensor side. Additionally, on singlemetal sensors an interstrip connecting cable must be allocated and bonded on one side of the sensor. It serves to interconnect the inclined strips that end on the sensor side to form a continuous strip over the sensor. Therefore a whole set of assembly tools must be developed and - if needed - improved. To start with simplest element, the tool for the first cable layer on the chip was design, produced and tested. This first version was already shown in [1].

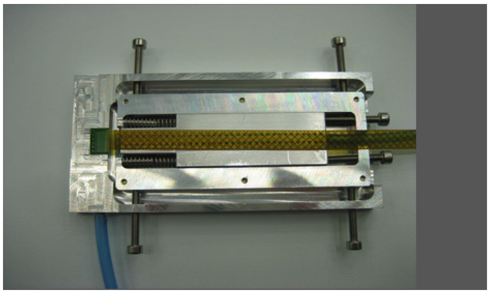

Figure 1: Tool for 1st layer on chip

In Fig. 1 the improved version is depicted.It has small bumps to avoid crashes between the bond needle and the tool. This change increases the safety of operations and will be an advantage for the mass production by reducing the machine downtime due to such crashes. The chip and the cable in this design were still held by vacuum and manipulated via a bottom-side mechanics. Second, a tool for bonding of the second layer of the micro cable to the chip was designed.Because of the presence of the first layer, already bonded and glued to the chip, the second cable layer needs to be mounted from the top side. The chip is still fixed from the bottom-side, but the jig for micro cable mounting is now above it. This does increase the height of the tool, but this height is not a showstopper, because the operating range of the tab-bond needle is not above the cable but the chip. See Fig. 2.

To assembly the microcables with the chips to the sensor a third tool with a movable bottom-side sensor holder and a top-side mechanics for the microcables was designed. It is shown in Fig. 3.

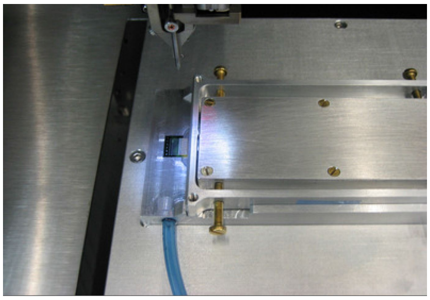

Figure 2: Tool for 2nd layer on chip

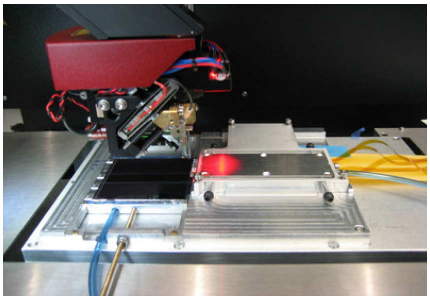

Figure 3: Tool for 1st and 2nd layer on sensor

It turned out that a movable sensor holder is not the best way for this assembly step, because the flimsy microcables are destroyed if they're moved too strong. An improvement of this tool is in work. Fortunately it also turned out, that this tool could be used to bond the interstrip connecting cables on the p-side of the sensor (see Fig. 4).

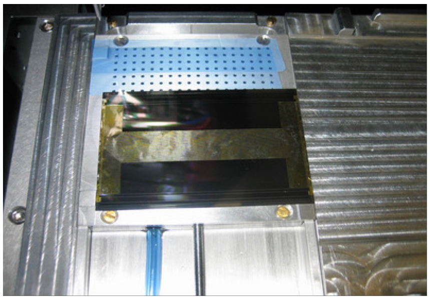

Figure 4: Interstrip cable on sensor

References

[1] D. Soyk et al., CBM Progress Report 2013, Darmstadt 2014, p. 42

Manufacturing detector modules for the CBM Silicon Tracking System

V. M. Borshchov[1], *Yu. A. Murin*[2], *C. J. Schmidt*[3], *M. A. Protsenko*[1], *I. T. Tymchuk*[1], *J. M. Heuser*[3], *R. A. Kushniruk*[1], *N. F. Chernikova*[1], *L. V. Klimova*[1], *and M. S. Tykhomirova*[1]

[1]LED Technologies of Ukraine (LTU) Ltd, Kharkov, Ukraine; [2]JINR, Dubna, Russia; [3]GSI, Darmstadt, Germany

Based on the new module assembly concept [1] and its preliminary test on the first half-detector module mock-up [2], three types of detector modules were developed and 18 module mock-ups manufactured to verify the technical approach. The module mock-ups allowed specifying their exact composition, defining nomenclature and marking of components, and the work-off of the assembly procedure. The work, coordinated by JINR, was co-funded through the BMBF-JINR project 5.2 "Development of ultra-low-mass silicon micro-strip detector systems for precision tracking in high-energy heavy-ion collision experiments" with project partners at GSI and JINR.

The detector module mock-ups have been developed according to the composition of the smallest STS ladder comprising 6 modules:

- 2 double-sensor modules with sensor-to-FEB distance 111 mm (one left and one right type),
- 2 single-sensor modules with sensor-to-FEB distance 212 mm (one left and one right type),
- 2 single-sensor modules with sensor-to-FEB distance 252 mm (one left and one right type).

Each module mock-up includes following components:

- one or two dummy sensor with interstrip cable;
- multilayered connection microcables;
- dummy chips;
- dummy FEBs.

For sensor-to-FEB connection [1,2] following components are foreseen:

- eight multilayered microcables (128 lines for chip to sensor connection). Each multilayered cable includes two connecting layer (FDI-A-24, 64 traces at 113 μm pitch) and eight meshed spacers (Kapton 50 μm thick).
- overall meshed spacer for all 8 multilayered microcables (two Kapton spacers 50 μm thick).
- overall shielding layer for all 8 multilayered microcables (FDI-A-24) with glued meshed spacer (Kapton 50 μm thick).

Taking into account abovementioned types of components for each module from 16 to 19 types of components were developed and produced. Also was defined following nomenclature and marking of components for further production:

1. AC-P-S-T- *- analog cable, P-side, short, top
2. AC-P-L-T- *- analog cable, P-side, long, top
3. AC-P-S-B- *- analog cable, P-side, short, bottom
4. AC-P-L-B- *- analog cable, P-side, long, bottom
5. AC-N-S-T- *- analog cable, N-side, short, top
6. AC-N-L-T- *- analog cable, N-side, long, top
7. AC-N-S-B- *- analog cable, N-side, short, bottom
8. AC-N-L-B- *- analog cable, P-side, long, bottom
9. SL-P- *- shielding layer, P-side
10. SL-N- *- shielding layer, N-side
11. MS-P-N-S- *- meshed spacer, P-side, narrow, short
12. MS-P-N-L- *- meshed spacer, P-side, narrow, long
13. MS-N-N-S- *- meshed spacer, N-side, narrow, short
14. MS-N-N-L- *- meshed spacer, N-side, narrow, long
15. MS-P-W- *- meshed spacer, P-side, wide
16. MS-N-W- *- meshed spacer, N-side, wide
17. ISC-**- interstrip cable,
18. DCC-P- daisy-chain cable, P-side,
19. DCC-N- daisy-chain cable, P-side

* *base sensor-to FEB distance (111, 212, 252 mm)*
** *length of sensor (42, 62 mm)*

Example of cable marking: AC-N-S-T-111 = analog cable, N-side, short, top with sensor-to-FEB distance 111 mm.

According to the above mentioned composition of STS ladder, modules and multilayered connection microcables for three types of modules (111, 212, 252 mm) about 100 photomasks were developed and produced. Using those photomasks for 18 modules more than 1300 microcables and spacers (about 70 components for one module) were manufactured. Six types of assembled modules are depicted in Fig.1. The mock-ups of the detector modules (6 pcs) will be used to assemble the first mock-up of a full-scale ladder [3].

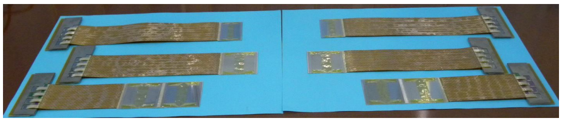

Figure 1: Detector module mock-ups

References

[1] V. M. Borshchov *et al.*, CBM Progress Report 2013, p. 41

[2] C. J. Schmidt *et al.*, CBM Progress Report 2012, p. 18

[3] V. M. Borshchov *et al.*, *The first mock-up of a CBM STS full-scale ladder*, this report

Design and prototyping of a carbon fiber support frame for the central ladders of the CBM Silicon Tracking System

S. Igolkin[1], *S. Belogurov*[2], *A. Chernogorov*[2], *A. Kolosova*[2], *Yu. Murin*[3], *and A. Semennikov*[2]
[1]CERN, Geneva, Switzerland; [2]ITEP, Moscow, Russia; [3]JINR, Dubna, Russia

The ladders of the STS placed in the central part of the station have to be specially designed to pass through the beampipe. The original concept of the beampipe was optimized to conduct experiments at SIS 300 and at SIS 100 with the energy of the incident gold ions above 8 AGeV. Further development of the CBM@SIS100 physical program required tuning of the setup to work with the energy of incident gold ions lowered down to 4 AGeV. The principal change of experimental conditions at low energies relevant to the beampipe and central ladders design is higher multiple scattering of gold ions inside the target. At present, there is no single reliable parameterization of multiple scattering of heavy ions at wide angles. The CbmRoot (Geant3), Geant4, and FLUKA codes provide a possibility to simulate this process, but since they give different results, the most conservative estimate (3.2 degrees at 4 AGeV given by GEANT4) was used for definition of the beampipe opening angle. The original design of the central ladder suitable for the beampipe with a 1.6 degree opening angle is shown in Fig. 1.

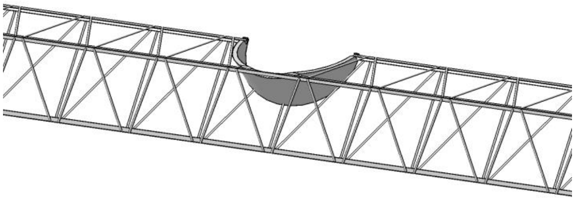

Figure 1: Design of the CF frame of central ladder

One can see that the middle rib of the carbon fiber (CF) frame is not broken thus providing the necessary rigidity of the construction. The 3.2 degrees opening angle for the beampipe is not compatible with the original design of the central ladder CF frame. One has to increase the diameter of the cylindrical insert by a factor of two. The new type of the central ladder with a 118 mm diameter of the cylindrical part has been designed and built. Figure 2 shows the overall view of such a ladder, the components of the central ladder are shown in Figure 3. In Fig. 4 a mold is presented used in the manufacturing the ladder. The ladder obtained has the necessary rigidity at the mass of the cylindrical part of 5 g. Depending on the result of the ongoing simulations, the mass of the cylindrical part can be reduced by removing the excess material in the regions with low mechanical stress.

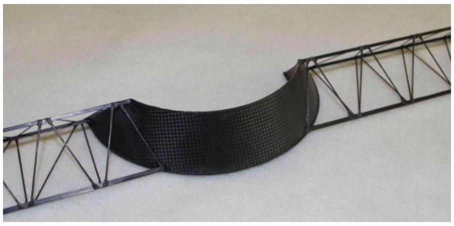

Figure 2: Prototype CF frame of a central ladder

Figure 3: Components of the prototype CF frame

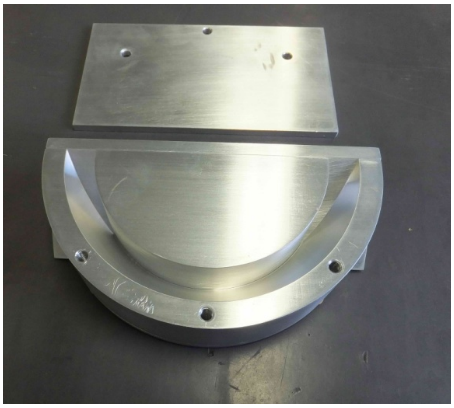

Figure 4: Mold for the production of the CF frames.

The first mock-up of a CBM-STS full-scale ladder

V. M. Borshchov[1], *N. F. Chernikova*[1], *V. V. Elsha*[1], *V. G. Kucherenko*[1], *Yu. A. Murin*[2], *G. I. Nikitskiy*[1], *M. A. Protsenko*[1], *and I. T. Tymchuk*[1]
[1]LED Technologies of Ukraine (LTU) Ltd, Kharkov, Ukraine; [2]JINR, Dubna, Russia

The first mock-up of the CBM STS ladder has been developed and manufactured by the Kharkov team at the assembly site of LTU Ltd (Figs. 3 and 4). The ladder mock-up was developed for verification of ladder assembly route [1,2]. The work was funded and coordinated by JINR.

The ladder mock-up includes the following components, similar as in real full-scale ladder (Fig. 1):

- mock-ups of silicon strip modules (6 pcs) [3];
- containers for the FEBs (2 pcs);
- carbon fiber frame (CF-frame) on the support units (1 pc).

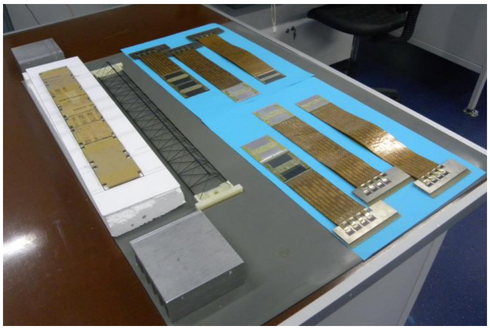

Figure 1: Components of the ladder mock-up

For the assembly of the ladder mock-up, the sequence of work steps has been developed. It includes following steps:

- mounting and fixation of double-sensor modules #1 and #2 to jig (Fig. 2);
- mounting and fixation of single-sensor modules #3 and #4 with the necessary overlapping of sensors to fixture;
- mounting and fixation of single-sensor modules #5 and #6 with the necessary overlapping of sensors to fixture;
- mounting and fixation of CF-frame to fixture;
- gluing of sensor holders to sensors and CF-frame. Glue polymerization;
- mounting of the FEB mock-ups in the container on thermal paste;
- turning of containers with the FEBs by 90 degree.

The assembled mock-up is depicted in Figs. 3 and 4. The completed work allows us to conclude on the feasibility of the previously selected design ladder for the CBM STS. The obtained results will be used for the clarification of technical tasks for sthe pecialists of PLANAR for designing and manufacturing of the optical-mechanical assembly tools. Further efforts of should be aimed at the clarification of the ladders composition, applied materials and geometrical dimensions of all ladder components.

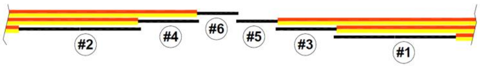

Figure 2: Diagram of sensor overlap

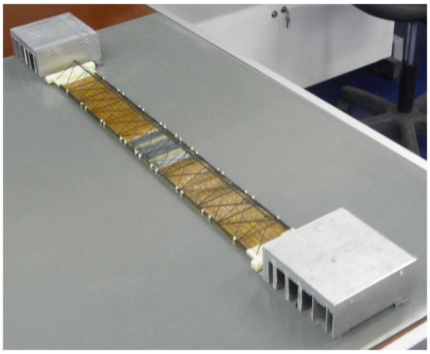

Figure 3: First mock-up of the CBM STS ladder

Figure 4: Team at the assembly site of LTU Ltd

References

[1] Workshop on module and ladder components production and assembly for the CBM Silicon Tracking System, LTU Ltd, Kharkov, Ukraine, 14-17 January 2014

[2] Workshop ”From Consortium to Cooperation”, LHEP JINR, Russia, 1-3 October 2014

[3] V. M. Borshchov *et al.*, *Manufacturing detector modules for the CBM Silicon Tracking System*, this report

Setting up the STS module and ladder assembly site at JINR-LHEP

Yu. A. Murin[1], *V. V. Elsha*[1], *V. A. Penkin*[1], *O. D. Sheremetyev*[1], *V. M. Borshchov*[2],
M. V. Gerasimenko[2], *M. A. Protsenko*[2], *and I. T. Tymchuk*[2]
[1]LED Technologies of Ukraine (LTU) Ltd, Kharkov, Ukraine; [2]JINR, Dubna, Russia

Works on the organization of module and ladder assembly site at LHEP JINR for CBM STS were performed.This assembly site is developed jointly by the specialists from JINR and LTU. The work was supervised and coordinated by JINR.

The assembly site includes: dressing room, changing room and clean room (see Fig. 1). The range of clean room purity should correspond to the ISO 7 class. The total area of the site exceeds 100 square meters, including more than 50 square meters of clean room.

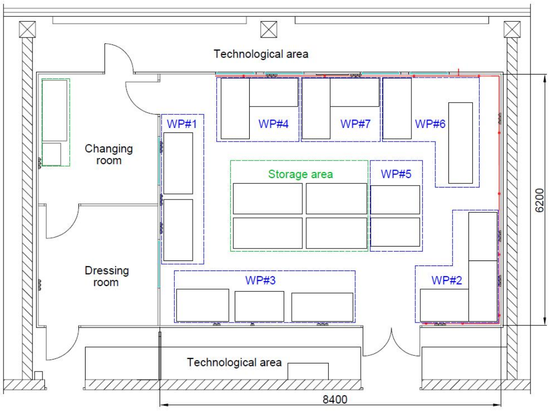

Figure 1: Layout of the assembly site

In the cleanroom seven workplaces will be created with the following indicated equipment [1-2]:

1. Workplace for parts kitting.
2. Workplace for modules and components assembling (automatic bonder for TAB-bonding).
3. Workplace for bond joints protecting and gluing (dry box, scales, dispenser, oven).
4. Workplace for chip-to-FEB wire bonding (semi-automatic bonder for wire-bonding).
5. Workplace for modules and components testing.
6. Workplace for ladders assembling (optical-mechanical system).
7. Workplace for ladders testing.

All work places must be equipped by microscopes and ionizers. Also the area for modules and components storage must be prepared.

In the beginning of 2014 space for the construction of the cleanroom was prepared in the building of JINR-LHEP. In the beginning of 2015 the creation of the cleanroom was finished and its certification completed (Fig. 2).

Figure 2: Cleanroom prepared at JINR-LHEP

Further works on the establishment of an assembly site will comprise: installation of equipment on workplaces, connecting line of the vacuum and compressed air, start-up of the site, training of technical staff of the basic assembly operations. After completion of the abovementioned works, this site will be able to provide assembly productivity (within production stage) in the range of 15 to 16 modules per month and 3 ladders per month [3]. At full load, the staff working in the cleanroom will amount to at least seven technicians.

References

[1] Workshop on module and ladder assembly for the CBM Silicon Tracking System, JINR, Dubna, Russia, 6-7 June 2013

[2] Workshop on module and ladder components production and assembly for the CBM Silicon Tracking System, LTU Ltd, Kharkov, Ukraine, 14-17 January 2014

[3] V. M. Borshchov *et al.*, CBM Progress Report 2013, Darmstadt 2014, p. 44.

Development of a CO_2 cooling prototype for the CBM Silicon Tracking System*

J. Sánchez[1], *J. M. Heuser*[1], *W. Niebur*[1], *C. Sturm*[1], *H. R. Schmidt*[2], *A. Lymanets*[2], *P. Petagna*[3], *B. Verlaat*[3], *and L. Zwalinski*[3]

[1]GSI, Darmstadt, Germany; [2]Universität Tübingen, Tübingen, Germany; [3]CERN, Geneva, Switzerland

The CBM Silicon Tracking System is based on silicon sensors with double-sided strip readout. These sensors must be kept at least at -5° C to ensure the required performance. Due to this cooling demand the design and manufacturing of a 1 kW prototype called TRACI-XL, shown in Fig. 1, was chosen as the best option as starting point for specifying the technical features and requirements of the final cooling plant.The main heat sources of the detector are the read-out electronics, which dissipate about 40 kW according to the current specifications and they must be removed completely. This does not mean that the final plant will be 40 times bigger but it will allow to scale the experimental results and to get conclusions about the CO_2 nucleate boiling behavior and to start the engineering development of the cooling plates, fluid distribution and other important aspects.

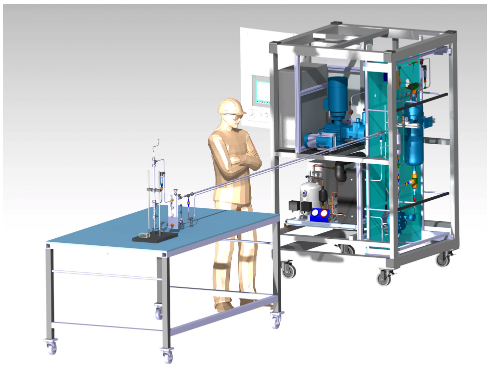

Figure 1: A CATIA model of TRACI-XL

Preparations for the commissioning phase

In order to ensure a correct performance of the plant an exhaustive protocol has been defined. The commissioning phase comprises the following tests:

- Safety verifications: Electrical safety (Electrical cabling, PLC I/O testing, alarms testing), mechanical safety (Pressure test and leak test).
- Basic functionalities tests: Real conditions analog alarm testing, chiller operation, pump operation, accumulator pressure regulation.
- Advanced performance tests: Automatic procedure testing, stable chiller operation over the full operating range, stable pressure (temperature) regulation in every condition, stable flow control.
- Thermodynamic performance: Test with a 1 kW dummy load in a wide range of temperatures, test with gradual power supply, shock test: sudden disconnection of electronics.

The PLC parameters such as pressures, temperatures, mass flow, alarms, interlocks etc. can be forced to bring the plant to extreme conditions and to check that all the safety and recursive procedures work as expected. In addition a 1 kW dummy heat load which simulates the future connected read out electronics was developed. This experimental heat source is based in a 3/4" pipe with a concentric fire rod providing a power of 1 kW and the respective sensors.

Finalizing the assembly stage

Once the concept design phase finished, the mechanical assembly stage (Fig. 2) takes a great relevance because it is the moment to introduce changes into the design after analyzing the evolution of the prototype and detecting possible defects or improvements. Parts of the mechanical frame were adapted to gain in stability and to reduce noise installing materials for vibration damping. Some other parts were relocated in order to facilitate the accessibility to every component in case they must be replaced, or distributed to ensure sufficient ventilation in the plant.

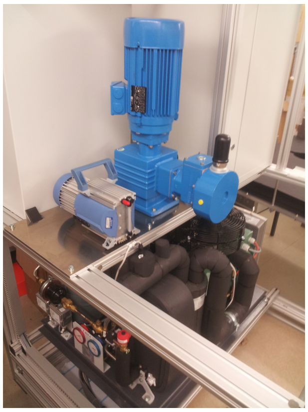

Figure 2: Vacuum pump set-up with condensing unit

References

[1] R. W. Lockhart and R. C. Martinelli, Chem. Eng. Progr. **45** (1949) 39

---

* Work supported by EU-FP7 CRISP.

Development of a compact, highly efficient heat exchanger assembly for bi-phase CO_2 Cooling of the CBM Silicon Tracking System

E. Lavrik[1], *A. Lymanets*[1,2], *and H.-R. Schmidt*[1]
[1]Universität Tübingen, Tübingen, Germany; [2]KINR, Kiev, Ukraine

The CBM Silicon Tracking System (STS) is a compact detector that consist of double-sided silicon microstrip sensors with an overall volume of about 2 m^3 defined by the aperture of the dipole magnet[1]. In order to reduce the material budget of the detector all heat producing readout electronics were moved outside of the acceptance zone, which in turn greatly reduced the space available for cooling. In order to avoid thermal runaway during the operation of the detector, the silicon sensors have to be kept at temperatures below -5°C. This is quite challenging as up to 50 kW of heat is dissipated from the STS Front-End-Electronics (FEE) in a rather small volume with very limited space for heat exchanger plates. We use bi-phase CO_2 cooling due to its superior volumetric heat transfer coefficient, which is about an order of magnitude better than conventional freons. The aim of this research project is to optimize the Front-End-Board (FEB) box housing FEE elements in terms of heat transfer efficiency under the given space constraints.

Open CO_2 Cooling system

In order to find the most effective FEB box design (Fig. 1), a series of Finite Element Method (FEM) studies were conducted as well as an open CO_2 cooling system was built, which allowed us to utilize the bi-phase CO_2 cooling.

The cooling system is designed to absorb about 200 W thermal load under realistic geometrical constraints. One has to verify the cooling efficiency of various FEB box designs. The heat generated by a resistive thermal load will be dissipated in the FEB box and removed by a cooling plate with integrated capillaries of about 2 m total length and about 2 mm diameter[2].

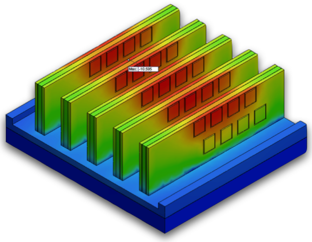

Figure 1: Sample FEB box design with heat distribution information obtained from thermal FEM studies

Results

To find out the most effective FEB box design, different FEB box were produced with varying thickness of the FEE supporting structure (shelve). These designs were then tested under different heat loads. Table 1 shows the experimental results from selected measurements. The experimentally measured trends were reproduced by the simulations.

Table 1: Experimentally measured maximal temperature on the FEB box in dependence of power applied and shelve thickness

Power Applied, W	Maximum Temperature, °C		
	1 mm	2 mm	3 mm
140	15	-14.2	-22.6
200	24	0.2	-15

The optimal FEB box design was found to be with shelve thickness of 3mm. Resulting FEB box dimensions are $105 \times 85 \times 35{,}6\,\mathrm{mm}^3$. This design was proposed to be used in the construction of the STS detector.

To make the operation of the STS detector cooling safer one wants to move further away from the triple point of liquid CO_2 (-56.6°C, 5.11 bar), i.e. eliminate the risk of solidifying the coolant. This is achieved by increasing the CO_2 temperature and pressure in the cooling lines, although this decreases cooling power. Table 2 shows the results of FEM simulations conducted to examine the dependence of maximal FEB box temperature versus coolant temperature. This study shows that safe operation and sufficient cooling can be achieved at -30°C.

Table 2: Result of simulations showing the expected maximal temperature on the FEB box in dependence of initial coolant temperature and power applied

Maximum temperature, °C		
T, coolant	T@200 W	T@140 W
-40	-10.6	-12.7
-30	-4.9	-9.9
-20	0.8	-4.1
-10	6.5	1.58

References

[1] J. Heuser *et al.*, Nucl. Instrum. Methods **A 568** (2006) 258

[2] E. Lavrik, A. Lymanets and H.-R. Schmidt, CBM Progress Report 2013, Darmstadt 2014, p. 40

Status of the CBM STS CAD design

J. Kunkel[1], *S. Belogurov*[2], *and J. Sánchez Rosado*[1]
[1]GSI, Darmstadt, Germany; [2]ITEP, Moscow, Russia

A virtual model of the planned CBM STS detector system gets designed in the CATIA CAD software in full detail [1]. It is used to visualize the space dependencies of all sub-systems like mechanics, electronics and cooling. In this report the status of the work on this model is shown.

Repository

Several people of the CBM STS collaboration work with the CAD model. Since they work in different institutes all over the world a platform was needed to enable collaborative work. As control system Subversion was chosen because of the instant availability and the ease of use. GSI hosts a Subversion server on which all CAD files are now located. This Repository not only gives access for everybody involved but also brings file versioning and backup.

Sensor layout

The sensor layout has been improved in the area around the beampipe and in the outer edges at the large stations. To optimise the amount of different parts and lengths of cables the readout electronics have been re-arranged to appropriate positions (see Fig. 1 and Fig. 2). Now only 16 different lengths of carbon ladders are needed.

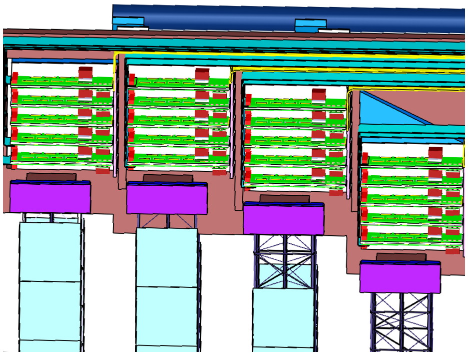

Figure 1: Detailed view of the upper end of ladders. Space between uppermost sensor and electronic not optimised for cables lengths (not shown).

Cooling plates

The detailed construction of the cooling plates has started (see Fig. 3). Different manufacturing methods and their influence to the shape of the plates were considered.

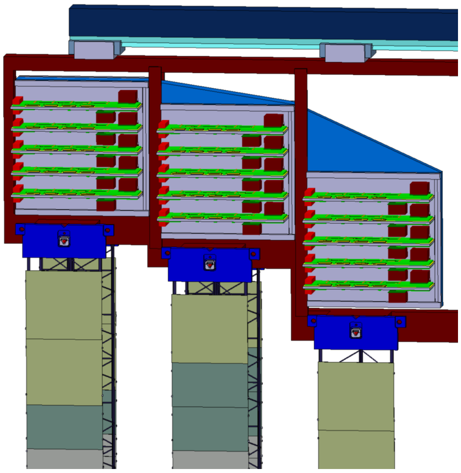

Figure 2: Detailed view with re-arranged electronics. Distances between sensors and electronics shorter and more regular.

Two special joining processes (with and without additional material) for aluminium are tested. At first two different sizes of plates are designed to prove the desired cooling power, pressure stability and the reliability of the production process.

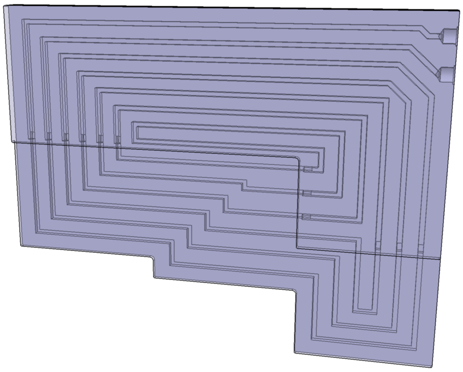

Figure 3: Semi-transparent view of a cooling plate. Length of inside channel is more than 5 m, cross section 4 × 4 mm. Connectors will be at the upper right corner.

References

[1] S. Belogurov, A. Kolosova and J. Kunkel, CBM Progress Report 2013, Darmstadt 2014, p. 46

Ring-Imaging Cherenkov Detector

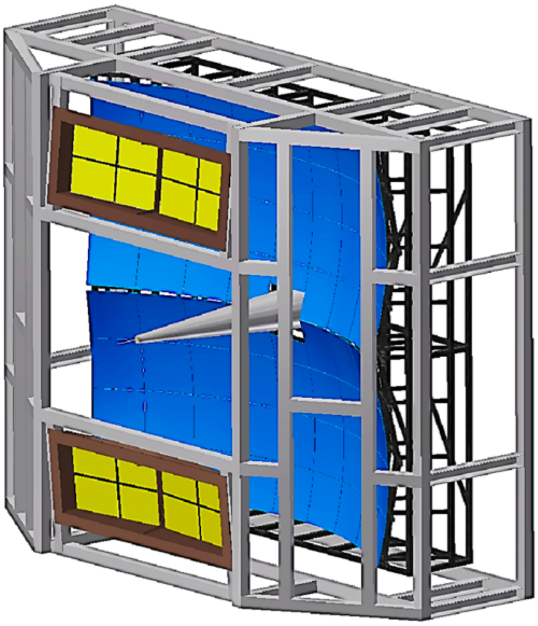

Mirror misalignment control system and prototype setup*

J. Bendarouach, C. Höhne, and T. Mahmoud
Justus-Liebig-Universität, Gießen, Germany

An important aspect to guarantee a stable and precise operation of any RICH detector is the alignment of the mirrors. The alignment itself has two aspects: the initial alignment during setup and a misalignment monitoring during operation. For the monitoring, methods have been established based on data or an independent control of the mirror positions. The CLAM method, developed by COMPASS [1], is an example of the latter and is tested for a future realization in the CBM-RICH. This article describes a test setup on a small scale that was implemented in the RICH prototype and tested in beam during the RICH beam time at CERN-PS in November 2014.

The principle of the CLAM (Continuous Line Alignment Monitoring) alignment procedure [1] is to monitor over time mirror displacements via photographic images. A grid of retro-reflective material is glued on the inner part of the RICH entrance window.

The grid is made of retro-reflective stripes, forming a regular grid-shaped pattern, and of photogrammetric target dots, glued at each of the stripes crossings and on the mirror frame (Fig. 1 left). A set of four cameras are arranged at the edges of the entrance window and around each camera a set of three LEDs are fixed (Fig. 1, right). The LEDs are switched on to illuminate the grid through the mirrors. A downscaled version with one camera only was implemented in the RICH prototype detector and tested at CERN.

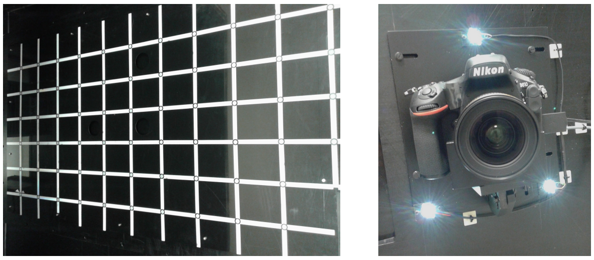

Figure 1: CLAM equipments used in the RICH prototype. Left: Retro-reflective grid with target dots; right: CLAM camera, surrounded by three LEDs.

Figure 2 shows two pictures taken for the aligned mirror system (left picture) and with misalignment of the lower left mirror by 2 mrad (right picture). Figure 3 illustrates ring reconstructions using these two setups. For the misaligned case an extreme example is shown with a B axis of the ellipse fit of 3.6; the average radius is 4.6.

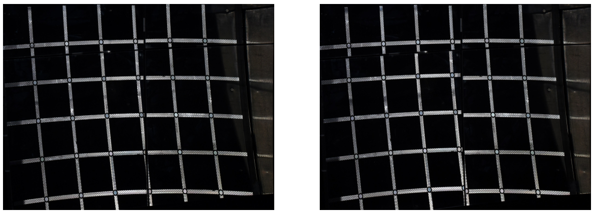

Figure 2: Reflection of the grid on the RICH mirrors. Unbroken lines not broken at mirror are a sign of alignment (left); broken lines reveal misalignment (right). Here, the misalignment of the lower left mirror is 2 mrad.

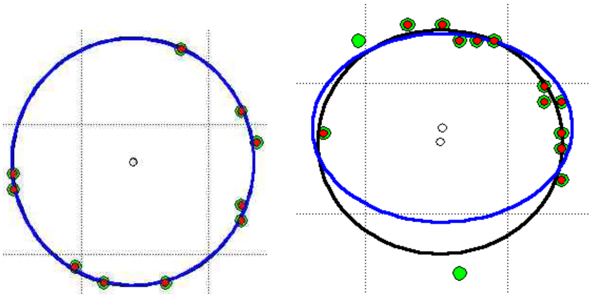

Figure 3: Single event reconstructions for beams passing between the two lower mirrors. Left: aligned setup; right: misalignment of 2 mrad.

A first qualitative look at mirror displacements can be obtained from the continuity of the reflected stripes. If a mirror is displaced with regard to one of its neighbors, stripes will appear broken at mirror edges (Fig. 2, right). Stripes are then cut into two shifted parts. From the shift it is possible to deduce the relative misalignment of mirrors [2].

A quantitative evaluation is also possible with this setup when considering photogrammetry. From the relative positions of target centers to external marked reference points, the orientation of mirrors can be extracted [3]. This procedure will be implemented in a next step.

Currently, the analysis of the beam time data is ongoing, and correction routines for the misalignment are in preparation.

References

[1] S. Costa *et al.*, Nucl. Instrum. Methods **A 553** (2005) 135

[2] M. Sulc *et al.*, Nucl. Instrum. Methods **A 595** (2008) 194

[3] L. Steiger *et al.*, Nucl. Instrum. Methods **A 639** (2011) 219

---

*This work was supported by HIC for FAIR, by the GSI F&E-Cooperation with Giessen, and by BMBF grant 05P12RGFCG.

Study of CBM RICH mirror supporting frame prototype

N. Boldyreva[1], *Ya. Berdnikov*[4], *A. Berdnikov*[4], *V. Dobyrn*[1], *C. Höhne*[2], *E. Leonova*[1], *N. Mifstahov*[1], *C. Pauly*[3], *Yu. Ryabov*[1, 4], *V. Samsonov*[1], *and O. Tarasenkova*[1]

[1]PNPI, Gatchina, Russia; [2]Justus-Liebig-Universität, Gießen, Germany; [3]Bergische Universität, Wuppertal, Germany; [4]SPbSPU, St.Petersburg, Russia

According to the basic layout of the CBM spectrometer, the RICH detector will be located right behind the magnet, in front of other sub-detectors [1]. The RICH concept foresees a classical scheme of the gaseous radiator and a focusing mirror surface. The latter consists of 36 individual mirror tiles of an area of approximately 400×400 mm^2 and a thickness of 6 mm each. These facts, together with the location of the RICH, impose special requirements on the design of its mirror supporting frame. It must ensure a safe assembly procedure and a stable optical system over many years while keeping the material budget minimal.

A mirror supporting frame made of aluminum profiles was simulated with ANSYS (Fig. 1). The results show that with a rigid fixation of the frame perimeter (outside the acceptance), the maximal deformation will not exceed 200 microns with the full load at the normal temperature. The deformation does not exceed 500 microns when the model is heated by 20°.

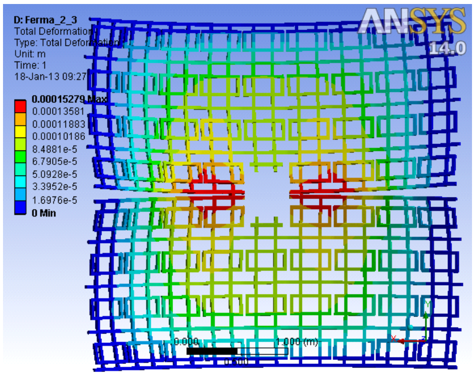

Figure 1: Deformations estimated in ANSYS

In order to verify these calculations, a prototype of the supporting frame was built with 3×4 tiles corresponding to $1/6$ of the total frame [2]. It consists of aluminum profiles connected via crosswise parts with high accuracy and precise connecting angles. This structure was placed in a rectangular outer frame with rigidly fixation on the perimeter. Mirror tiles were imitated with curved aluminum sheets (Fig. 2). Three options of mirror mounts to the frame were tested (Fig. 3). In the basic one the tiles are mounted to a rectangular form, which, in turn, is mounted to the frame.

Deformation tests were done with and without the mirror tiles each 24 hours for the duration of 20 days. In each test the distances between the centers of each two tiles and btween each center and the outer frame were measured. The accuracy of the measurements was 0.01 mm. With a weight of 150% of the nominal design parameters of the mirror tiles, the maximal deformation is less than 50 microns, which is in good agreement with simulations.

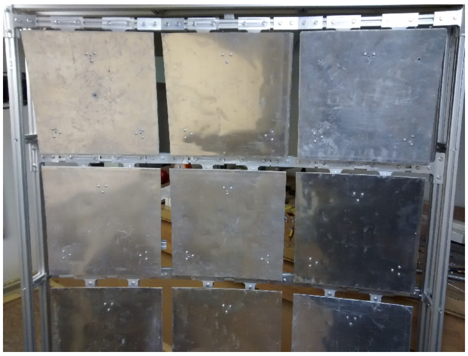

Figure 2: Prototype of the RICH mirror supporting frame

Figure 3: Mounting options for the mirror tiles. Left: base case (aluminum rectangle); middle: 3 independent mounts; right: 2 aluminum bars.

The other two mirror mounting options reduce the weight of the structure without loss of its strength and technological properties. The first considers three independent mounts of the mirrors to the frame; the second considers two aluminum bars (instead of a rectangle as in the base case). Although the 3-points option provides the minimal weight, it holds a high damage potential for the tiles during assembly. The 2-bars option reduced the weight by a factor of two and offers a safer and comfortable handling.

With the achieved results with the prototype we can state that the selected design and materials meet the construction requirements of reliability, durability and processability.

References

[1] V. Dobyrn *et al.*, CBM Progress report 2012, Darmstadt 2013, p. 40

[2] V. Dobyrn *et al.*, CBM Progress report 2013, Darmstadt 2014, p. 57

Acceptance studies of the CBM-RICH photodetector plane*

E. Lebedeva and C. Höhne
Justus-Liebig-Universität, Gießen, Germany

The CBM-RICH detector is designed to provide identification of electrons and suppression of pions in the momentum range below 10 GeV/c. This will be achieved using a gaseous RICH detector with focusing mirror elements and a photon detector. In this report we discuss studies in which the dimensions of the photon detector planes were decreased in order to investigate the influence on the reconstruction of low-mass di-electrons.

The distributions of $e^{\pm}$ from different sources on the upper photon detector plane are shown in Fig. 1. The signal $e^{\pm}$ as well as background $e^{\pm}$ are located mostly in the inner part of the PMT planes.

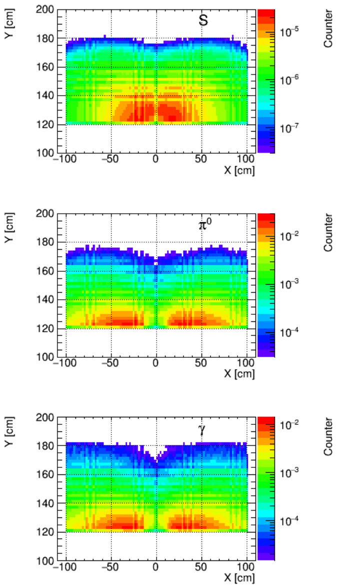

Figure 1: Distribution of $e^{\pm}$ from ρ-meson (top), π^0-Dalitz decay (middle) and γ-conversion (bottom) on the upper photon detector plane for central Au+Au collisions at 25A GeV beam energy

Two cases of eduction of the PMT planes were studied. The photodetector planes were cut a) from **the outer**, left and right sides and b) from **the inner**, left and right sides (see Fig, 2). 10%, 20% and 30% of the size were cut. 10% corresponds to 6 cm, i.e., approximately one row of MAPMTs.

The low-mass di-electron reconstruction was performed with the standard procedure (for more information see [1]). Electron identification was performed with the RICH, TRD and ToF detectors. The combinatorial background was rejected with a γ-conversion cut, two topology cuts and a transverse momentum cut.

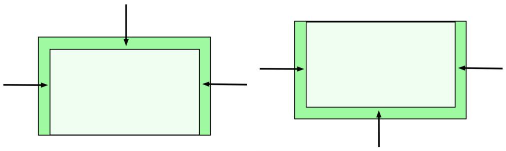

Figure 2: Cut of the PMT plane from a) outer; b) inner side.

The final signal-to-background ratios and reconstruction efficiencies of mesons for central Au+Au collisions at 8A GeV and 25A GeV beam energies are presented in Table 1. The signal-to-background ratio stays at the same level when reducing the photon detector planes. However, the reconstruction efficiencies change drastically if reducing in particular the inner part of the PMT plane.

Table 1: S/B ratios and reconstruction efficiencies after applying all cuts for central Au+Au collisions at 8A GeV and 25A GeV beam energies

	Full size	outer side [%]			inner side [%]	
		10	20	30	10	20
8A GeV beam energy						
ρ [eff.]	2.29	1.95	1.62	1.2	1.73	0.96
ω [eff.]	2.54	2.16	1.8	1.29	1.92	1.06
ω [S/B]	0.5	0.6	0.49	0.47	0.54	0.45
ϕ [eff.]	3.33	2.82	2.42	1.9	2.51	1.57
ϕ [S/B]	0.06	0.07	0.06	0.05	0.07	0.035
25A GeV beam energy						
ρ [eff.]	2.81	2.3	1.93	1.36	1.95	1.0
ω [eff.]	2.97	2.48	2.05	1.43	2.1	1.1
ω [S/B]	0.13	0.14	0.13	0.14	0.13	0.14
ϕ [eff.]	3.8	3.25	2.63	2.07	2.8	1.63
ϕ [S/B]	0.05	0.05	0.05	0.07	0.05	0.09

These exploratory studies show that the innermost part of the PMT plane is the most important one if looking at global efficiencies only. Consequently, if for some reason the PMT plane cannot be equipped at once with a sufficient number of PMTs, the outer part might be left out in the beginning and equipped at a later time.

References

[1] E. Lebedeva and C. Höhne, CBM Progress Report 2012, Darmstadt 2013, p. 106

---

* This work was supported by HIC for FAIR, by the GSI F&E-Cooperation with Giessen, and by BMBF grant 05P12RGFCG.

Determination of cross talk in MAPMTs covered with WLS films*

J. Kopfer[1], *C. Pauly*[1], *K.-H. Kampert*[1], *and M. Dürr*[2]
[1]Bergische Universität, Wuppertal, Germany; [2]Justus-Liebig-Universität, Gießen, Germany

The sensitivity of PMTs in the shorter wavelength region of the electromagnetic spectrum is limited by the reduced transparency of the PMT front windows for UV light. However, given the behaviour of the Cherenkov spectrum (the total number of photons is proportional to $1/\lambda$), the short wavelength limit is of particular importance when using PMTs in Cherenkov detectors: the more sensitive the photon detector is for short-wavelength Cherenkov photons, the larger is the integrated photon yield. For gaseous Cherenkov detectors, the short wavelength cutoff is given by the radiator gas; it is typically below the cutoff given by the PMT windows. E. g., for CO_2 as foreseen as radiator gas for the Ring Imaging Cherenkov (RICH) detector at CBM [1], the cutoff is $\lambda_{\text{min}} \approx 185$ nm.

Wavelength shifting (WLS) films on PMTs are seen as a cost efficient possibility to extend the sensitivity of the PMTs into the region where the glass of the front window absorbs most of the UV light [2]. However, with respect to multianode PMTs (MAPMTs), one expects an increase of crosstalk between neighboring pixels when using WLS films on MAPMTs due to the isotropic fluorescence of the WLS material. Crosstalk is defined here in the sense of charge sharing between neighboring pixels and was experimentally determined in the following way: we illuminated the central 5×5 mm^2 of a MAPMT pixel (pixel size: 5.8×5.8 mm^2) with single photons from a pinhole. The hits in the illuminated as well as in the adjacent pixels were detected. The crosstalk is then defined by the number of hits in adjacent pixels normalized to the number of hits in the illuminated pixel.

Figure 1 shows the number of hits as function of the MAPMT pixel position for the illumination of the central 5×5 mm^2 of one pixel. In the left plot, an uncoated pixel and in the right plot a pixel coated by a WLS film was illuminated. An enhanced crosstalk is observed in the right plot, especially in the diagonal neighbors.

Figure 2 shows the crosstalk in next neighboring pixels measured for one and the same H8500D-03 MAPMT with and without WLS films. To quantify the overall crosstalk, we consider hits in the next as well as in next-to-next neighboring pixels. Without film, the crosstalk adds up to 3.8 % at 470 nm and also 3.8 % at 245 nm. For WLS coated pixels the crosstalk is 3.8% at 470 nm and 4.7% at 245 nm. These numbers show that at 470 nm, a wavelength at which the WLS film is transparent, crosstalk is comparable with and without coating. At 245 nm, however, the crosstalk is larger by 24% with WLS coating because of the isotropic fluorescence of the film. However, the effect is small, and the Cherenkov ring resolution was not significantly affected for MAPMTs with WLS films when operated in a gaseous RICH prototype detector [3].

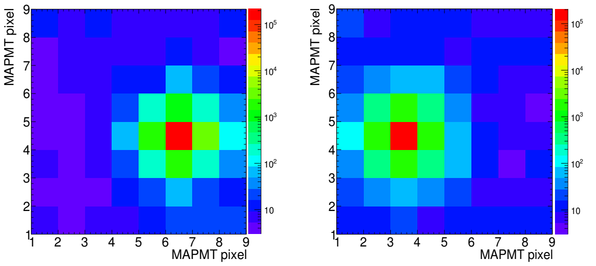

Figure 1: Number of hits per pixel for the illumination of the central 5×5 mm^2 of an uncoated (left) and a WLS coated pixel (right) with single photons. More crosstalk is observed in the neighboring pixels when using WLS films. Note the logarithmic scale of the color coding.

uncoated, 245 nm

0.1	0.6	0.1
0.8	CP	1.1
0.1	0.7	0.1

coated, 245 nm

0.2	0.7	0.2
1.1	CP	1.0
0.2	0.8	0.1

uncoated, 470 nm

0.1	0.5	0.1
0.7	CP	1.1
0.1	0.7	0.2

coated, 470 nm

0.1	0.6	0.1
0.9	CP	0.8
0.1	0.7	0.1

Figure 2: Crosstalk of an uncoated (left) and a different but coated (right) pixel of a H8500-03 MAPMT illuminated at 245 nm (top) and 470 nm (bottom). The charge detected in the pixels in the direct neighborhood of the center pixel (CP) is given in percent with respect to the charge detected in the center pixel (= 100%).

References

[1] C. Höhne *et al.*, Nucl. Instrum. Methods **A 595** (2008) 187

[2] E. L. Garwin, Y. Tomkiewicz, and D. Trines, Nucl. Instrum. Methods **107** (1973) 365

[3] J. Adamczewski-Musch *et al.*, Nucl. Instrum. Methods **A 783** (2015) 43

---

* This work was supported by HIC for FAIR, by the GSI F&E-Cooperation with Giessen, and by BMBF grants 05P12RGFCG and 05P12PXFCE.

Optimizing the RICH geometry*

T. Mahmoud and C. Höhne
Justus-Liebig-Uiversität, Gießen, Germany

The RICH detector used so far in simulations (v09a, v14a) was optimized in 2009. Since then two main modifications became necessary related to the CBM dipole magnet located upstream of the RICH. The latter had to be shifted 20 cm downstream. This in turn calls for a slight increase of the mirror and the photon detector (PMT) plane to keep the same acceptance. Second, the magnetic stray field is too large at the photon detector plane for operation of MAPMTs. In order to reduce the fringe field at the photon detector plane, we foresee two measures: Tilting the mirror by 10 degrees and shielding the PMT plane by an external shielding box. The position of the PMT plane has to be adopted accordingly and carefully optimized. In this report, the method for optimization and first results will be presented.

In an extensive study the PMT plane rotation angles around the x-axis and the y-axis, θ_x and θ_y, were scanned systematically to find the optimal θ_x-θ_y combination, for which the focus of the rings is optimal. The criteria investigated are the ellipticity of the rings, i.e., the ratio of minor to major axis of an ellipse fit B/A, the ring resolution parameter dR[1], and the incident angle α of photons impinging on the PMT plane with respect to its normal. The best case is given by maximizing B/A and minimizing dR and α.

The study was carried out for a mirror rotation angle of $-1°$ (as in the v08a and v14a geometry versions) and $10°$. Single electrons and positrons were generated isotropically in space concerning azimuthal and polar angle, and with a flat distribution in transverse momentum from 0 to 4 GeV/c.

For a mirror rotation of $-1°$, it is found that any combination within the intervals $15° < \theta_x < 17°$ and $15° < \theta_y < 17°$ leads to a maximum in B/A of about 0.94 and minima in dR and α of about 0.17 cm and 11.6°, respectively.

Figure 1 shows the B/A ratio as a function of θ_x and θ_y with a mirror rotation angle of $10°$. A maximum in the B/A ratio of about 0.9 is achieved with a θ_x-θ_y combination of 22° and 16°, respectively. However, any combination in the range of $18° < \theta_x < 26°$ and $14° < \theta_y < 18°$ leads to similar results. Within this range, the dR values also become minimal (0.25 cm). The photon incident angle of the PMT plane, however, does not become minimal anymore for the same tilting angles (θ_x, θ_y). α has a minimum of about 12° at larger values of θ_x and θ_y while it is 15.8° at the maximum of B/A. The fact that the optimal positions with respect to B/A and dR on one side and α on the other side differ is probably related to the large tilting angle of the mirror. Still, achieving a B/A ratio of 0.9 is a very promising sign that a RICH geometry with 10° tilting angle of the mirrors can be realized.

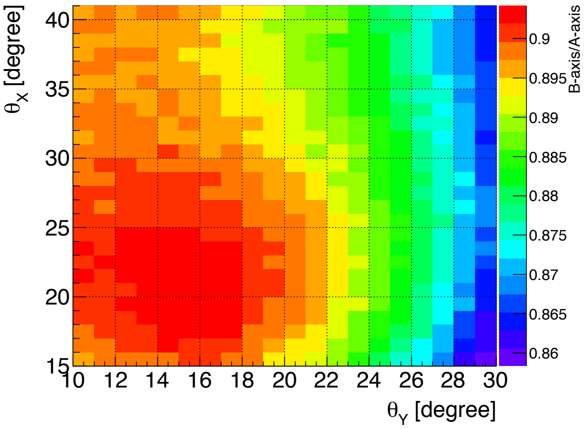

Figure 1: B/A ratio as a function of θ_x and θ_y

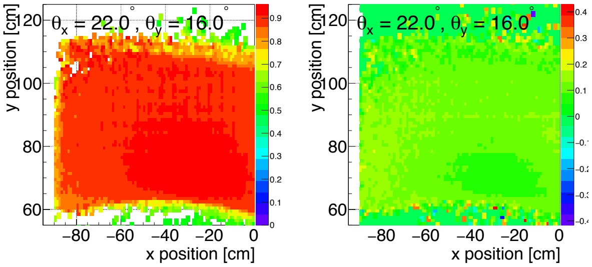

Figure 2: B/A and dR distributions on the PMT plane

Each of the values discussed above is the mean value of a distribution of all photons / reconstructed rings on the PMT plane. Figure 2 shows the B/A (left) and dR (right) distributions. Within tolerances both are distributed homogeneously on the plane.

The results presented here already show a very promising design of the RICH with mirror tilting angles of 10°. The setup will be optimized and investigated further before becoming the new standard.

---

* This work was supported by HIC for FAIR, by the GSI F&E-Cooperation with Giessen, and by BMBF grant 05P12RGFCG.

[1] dR is the distance between each hit in the ring and the fit.

The CBM RICH camera and readout chain for the 2014 CERN PS beamtest[*]

J. Förtsch, C. Pauly, D. Pfeifer, S. Reinecke, and K.-H. Kampert
Bergische Universität, Wuppertal, Germany

Among the main goals for the 2014 CERN PS beamtest was a direct in-beam comparison of the Hamamatsu H8500 to the new H12700 MAPMT, and the test of a new, fully FPGA-based readout chain. For this purpose, a new photon camera was constructed, carrying 4x4 MAPMTs (similar to 2011), with the back side matching the new elecronic readout modules. The new readout chain consists of two major parts: The PADIWA front end module (developed by the GSI electronics group for the PANDA DIRC detectors) serves as discriminator of the anaolg PMT signals. Each PADIWA front-end module provides 16 ch; groups of 4 modules were combined for the readout of a single PMT. Figure 1 shows a photograph of the camera backside, equiped with 64 PADIWA readout boards grouped to 16 readout modules.

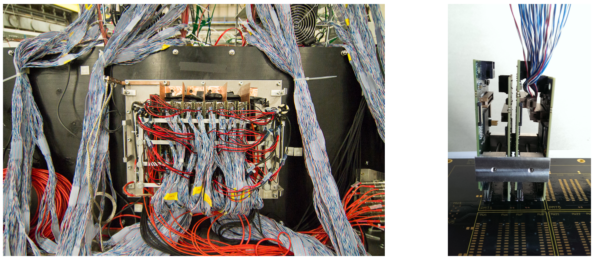

Figure 1: Photograph of the camera readout electronics (left) and a single 4xPADIWA PMT readout module (right)

Signal discrimination on the PADIWA is done using the LVDS receivers on the FPGA, which serve as a high-speed comparator: The analog signals are first amplified and then connected to one of the two inputs of the differential line receivers on the FPGA. The second receiver input is connected to a channel-individual threshold voltage, which is generated on the FPGA itself using pulse-width modulation (PWM). The discriminated, logical output pulse (its width corresponding to the Time-over-Threshold) is provided as differential output signal and transmitted via flat cable to the second main readout component, the TRB3 FPGA-TDC readout board.

The TRB3 [1] is a multi-purpose FPGA board, consisting of 4+1 Lattice ECP3 FPGAs. Each of them can be configured as a FPGA TDC, providing up to 4x64 TDC channels of high precision (up to $\sim$10 ps RMS). Because of temporary limitations and the fact that both leading- and trailing edge should be measured, only 16ch per FPGA could be implemented during the beamtime, requiring one TRB3 board per MAPMT. A 17th TRB3 board served as data hub, providing two distinct data streams: A CBMnet data stream, received on the central DAQ PC via FLIB interface, and a second, independent TRBnet data stream, being read by a separate DAQ PC only for the RICH data. All individual TRB3 boards were operated synchronously by using a common 200 MHz clock generator, allowing for easy synchronization of TDC channels on different boards. A sketch of the full readout scheme is shown in Fig. 2.

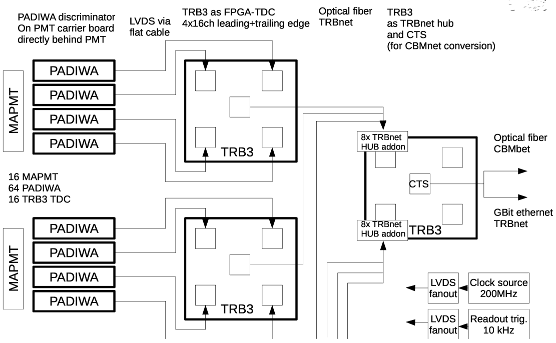

Figure 2: Readout scheme for the CBM RICH prototype readout based on PADIWA frontend and TRB3 TDC

The 2014 CERN beamtime was the first full-scale test of the FPGA-based readout chain as we intend to implement it also for the final CBM RICH detector. Utilizing this readout chain we were able to measure clean Cherenkov rings on all camera positions; the detailed analysis of the data is ongoing. As a first result of this test, it turned out that the detection efficiency (measured in terms of detected photons per Cherenkov ring) is some 20% - 30% lower as compared to the previous nXYTER-based readout chain. Two main reasons for this inefficiency were already found. One problem is the transmission of the short discriminated pulses (only 1-2 ns pulse width, corresponding to the PMT signals) from the PADIWA discriminator via flat cable to the TRB3-TDC. Activating the output pulse stretching on the PADIWA increases the efficiency significantly, but then does not allow to obtain Time-over-Threshold measurements because of the discrete stretching of the trailing pulse. A second problem is the noise level encountered in the full-scale system, leading to unnecessarily high threshold values in some, but not all channels. Here, a bandwidth reduction via a low-pass filter seems to help and has to be further evaluated.

References

[1] M. Traxler *et al.*, JINST **6 C** (2011) 12004

---

[*] Work supported by BMBF contract No. 05P12PXFCE

First evaluation of the 3d Hall effect sensor MagVector2*

C. Pauly, D. Schwab, and K.-H. Kampert
Bergische Universität, Wuppertal, Germany

The Photon sensors of the CBM RICH camera have to be operated inside the fringe field of the CBM dipole magnet. Heavy iron shielding boxes will be needed to reduce the maximum field strength to 1-2 mT in the region of the photon sensors. Design and performance of these shielding boxes will be based on simulations of the actual field distribution using standard simulation software. For fringe fields, these simulations are difficult and subject to large errors due to saturation effects of the dipole yoke, and in particular the field clamps. In order to validate and optimize proper shielding efficiency, we would like to measure the fringe fields close to the photon sensors during operation of the RICH by equipping the sensor PCBs with individual Hall sensors read out by a common data bus. Nowadays, such Hall sensors are a cheap mass product used in the mobile market as compass sensors. However, these sensors usually have a maximum range of only 1-2 mT, which is too small for our purpose. Professional probes are much more expensive and rare. We recently started an evaluation of a new sensor device, MagVector2 from Sensima Technologies [1], which seems to perfectly match our requirements for a price of ca. 150 $ per sensor. MagVector2 is a 3D hall probe with a configurable maximum field range of 100 mT / 300 mT / 1 T / 3 T and a maximum sensitivity of 5 μT (least significant bit, LSB). It is only 3×3 mm^2 large, can be operated in both analog and digital mode (16 bit resolution) and includes a digital SPI bus control interface.

We built two PCB test boards for evaluation of this sensor, which also allow for a future use of the sensor in the lab, e.g., for measurements of the μ-metal PMT shielding performance. Readout and control of the sensor via SPI bus is done with a RaspberryPi. The Raspberry is running an EPICS IOC, which maps the full sensor functionality to EPICS Process variables. Figure 1 shows a photograph of the full readout chain.

Using this test setup, we have started to evaluate the performace of the sensor. A first result on the long-term stability and noise figure of the sensor is shown in Fig. 2. The sensor was mounted in a calibration Helmholtz coil under constant current, with a calculated B-field at the sensor position of 1.48 mT. The sensor was read out every 3 s for a total time span of 10 minutes. The histogram shows the obtained measurement results, which are all very close to the expected value. The variation of measured field values has an RMS of the order of 0.01 mT. Further tests include the proper calibration of each sensor axis, the determination of the cross talk between individual axis, and the temperature coefficient. Based on these tests we conclude that the Sensima MagVector2 proved to be fully sufficient for a future measurement of the the 3d fringe field in the region of the photon detector with an accuracy well below 1 mT.

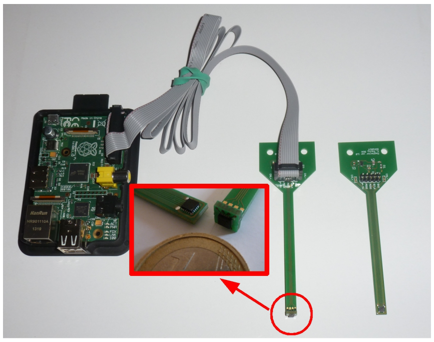

Figure 1: Photograph of the two MagVector2 sensor PCBs, connected to a RaspberryPi for readout via SPI bus

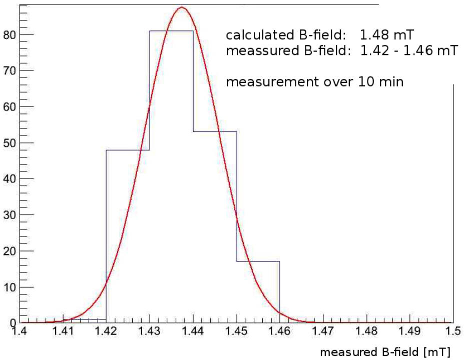

Figure 2: Accuracy and noise level for about 200 consecutive field measurements (10 minutes in total) of a fixed B-field inside the Helmholtz coil used for calibration

Mounting the sensor to a XY stage in the lab, we can now measure the magnetic field distribution directly at the photomultiplier window, if the PMT is operated inside a homogenious magnetic field. With this setup we plan to evaluate a possible benefit of additional magnetic μ-metal shielding surrounding each individual PMT, in addition to the iron shielding boxes surrounding the full CBM RICH photon detector.

References

[1] `www.sensimatech.com`

---

* Work supported by BMBF contract No. 05P12PXFCE

The new H12700 PMT for CBM RICH*

J. Förtsch, C. Pauly, S. Querchfeld, and K.-H. Kampert
Bergische Universität, Wuppertal, Germany

In detailed studies we could confirm the good single photon detection capabilities of the Hamamatsu H8500-03 Multianode Photomultiplier, qualifying it for the baseline design of the CBM RICH detector. The major advantage of the H8500 (besides price) is its large size (2x2 inch) and good geometric efficiency. This allows to compete with smaller, single-photon optimized tubes like e.g the Hamamatsu R11265 (1x1 inch), despite the fact that these tubes have significantly higher collection- and quantum efficiency because of Super-bialcali photo cathodes. Just recently, Hamamatsu has adapted the beneficial single-photon properties of the R11265 to the larger H8500, resulting in the new H12700 MAPMT: a 2x2 inch, single-photon optimitzed tube with increased quantum efficiency due to SBA cathode. Very recently, the quantum efficiency could be even further optimized for Cherenkov applications by shifting the peak efficiency towards shorter wavelengths (”blue shifted cathode”). We tested and compared this new H12700 based on first available samples. Some of the results are summarized in the following.

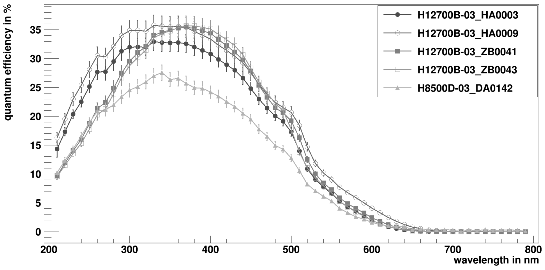

Figure 1: Quantum efficiency for a standard (DA0142), a SBA (HA000x) and a SBAblue (ZB00xx) cathode

Figure 1 shows a comparison of spectral quantum efficiency for several H12700 with standard and blue-shifted cathode, with respect to a typical H8500 tube. The peak quantum efficiency is significantly increased to 30% - 35%; the increased UV sensitivity of the blue-shifted cathode is clearly visible. The increased quantum efficiency, combined with a better collection efficiency, results in a significantly higher single-photon detection efficiency. This could be confirmed in single-photon scans at 405 nm as shown in Fig. 2. The X-axis shows a relative comparison in terms of photon detection efficiency (averaged over the active area). This efficiency is clearly correlated with the Blue Sensitivity Index (Y-axis) from the Hamamatsu data sheets (see [1] for details). The H12700 with blue-shifted cathode (blue triangles) are underestimated in this plot because of their shifted peak efficiency.

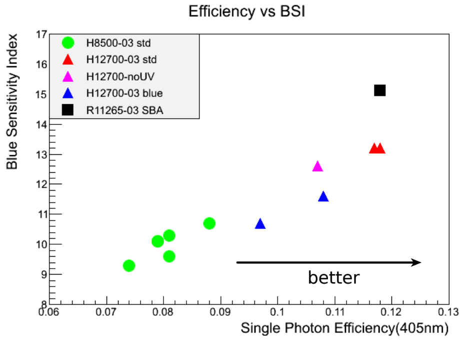

Figure 2: Comparison of several H8500 (BA cathode), H12700 (SBA/SBAblue), and R11265 (SBA) MAPMTs in terms of relative single photon-detection efficiency (X-axis) and Blue Sensitivitiy Index from the data sheets (Y-axis)

The improved dynode structure is also reflected in the single-photon spectral response shown in Fig. 3. All H12700 MAPMTs show a much narrower and better separated single-photon peak distribution than the H8500. The well pronounced peak at low amplitiudes, visible for the H8500, stems form cross talk to neighbouring pixels. This cross talk is substantially lower for the H12700, as confirmed in single-photon scans.

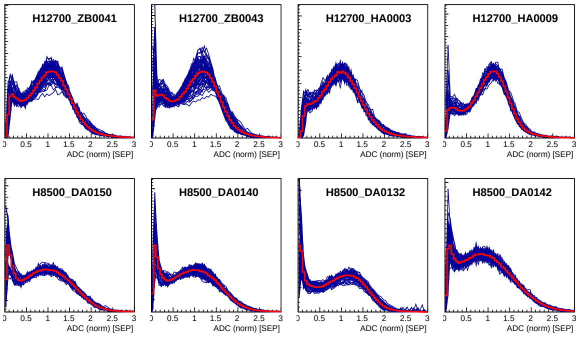

Figure 3: Gain normalized single-photon spectra for four Hamamatsu H12700 MAPMTs (upper line), and four H8500 (lower line). Red line: average over all pixels.

References

[1] C. Pauly *et al.*, CBM Progress Report 2013, p 56

---

* Work supported by BMBF contract No. 05P12PXFCE

Data analysis for the RICH prototype beamtest data 2014*

S. Lebedev[1,2], *E. Ovcharenko*[2,3], *and C. Höhne*[1]
[1]Justus-Liebig-Universität, Gießen, Germany; [2]LIT JINR, Dubna, Russia; [3]ITEP, Moscow, Russia

The real-size prototype of the Ring Imaging Cherenkov detector (RICH) was tested for the third time together with other CBM groups at the CERN PS/T9 beam line in November 2014 [1]. For the first time the analysis of the RICH data was fully performed within the CbmRoot framework.

The RICH data were written in HLD file format [2]. The data analysis starts from data unpacking which includes several steps: **1) Retrieving raw messages from the data stream.** One MAPMT pixel was read out by one PADIWA channel which is split to two TDC channels – one for the leading edge and one for the trailing edge of a signal [3]. **2) Matching leading and trailing edges. 3) Fine time calibration.** The fine time counter in the TDC uses the *Tapped Delay Line*. The standard calibration procedure based on *Look Up Tables* is implemented. **4) Synchronization of TDCs.** The time offset for each TDC is calculated based on a synchronization signal in channel 0. **5) Calibration of channels within one TDC.** The first results showed that there is a difference in the time required by different channels to transport the signal. The implementation of a calibration procedure is ongoing. **6) Creation of raw hits.** The raw hits contain the information about leading and trailing time, TDC identifier and TDC channel number.

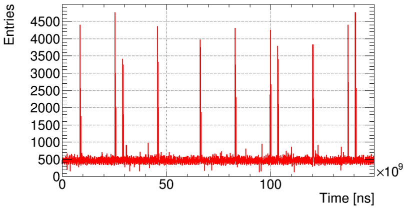

Figure 1: Distribution of the number of RICH hits with time. Peaks corresponds to beam spills.

The raw hits are not grouped into events and stored as free streaming data. Figure 1 shows the distribution of the number of RICH hits with time. The implemented event building procedure uses the reference time signal from the hodoscope (or UV-LED pulser, laser pulser, finger scintillator). All raw RICH hits which belong to a time window (300 ns) around the reference time are collected into one event. Then the TDC identifier and the channel number information from the raw hits are converted to x and y positions on the PMT plane using a corresponding mapping mechanism. After this step the hits are sorted into events and stored in the standard CbmRoot containers, namely a *TClonesArray* of *CbmRichHits*. From this step on the standard CbmRoot routines can be used for further analysis. Rings are reconstructed using an algorithm based on the Hough Transform method, and their parameters are derived with high accuracy by circle and ellipse fitting procedures [4]. The algorithms are the same as used in the event reconstruction for simulated data. A number of histograms controlling parameters such as number of hits, ring radius etc. are automatically generated (see Fig. 2 for an example). For the visual representation of events, an event display was implemented. Two example events are shown in Fig. 3.

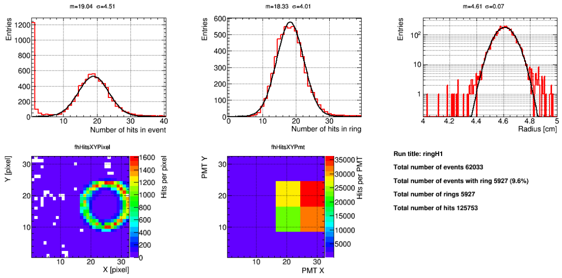

Figure 2: Examples of analysis results. From left to right: number of hits in event, number of hits per found ring, ring radius, number of hits per pixel, number of hits per PMT.

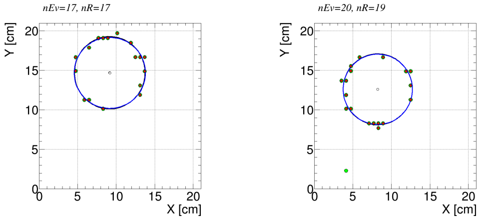

Figure 3: Examples of single events

References

[1] C. Bergmann *et al.*, *Common CBM beam test of the RICH, TRD and TOF subsystems at the CERN PS T9 beam line in 2014*, this report

[2] `http://trb.gsi.de`

[3] C. Pauly *et al.*, *The CBM RICH prototype camera and readout chain for the 2014 CERN PS beam test*, this report

[4] S. Lebedev *et al.*, J. Phys. Conf. Ser. **396** (2012) 022029

---

* This work was supported by HIC for FAIR, by the GSI F&E-Cooperation with Giessen, and by BMBF grant 05P12RGFCG.

Different layouts of a mirror support structure for the RICH detector*

S. Lebedev[1,2], *E. Ovcharenko*[2,3], *C. Höhne*[1], *and Y. Ryabov*[4]
[1]Justus-Liebig-Univ., Gießen, Germany; [2]LIT JINR, Dubna, Russia; [3]ITEP, Moscow, Russia; [4]PNPI, Gatchina, Russia

The CBM-RICH detector is a gaseous detector with focusing mirror elements made from 6 mm thick spherical glass and a photon detector. The mechanical design of the RICH detector has to provide a mirror mount structure which on the one hand is stable enough in order to hold the mirror tiles in a precise position. On the other hand this mirror support frame is in the CBM acceptance and thus should have low material budget in order to prevent secondary particle production. In this report, simulation studies using a number of different RICH geometries will be presented based on a preliminary mechanical design [1].

The effect of material budget on the tracking performance in the TRD and TOF detectors was studied. The following five RICH geometries were investigated: **1)** *v08a*. This geometry is used as a reference and has only a very approximate material budget implemented. **2)** *v14a*. This is the current standard geometry based on a complete mechanical design [1]. **3)** *Nobelts*. Same as *v14a* but without belt structure. **4)** *Noframes*. Same as *v14a* but without belt structure and main frame. **5)** *Rohacell*. Large *Rohacell* structures are used to hold the mirror tiles. Figure 1 shows the *v14a* and *Rohacell* geometries.

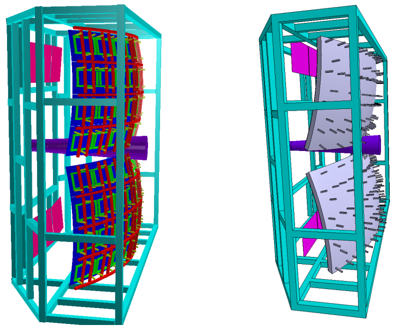

Figure 1: *v14a* (left) and *Rohacell* (right) geometries. The red structures are removed for the *Nobelts* geometry; in addition the outer big frames are removed for the *Noframes* geometry.

The material budgets of two of the five geometries for parallel tracks are shown in Fig. 2. The mirror support structure is the dominant source of material. The main frame and belt structures for the *v14a* geometry can be clearly seen. For the *Rohacell* geometry the material budget is spread uniformly except for the main frame. This material budget is very similar to the *Nobelts* structure.

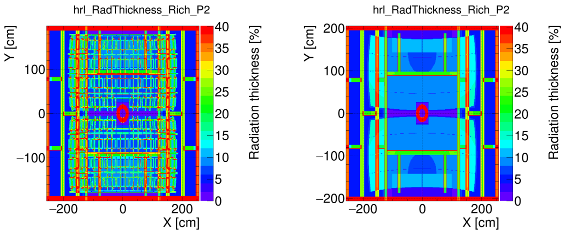

Figure 2: Radiation length of the *v14a* (left) and *Rohacell* (right) geometries for parallel tracks.

The tracking performance was studied with simulations for central Au+Au collisions at $25A$ GeV beam energy embedding 10 additional $e^{\pm}$ in each event. The following geometries were used: *sts_v13d.geo.root*, *trd_v14a_3e.geo.root* (smearing) and *tof_v13b.geo.root*. The results are summarized in Table 1. The largest effect is seen for the *v14a* geometry by adding 10% hits compared to *v08a* and a degradation of 2% in tracking efficiency. However, overall the observed degradation is very modest despite the partially large and very inhomogeneous material budget. For the final RICH geometry it might be sufficient to optimize (reduce) the material budget of this proposal. For a final conclusion the effect of electron identification in the TRD still has to be investigated.

Table 1: Summary of the simulation results

Geometry	v08a	v14a	No B	No F	RC
Number of hits in TRD per event					
All	10660	11900	11460	11480	11620
1st st.	780	930	880	880	900
2nd st.	840	980	930	930	950
5th st.	1040	1170	1120	1125	1140
10th st.	1410	1510	1470	1475	1485
Number of hits in TOF per event					
All	2400	2530	2490	2485	2505
Tracking efficiency for primary $e^{\pm}$ [%]					
TRD	79.2	77.0	80.0	79.2	79.6
TRD+STS	78.5	76.5	79.5	78.6	79.1

References

[1] Yu. Ryabov *et al.*, CBM Progress Report 2012, p. 40

---

* This work was supported by HIC for FAIR, by the GSI F&E-Cooperation with Giessen, and by BMBF grant 05P12RGFCG.

Muon Detection System

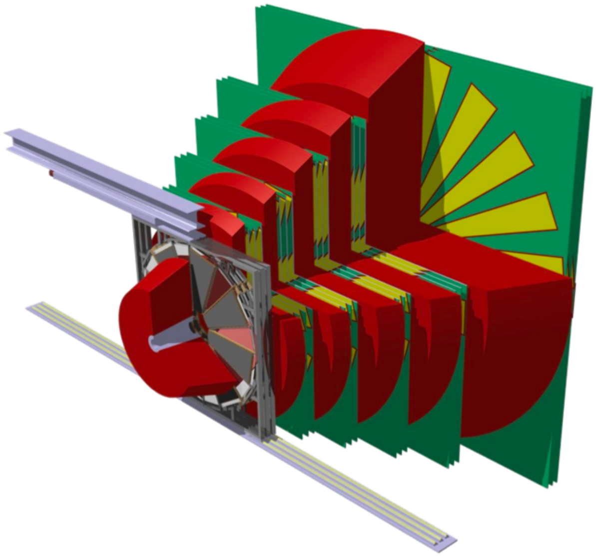

The muon detection system of CBM for SIS100

A. Senger
GSI, Darmstadt, Germany

The CBM muon detection system [1] was optimized to measure muon pairs from the decay of light vector mesons (ρ, ω, ϕ) produced in heavy-ion collisions at SIS100 energies. The muon momenta in this energy range are rather low; therefore, we developed a modular muon detection system. For Au beams with energies from $2A$ to $4A$ GeV, the system consists of three absorbers (one carbon plate of thickness 60 cm with lead shielding around the beam pipe and two iron plates of thickness 20 cm each) and of three detector stations. For Au beams with energies from $6A$ to $10A$ GeV, the system consists of four absorbers (with an additional 30 cm iron absorber) and of four detector stations. For the additional suppression of punch-through hadrons, the ToF (time-of-flight) detector is used. Different types of tracking detectors were investigated by simulations:

- **Setup with three stations**
    - all stations with GEM-like detectors;
    - two stations with GEM-like detectors, last station with six straw-tube layers.
- **Setup with four stations (see Fig. 1)**
    - all stations with GEM-like detectors;
    - three stations with GEM-like detectors, last station with six straw-tube layers;
    - two stations with GEM-like detectors, two stations with six straw-tube layers each;
    - three stations with GEM-like detectors, transition radiation detector (TRD) behind the last absorber.

The simulations were performed using the CbmRoot framework. The full setup of the CBM spectrometer for muon measurements at SIS100 consists of the following detectors: STS (Silicon Tracking Stations) located in the magnet for the reconstruction of track, momentum and vertex, MuCh (muon chamber system) for muon identification, and ToF detector for hadron identification. Realistic detector segmentations, detector response and cluster finder were used for all detector subsystems in the simulation. Tracks are considered as muon tracks if they pass through all detector stations in the muon system and are identified by ToF as muon candidates. The simulations show almost the same results of signal-to-background ratio and efficiency for all setups under study. An example of a reconstructed invariant mass spectrum and the corresponding signal-to-background ratio for Au+Au collisions at $8A$ GeV is shown in Fig. 2 for the muon system setup with TRD as last tracking station.

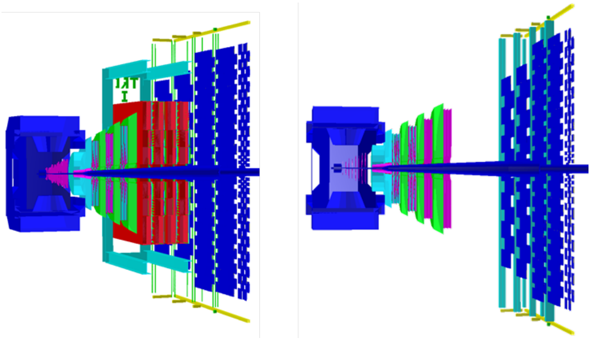

Figure 1: Muon detector setup for the measurements with Au beam at energies from $6A$ to $10A$ GeV. Left: muon setup with TRD; right: muon system with GEM detectors and straw tubes (see text).

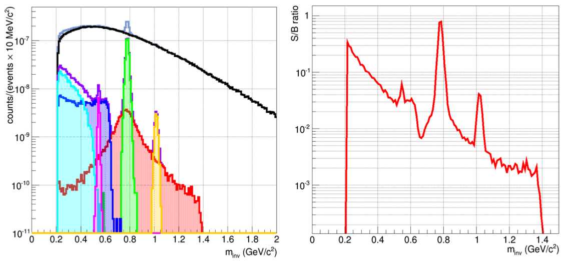

Figure 2: Di-muon invariant mass spectrum (left) and signal-to-background ratio (right) for Au+Au collisions at $8A$ GeV using the muon system with TRD as last tracking station

References

[1] A. Kiseleva *et al.*, CBM Progress Report 2009, Darmstadt 2010, p. 65

Design of the first MUCH absorber

V. Kozlov, N. Miftakhov, V. Nikulin, V. Samsonov, and O. Tarasenkova
PNPI, Gatchina, Russia

The Muon Detection System for the CBM experiment (MUCH) can be described as a set of absorbers with tracking chambers between them [1]. The sizes and the materials of the absorbers were chosen in order to optimize the detector performance in identification of the muon pairs originating from the decays of various mesons.

The design of the first MUCH absorber is the most advanced compared to other MUCH mechanics. Figure 1 shows its cut view: a biconical carbon piece and a conical lead insert. The beam axis is the axis of the absorber, the lead insert is located inside the the central opening of the absorber. The surface of the part of the absorber located inside the dipole magnet is conical with an opening angle of 25°. The radius of the outside part is 300 mm larger in order to eliminate edge effects.

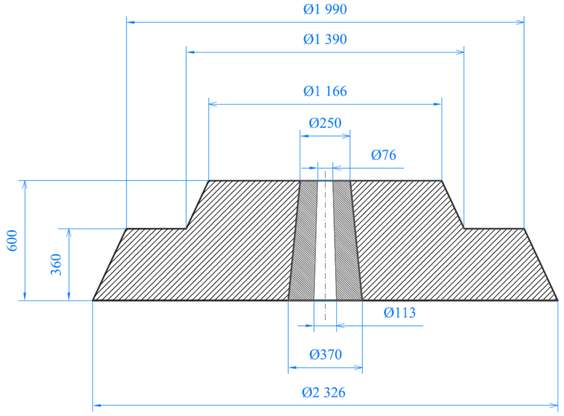

Figure 1: Cut view of the carbon and lead parts of Absorber-1. The beam hole corresponds to an opening angle of 3.5°; the beam goes from top downwards.

Figure 1 also shows the lead insert with an inside angle of 3.5° and an outside angle of 5.7° with respect to the target point. This inner angle takes into account the bending of the lead beam in the magnetic field at low energies and prevents the beam halo from touching the lead walls [2]. If necessary, it could be changed to another value optimized for SIS100 conditions. The front (upstream) surface is equipped by the connector with the STS beam pipe; at the rear part there is a connection clamp with the MUCH beam pipe. The lead insert shields the beam pipe from direct particle flux and allows to use a relatively thick cone (3 - 5 mm).

The carbon and the lead components of the absorber are located inside a shell made of aluminum alloy. In order to keep the required rigidity, the shell is reinforced with stiffness ribs (Fig. 2) that split the inside volume into six equal parts. The thickness of the shell is preliminarily estimated to be 12 mm; the fixation elements are approximately 30 mm thick. The absorber is equipped with Mercedes star type mounting that will be fixed onto the downstream surface of the dipole magnet by means of screws and precision fingers. The positioning tolerance of the absorber should be within $\pm 0.2°$, which corresponds to ± 4 mm at the upstream side and ± 6 mm at the downstream side. The position will be checked with a theodolite.

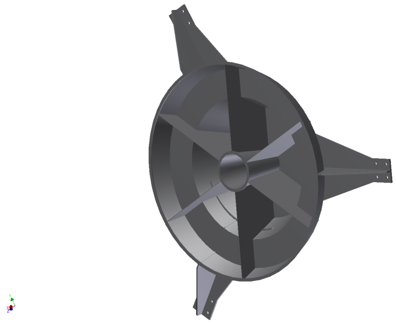

Figure 2: General view of the shell and mounting for Absorber-1

The shell, mounting and the inserts are expected to be manufactured at the experimental workshop of PNPI. The production of the carbon parts of the absorber and the final assembly is planned to be performed at Moscow Electrode Plant [3]. The graphite to be used has a density of $1.69\ \mathrm{g/cm^3}$ with a carbon content of more than 98%. The main possible admixtures do not exceed 1% for water and cinder and 0.05% for sulphur. A pyro-contraction process will improve the mechanical properties of the carbon. In order to fix the graphite pieces inside the shell, a special carbon-enriched glue will be used.

As was demonstrated by a Monte-Carlo analysis [4], a graphite density of $1.7\ \mathrm{g/cm^3}$ does not produce much differences compared to a density of $2.1\ \mathrm{g/cm^3}$ and could be safely used for our purposes.

References

[1] The CBM Collaboration, *Technical Design Report for the CBM Muon Chambers (MUCH)*, in press

[2] S. Belogurov, private communication

[3] `http://www.graphitel.ru/index.php?l=1`

[4] A. Senger, private communication; P. P. Bhaduri, private communication

Simulation of beam-pipe shielding for CBM-MUCH

S. Ahmad[1], *M. Farooq*[1], *and S. Chattopadhyay*[2]
[1]University of Kashmir, Srinagar, India; [2]Variable Energy Cyclotron Center, Kolkata, India

In the CBM experiment, the probability of beam-target interactions is just 1%. Nearly 100% of the beam propagate towards the beam-dump, and some of the beam particles might interact with the beam pipe and thus generate radiation background affecting the detectors. The purpose of the beam-pipe shielding is to reduce such background without affecting the detection process. The current baseline design is a segmented shielding with 60 cm Pb beneath the first absorber and Fe beneath the rest of the absorbers with no shielding below the detector stations.

We analyzed the performance of the MUCH system (SIS300 set-up) for different types of beam-pipe shielding materials (like tungsten, lead, iron) and two options: (1) complete monolithic shielding as shown in Fig. 1a, and (2) segmented shielding with no shield beneath the stations as shown in Fig. 1b. A new monolithic shielding, a combination of 40 cm W, 70 cm Pb and 335 cm Fe (Fig. 1c), was also studied. The simulations were carried out using GEANT3 with Au+Au events at $25A$ GeV Au+Au from the UrQMD event generator for the background and the ω signal from the PLUTO event generator.

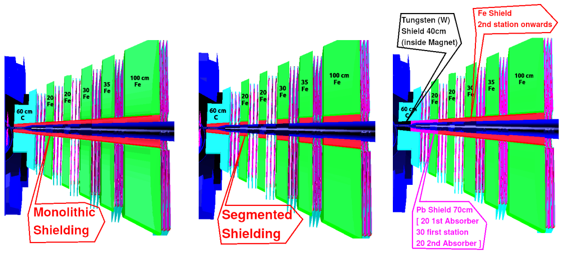

(a) monolithic (b) segmented (c) W+Pb+Fe

Figure 1: Muon Chamber with (a) monolithic, (b) segmented, and (c) new beam-pipe shielding [W(40cm) + Pb(70cm) + Fe(335cm)] optimized for central Au+Au collisions at $25A$ GeV

Fig. 2 shows the hit density in the first station, which is lowest for the monolithic Tungsten case and 10 % less than the present baseline for the new combination. In the fifth station, both monolithic W and the new combination give similar results, while the current design produces a much higher load. Here, where the hit density is relatively low, the monolithic shielding performs better than the segmented one. The same holds when studying the occupancy.

Next we analyzed the overall detector performance in terms of ω reconstruction efficiency and background reduction. The used cuts are: STS hits ≥ 6, MUCH hits ≥ 14, $\chi^2_{\mathrm{vertex}} \leq 2.0$, and $\chi^2_{\mathrm{MUCH}} \leq 1.5$. The efficiency for ω of about 1% is not influenced by the choice of the shielding material. However, as Fig. 3 shows, the background is largest for the monolithic Tungsten shield. A segmented Iron shield performs best in terms of background, but produces a high hit density as shown above. The new shield design (W+Pb+Fe) gives both low hit density as well as low background, and seems hence the best compromise between hit density/occupancy and background reduction.

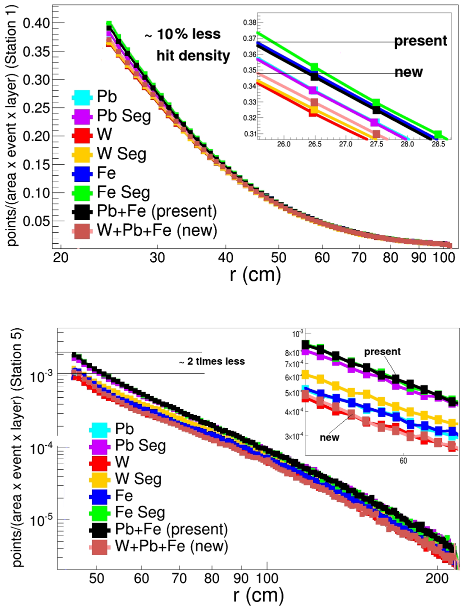

Figure 2: Hit density in Au+Au collisions at $25A$ GeV in the first (upper panel) and the fifth (lower panel) MUCH detector station for different beam-pipe shielding materials (here Pb/W/Fe means monolithic and Pb/W/Fe Seg segmented shielding)

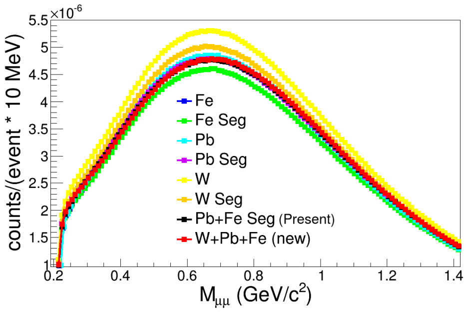

Figure 3: Combinatorial di-muon background from the MUCH detector after applying proper track cuts for central Au+Au collisions at $25A$ GeV

A real-size prototype for CBM-MUCH

A. K. Dubey, J. Saini, G. S. Murthy, and S. Chattopadhyay
Variable Energy Cyclotron Centre, Kolkata, India

The first few stations of the CBM-MUCH system will employ large-size triple-GEM detectors. In this paper, we report on the assembly and initial tests of the first real-size prototype for the first station of CBM-MUCH, wherein the dimensions of the active area are identical to the real size as optimized and implemented in the CBM-MUCH simulations.

For the real-size prototypes, instead of thermally stretching and gluing the foils, we have used the glue-less "NS2 (no stress, no spacer)" technique for framing followed by simultaneous stretching of all three GEMs. Single-mask GEM foils with a trapezoidally shaped active area, having 80 cm and 40 cm as lengths of the parallel sides and extending 80 cm longitudinally, were fabricated at the CERN-PCB lab as shown in Fig. 1. Each GEM foil was segmented into 24 sections on its upper surface. The innermost four segments were 25 cm^2 large, all others 100 cm^2. The inner segments were made slightly finer in order to handle high rates. As per first calculations, it is seen that at $10\,\mathrm{MHz/cm}^2$, with a protection resistance of 1 $\mathrm{M}\Omega$ and for an area of 100 cm^2, the expected voltage drop due to pulsed current is about 0.4 V, which does not lead to any significant change in gain.

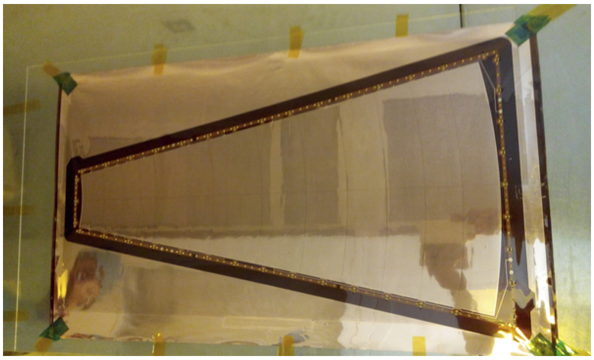

Figure 1: Picture of the trapezoidal GEM foil for the first real-size MUCH prototype

Each of these segments was connected via surface-mounted protective resistors of $1\,\mathrm{M}\Omega$, which was part of the production. The 24 segments of each foil were grouped into 4 zones with 6 segments each in order to facilitate the independent powering of each zone using 4 resistive chains. This scheme was adopted as a precautionary measure. However, during the lab tests, all these were shorted together and connected to one resistive chain. All segments were tested, and no shorts or high leakage currents were found before and after the assembly.

The eight-layered, 2.7 mm thick readout PCB consisting of 1920 projective pads and fifteen n-XYTER-based FEB connectors soldered on the outer side was designed at VECC and fabricated by the Indian industry. A $10\,\Omega$ protection resistance was soldered at every channel. The 3 mm thick drift PCB, fabricated by the CERN-PCB division, was extended laterally by 5 mm compared to the design given in the MUCH-TDR, to accommodate the HV lines for powering the segments. Holes of 1 mm were made at appropriate places on the drift plane to allow X-rays to pass through. The entire assembly of the detector was performed at the RD51 lab at CERN. In this "NS2" technique [1], the GEM foils were sandwiched between 1 mm G10 spacer frames. Thin metallic pins of appropriate lengths soldered on the drift plane and passing through the spacers provided the contact with the respective GEM layer. No cross grids were used in the active area for any kind of support to the foils as opposed to the previous intermediate-size case. Metallic brass pieces fixed on the drift plane at regular intervals at the boundaries acted as pillars against which the three foils were stretched. The readout plane then sealed the chamber via an O-ring. The entire chamber was then inserted in an ultrasonic bath for some minutes, and after thorough drying in an oven it was put under gas (Ar/CO_2 - 70/30) for tests.

Figure 2 shows a picture of the final chamber, the inset showing the typical pulse-height spectrum from this detector when exposed to a 5.9 keV X-ray source.

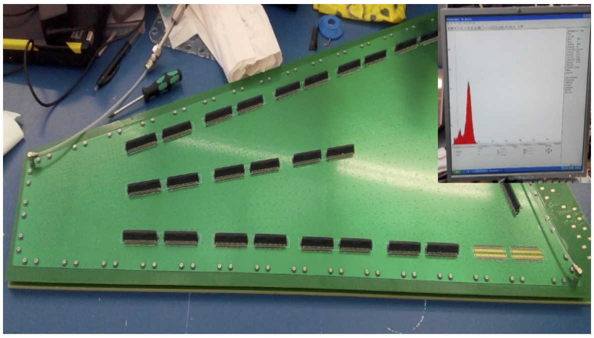

Figure 2: Picture of the first real-size prototype. Inset: Fe^{55} signals from the tests.

References

[1] S. Colafranceschi *et al.*, *Beam test results for new full-scale GEM prototypes for a future upgrade of the CMS high-η muon system*, IEEE NSS/MIC 2012, 1172

Design and fabrication of a full-size PCB for the CBM-MUCH chambers

J. Saini, A. K. Dubey, and S. Chattopadhyay
Variable Energy Cyclotron Center, Kolkata, India

Introduction

A GEM-based detector system is being developed at VECC, Kolkata, for use as muon tracker [1] in the Compressed Baryonic Matter (CBM) experiment. Because of the high-rate environment, a progressive pad geometry was chosen to optimize the occupancy versus the number of channels per chamber for the first two stations. This pad geometry results in a higher density of pads in the inner ring and hence requires the design of a 8-layered PCB.

PCB design and constraints

GEM chambers of the first two stations are located in a high track-density zone. To take care of the hit rate, the pad size was optimized to one degree ($\delta\phi$, r$\delta\phi$) through simulations. To fit in the sector geometry and have the lowest dead area, each pad is a trapezoid where the two larger angles are $90.5°$ each.

In the current design, the minimum pad size (innermost ring) is $3.96\,\mathrm{mm} \times 3.96\,\mathrm{mm}$, while the maximum pad size in the outermost ring is $16.6\,\mathrm{mm} \times 16.6\,\mathrm{mm}$. This GEM chamber is designed to cover $22.5°$ of a layer, which makes 16 chambers to cover the entire layer of the station. To cover the full region, alternating chambers are planned to be placed back-to-back, thus avoiding dead areas due to the mechanical structure of the chamber. To further reduce the dead space, this design is made with $23°$ coverage so as to have an overlap of half a degree of consecutive sectors. With $23°$, the PCB has 23 pads in an annular ring and 79 pads in radial direction, giving the total number of pads to be 1817.

To cover these 1817 pads with FEE boards of 128 channels each, the PCB is divided into 15 readout zones. Furthermore, this PCB is designed to meet an active area from $5.4°$ to $25°$. Excluding the unavoidable inner mechanical structure, 708 mm in radial direction and 381 mm width at the outermost ring gives the active area. To accommodate the mechanical fittings, the final dimension of this PCB is $471\,\mathrm{mm} \times 798\,\mathrm{mm}$. Figure 1 shows the final fabricated detector readout PCB, illustrating the progressive pad geometry along with the dimensions.

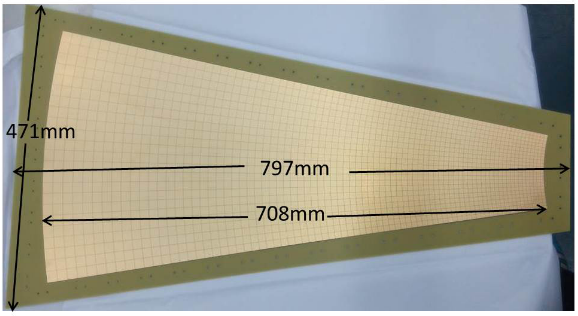

Figure 1: Progressive pad layout of the fabricated chamber PCB

As the radiation in the innermost region is very high, the first connector close to the beam pipe is 146 mm away from the PCB edge. FLUKA calculations showed that this distance reduces the radiation by a factor of three (i. e. from 30 krad to 10 krad for 10 years of operation), thus relaxing the constraints on the selection of components.

To reduce the noise, the tracks are drawn beneath the pads, and the bottom plane is used as a ground plane. Although this extra ground plane adds to the capacitance, additional shielding is not required to achieve acceptable noise levels. The maximum track length is approximately 30 cm at the outer zone where pads are more scattered.

Fabrication

Because of the multi-layered design of the PCB and the minimum track width of 6 mm, there are limitations with PCB manufacturers. They have zigs of $800\,\mathrm{mm} \times 600\,\mathrm{mm}$, but they ensure the quality only in the area of $600\,\mathrm{mm} \times 400\,\mathrm{mm}$. For this particular PCB, the manufacturer used their fullest zig with some reduced accuracy at the edges. For this purpose, special care is taken at the edges in the design.

Performance

A GEM chamber was assembled using this PCB and was tested in a proton beam at COSY in December 2014. The noise with the self triggered n-XYTER-based readout was within acceptable limits. The chamber also showed an efficiency of more then 90% in all zones, thus demonstrating that this is an acceptable design.

References

[1] The CBM Collaboration, *Technical Design Report for the CBM Muon Chambers (MUCH)*, in press

Testing of a real-size GEM prototype at COSY

R. P. Adak[1], *S. Samanta*[1], *A. K. Dubey*[2], *J. Saini*[2], *S. Chattopadhyay*[2], *S. Das*[1], *J. Hehner*[3], *I. Sorokin*[3], *T. Balog*[3], *F. Uhlig*[3], *V. Friese*[3], *J. M. Heuser*[3], *and W. Niebur*[3]
[1]Centre for Astroparticle Physics and Space Sciences, Bose Institute, Kolkata, India; [2]Variable Energy Cyclotron Centre, Kolkata, India; [3]GSI, Darmstadt, Germany

For the first two stations of CBM-MUCH, GEM-based, sector-shaped chambers will be employed. Several in-beam tests with small size prototypes were reported earlier [1, 2]. Here we report for the first time on the performance of a GEM prototype of size suitable for the first station, tested in December 2014 at COSY using a proton beam. The details of the fabrication of this chamber are described in [3].

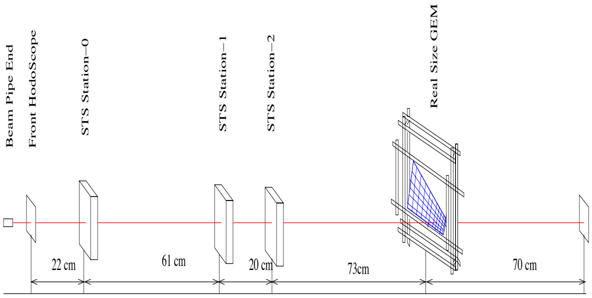

Figure 1: Experimental setup at COSY

The schematic layout of the experimental setup is shown in Fig. 1. The tested GEM detector tested is trapezoidal in shape, the lengths of the two bases being 38.2 cm and 10.0 cm, respectively. The leg of the trapezoid is 80 cm long. The anode readout PCB and the pads are also of trapezoidal shape. The readout pads are of progressively increasing size ranging from $3.96\,\mathrm{mm} \times 3.96\,\mathrm{mm}$ to $16.6\,\mathrm{mm} \times 16.6\,\mathrm{mm}$. The readout granularity is based on the simulations results for the first MUCH station [1]. The drift, transfer and induction gaps are 3 mm, 1 mm and 1.5 mm, respectively. The gas mixture used is Ar:CO$_2$ in 70:30 ratio by mass. Data were acquired using 4 n-XYTER FEBs connected to 2 ROCs in self-triggered mode. The feedback parameter $v_b f_b$ was set to 150. The set of 4 FEBs was shifted depending on the illuminated zone of the detector. Thus data were collected for different zones and at different voltages. All hits above a predefined threshold value ($V_{\mathrm{thr}} = 50\,\mathrm{V} - 60\,\mathrm{V}$) were digitised and stored.

As first part of the analysis, the time correlation of hits in the front hodoscope and in the GEM detector was obtained. Hits within a time correlation window were considered for analysis.

The ADC distribution was obtained by subtracting the pedestal value using an auto-calibration method. It is fitted with a Landau distribution function to obtain the Most Probable Values (MPV). The variation of MPVs with ΔV_{GEM} is shown in Fig. 2 (A). The average cell multiplicity in the region of cell size $5.46\,\mathrm{mm} \times 5.46\,\mathrm{mm}$ is about 1.5 as shown in Fig. 2 (B).

For the calculation of the efficiency, the coincidence of signals from the front and rear hodoscopes was taken as input trigger. As shown in Fig. 2 (C), the detection efficiency increases with ΔV_{GEM} and reaches $> 95\%$ at $\Delta V_{\mathrm{GEM}} = 366.67$ V. This meets the criterion for CBM-MUCH, requiring an efficiency of $> 95\%$ for the efficient detection of muons [4]. The efficiency is seen to be uniform over the beam rate range which reached up to 800 kHz as shown in Fig. 2 (D).

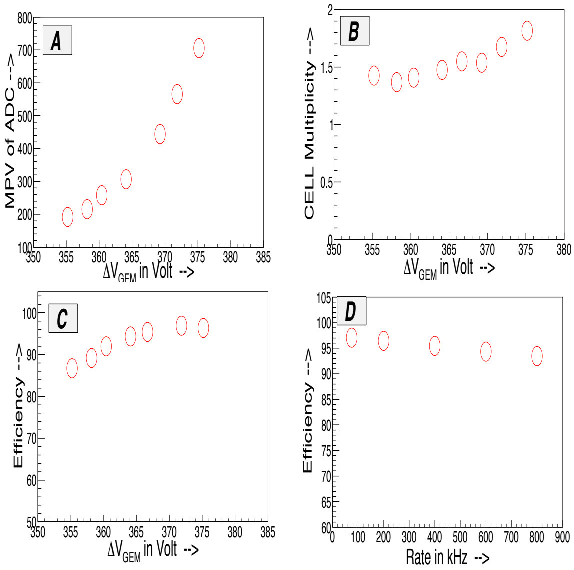

Figure 2: Variation of (A) MPV of ADC Distribution, (B) cell multiplicity, and (C) efficiency with ΔV_{GEM}. (D): Efficiency as function of beam rate.

References

[1] A. K. Dubey *et al.*, Nucl. Instrum. Meth. **A 718** (2013) 418

[2] A. K. Dubey *et al.*, Nucl. Instrum. Meth. **A 755** (2014) 62

[3] A. K. Dubey *et al.*, *A real-size prototype for CBM-MUCH*, this report

[4] S. Ahmad *et al.*, Nucl. Instrum. Meth. **A 775** (2015) 139

Neutron dose test of active LVDB components of CBM-MUCH using the K-130 cyclotron at VECC

V. Jain[1], *J. Saini*[1], *A. K. Dubey*[1], *S. Chattopadhyay*[1], *R. Ravishankar*[1], *T. Bandyopadhyay*[1], *S. Mandal*[1], *J. Mitra*[1], *and P. Koczon*[2]

[1]VECC, Kolkata, India; [2]GSI, Darmstadt, Germany

A GEM-based detector system (MUCH) is being developed at VECC, Kolkata, for use as muon tracker in the Compressed Baryonic Matter (CBM) experiment at the upcoming FAIR facility at Germany [1, 2]. This system adds immensely to the neutron background. FLUKA calculations show that the electronics will have to withstand a neutron dose of the order of $10^{11}\ \mathrm{n_{eq}/cm^2}$ in the lifetime of the detector [3]. To study the effect of the neutron dose on the electronic components to be used near the detector, voltage regulators were exposed to secondary neutrons generated by the bombardment of protons from the Cyclotron at VECC on a thick Ta target.

The aim of the neutron tests is to study any physical or characteristics damage on the regulator. In this direction, we conducted the first of such tests for the LTC3605 voltage regulator in the VECC cyclotron. As schematically shown in Fig. 1, a 15 MeV proton beam with an average beam current of 4 μA was bombarded on a thick Ta target to produce secondary neutrons. This experiment was performed for about 10 days to achieve the required neutron dose. To measure the efficiency over this time period, input and output voltage and current were periodically monitored using a multimeter and a power supply display as shown in Fig. 2. Two sets of regulators were used, one of which was exposed to 8 kGy γ irradiation from Co^{60} before the neutron exposure. The efficiency was calculated by taking the ratio of output and input powers.

Figure 3 shows the efficiency of both the γ-irradiated and the non-irradiated voltage regulator with respect to the neutron flux on the regulator. We find the efficiency of the regulator to be almost stable up to a dose of $7.1 \times 10^{10}\ \mathrm{n/cm^2}$.

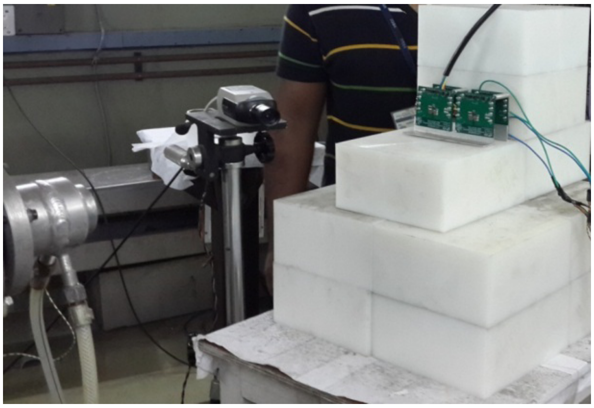

Figure 1: Neutron test setup at the VECC Cyclotron

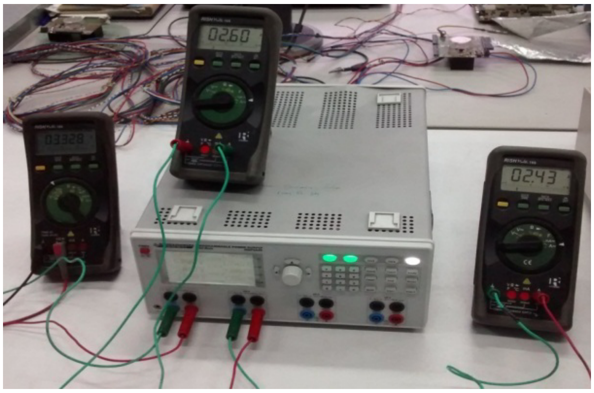

Figure 2: Voltage and current monitoring setup

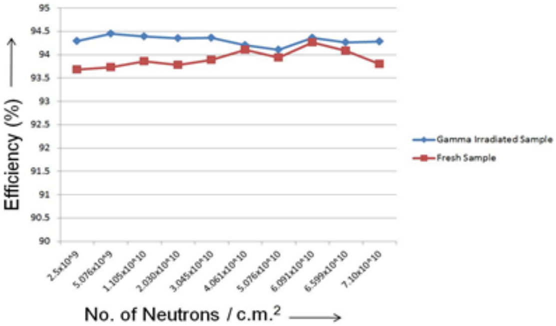

Figure 3: Efficiency as function of neutron flux

References

[1] The CBM Collaboration, *Technical Design Report for the CBM Muon Chambers (MUCH)*, in press

[2] A. K. Dubey *et al.*, Proc. DAE Symp. Nucl. Phys. 2010, p. 692; A. Kiseleva *et al.*, Indian J. Phys. **85** (2011) 211

[3] A. Senger, CBM Progress Report 2012, Darmstadt 2013, p. 26

Total dose effect test of active LVDB components for CBM-MUCH with a Co^{60} gamma chamber

V. Jain[1], *J. Saini*[1], *A. K. Dubey*[1], *S. Chattopadhyay*[1], *A. Saha*[2], *and P. Koczon*[3]
[1]VECC, Kolkata, India; [2]UGC-DAE Consortium for Scientific Research, Kolkata, India; [3]GSI, Darmstadt, Germany

A GEM-based detector system (MUCH) is being developed at VECC, Kolkata, for use as muon tracker in the Compressed Baryonic Matter (CBM) experiment at the upcoming FAIR facility at Germany [1, 2]. The MUCH system consists of alternating layers of six absorbers and detector stations. The harsh radiation dose in CBM owing to the high track density and interaction rate poses severe constraints on the design and selection of the electronic components to be used along with the detectors. To make sure that the selected components work in this environment, we have performed Gamma dose testing on one such component in a Co60 chamber at UGC-DAE Consortium for Scientific Research, Kolkata.

The most upstream detector station of MUCH will receive a dose of 300 Gy / 2 months as was obtained by FLUKA calculations [3]. As the total CBM-MUCH operating period in 10 years is expected to be 20 operational months [1], the CBM readout electronics have to withstand a total dose of 315 krad.

Figure 1: Gamma irradiation testing setup

Figure 1 shows the Co^{60} gamma chamber used as irradiation source. The equivalent dose rate inside this chamber was 3.1 kGy/h. Two voltage regulators were inserted in this chamber, one with load and the other without load. As the chamber constituted a thermal enclosure, the possibility of temperature rise due to load existed. Hence a small fan arrangement was located inside the chamber and operated continuously. In addition, the chamber was taken out every 10 minutes to further cool it down to ambient room temperature. Input and output voltages and currents were measured every 10 minutes. The efficiency, calculated by the ratio of output power to the input power of the voltage regulator, was measured with respect to the cumulative gamma dose.

Figure 2 shows the efficiency of the voltage regulator as function of the cumulative gamma dose up to 8 kGy. The efficiency of voltage regulator in the entire irradiation period decreased from 92.5% to 91.5%, which is well within the acceptable range of the current design of the low voltage distribution board (LVDB) to be used for CBM-MUCH electronics.

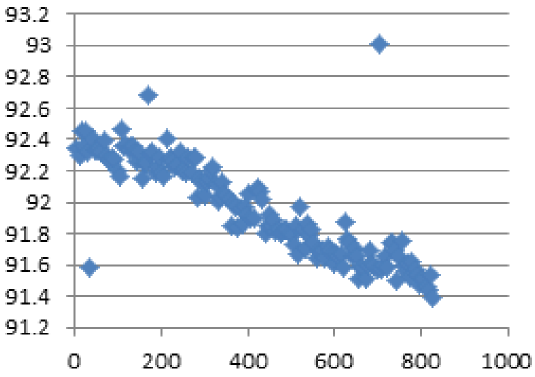

Figure 2: Efficiency as function of gamma dose

References

[1] The CBM Collaboration, *Technical Design Report for the CBM Muon Chambers (MUCH)*, in press

[2] A. K. Dubey *et al.*, Proc. DAE Symp. Nucl. Phys. 2010, p. 692; A. Kiseleva *et al.*, Indian J. Phys. **85** (2011) 211

[3] A. Fasso *et al.*, *FLUKA: a multi particle transport code*, CERN-2005-10 (2005)

Transition Radiation Detector

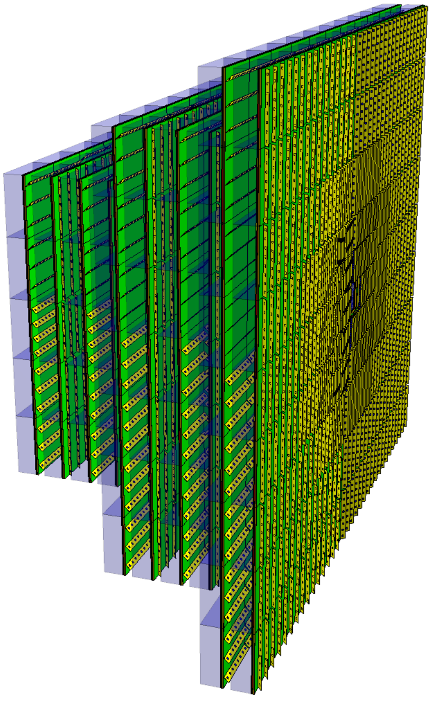

Test of Münster CBM-TRD real-size detector and radiator prototypes at the CERN PS/T9 beam line*

C. Bergmann[1], *D. Emschermann*[2], *R. Berendes*[1], *N. Heine*[1], *M. Kohn*[1], *W. Verhoeven*[1], *and J. P. Wessels*[1]

[1]Institut für Kernphysik, Münster, Germany; [2]GSI, Darmstadt, Germany

The Münster real-size CBM-TRD 2014 prototype of 57×57 cm^2 shown in Fig. 1 is derived from the design of the ALICE-TRD modules. An amplification region of $(3.5 + 3.5)$ mm is combined with a 5 mm drift section leading to an active gas volume thickness of 12 mm. This design combines a fast signal creation of the order of 200 ns with high TR-photon absorption probability due to a total gas thickness of 12 mm. Signals are induced on rectangular pads of 7.125 mm width, allowing charge collection on three adjacent pads along the anode wire direction. This design corresponds to the smallest module size next to the beam pipe, required for 12% of the total CBM-TRD area, and is scalable to detector modules of 95×95 cm^2 size, which are used in the outer part of each detector layer. TR-photon losses due to material budget between the radiator and the active gas volume were minimized in order to reach maximum particle identification (PID) performance per module. The entrance window is built from a 25 μm single-side aluminized Kapton foil stabilized by a carbon fiber lattice support structure as presented in Fig. 1. This support structure limits the mechanical deformation of the foil to 1 mm per mbar differential pressure. The lattice covers only 2% of the total active area.

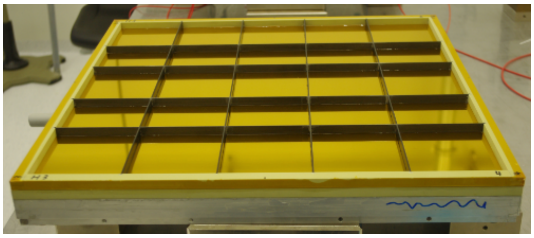

Figure 1: Foil window of the real-size TRD 2014 prototype

The maximum PID performance can only be realized with a radiator optimized to the photon absorption characteristic of the detector. We identified a polyethylene foam foil radiator in previous in-beam tests at CERN in 2011 and 2012 [2]. The first radiator prototype $H{+}{+}$ was scaled to the full detector surface. The active radiator material is mechanically supported by a light-weight structure built from a PMMA foam (Rohacell). The radiator mounted on a detector is presented in Fig. 2.

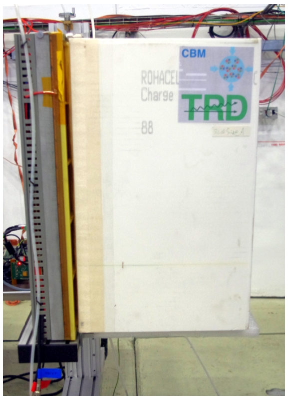

Figure 2: Side view of the real-size TRD prototype in the PS/T9 beam line in 2014 with a mounted full-size foam foil radiator

In addition to the improved detector and radiator design, this beam time was the first one using a FLIB-based Data AcQuisition (DAQ) system. A combination of SPADIC v1.0 mounted on single FEB and three ASIC FEBs (presented in Fig. 3) and SysCore v3.1 were used to read out the TRD prototypes in beam.

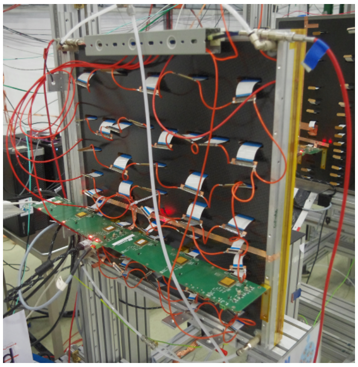

Figure 3: Back view of the real-size TRD prototype with 6 SPADICv1.0 ASICs on two 3 ASIC FEBs mounted on the chamber

References

[1] C. Bergmann *et al.*, *Common CBM beam test of the RICH, TRD and TOF subsystems at the CERN PS T9 beam line in 2014*, this report

[2] C. Bergmann *et al.*, CBM Progress Report 2012, Darmstadt 2013, p. 57

---

* Work supported by BMBF and the HadronPhysics3 project financed by EU-FP7

Construction and test of a new CBM-TRD prototype in Frankfurt*

M. Tanha, W. Amend, H. Appelshäuser, A. Arend, A. Arend, C. Blume, P. Dillenseger, S. Gläßel, and F. Roether
Goethe-Universität, Frankfurt, Germany

A new TRD prototype based on a thin Multi Wire Proportional Chamber (MWPC) without a drift region and with carbon frame was designed at the Institute for Nuclear Physics in Frankfurt (IKF) and tested in the test beam at CERN-PS in November 2014. According to this design, two identical real-size prototypes with outer dimensions of $586 \times 580 \times 38.5$ mm^3 were developed with a pitch of 2.5 mm between field and sense wires. Cathode (field) wires made of Cu-Be with a diameter of 80 μm are placed between gold-plated tungsten anode (sense) wires with a diameter of 20 μm. The gas gap region, the distance between entrance window and pad-plane, is (3.5+3.5) mm (see Fig. 1). The chambers were build with the same type of pad plane as used in the prototypes from Münster [1].

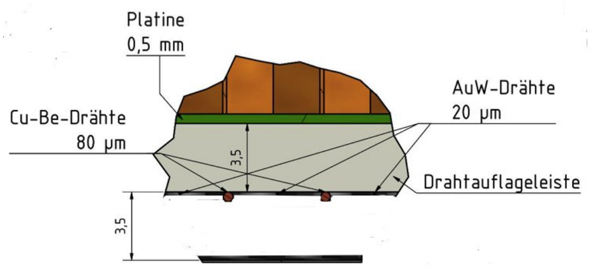

Figure 1: Schematic drawing of alternating wires, their pitch and diameters

Applying cathode wires with alternating HV (alternating wires) has an improved result as it reduces the effect of a deformation of the cathode plane by about a factor of 6, which distorts the gas gain inside the detector via electric field deformation [2].

The MWPC with thin and symmetric geometry (3.5+3.5 mm) provides fast signal collection and efficient e/π separation, which is desired in the CBM experiment [3]. The carbon frame, instead of an aluminium or vetronit frame, provides optimum mechanical properties, low thermal expansion, high friction resistance and low material budget. Figure 2 shows the technical drawing of the prototype with the aforementioned components.

Figure 3 shows the gas feed-through that is embedded inside the frame in the corners. Thus, it meets the structural conditions of the TRD chambers, which will have to be mounted close to each other in the final setup.

The data from the CERN-PS test beam in November 2014 are currently being analysed. The development of a large size (1.0×1.0 m^2) prototype of the TRD is planned at IKF.

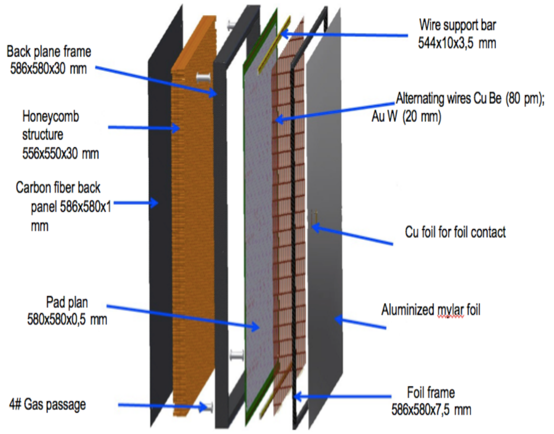

Figure 2: Technical drawing of the TRD prototype with alternating wires and carbon frame

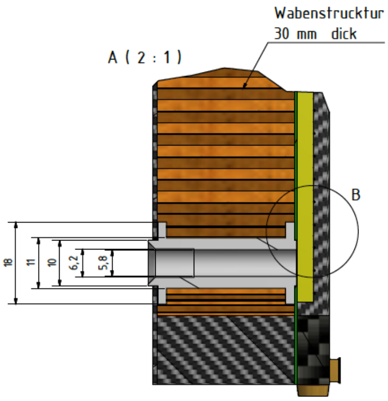

Figure 3: The gas feed-through inside the frame

References

[1] C. Bergmann *et al.*, *Test of Münster CBM-TRD real-size detector and radiator prototypes at the CERN PS/T9 beam line*, this report

[2] S. Gläßel *et al.*, CBM Progress Report 2013, Darmstadt 2014, p. 70

[3] E. Hellbär *et al.*, CBM Progress Report 2012, Darmstadt 2013, p. 54

---

[*] Work supported by BMBF, HIC4FAIR and HGShire

Progress in TRD readout using SPADIC 1.0

M. Krieger and P. Fischer
ZITI, Universität Heidelberg, Mannheim, Germany

After all features of the SPADIC 1.0 chip had been verified to be functioning in the laboratory [1], the next steps in the development of a readout system for the CBM transition radiation detector were taken.

During this year's common beam time of several CBM detector subsystems at CERN [3], the latest "rev. B" front-end boards [2] were used to read out TRD modules (depicted in Fig. 1). The design of the front-end boards including the packaged chips showed to be a viable solution, and a few aspects concerning the low voltage supply and reset mechanism were identified, which need to be improved in future revisions.

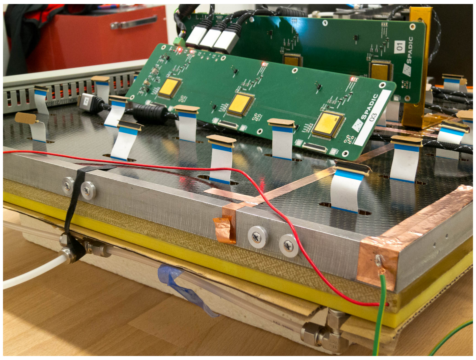

Figure 1: Two SPADIC "rev. B 3x" front-end boards on a TRD module

Once a proper ground connection between the various components of the detector and readout setup had been found, the noise contained in the measured signals could be reduced to levels not much higher than what had been observed under laboratory conditions without any detector connected to the readout electronics (equivalent noise charge: 2.0±1.0 ke$^-$ vs. 0.9±0.1 ke$^-$). Examples of measured TRD pulses and a histogram of pulse amplitudes can be seen in Fig. 2.

A significant effort was the development of software components necessary to operate the SPADIC chips in the beam test environment. These include

- libraries to extract the SPADIC data from the *timeslice* objects provided by the FLESnet data acquisition system [4] and to decode the SPADIC data stream into a format understood by the CBMroot analysis framework,
- user interfaces for controlling and monitoring the SPADIC configuration, and
- various automation scripts, for example to load previously determined configurations or to equalize baseline levels between channels.

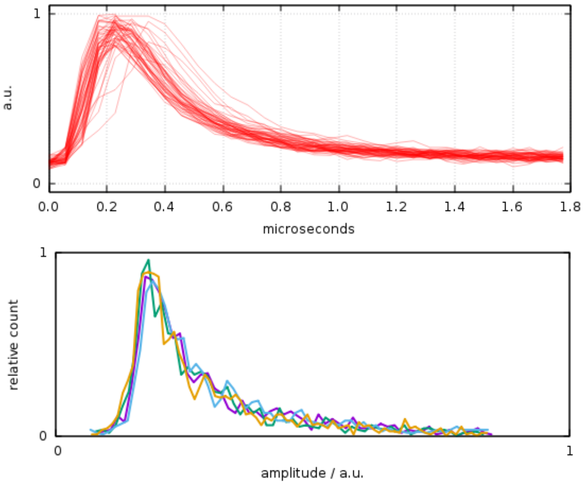

Figure 2: Top: An overlay of approximately 50 recorded pulse shapes. The horizontal axis covers a time interval of 1.8 microseconds, corresponding to 32 samples taken at a rate of 17.5 MHz. Bottom: Distribution of pulse amplitudes for four different channels.

The operation of the chips was complicated by two known bugs in the SPADIC 1.0 implementation. These are an instability in the charge sensitive amplifier and a glitch in the serial data output. In the near future, an intermediate version 1.1 of the ASIC will be produced, where among a few other smaller improvements these two problems will be solved, but which otherwise remains compatible to SPADIC 1.0 such that the existing infrastructure can be reused in upcoming beam tests.

References

[1] M. Krieger and P. Fischer, CBM Progress Report 2013, Darmstadt 2014, p. 72

[2] M. Krieger, CBM Progress Report 2013, Darmstadt 2014, p. 73

[3] C. Bergmann *et al.*, *Common CBM beam test of the RICH, TRD and TOF subsystems at the CERN PS T9 beam line in 2014*, this report

[4] D. Hutter, J. de Cuveland and V. Lindenstruth, *CBM FLES input interface developments*, this report

Two-dimensional MWPC prototype for CBM-TRD*

A. Bercuci, D. Bartoş, G. Caragheorgheopol, V. Cătănescu, F. Constantin, M. Petriş, and M. Petrovici
IFIN-HH, Bucharest, Romania

The signal induced on a segmented conductive electrode is used in a large number of MWPC applications for position information. Additionally, the firing anode can be used for orthogonal position information at an increased operational cost. The drawback of such a procedure is the poor localization along the wire and the impossibility to operate in conditions of high local occupancies and counting rates. In the current report the performance of an innovative geometry of the read-out electrode is presented. The $2D$ information can be extracted in high fluxes without additional anode read-out channels.

The TRD developed in Bucharest for the CBM experiment [1] is characterized by a 4 mm drift, a 2×4 mm amplification region, and wire pitches of 1.5 mm for the cathode and 3 mm for the anode wires (Fig. 1, left). The conductive electrode is segmented in triangular-shaped pads of 7.3×27.7 mm^2 with 0.2 mm spacing arranged with respect to the anode wires as shown in Fig. 1, right.

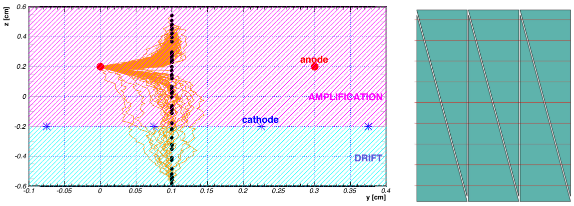

Figure 1: Active volumes (drift, amplification) and elements (anode, cathode wires and the pad plane structure) as well as signal formation in the TRD as simulated with Garfield++ [2]

Because of the varying cross section of the pads with respect to the anode wires in our current set-up and because of the localization of the induced signal, the Pad Response Function (PRF) varies with the position of the firing anode wire along the pads. Thus, an Anode Response Function (ARF) for anode identification can be built. In Fig. 2, left, the method is tested using a uniform illumination of the TRD detector with a ^{55}Fe source. For each PRF value, nine maxima are found corresponding to the anodes covered by a pad row. Each local maximum is fitted, and the mean and sigma parameters of the Gaussian distributions are extracted (see markers on Fig. 2, left, and the sine interpolation). A very good separation between each curve is obtained for the whole pad height.

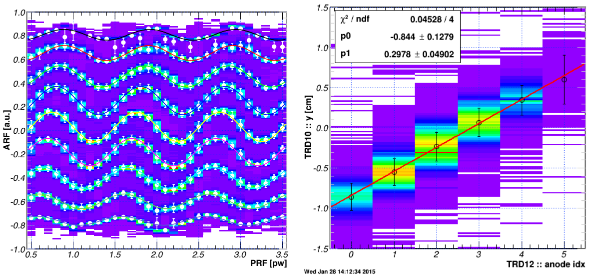

Figure 2: ARF correlations with PRF as measured with a TRD prototype for a uniform illumination with ^{55}Fe (left) and with the position measurement by a reference TRD for MIPs (right), respectively. The slope of the fit ($p1$) gives the measured distance between the anodes in cm.

In November 2014, the TRD prototype operated with Xe/CO$_2$ (80/20) was tested with MIPs at the CERN-PS. To estimate the resolution of the ARF method, a reference position-sensitive TRD was mounted orthogonal to it. The reference detector was operated with a rectangular-shaped pad geometry for good position resolution across pads. The correlation between position measurements in the reference detector and anode identification by ARF is shown in Fig. 2, right. The measured distance of (2.98 ± 0.05) mm between the anode wires is in good agreement with the designed pitch of 3 mm.

The measurement across pads is performed for the time being using the pairing of triangular pads. A resolution of $\approx 500\ \mu$m is obtained from a ^{55}Fe position scan operated with Ar/CO$_2$ (80/20) and FASP v0.1 FEE.

In summary, it was demonstrated that the usage of a varying PRF along pads can provide good local anode identification. The method opens the possibility of using reduced *effective* pad geometries with implications in position resolution at constant read-out costs and experimental material budgets.

References

[1] M. Tarzila *et al.*, CBM Progress Report 2012, Darmstadt 2013, p. 60

[2] `http://garfieldpp.web.cern.ch/garfieldpp`

---

* Work supported by Romanian ANCSI/CAPACITATI Modul III Contract F02 and NUCLEU Project Contract PN 09370103

Fast Analog Signal Processor FASP-02*

V. Cătănescu
NIPNE, Bucharest, Romania

A second version of the FASP ASIC dedicated for high counting rate CBM TRD prototypes developed by the Bucharest group [1, 2, 3, 4] was designed and produced. Similar to the first version, it is based on AMS 0.35 μm N-well technology. The die size is 4.65×3.45 mm^2 (Fig. 1). Besides the main features of its precursor, new ones are implemented in FASP-02, considering the specific architecture of the fast TRD prototypes mentioned above and the results obtained in the tests carried out in the meantime. The most relevant new features are:

- 16 input channels;
- selectable positive or negative polarity of the input signals;
- multiplexed analog outputs, i.e., selectable semi-Gaussian or flat top;
- channel-wise clock synchronized logic time for individual ADCs;
- channel-wise logic time signal generated at the selectable threshold level or at the signal peak detection, according to the user setting;
- selectable trigger of neighboring channels relative to the one with the signal above the threshold;
- tilted and rectangular pairing of the triangular pads.

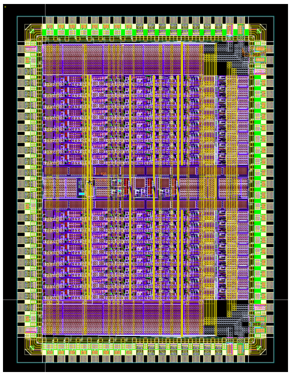

Figure 1: Photo of the FASP-0.2 ASIC

Good response to double pulses, to high pulse rates, fast recovery from positive/negative overload, base line restoration due to pulse rate shift, detector leakage current, temperature and voltage supply variations are also implemented to the FASP-0.2 ASIC. Additionally, the self-triggering capability working with a new channel-wise input/output interface enhances the ASIC performance.

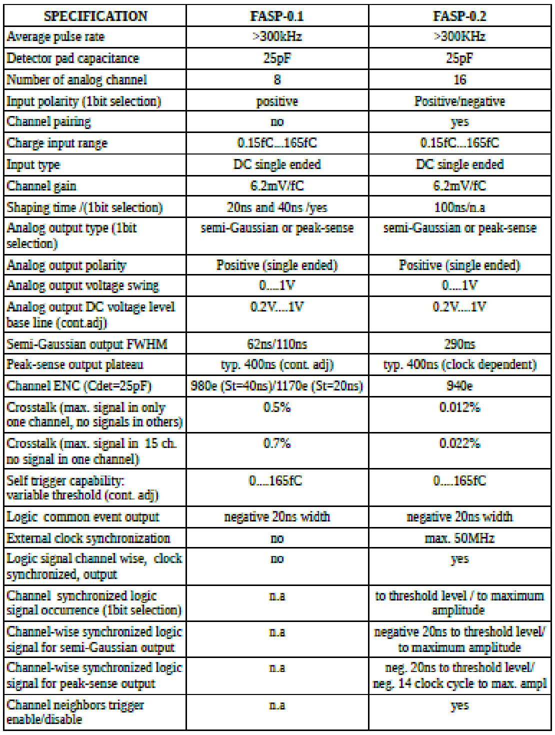

SPECIFICATION	FASP-0.1	FASP-0.2
Average pulse rate	>300kHz	>300KHz
Detector pad capacitance	25pF	25pF
Number of analog channel	8	16
Input polarity (1bit selection)	positive	Positive/negative
Channel pairing	no	yes
Charge input range	0.15fC...165fC	0.15fC...165fC
Input type	DC single ended	DC single ended
Channel gain	6.2mV/fC	6.2mV/fC
Shaping time /(1bit selection)	20ns and 40ns /yes	100ns/n.a
Analog output type (1bit selection)	semi-Gaussian or peak-sense	semi-Gaussian or peak-sense
Analog output polarity	Positive (single ended)	Positive (single ended)
Analog output voltage swing	0....1V	0....1V
Analog output DC voltage level base line (cont.adj)	0.2V....1V	0.2V....1V
Semi-Gaussian output FWHM	62ns/110ns	290ns
Peak-sense output plateau	typ. 400ns (cont. adj)	typ. 400ns (clock dependent)
Channel ENC (Cdet=25pF)	980e (St=40ns)/1170e (St=20ns)	940e
Crosstalk (max. signal in only one channel, no signals in others)	0.5%	0.012%
Crosstalk (max. signal in 15 ch. no signal in one channel)	0.7%	0.022%
Self trigger capability: variable threshold (cont. adj)	0....165fC	0....165fC
Logic common event output	negative 20ns width	negative 20ns width
External clock synchronization	no	max. 50MHz
Logic signal channel wise, clock synchronized, output	no	yes
Channel synchronized logic signal occurrence (1bit selection)	n.a	to threshold level / to maximum amplitude
Channel-wise synchronized logic signal for semi-Gaussian output	n.a	negative 20ns to threshold level/ to maximum amplitude
Channel-wise synchronized logic signal for peak-sense output	n.a	neg. 20ns to threshold level/ neg. 14 clock cycle to max. ampl
Channel neighbors trigger enable/disable	n.a	yes

Figure 2: Main specifications for FASP-0.1 and FASP-0.2

The shaping time for FASP-0.2 is increased to 100 ns in order to meet the requirements of the new TRD prototypes with a drift region of 4 mm. The crosstalk is about ten times lower compared to FASP-0.1. The main specifications for FASP-0.1 and FASP-0.2 are summarized in Fig. 2, where the new features and the modified specifications for FASP-0.2 are described.

References

[1] M. Petriş *et al.*, Nucl. Instrum. Methods **A 714** (2013) 17

[2] M. Petriş *et al.*, Nucl. Instrum. Methods **A 732** (2013) 375

[3] M. Târzilă *et al.*, CBM Progress Report 2012, Darmstadt 2013, p. 60

[4] A. Bercuci *et al.*, *Two-dimensional MWPC prototype for CBM-TRD*, this report

---

* Work supported by EU-FP7/HP3 Grant No 283286, Romanian NASR/CAPACITATI-Modul III contract RO-FAIR F02 and NASR NUCLEU Project PN09370103

Free-running acquisition system for Transition Radiation Detectors - in beam tests[*]

F. Constantin, D. Bartoş, A. Bercuci, G. Caraghergheopol, V. Cătănescu, M. Petriş, M. Petcu, and M. Petrovici
NIPNE, Bucharest, Romania

The present acquisition system was developed as a test benchmark of a free running concept for high counting rate TRDs [1] based on the FASP ASIC and analog converters of the type foreseen to be implemented in a later stage in a hybrid updated version of the FASP analog processor. This version can operate 64 TRD readout channels with a sampling rate of 2 Msps and 12 bit resolution MAX 11105 ADC. The system is based on a Spartan 6, SP601 evaluation board and a custom designed board for MAX 11105 analog converters [2, 3]. Two such systems were built, each of them processing data from 32 pads. In order to merge the correlated data between several sub-detectors, a synchronization signal is used. The main tasks assumed by the system are:

- data unpacking from the 2 x 32 MAX 11105 and synchronisation management;
- capture of the MBS_sync signal from a MBS (Multi-Branch System) system [4];
- packing the data and Ethernet transmission through UDP protocol.

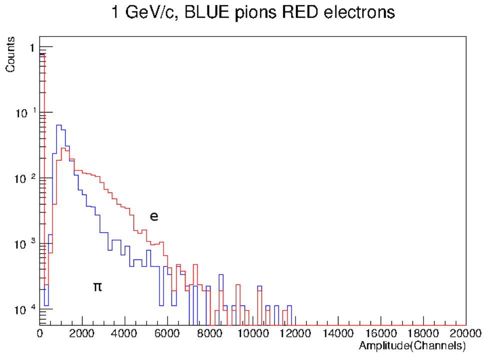

Figure 1: Pulse height distributions for electrons (red) and pions (blue) at 1 GeV/c momentum

The mixed acquisition system, a trigger driven (MBS) and the free running, generates acquisition files which are later paired by a dedicated software. Data for the TRD were collected based on the free-running system described above, while Cherenkov and lead glass information was acquired by the MBS system. The correctness of the data synchronisation is proven by the electron and pion pulse height distributions at three different momenta presented in Figs. 1-3.

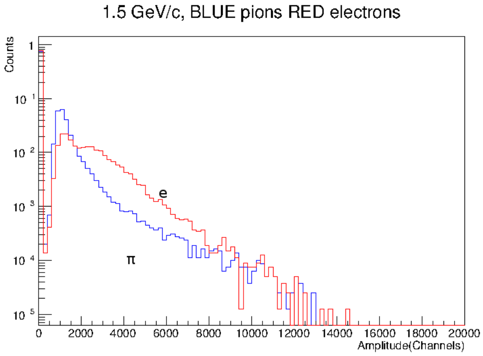

Figure 2: Pulse height distributions for electrons (red) and pions (blue) at 1.5 GeV/c momentum

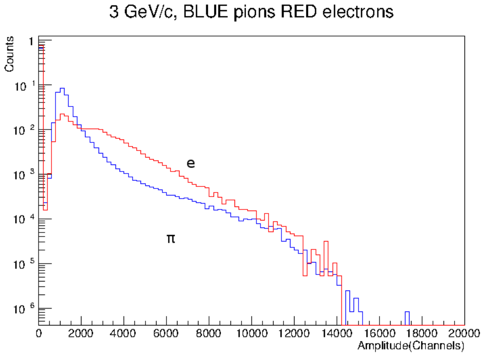

Figure 3: Pulse height distributions for electrons (red) and pions (blue) at 3 GeV/c momentum

References

[1] M. Târzilă *et al.*, CBM Progress Report 2012, Darmstadt 2013, p. 60

[2] `http://www.xilinx.com/publications/prod_mktg/sp601_product_brief.pdf`

[3] `http://www.maximintegrated.com/en/datasheet/index.mvp/id/6419`

[4] `https://www.gsi.de/work/fairgsi/common_systems/csee_electronics/datenverarbeitung/datenerfassung/mbs.htm`

---

[*] Work supported by Romanian NASR/CAPACITATI-Modul III contract F02 and NUCLEU contract PN09370103

Construction and commissioning of a setup to study ageing phenomena in high rate gas detectors

A. Abuhoza[2,3], *U. Frankenfeld*[3], *J. Hehner*[3], *and H.-R. Schmidt*[1]
[1]Eberhard-Karls-Universität, Tübingen, Germany; [2]Goethe-Universität, Frankfurt, Germany; [3]GSI, Darmstadt, Germany

A setup dedicated to the investigation of ageing properties of gaseous detectors due to materials used for their construction was constructed and commissioned at the GSI detector laboratory. An outstanding feature of the setup is that tedious and repetive measurements can be conducted fully automatically.

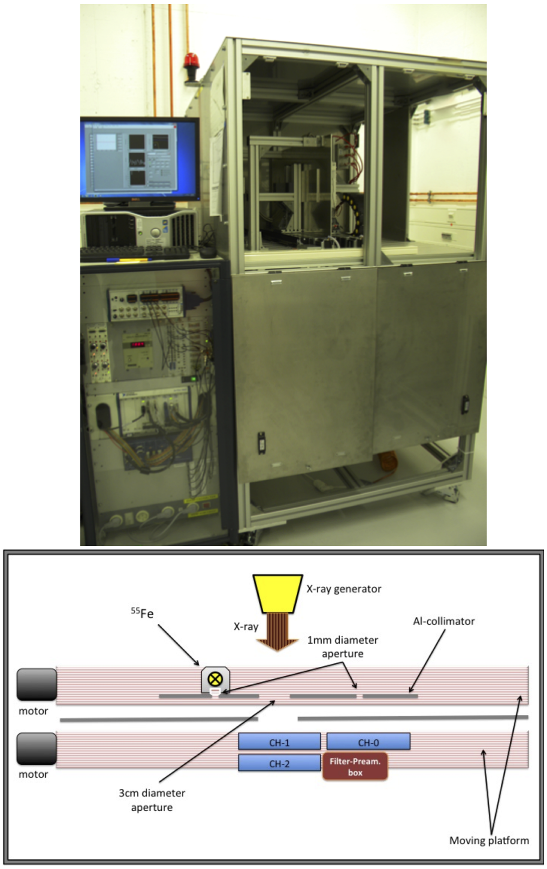

Figure 1: Photograph of the setup mounted in a metallic enclosure and the associated data acquisition system (top). Sketch of the components of the ageing setup (bottom).

The setup consists of three identical Multi Wire Proportional Chambers (MWPCs) mounted onto a moving platform, an X-ray generator to produce ionizing radiation and a ^{55}Fe source for gain diagnostics. A second moving platform holds an aluminium collimator plate which has three different apertures. Two of the chambers are flushed with gas which has passed through outgassing boxes containing the materials under investigation. One of the chambers is operated with clean gas for reference purposes. All gas lines are equipped with individual Mass Flow Controllers (MFC). The data acquisition and control system based on LabView is configured to allow fully automated measurements during long term tests. Figure 1 shows a photograph of the setup and a sketch of the components.

Before fabrication of the MWPCs, simulations of their electric field and gain had been done using a combination of a gas simulation program (Magboltz) and an electric field simulation program (Garfield). The accuracy of the gas temperature measurement was greatly improved which allows a very accurate gain measurement. Over a period of eight months, cleaning procedures were developed and all sources of contamination of the equipment were eliminated. Thereafter, the setup was operated with very stable behaviour, evidenced by the fact that around 0.5% peak-to-peak residual variation of the normalised gain was achieved. Thus, the setup shows the required high stability to be used for precise ageing studies.

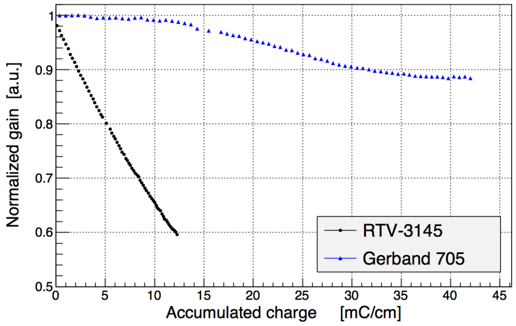

Figure 2: Normalised gain of a chamber tested with Gerband 705 (blue) and a chamber tested with RTV-3145 (black) as a function of accumulated charge per unit length of the anode wires

First ageing tests were carried out with two materials over two weeks: Aluminium tape named Gerband 705 and a glue named RTV-3145. At the end of these two weeks, the ageing rate (R) caused by Gerband 705 was about 0.3%/mC/cm while it was 3%/mC/cm for RTV-3145. The blue and black curves of Fig. 2 illustrate the normalised gain of the MWPC contaminated with Gerband 705 and RTV-3145, respectively, as a function of the accumulated charge per wire length.

Time-of-Flight Detector

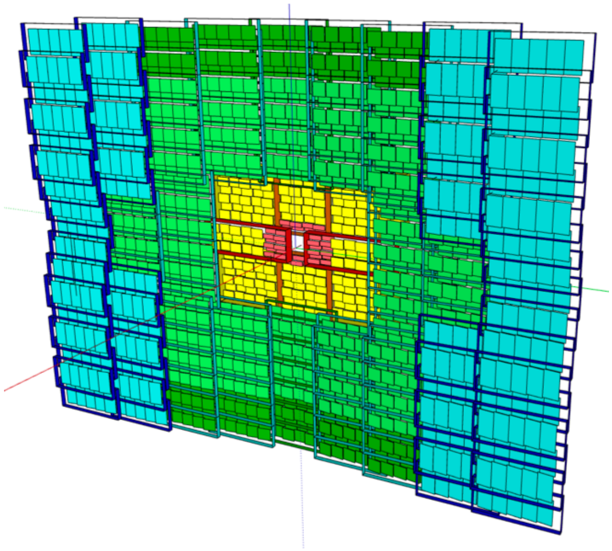

MPRC performance evaluation in a heavy ion beam test at GSI *

I. Deppner[1], *N. Herrmann*[1], *P.-A. Loizeau*[1], *C. Simon*[1], *Y. Söhngen*[1], *M. Ciobanu*[2], *J. Frühauf*[3], *and M. Kis*[3]

[1]Physikalisches Institut, Universität Heidelberg, Germany; [2]ISS, Bucharest, Romania; [3]GSI, Darmstadt, Germany

The CBM Time-of-Flight-wall will be composed of Multi-gap Resistive Plate Chambers (MRPCs) [1]. In order to approach a final MRPC design, several counters from different groups were tested in October 2014 in a heavy ion test beam time in the HADES cave of GSI. A Sm beam of an incident energy of 1.1A GeV beam energy was used to produce a spray of reaction products by hitting a 5 mm thick lead target. By this a full illumination of the counters was achieved, which is extremely important for determining the counter properties under real usage condition.

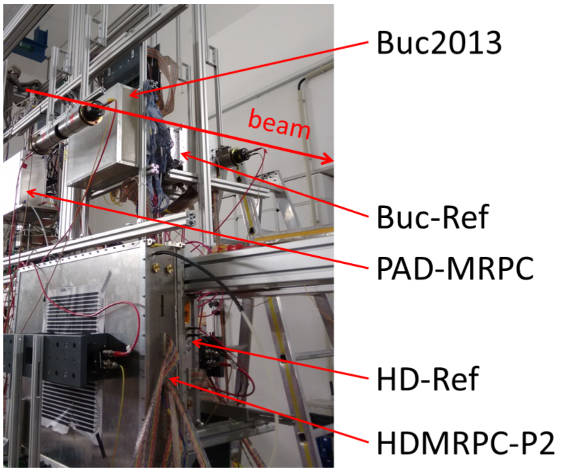

Figure 1: Setup used in the Oktober beam time. For details see text.

Figure 1 depicts the test beam setup that is constitued from two parts. Each part consist of two MRPC counters under test, a reference MRPC and a plastic scintillator in front and behind the counter stack. The scintillators were read out on both sides with PMTs. The counters in the upper part of the setup were located close to the beam line in order to get the highest possible particle flux. The counters under test were a narrow strip prototype from Bucharest [2] (called Buc2013) and a PAD-MRPC [3] from Tsinghua University, China. These two counters were mounted in the upper part on a rail in order to exchange their position. The measured flux (estimated from the plastic scintillator) at this position was about 1 kHz/cm^2. In the lower part of the setup the counter under test was a full size prototype from Heidelberg [4] (called HDMRPC-P2) that was exchanged after half of the beam time by a strip counter from Tsinghua University. These two counters have similar dimensions and the same pickup electrode geometry. However, they differ significantly in the design of the HV regions (single stack (P2) vs. double stack (Tsinghua). The measured flux at the location of these counters was about a few hundred Hz/cm^2. Additional timing information was provided by a diamond detector which was installed a few cm in front of the target.

The data acquisition during this in-beam test was based on the TRB3 platform [5] providing trigger and readout handling of more than 30 FPGA-TDCs with 32 timing channels each. The TDCs digitize the arrival times of both leading and trailing edges of LVDS signals created by the preamplifier/discriminator ASIC PADI [6] directly connected on the MRPC readout electrodes. The width of these LVDS signals corresponds to the time over discrimination threshold (ToT) of the analog detector signals. The TDC core [7] is implemented on Lattice ECP3 FPGAs, residing both on the TRB3 board and on TDC front-end cards (CBM-TOF-FEE1) hooked up in close vicinity to the MRPCs [8].

The analysis of the data proceeds in the following steps:

1. Data unpacking and TDC nonlinearity calibration. For the nonlinearity calibration 8 hours of data taking is used for a calibration file in order to have a statistical sufficient data sample that ensures sufficient population in every TDC bin.

2. Time and position offset calibration, cluster building and walk correction. A firing strip delivers a time information on both ends of the strip. The mean of the two signals provides the arrival time of the signal of the strip. The difference delivers in combination with the signal velocity the position of the hit along the strip. Neighboring firing strips in the MRPC are grouped together to a cluster if they are correlated in time and space. The correlation window was set to 500 ps in time and about 8 cm in space. The cluster time is calculated by taking the mean of the strip times weighted with the time over threshold information. In an event several clusters can occur on the MRPC surface.

3. Correction for particle velocity spread and hit position. Steps 2 and 3 are done iteratively.

4. Data analysis with different cut settings. Cuts are applied on the reference counters in order to provide an as clean as possible event sample.

---

* Work supported by BMBF 06HD7141I and EU/FP7 HadronPhysics3

Here we present the results obtained with the Heidelberg prototype HDMRPC-P2. Figure 2 shows the counter efficiency as function of the applied high voltage (HV) for a PADI6 threshold of 150 mV (red triangles) and for 200 mV (blue squares). The efficiency is calculated by comparing the matched hits between the counter under test and the reference MRPC with the matched hits between the diamond start counter and the reference MRPC. At an applied high voltage of ±10.5 kV the effect of the discriminator threshold is visible. A smaller electric field produces smaller signals that can be detected with a lower threshold. This effect disappears with higher HV, i.e., with higher electrical field. The outlier at ±12.5 kV needs further investigation. An overall efficiency of larger than 98% is observed at the nominal working voltage (±11 kV to ±11.5 kV). The statistical errors are too small to be visible in the plot.

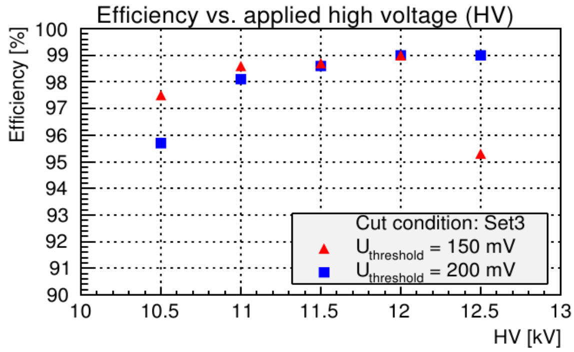

Figure 2: Efficiency as function of the applied high voltage at a PADI6 threshold of 150 mV (red triangles) and 200 mV (blue square)

The system time resolution obtained between HDMRPC-P2 and HD-ref is presented in Fig. 3. It is calculated by subtracting the time of those clusters from both counters that have the best χ^2 matching value, i.e., those that are best correlated in time and space. The excitation function of the time resolution shows a broad minimum at about ±11.0 kV (corresponding to an electrical field of 125 kV/cm) for both threshold settings. The best system time resolution is about 62 ps. Assuming both MRPCs to have the same performance, the individual MRPC has a time resolution on the order of 44 ps including the jitter of all electronic components. The increase towards higher voltages can be explained by two facts: 1) with higher voltage more and more streamers are produced, and 2) the increasing noise rate disturbs the cluster time. The results at a PADI6 threshold of 150 mV are slightly worse than for 200 mV. The statistical error is about 0.5 ps.

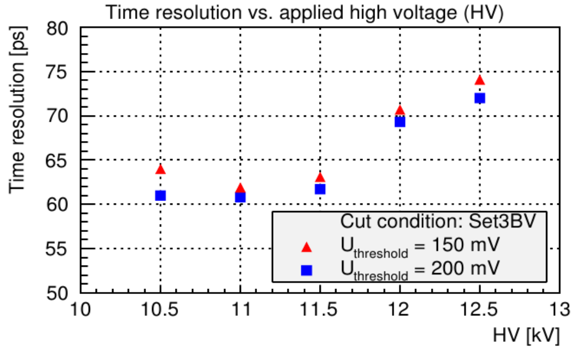

Figure 3: System time resolution as function of the applied high voltage at a PADI6 threshold of 150 mV (red triangles) and 200 mV (blue square)

Figure 4 illustrates the mean cluster size as function of the applied high voltage (HV) for a PADI6 threshold of 150 mV (red triangles) and for 200 mV (blue squares). The data show an almost linear increase with HV for both thresholds reaching a maximum at ±12.0 kV. At ±12.5 kV the mean cluster size drops again and has the same value for both threshold settings. This behavior is still under investigation.

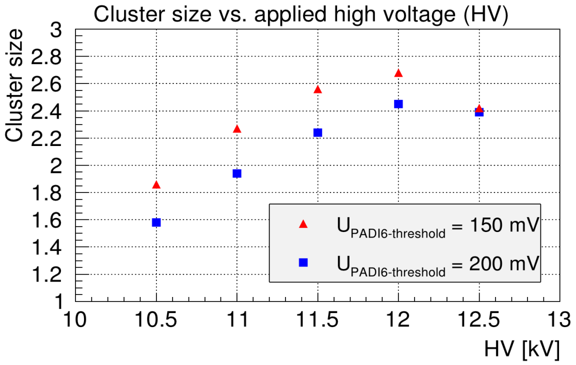

Figure 4: Mean cluster size as function of the applied high voltage at a PADI6 threshold of 150 mV (red triangles) and 200 mV (blue square)

We acknowlegde the contributions of all members of the CBM-TOF group to this report.

References

[1] I. Deppner *et al.*, Nucl. Instrum. Methods **A 661** (2012) S121

[2] V. Aprodu *et al.*, CBM Progress Report 2013, p. 79

[3] WeiPing Zhu *et al.*, Sci. China. Technol. Sc. **56** (2013) 2821

[4] I. Deppner, PhD thesis, Universität Heidelberg 2013

[5] A. Neiser *et al.*, JINST **8** (2013) C12043

[6] M. Ciobanu *et al.*, IEEE Trans. Nucl. Sc. **61** (2014) 1015

[7] C. Ugur *et al.*, IEEE NoMeTDC (2013), doi:10.1109/NoMeTDC.2013.6658234

[8] C. Ugur *et al.*, GSI Scientific Report 2013, HSD-11

Progress in ceramic RPCs for the beam fragmentation T_0 counter

A. Laso Garcia[1], *A. Akindinov*[2], *J. Hutsch*[1], *B. Kämpfer*[1], *M. Kaspar*[1], *S. Kiselev*[2], *R. Kotte*[1], *D. Mal'kevich*[2], *L. Naumann*[1], *V. Plotnikov*[2], *M. Sobiella*[1], *D. Stach*[1], *R. Sultanov*[2], *K. Voloshin*[2], *C. Wendisch*[1], *and J. Wüstenfeld*[1]

[1]Helmholtz-Zentrum Dresden-Rossendorf, Dresden, Germany; [2]ITEP, Moscow, Russia

One of the solutions proposed for the start time determination for time-of-flight measurements in the CBM experiment is the Beam Fragmentation T_0 Counter (BFTC) [1]. This detector will be located at the most central part of the ToF Wall, partially covering the region of the PSD. The high fluxes at this region are expected to reach $2.5 \times 10^5\,\mathrm{cm}^{-2}\,\mathrm{s}^{-1}$ [2]. Therefore, ceramic RPCs could be used because of their high rate capabilities [3].

The RPCs with grooved ceramic electrodes were already introduced in previous reports [4]. They consist of double gap stacks, where the outer electrodes are Al_3O_2 ceramics with a Chromium layer deposited on. The floating electrodes are made of Si_3N_4/SiC ceramics. The full module is formed by three such stacks forming a six-gap RPC. The gas mixture is 90% Freon / 10% SF_6 or 95% Freon / 5% SF_6.

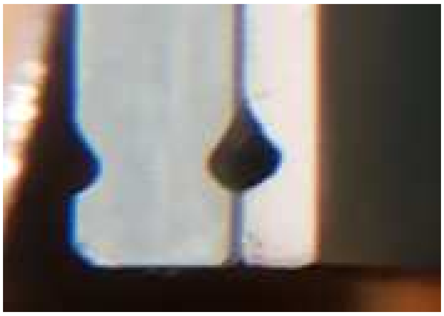

Figure 1: A photograph of the result of the grooving of the floating electrode (left) and outer electrode (right)

The production of grooved electrodes was established. Both outer electrodes are grooved on the side facing the gas gap, while the floating electrode is grooved on both sides. This effectively reduces the dark currents of the detector and allows to reach higher electric fields. The current set-up of grooving diamond tools is capable of grooving several plates without the need of exchanging the disks. Figure 1 shows the grooving of both outer and inner electrodes. The small differences in the groove shape are due to the higher hardness of the Si_3N_4/SiC ceramics.

Four modules were assembled and tested during the last year. The bulk resistivity of the Si_3N_4/SiC ceramics was $10^{10} - 10^{11}\,\Omega\,\mathrm{cm}$. The modules were tested at ELBE (HZDR) and at the T10 beam line (CERN). Analysing the data taken at the test experiments, the achieved (max.) detection efficiency ranges between 88% and 95% as shown in Fig. 2. Several modules show a plateau not higher than 90%. This was attributed to the formation of unusual signals in the detector not correlated with gas discharges due to the arrival of an ionizing particle. One such signal is shown in Fig. 3.

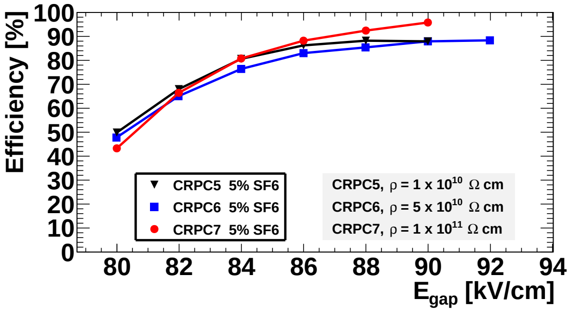

Figure 2: Efficiency as function of the electric field in the gas gap

Further investigations on the efficiency will be performed in the following year with the assembly of new modules and beam tests at ELBE and CERN.

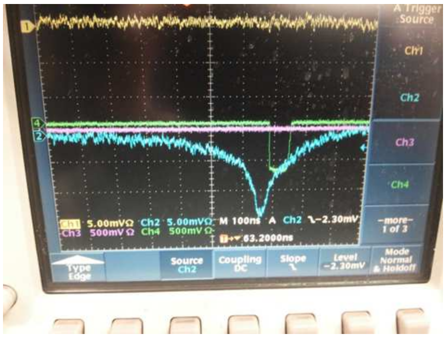

Figure 3: Oscilloscope recording of a pulse not correlated with the arrival of a particle

References

[1] S. M. Kiselev, CBM Progress Report 2013, p. 109

[2] R. I. Sultanov, CBM Progress Report 2013, p. 82

[3] A. Laso Garcia, PhD thesis, Technische Universität Dresden 2015

[4] A. Laso Garcia *et al.*, CBM Progress Report 2013, p. 76

Cosmic-ray and in-beam tests of 100 Ohm transmission line MGMSRPC prototype developed for the inner zone of CBM-TOF *

M. Petriş, V. Aprodu, D. Bartoş, A. Bercuci, G. Caragheorgheopol, F. Constantin, V. Duţă, M. Petrovici, L. Prodan, A. Radu, L. Rădulescu, and V. Simion
NIPNE, Bucharest, Romania

As a solution for the high granularity required for the innermost zones of the CBM-TOF, a new MGMSRPC prototype (called RPC2013) was designed and built. Construction details of the tested prototype are presented in [1]. The strip structure of the readout and high voltage electrodes (4.19 mm strip pitch with 2.16 mm width and 200 mm strip length) was decided based on APLAC simulations. The aim was to obtain a differential readout impedance as close as possible to 100 Ω in order to match the input impedance of the front-end electronics. The prototype is based on low resistivity ($\sim 10^{10}$ Ω·cm) glass plates in order to cope with the high counting rate anticipated for the inner zone of the CBM-TOF wall. High counting rate tests performed with MGMSRPCs using low-resistivity glass electrodes were already reported [2, 3].

The response of the new prototype was first tested with cosmic rays and radioactive sources in the detector laboratory of the Hadron Physics Department of IFIN-HH. The prototype was operated at 2 x 5.5 kV high voltage with 95% $C_2F_4H_2$ + 5% SF_6 gas mixture. For this measurements the strip signals were processed by fast amplifiers/discriminators NINO chips [4], their differential output being converted by CAEN V1290A TDCs.

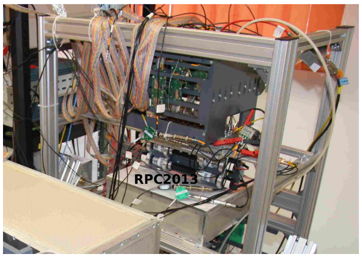

Figure 1: Cosmic ray experimental set-up

The experimental setup used in the cosmic ray test is presented in Fig. 1. The position along the strips, triggered by the plastic scintillators positioned above the detector across the strips, is presented in the left side of Fig. 2 as a function of strip number. The right part of Fig. 2 shows the correlation between the position along the strip and the position along the 10 cm length plastic scintillator, read out at both ends.

In-beam tests of this prototype were performed in a test campaign of the CBM-TOF Collaboration in October 2014 at GSI Darmstadt and in November 2014 at the CERN-PS accelerator, together with several other CBM subsystems.

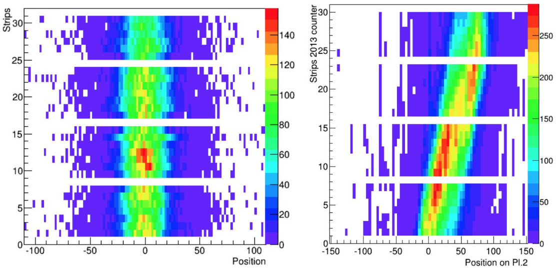

Figure 2: Cosmic-ray test. Left: position along the strip as function of strip number; right: correlation between position along the strips and position in the plastic scintillator.

In the CERN in-beam test the MGMSRPC signals were processed by the same electronic chain as in the cosmic ray test. As reference for the estimation of the time resolution, a plastic scintillator readout at both ends was used. Preliminary results show a time resolution of 52 ps using pure $C_2F_4H_2$ and of 61 ps using a gas mixture of 95% $C_2F_4H_2$ + 5% SF_6, after performing walk corrections and subtraction of the contribution of the reference counter (Fig. 3).

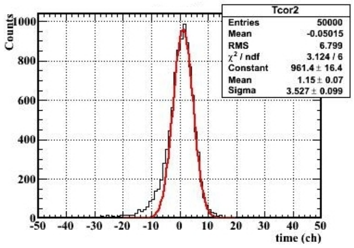

Figure 3: CERN in-beam test time spectrum using a gas mixture of 95% $C_2F_4H_2$ + 5% SF_6

The October 2014 in-beam test was focused on the compatibility with the new PADI8 FEE, intended to be used in the CBM-TOF wall. The MGMSRPC signals were converted by FPGA TDCs [5]. Data analysis is in progress.

References

[1] V. Aprodu *et al.*, CBM Progress Report 2013, p 79
[2] M. Petrovici *et al.*, JINST **7** (2012) P11003
[3] A. Bălăceanu *et al.*, CBM Progress Report 2013, p. 78
[4] F. Anghinolfi *et al.*, Nucl. Instrum. Meth. **A 533** (2004) 183
[5] J. Frühauf *et al.*, CBM Progress Report 2012, p. 71

---

* Work supported by EU-FP7/HP3 Grant No 283286, Romanian NASR/CAPACITATI-Modul III contract RO-FAIR F02 and NASR/NUCLEU Project PN09370103

Calorimeters

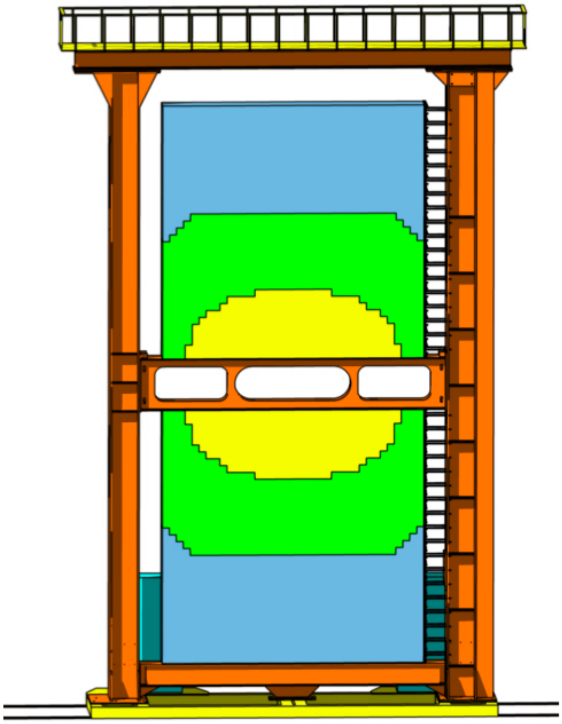

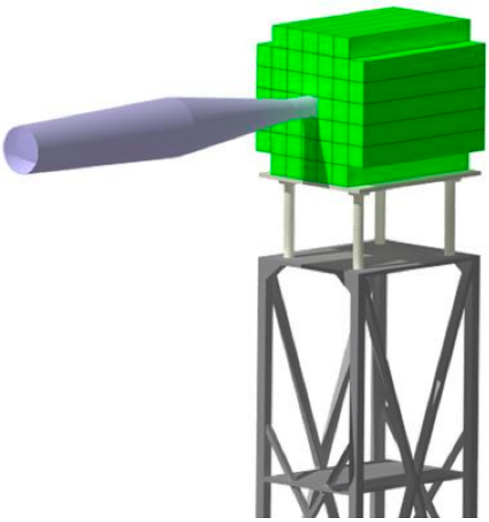

Calorimeter optimization for SIS100*

M. Prokudin, I. Korolko, and Yu. Zaitsev
ITEP, Moscow, Russia

One of the most challenging goals for the CBM experiment at SIS100 accelerator is the measurement of J/ψ meson production in Au+Au collisions at $10A$ GeV. At this energy, the production of J/ψ is sub-threshold (i. e., the invariant mass of the colliding nucleons is less than the sum of masses of the J/ψ meson and of a pair of baryons), and the multiplicity is as low as 1.7×10^{-7} according to model predictions. In this report, we investigate the possibility to measure $\mathrm{J}/\psi \to \mathrm{e}^+\mathrm{e}^-$ with the RICH and ECAL detectors.

It is assumed that the CBM detector setup at the SIS100 accelerator will consists of STS, magnet, RICH, TOF, calorimeter, PSD and, probably, several planes of TRD. It is proposed to place the TOF wall at 6–7 meter from the target because of the lower beam energy at SIS100 in comparison with SIS300. In this case, there is enough room for 1–2 TRD stations between RICH and TOF.

The calorimeter is located at 7.5 m downstream the target and consists of two halves. The size of each half is 408×192 cm^2 (34×16 modules). The distance between the halves is 216 cm. The cell size is 6×6 cm^2. In total, the calorimeter consists of 1,088 modules and 4,356 readout channels.

Calculations were performed using the April 2014 trunk version of CbmRoot. The setup consists of STS (version v13c), magnet, RICH (version v08a) and TOF (version v13-5b). Tracking was performed using STS only and electron identification with RICH and calorimeter. TOF information does not influence the quality of track reconstruction and electron identification, because TOF was optimized for hadron identification. So TOF in this simulations performs like dead material in front of the calorimeter.

5×10^5 central Au+Au events at $10A$ GeV, generated with UrQMD, were transported with GEANT and and reconstructed with the standard chain. 10^5 $\mathrm{J}/\psi \to \mathrm{e}^+\mathrm{e}^-$ decays embedded into background events were used as signal. The invariant mass of J/ψ was reconstructed using pairs of tracks with different charge. Each track was required to have a transverse momentum above 1 GeV/c. The χ^2 of the track fit into the primary vertex had to be less than 6. The identification quality of the track as an electron in RICH (RICHANN) had to be larger than 0.8, the χ^2 of calorimeter clusters less than 49 (because of occupancy), and the parameter $P_E > 0.01$ (criterion based on comparison of the energy deposition in the calorimeter cluster and momentum of the track taking into account the energy resolution of the calorimeter).

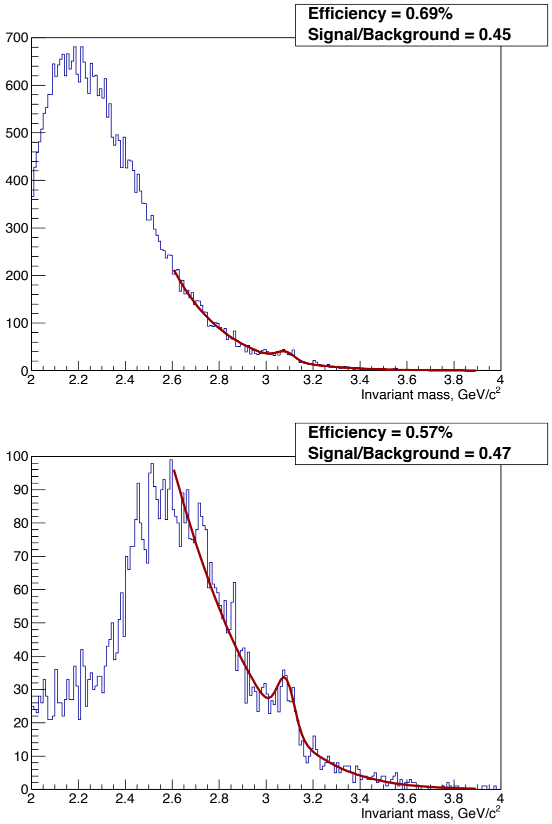

Figure 1: Invariant mass of e^+e^- pairs from $J/\psi \to e^+e^-$ in central Au+Au collisions at $10A$ GeV. The transverse momentum cut on each electron (positron) is 1.0 GeV/c (upper panel) and 1.2 GeV/c (lower panel).

The reconstruction efficiency for $\mathrm{J}/\psi \to \mathrm{e}^+\mathrm{e}^-$ was found to be 0.69%, with a signal to background ratio (taking into account multiplicity and branching ratio) of 0.45 (Fig. 1, upper panel). The invariant-mass peak is more pronounced if the p_t cut value on single tracks in increased, while the signal-to-background ratio stays approximately the same (Fig. 1, lower panel).

The reconstruction quality of J/ψ and χ_c mesons was also studied for proton-nucleus collisions. Here, 10^7 proton-carbon collisions modeled by the UrQMD generator were used for the combinatorial background. 50000 J/ψ modeled by the HSD generator were used for $\mathrm{J}/\psi \to \mathrm{e}^+\mathrm{e}^-$

---

* The work was carried out with the financial support of SAEC “Rosatom” and the Helmholtz Association.

decay reconstruction and χ_c background. Each J/ψ was embedded into a proton-carbon collision from UrQMD. This method of J/ψ background generation results in a conservative estimate of the background, because the total energy of all particles produced in the collision exceeds the energy of colliding system. 50000 χ_c modeled by the HSD generator were used as signal. Each signal χ_c was mixed with a proton-carbon collision modeled by UrQMD to estimate occupancy effects. The J/ψ multiplicity was predicted by the HSD generator to be 5.12×10^{-8}. The multiplicity of χ_c is 1.66×10^{-8} according to the HSD model.

The reconstruction of J/ψ was performed as described above. The J/$\psi \rightarrow$ e$^+$e$^-$ decay reconstruction efficiency was found to be 1.23%, with a signal-to-background ratio of more than 300.

The χ_c meson was reconstructed in the decay $\chi_c \rightarrow$ J/$\psi\,\gamma$. The invariant mass of e^+e^- pairs was required to be within $\pm 80\,\mathrm{MeV/c^2}$ from the book value of the J/ψ mass. The photon was reconstructed in the calorimeter. The χ^2 of the photon cluster had to be be less than 16, the energy of the reconstructed photon larger than 0.8 GeV. We obtained a reconstruction efficiency for the χ_c meson of 0.27%. Taking into account the branching ratios, we expect about 0.9 reconstructed χ_c mesons per day assuming 10^7 proton-carbon interactions per second. The background is dominated by the J/ψ. The signal-to-background ratio is 1.34 (Fig. 2). Taking into account the efficiency of χ_c meson reconstruction, a χ_c measurement will require several months of CBM running with 10^7 proton-carbon collisions per second.

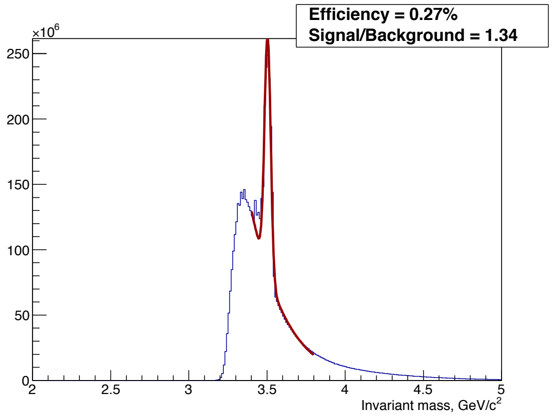

Figure 2: Invariant mass of χ_c meson reconstructed from $\chi_c \rightarrow$ J/$\psi\,\gamma$ decay in proton-carbon collisions. The energy of the incoming proton was 30 GeV.

To demonstrate the photon identification capabilities of the calorimeter, Tables 1-3 summarize efficiencies and signal-to-background ratios for γ, $\pi^0 \rightarrow \gamma\gamma$ and $\eta \rightarrow \gamma\gamma$. The efficiency for γ is defined as the ratio between reconstructed and reconstructable photons. The photon is reconstructable if $E_\gamma > 0.5$ GeV. The photon is reconstructed if the χ^2 of corresponding calorimeter cluster is less than 16.The π^0 and η are reconstructable if they decay in a pair of reconstructable photons. They are considered reconstructed if both decay photons are reconstructed and the pair has proper invariant mass.

Table 1: Reconstruction efficiency for photons

System	γ efficiency
p+C, 30 GeV	19.9%
Ni+Ni, 10A GeV	20.9%
Au+Au, 10A GeV	14.0%

Table 2: Reconstruction efficiency and signal-to-background ratio for π^0

System	efficiency	S / (S + B)
p+C, 30 GeV	6.09%	0.27
Ni+Ni, 10A GeV	7.56%	0.015
Au+Au, 10A GeV	4.6%	3.3×10^{-3}

Table 3: Reconstruction efficiency and signal-to-background ratio for η

System	efficiency	S / (S + B)
p+C, 30 GeV	3.6%	5.4×10^{-3}
Ni+Ni, 10A GeV	4.5%	2.2×10^{-4}
Au+Au, 10A GeV	2.6%	4.9×10^{-4}

Radiation hardness of the PSD APDs for the CBM experiment[*]

V. Kushpil[1], *A. Kugler*[1], *S. Kushpil*[1], *V. Mikhaylov*[1,2], *O. Svoboda*[1], *and P. Tlusty*[1]
[1]NPI of ASCR, Řež, Czech Republic; [2]CTU, Prague, Czech Republic

The projectile Spectator Detector (PSD) of the CBM experiment is designed to register forward spectator nucleons and fragments emitted in nucleus-nucleus collisions at very low polar angles. It will be used to determine the collision centrality and the reaction plane orientation.

The PSD is a fully compensating modular lead-scintillator calorimeter. The Avalanche Photo-Diodes (APD) are used to read out the scintillation light via wavelength shifting fibers. An important characteristic of the APD is its radiation hardness to a neutron fluxes of 10^{13} n/cm^2 which corresponds to two months of CBM experiment operation.

Two different APD samples, Ketek PM3375 and Zecotek MAPD-3N, were irradiated at the NPI Řež Cyclotron Facility by quasi-monoenergetic secondary neutron beam with energy of 35 MeV. A sample of Zecotek APD was irradiated with a dose of $3.4\pm0.2\ 10^{12}$ n/cm^2, while two samples of Ketek APDs were irradiated with $2.5\pm0.2\ 10^{12}$ n/cm^2. Doses were measured with a special PIN diode calibrated with a dose equivalent to 1 MeV neutron [1]. The operation temperature during the tests was kept at $22\pm0.5^\circ$ C.

The APD characteristics were measured before and after the irradiation. The Capacitance-Voltage (C-V), Current-Voltage (I-V), and Capacitance-Frequency (C-F) characteristics were studied using dedicated testing setup at NPI Řež [2,3]. After irradiation, the C-V technique showed significant decrease of hysteresis and fast but not complete self-annealing. The I-V curve revealed about 1000 times increase of dark current after irradiation. The C-F study showed significant increase of short-living traps in Silicon. The test results suggest an increase of internal APD noise, especially of the high frequency, which dependents on the amount of short-living traps in the APD volume.

Figures 1 (2) show the results of the Ketek (Zecotek) APD tests with LED and cosmic muons. Both APDs have a maximum signal (noise) amplitude of about $0.3-0.4$ V (0.05 V) which corresponds to $20-30$ ph.e (3 ph.e). After irradiation both APDs are unable to resolve single photons due to high noise levels. This is not critical for the PSD performance since there are at least 15 ph.e. produced in one PSD module already by a cosmic muon. The signal and noise peaks for irradiated Ketek APD are very close which makes it very difficult to separate signal from noise. On a contrary, signal and noise peaks for Zecotek APDs are well separated from each other, what allows reliable signal from noise separation even after irradiation.

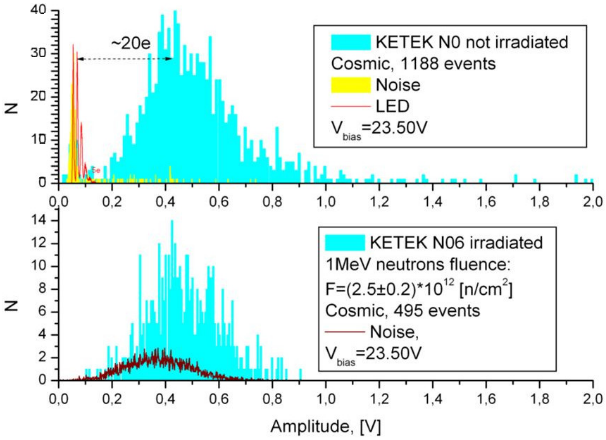

Figure 1: Test results with LED and cosmic muons of Ketek APD before (upper) and after (lower) irradiation.

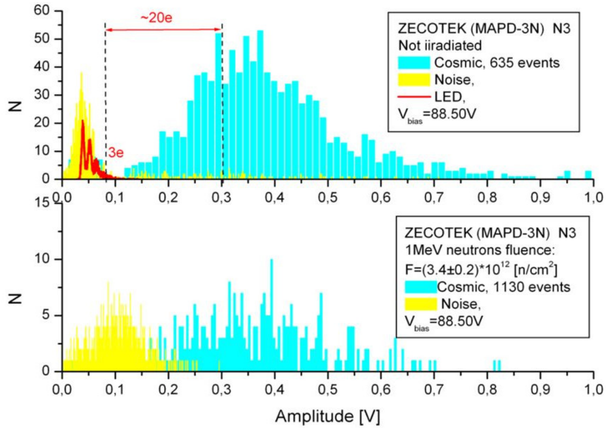

Figure 2: Test results with LED and cosmic muons of Zecotek APD before (upper) and after (lower) irradiation.

References

[1] V. Kushpil, S. Kushpil and Z. Huna, EPJ Web of Conferences 24 (2012) 07008.

[2] V. Kushpil, V. Mikhaylov, S. Kushpil, P. Tlusty, O. Svoboda, A. Kugler, doi:10.1016/j.nima.2014.11.071

[3] V. Kushpil, S. Kushpil, JINST 7 (2012) C01084.

---

[*] Work supported by the European Community FP7 – Capacities, contract HadronPhysics3 n°283286, LG12007 of the MECR and M100481202 of the ASCR grants, by project MSMT LG14004 of Cooperation Program between JINR and NPI in 2013-2014.

DAQ and Online Event Selection

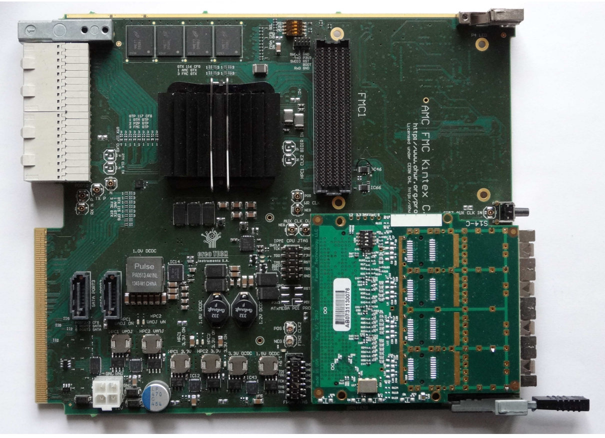

STS-HCTSP, an STS Hit & Control Transfer Synchronous Protocol*

K. Kasinski[1], *W. Zabolotny*[2], *J. Lehnert*[3], *C.J. Schmidt*[3], *W.F.J. Müller*[4], *and R. Szczygiel*[1]

[1]Department of Measurement and Electronics, AGH University of Science and Technology, Cracow, Poland; [2]Institute of Electronic Systems, Warsaw University of Technology, Warszawa, Poland; [3]GSI, Darmstadt, Germany; [4]FAIR, Darmstadt, Germany

The data communication between the STS detector readout chip (STSXYTERv2 [1]) and the Data Processing Board DPB [2] via the GBTx data combining ASIC [3] requires a robust and optimized protocol. The specific requirements and a preliminary protocol were published in [4]. During development of the STSXYTERv2 and DPB systems the protocol was further refined.

The protocol specification includes a detailed description of: frames' structure in both uplink & downlink directions, methodology for time-allocating hits and error correction, link synchronization procedures (enabling low-level reset, bit position alignment and optimal adjustment of data/clock delays) and specification of STSXYTERv2-specific registers.

The protocol is optimized for the data structure of the STS detector read-out ASIC but can be reused also in other systems. It maximizes the hit data throughput in the uplink (from ASIC to DPB) direction and data integrity in downlink (from DPB to ASIC) direction. The protocol is fully synchronous. Both uplink and downlink frames use 8b/10b encoding for DC-balance, and the frames in each direction have constant lengths and are transferred continuously.

Downlink frames support 4 request types: *no_op* (no operation), *WRaddr*, *WRdata*, *RDdata* (used for register access with 14-bit payload). A 4-bit chip address enables both individual chip addressing on FEBs and broadcasting messages. Since the full-path delay can reach 1 μs, multiple commands in-flight are supported by using a sequence number. Each register access command should be acknowledged on the uplink. The error correction scheme is the modified selective repeat ARQ, where not-acknowledged requests are retransmitted and register values can be verified by readback. The frames are 60-bit long (after 8b/10b encoding) and last 375 ns. They consist of K28.5 comma character, 4-bit chip address, 4-bit sequence number, 2-bit request type, 14-bit payload (address/data) and 16-bit CRC (0xC86C).

The uplink communication contains mainly hit data but also control responses and special information (e.g. alerts). After all optimizations a throughput of 9.41 MHit/s/link is achieved, which results in a 71% link occupancy for the design target of 250 khit/s/channel in a 5 links/ASIC configuration. The frames have constant length of 30 bits (after 8b/10b encoding), last 92.75 ns and support 5 frame types: dummy hit (equivalent of no_op, used to fill the link when idle and to transfer the timestamp MSB to keep the synchronization), hit (containing: 6-bit channel address, 5-bit ADC value, 10-bit timestamp LSBs, 1-bit error status marker), TS_MSB (used for data compression, transfers triplicated 6-bit timestamp MSBs and 4-bit 0x9 CRC), RDdata_ack (acknowledge message for RDdata command, contains 14-bit register content, 3-bit sequence number LSB and 4-bit 0x9 CRC), Ack (general acknowledge message with 2-bit ack-type: ack, nack, alert, 4-bit sequence number, 1-bit configuration parity, 4-bit status, 6-bit current timestamp, 4-bit 0x9 CRC).

The chip has built-in mechanisms for monitoring the link itself and the in-ASIC data flow. Multiple alert states can be configured and generated. The DPB is informed on the alert status by ack frames or error status markers in hit frames. Further information on alerts and means to manage them are foreseen in the ASIC's address space.

The link synchronization procedure is used for tuning the data/clock delays in the GBTx ASIC and also for alignment of frame and bit positions. Even though during regular operation the comma characters are periodically transferred, they are not used for on-line synchronization but only for link monitoring. During link synchronization, special 20-bit characters beyond 8b/10b code (SOS: start of sync, EOS: end of sync) are used together with K.28.1 and K.28.5 characters. SOS and EOS can be easily detected in any state of the link and can be used to remotely reset the chip and communication. SOS triggers the procedure. First, using a SOS character, the clock/downlink data phases are adjusted, then K.28.1 is used to adjust the uplink data phases. The procedure is ended by EOS character. Finally bit and frame alignment is made on the first comma characters received through the links during regular operation.

References

[1] K. Kasinski *et al.*, *Towards the STS-XYTERv2, a silicon strip detector readout chip for the STS*, this report

[2] W. Zabolotny *et al.*, *Towards the Data Processing Boards for the CBM experiment*, this report

[3] J. Lehnert *et al.*, *The GBT based readout concept for the CBM Silicon Tracking System*, this report

[4] K. Kasiński, W. Zabołotny and R. Szczygieł, Proc. SPIE Int. Soc. Opt. Eng. **9290** (2014) 929028

---

* Work supported by GSI

Towards the Data Processing Boards for the CBM experiment*

W. Zabołotny, G. Kasprowicz, A. Byszuk, M. Gumiński, K. Poźniak, and R. Romaniuk
Institute of Electronic Systems, Warsaw University of Technology, Warszawa, Poland

The Data Processing Boards (DPB) [1] are an important part of the CBM readout and detector control systems, providing concentration (possibly combined with local preprocessing) of readout data before they are sent to the First Level Event Selector (FLES). Additionally, DPBs should provide fast and slow control for the Front End Electronics (FEE) and distribute the reference clock and time-critical information like synchronization and flow control messages from the Timing and Flow Control system (TFC).

To allow testing of different possible implementations of these functionalities, the versatile prototyping Open Hardware platform AMC FMC Carrier Kintex (AFCK) [2] was created. The first version of AFCK is shown in Fig. 1.

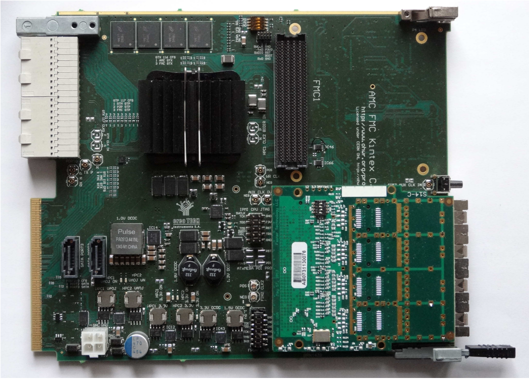

Figure 1: The AFCK board with an FMC card with 4 SFP+ cages connected to the FMC2 connector

The AFCK board may be used in an MTCA crate or in stand-alone mode. The board is equipped with the XC7K325T FFG900 FPGA, containing 16 high-speed GTX transceivers, which can be connected to 2 FMC slots (4 GTXs to each) or to the RTM connector. Another 8 GTXs may be connected to the MTCA backplane ports 0 to 11. This solution allows to test different transceivers mounted on FMC boards, without modifying the AFCK board itself. AFCK is also equipped with a flexible clocking system allowing it to operate with gigabit links of different speed and also to recover a jitter cleaned clock signal from a high-speed receiver. The board is also equipped with 2 GB of DDR3 SDRAM which may be used to store the processed data, but also for debugging purposes. These resources make the AFCK board a suitable platform for the development of data concentration and preprocessing algorithms.

A first series of AFCK boards was manufactured, and functionality tests were performed. High-speed communication capabilities were tested with standard IBERT tests provided by Xilinx. Stable 10 Gbps transmission was achieved via GTXs connected to the FMC1 slot, while 5 Gbps transmission was possible via GTXs connected to the FMC2 and RTM (10 Gbps in FMC2 should be achievable in the next revision of the board).

A few basic IP core blocks, suitable for use in the prototype DPB firmware, were developed or ported and tested. These include the IPbus [3] core allowing to control the board via a 1 Gbps Ethernet interface and the GBT-FPGA [4] core used to communicate with GBTx ASICs. The Ethernet transmission of readout data at 10 Gbps rate was tested using the FADE IP core and protocol [5]. Stable transmission of 4x10 Gbps data streams was achieved using 4 SFP+ transceivers plugged in FMC board connected to FMC1. Porting of the White Rabbit [6] IP core to the AFCK board is currently in progress.

The results of tests performed with the AFCK board will be used to design a cost-optimized version of the DPB prototype.

Verification of the STS-XYTER communication protocol developed in collaboration with GSI and AGH [7] was performed in simulations and in hardware, using the KC705 evaluation board. The IPbus accessible controller, allowing to synchronize communication with the model of STS-XYTER (provided by the AGH team) and to control it, was developed and successfully tested. To achieve that, a dedicated environment for hardware-software co-simulation of IPbus-connected IP cores was prepared.

Verified blocks used in the controller will be used for the development of prototype DPB firmware, after porting to the AFCK board.

References

[1] W. Zabołotny and G. Kasprowicz, Proc. SPIE Phot. Appl. **9290** (2014) 929023

[2] `www.ohwr.org/projects/afck/wiki`

[3] `svnweb.cern.ch/trac/cactus`

[4] `espace.cern.ch/GBT-Project/GBT-FPGA/default.aspx`

[5] `opencores.org/project,fade_ether_protocol`

[6] `www.ohwr.org/projects/white-rabbit/wiki`

[7] K. Kasiński, W. Zabołotny and R. Szczygieł, Proc. SPIE Int. Soc. Opt. Eng. **9290** (2014) 929028

---

* Work partially supported by GSI

PCIe based test setup for the CERN GBT-FPGA core*

S. Sau[1], *S. Mandal*[2], *J. Saini*[2], *A. Chakrabarti*[1], *S. Pal*[2], *and S. Chattopadhyay*[2]
[1]University of Calcutta, Kolkata, India; [2]Variable Energy Cyclotron Centre, Kolkata, India

For efficient data aggregation from the MUCH-FEE, the CERN GBTx ASIC [1] is planned to be used as a bridge to the Data Acquisition (DAQ) system. GBTx will take the data from the STS-XYTER (MUCH-XYTER) through E-links and send it over an optical link using the GBT protocol to the FPGA based DPB layer, where CERN GBT-FPGA cores are used to implement the GBT protocol.

The GBT-FPGA core can also be used to implement the GBTx ASIC functionality with an FPGA. This is useful for the initial debug and test phase before the ASIC becomes widely available, but also for sites where the GBTx ASIC cannot be deployed because of export restrictions. As a first step of a GBTx emulator development, a PCIe-based test setup for the CERN GBT-FPGA core was developed (Fig. 1).

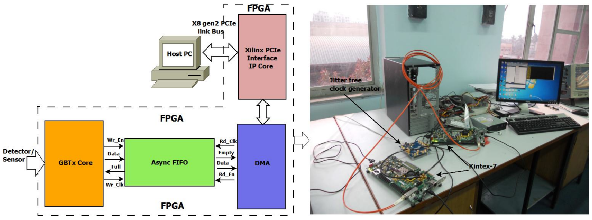

Figure 1: Test setup in VECC

A simplified diagram of the blocks within the GBT protocol stack used to generate the standard frame for optical communication is shown in Fig. 2.

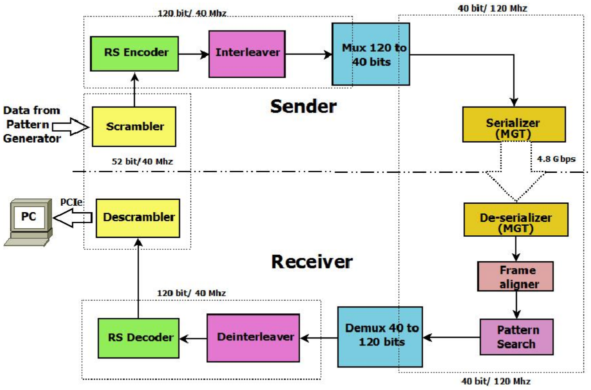

Figure 2: Test configuration setup blocks

Here for testing purposes 84-bit data (taking slow control field into consideration) are taken from a pattern generator and given as input to the scrambler. Later, the pattern generator will be replaced by an E-port interface which receives data from the STS-XYTER FEE ASICs. The Reed-solomon encoder block will take these 84-bit data along with a 4-bit header and give 120-bit output. The interleaver just reorders the data to reduce the effect of error bursts. A gearbox is used to divide the 120-bit data frame into three words with 40-bits width. The GBT frame sent to the transmitter consists of four bit header, 84-bit data (80-bit data with 4 bit for slow control), and 32-bit data for forward error correction. The GBT frame is shown in Fig. 3 (including a slow control field into the data field).

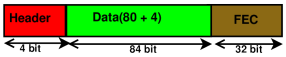

Figure 3: GBTx frame format

The GBT receiver side performs just opposite jobs like deinterleaving, decoding and descrambling. Frame aligner and pattern search blocks in the receiver side will be used to detect the header properly. In the latency-optimized mode another two blocks, frame clock phase aligner and automatic phase aligner, will come into play.

For testing of the GBT-FPGA core a KC705 board is used. A fabric clock (156.25 MHz) is generated internally from a Si570 3.3V LVDS I2C Programmable Oscillator. The MGT reference clock has to be a very low jitter clock and is generated by a jitter cleaned clock source using a Texas instruments CDCE62005. The GBT-FPGA is tested in standard and in latency-optimized mode.

A PCIe core is connected with the GBT-FPGA core on the receive side to send the receive data to a PC through one asynchronous FIFO and a scatter gather direct memory access (SGDMA) controller. The write frequency of the FIFO is 40 MHz, the read frequency is 125 MHz (because the PCIe core is running with 125 MHz frequency). SGDMA is used to transfer the data from board to PC without processor interruption. To capture the data we wrote a C program using Windows SDK. The data are written to file which can be accessed later. In the future the PCIe core will be removed and the GBTx emulator will be interfaced with the Data Processing Board (DPB).

References

[1] P. Moreira, J. Christiansen and K. Wyllie, *The GBTx Link Interface Asic*, Draft v1.7, October 2011

---

* Supported by BI-IFCC, DST and DAE, Govt. of India

High-level dataflow description of FPGA firmware components for online data preprocessing[*]

H. Engel and U. Kebschull
IRI, Goethe-Universität, Frankfurt, Germany

FPGA firmware is commonly described with low-level hardware description languages like VHDL or Verilog. With FPGAs getting bigger and faster, they become more and more suitable to also perform complex data processing algorithms. Describing complex algorithms with VHDL or Verilog creates code that is hard to maintain and makes it almost impossible to exploit the full capabilities of recent FPGAs. Frameworks are available that allow to describe hardware algorithms on a dataflow level. An existing cluster finding algorithm was ported from VHDL to dataflow description, compared against the original VHDL implementation and tested in hardware.

High energy physics detector readout chains rely widely on Field Programmable Gate Arrays (FPGAs) because of their flexibility and processing capabilities. The functional description of these FPGAs is usually realized with hardware description languages like VHDL or Verilog. These languages give fine control over the low level logic blocks inside the FPGAs like Lookup-Tables and Flip-Flops. The number of logic resources available in FPGAs has increased significantly over the last years, and the growth is expected to continue.

The algorithm investigated in this work is the FastClusterFinder [1] that was used in the High-Level-Trigger Read-Out Receiver Card at ALICE in the read-out of the Time Projection Chamber during LHC Run1. This algorithm was implemented in plain VHDL and was developed during a PhD thesis. The VHDL implementation is a rather complex design because of its flow control structures and the number of fixed point and floating point arithmetics. Comparing the size of this implementation with the number of resources available in the most recent generations of FPGAs makes it obvious that the possibilities of new devices cannot be exploited effectively with low-level hardware description languages.

The same algorithm was re-implemented in a dataflow description language from Maxeler Technologies [2]. This language uses a Java dialect to describe hardware on an algorithmic level. The compiler resolves the description into a dataflow graph, adjusts latencies, handles data transport, creates vendor specific IP cores and translates the description back into VHDL. The resulting files are then run through the regular vendor tools to create an FPGA configuration file.

The FPGA resource usage of the VHDL and the dataflow implementations are quite comparable as shown in Table 1.

Table 1: FPGA resource usage comparison of VHDL and two dataflow implementations

Resource Usage	VHDL	Dataflow 1	Dataflow 2
Flip-Flops	∼5200	∼4800	∼6000
Lookup Tables	∼4600	∼4900	∼5100
BRAMs	19	19	21
DSPs	8	8	8
Min. clock period	4.4 ns	4.1 ns	3.4 ns

The dataflow language allows to control the amount of pipelining to be used for the individual processing steps by specifying a pipelining factor. Column *Dataflow 1* shows the results with a pipelining factor of 0.5, which leads to a timing performance similar to the original VHDL implementation. Column *Dataflow 2* uses the maximum pipelining factor of 1.0 and creates a design that can be run at higher clock frequencies. The code base is the same for both pipelining settings and is significantly smaller and much easier to maintain than the VHDL implementation. Trying out different pipelining levels in VHDL could easily take several weeks alone.

The dataflow implementation was tested in a Max3 Dataflow Engine containing a Virtex-6 FPGA and using the data transport framework provided by Maxeler. Event data are written into the FPGA with the Maxeler software API, and the processed results are read back in the same way. The output of the algorithm was compared to that of the VHDL implementation using simulated and real detector data from LHC Run1.

A single instance of the cluster finder implementation from the dataflow description could also be extracted from the dataflow framework and ported to the C-RORC [3], which is used for the read-out of detector data in ALICE and ATLAS for LHC Run2. This allows to create netlists from dataflow implementations and integrate these cores into existing firmware environments. A deeper investigation on the performance of this integration is ongoing.

References

[1] T. Alt and V. Lindenstruth, GSI Scientific Report 2009, p. 283

[2] Maxeler Technologies, *Programming MPC Systems*, White Paper, June 2013

[3] A. Borga *et al.*, JINST **10** (2015) C02022

---

[*] Work supported by HGS-HIRe and HIC4FAIR

A feature extraction framework for automatic FPGA firmware generation*

C. García Chávez and U. Kebschull
IRI, Goethe-Universität, Frankfurt, Germany

Introduction

The design and development of a FPGA real-time data processing platform is a common task in every high-energy particle physics experiment. In most cases, it is a time consuming task that might take up to a couple of years to be developed. Despite the fact that most of the used algorithms in online data processing are very well known, for different hardware platforms and data structures specific implementation of those algorithms is required. In order to overcome those common problems, a framework for automatic firmware generation was developed, allowing the implementation of common algorithms for feature extraction. A brief overview of the framework as well as its experimental application in the Online Feature Extraction of the CBM Transition Radiation Detector (TRD) experiment will be presented here.

Feature Extraction Framework Overview

The feature extraction framework is presented as a graphical user interface, where a user is able to configure a FPGA hardware platform based purely on its feature extraction parameters. Commonly used processing algorithms such as peak finding, center-of-gravity calculation, time over threshold and cluster finding are implemented as processing cores inside the framework. The general structure of the framework is shown in Fig. 1. The framework user sets the configuration options for all the previously mentioned algorithms by means of a graphical user interface. After the configurations are set and a project is created, an autonomous compilation process is started where first a source code file written in a domain-specific language is automatically created, which serves as input for the framework. A parser then analyses the source code file and populates a semantic model, which from a technical point of view is hardware independent. The framework synthesizer takes the semantic model and generates an intermediate representation called the “Hardware Model”. The “Hardware Model” is a hardware-dependent description of a feature extraction platform for a given set of configurations (e.g., a specific FPGA device, development board and processing algorithms). From this point, the framework generator is able to use this representation to generate a set of Hardware Description Language (HDL) sources written in VHDL together with vendor-specific project files to perform a HDL synthesis by third-party tools [1]. As a result, a bitfile is generated to configure the target FPGA platform. Optionally, a validation platform can be used to communicate the framework to the FPGA development platform in order to test the correct implementation of the processing algorithms on hardware.

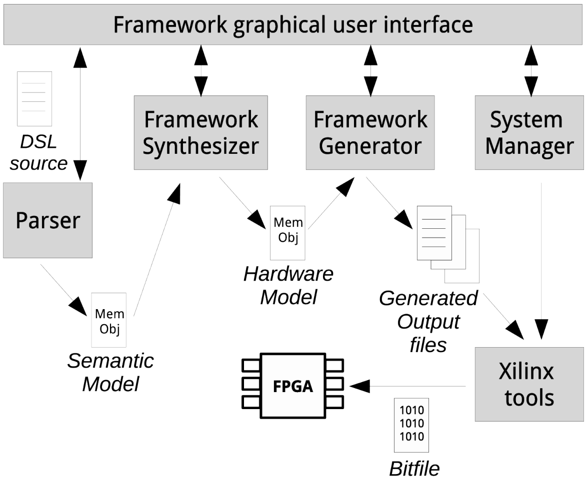

Figure 1: Framework structure

Current Status

The performance of the presented feature extraction framework is currently being tested in the CBM Transition Radiation Detector (TRD). The processing algorithms used for feature extraction were previously tested during a beam test as mentioned in [2, 3]. Current results show that there is no significant difference in FPGA resource consumption between hand-written code versus automatic-generated code; however, a significant improvement on design time is achieved when using the presented framework for automatic firmware generation.

References

[1] Xilinx Inc., *ISE Design Suite*, `http://www.xilinx.com`

[2] C. García Chávez and U. Kebschull, CBM Progress Report 2013, Darmstadt 2014, p. 74

[3] C. Bergmann *et al.*, *Common CBM beam test of the RICH, TRD and TOF subsystems at the CERN PS T9 beam line in 2014*, this report

---

* Work supported by BMBF No. 05P12RFFCM

CBM FLES input interface developments*

D. Hutter, J. de Cuveland, and V. Lindenstruth
FIAS, Goethe-Universität, Frankfurt, Germany

The First-level Event Selector (FLES) is the central event selection system in the CBM experiment. Its task is to select data for storage based on online analyses including a complete event reconstruction. To do so, the FLES timeslice building has to combine data from all input links to time intervals and distribute them to the compute nodes. To allow for efficient timeslice building, detector data streams are partitioned into microslices prior to combining them. Microslices are specialized containers covering a constant timeframe of real time, which is the same for all subsystems. This allows data-agnostic, subsystem-independent timeslice building. The partitioning will be performed by the Data Processing Boards (DPB) as last stage of the read-out tree which has to contain subsystem-specific components.

The FLES input interface is realized by a custom FPGA PCIe card, the FLES Interface Board (FLIB). Its purpose is to provides the optical interface to the DPBs as well as the interface to the FLES input nodes. The current development is based on the commercial HTG-K7-PCIE board form Hitech Global. It features a Xilinx Kintex-7 FPGA, a 8x PCIe 2.0 interface, up to eight 10 GBit/s links and optionally 8 GB of DDR3 memory.

The FPGA design includes the protocol for receiving microslices, a pre-processing engine preparing microslices for timeslice building and a custom full off-load DMA engine. Once configured the DMA engine is capable of constantly transferring microslices and metadata to the PCs memory without involving the host CPU. The only task the CPU needs to perform is to occasionally acknowledge processed data segments to allow reusing buffer space. A measurement of the DMA performance for one to four 10 Gbit/s microslice streams is given in Fig. 1. For up to three steams, data are transmitted at full input speed. For four streams, the input data rate exceeds the available PCIe bandwidth. The achieved maximum data rate is 3345 MB/s, which matches the absolute maximum PCIe data rate for the given configuration.

For demonstration and testing the input interface concept in real-live applications, the FLIB and flesnet software were used for read-out in the CERN-PS 2014 testbeam at T9 beamline. In contrast to the final system, current setups lack the DPB layer and do not support the creation of microslices. A specialized FLIB prototype firmware therefore includes a mockup of the DPB design and is capable of directly receiving CBMNet messages as delivered by the CBM front-end electronics. Simplified microslices are generated inside the FLIB and subsequently handled in the same way as foreseen for the final setup. Thus the setup is capable of delivering fully built timeslices to any given consumer. In case of the testbeam, timeslices were written to disk and simultaneously published via a ZMQ socket to CBMroot clients for front-end calibration and online monitoring. In addition, the firmware and software include support for front-end configuration and synchronization over CBMnet which is accessible via a ZMQ interface or from within CBMroot.

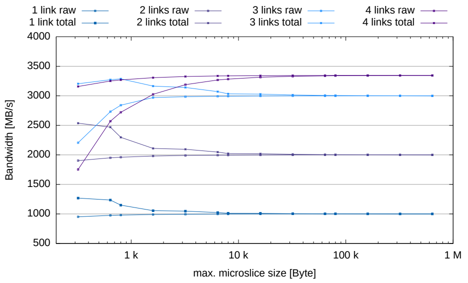

Figure 1: FLIB read-out bandwidth

During the testbeam a single FLIB in conjunction with the flesnet software was successfully used to read-out up to six detector setups in different configurations. Three different flavors of data sources were employed: Syscore 2, Syscore 3 and TRB boards.

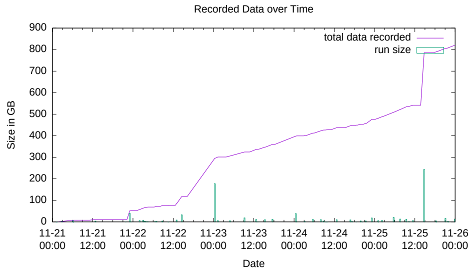

Figure 2: Recorded testbeam data over time

Figure 2 shows an overview over five days of data taking. In total 888 GB of data in 84 runs were written to disk without any major read-out related problems. Online data consistency checks and first offline analysis did not reveal any issues with the data.

To support future setups including DPBs, the FLES interface module is currently under development. It will provide a 10 GBit/s link transferring microslices to the FLIB, thus enabling full-featured microslice creation on the DPBs.

---

* Work supported by BMBF (05P12RFFCP) and HIC for FAIR

CBM First-level Event Selector data management developments[*]

H. Hartmann, J. de Cuveland, and V. Lindenstruth
FIAS, Goethe-Universität, Frankfurt, Germany

The First-level Event Selector (FLES) is a high-performance computing cluster functioning as the central event selection system in the CBM experiment. It combines data from a large number of input links to time intervals and distributes them to the compute nodes via a high-performance network. Simultaneously, the FLES carries out online analyses and complete event reconstruction on the data. Data rates at this point are expected to exceed 1 TByte/s. The FLES system will consist on one hand of a scalable supercomputer with custom FPGA-based input interface cards and a fast event-building network and will be constructed largely from standard components. On the other hand special developed software allowing to process the incoming data in real time builds up the FLES.

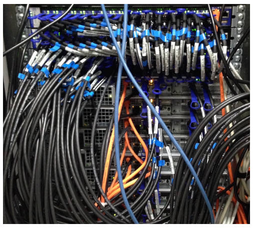

Figure 1: Upgraded FLES demonstrator system

A small-scale, highly customizable platform, the Micro-FLES cluster, was installed at GSI. Eight identical compute nodes provide a total of 192 logic cores and 512 GB memory plus one head node for infrastructural services. This test system enables studies on the development of the FLES such as elaborating performant software for timeslice building.

A *timeslice* is the fundamental data structure managing access to all detector raw data of a given time interval. In addition to existing timeslice-building prototype software based on InfiniBand Verbs, investigations of a more high-level interface to the network hardware were performed using MPI. For this purpose a specialized micro benchmark test suite was developed simulating the FLES timeslice building use case. Benchmark results for simultaneous data transfer on the Micro-FLES are displayed in Fig 2 (top). When communication is established only between three nodes, MPI's performance compares to the maximum data rate of point to point communication for Infiniband Verbs (green curve) on the Infiniband-FDR network. However, the data rate decreases by 15% when all eight nodes of the Micro-Fles are participating in an any-to-any communication. Further tests on bigger compute clusters are necessary to evaluate the achievable data rates for MPI on a big scale and are currently under investigation.

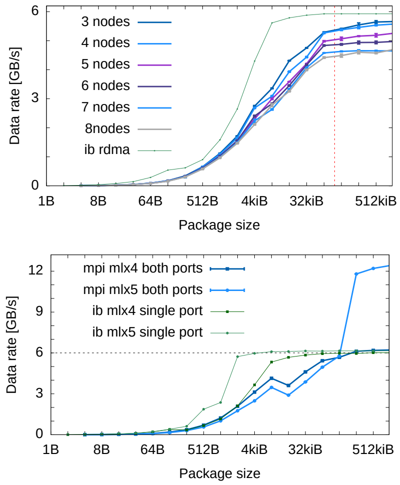

Figure 2: Top: MPI benchmark on the Micro-FLES. Bottom: perfomance tests for the Micro-FLES2.

In 2014 the FLES demonstrator system was significantly upgraded to the Micro-FLES2. First, the Micro-FLES2 was equipped with the latest Mellanox dual Connect-IB HCAs (mlx5), in addition to the existing Mellanox dual ConnectX-3 cards (mlx4). Overall, the new cards are faster than the old ones as shown in Fig. 2 (bottom). A data rate of 6 GB/s can already be achieved using only one of the four ports. Furthermore, the new cards feature a 16x PCIe 3.0 interface and therefore allow to saturate the full bandwidth of both ports. An accumulated data rate of 18 GB/s can be achieved utilizing all Infiniband ports. With this first upgrade the Micro-FLES2 can send data from node to node three times as fast as before (e.g., 18 GB/s instead of 6 GB/s). The improved performance is essential for the development of timeslice-building software.

Secondly, two further Mellanox SX6036 36-port 56Gb/s switches were installed in order to realize different network setups such as a fat tree. This helps investigating routing issues in the development of software when distributing the incoming data. The previous existing switch was connected with full bidirectional bandwidth to both of the new switches making them leaves of a fat tree. All first ports of mlx4 and mlx5 for each node were connected to leaf-switch1 and all second ports to leaf-switch2. Using this setup, the network structure and blocking ratio in case of a fat tree can be dynamically configured via the provided internet interface of the switches. The upgraded Micro-FLES2 provides better performance and a higher flexibility in testing different scenarios, allowing to evaluate a greater variety of possibilities for the final system – the FLES.

---

[*] Work supported by BMBF (05P12RFFCP) and HIC for FAIR

Maintenance of read-out controller firmwares for GET4 and n-XYTER chips*

S. Manz and U. Kebschull
IRI, Goethe-Universität, Frankfurt, Germany

Introduction

The read-out controller firmwares for the n-XYTER and GET4 chips required some substantial adaptions to keep up with the overall progress of CBM DAQ developments in 2014. In case of the read-out controller for the GET4 chips, the following points needed to be addressed:

- Backport of firmware with CBMNet v2 [1] to the SysCore v2 board,
- putting into service the SysCore v3 [2] firmware for the new GET4 prototypes (GET4 v1.23 [3]),
- implement netlist-based build flow for GET4 module, Auxiliary module and USB module,
- update CBMNet from v2 to v3 for all involved GET4 firmwares (SysCore v2 and v3).

In case of the read-out controller for the n-XYTER chips, the following actions had to be taken:

- Provide SysCore v2 firmware with CBMNet v2,
- Update CBMNet from v2 to v3 for n-XYTER firmwares.

Read-Out firmware for GET4 chips

Backport of firmware for SysCore v2 boards. A read-out firmware for the GET4 v1.23 chips that can be connected to a CBMNet v2 network was only available for the SysCore v3 board. As there was no GET4 v1.23 adapter hardware for the SysCore v3 available at the beginning of the year, the read-out based on legacy SysCore v2 hardware was desired. This was achieved by porting the existing SysCore v3 firmware back to the SysCore v2 board.

SysCore v3 firmware to read-out the GET4 v1.23. When the new GET4 v1.23 hardware for the SysCore v3 became available in autumn, the firmware had to be put into service. It now runs stably with this new hardware and is planned to be used in the next ToF beam time at CERN end of February 2015.

Netlist based build-flow. For better compatibility with the CBM build server [4], the build flow of the GET4 related firmwares was improved to first build netlists for each module that then can be put together to a full firmware. This allows a better and cleaner distribution of responsibilities among the developers of the different modules. The modules that were adapted are: the module to interface GET4 chips, the module with basic functionality (Auxiliary module), and the module to transport data via USB. One external module that implemented a comparable netlist build flow is used as well, the CBMNet transport module.

Update CBMNet to version 3. During preparation for the autumn beam times, CBMNet was updated from v2 to v3. This update was also integrated into the read-out controller firmwares for the GET4 chips.

Read-Out firmware for n-XYTER chips

Provide CBMNet version 2 firmware. The read-out controller firmware for the n-XYTER chip was only available for CBMNet v1 so far, while read-out for the STS-XYTER and the SPADIC chips relied on CBMNet v2. For the 2014 beam times it was foreseen to use the nXYTER chip in the same setup as STS-XYTERs and SPADICs. The n-XYTER was planned as a reference system and also to read-out the fiber hodoscopes. As a downgrade of STS-XYTER and SPADIC setup to CBMNet v1 was not possible, the n-XYTER read-out had to be updated to CBMNet v2.

Update CBMNet to version 3. The read-out controller firmware for the n-XYTER chips needed the same update as the above-mentioned update to CBMNet v3 in case of GET4 read-out.

References

[1] F. Lemke, S. Schatral and U. Brüning, CBM Progress Report 2013, Darmstadt 2014, p. 86

[2] J. Gebelein *et al.*, CBM Progress Report 2012, Darmstadt 2013, p. 87

[3] H. Flemming and H. Deppe, GSI Scientific Report 2013, Darmstadt 2014, p. 382

[4] J. de Cuveland and V. Lindenstruth, priv. comm.

---

* Work supported by BMBF No. 06HD9123I

CBM Control System Board with TMS570 micro-controller

J. A. Lucio Martínez and U. Kebschull
IRI, Goethe-Universität, Frankfurt, Germany

The Control System

A control system board is being designed to be used as an EPICS IOC (Input Output Controller) for the CBM experiment.

The Micro-controller: TMS570

The selected micro-controller is the cheap TMS570LS series for automotive safety-critical applications. It posseses interfaces capabilities such as Flex Ray, CAN, LIN and further communication interfaces [1]. The disadvantage of this micro-controller is that it is typically programmed by a very specific TI compiler.

This micro-controller implements ECC on SRAM. Furthermore, the CPU and memory contain Built In Self Test logic (BIST) which is normally used in harsh environments to let the system check it's own functionality. Such a design technique is called DFT (Design For Testing). Manufacturers use these kind of design methods to comply with the failure acceptance standards, normally issued for the automotive, medical, space and aviation industry. The Cortex R4 architecture of this processor also implies that the dual CPUs run in lock step (Dual Core Lock Step, DCLS); thus both CPUs run the same set of instructions in parallel to be able to detect errors with redundancy.

With DCLS an SEU (Single Event Upset) can be detected. According to [2], the ARM Cortex R4 supports that *all caches and TCMs (Tightly Coupled Memories) can be protected by ECC or parity against SEUs*. This is the case for the TMS570, which has ECC implemented on TCM RAM and parity check for external SDRAM [1]. It is also important to correct such errors. Fortunately, if one refers to the Cortex R4 data sheet one finds out that: *All parity or ECC errors detected on instruction cache reads are correctable* [3].

RTEMS for TMS570

The system will operate with the RTEMS Operating System as it supports EPICS applications, has a free open source license and has real time OS capabilities [4]. The RTEMS BSP (Board Support Package) for TMS570 is still being developed. Fortunately, the last version works, and the tests applications run successfully as shown in Fig. 1. The actual problem of this BSP is that there is still no network driver, but we are adapting an open source driver of a similar board to it. The TMS570 BSP developers used OpenOCD to program the micro-controller with a SDRAM initializing code and bootstrap it by writing the RTEMS executable binary in the SDRAM [5] (compiled with open source gcc). The SDRAM initializing C code is generated by a TI program, but the license allows the users to use and distribute it with minor conditions.

EPICS

EPICS is an Experimental Physics and Industrial Control System. It is structured in OPI (Operator Interface) clients and IOC (Input/Output Controller) servers. The IOCs control devices via a wide range of field busses. A basic IOC was compiled successfully for the TMS570 on RTEMS, but no setups were tested yet because the network driver of the operative system for the board is necessary. In order to test the software before building the Control System Board, the TMS570 Hardware Development Kit (HDK) is currently being used.

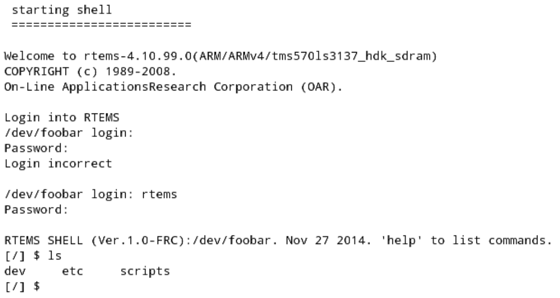

```
 starting shell
 =========================

Welcome to rtems-4.10.99.0(ARM/ARMv4/tms570ls3137_hdk_sdram)
COPYRIGHT (c) 1989-2008.
On-Line ApplicationsResearch Corporation (OAR).

Login into RTEMS
/dev/foobar login:
Password:
Login incorrect

/dev/foobar login: rtems
Password:

RTEMS SHELL (Ver.1.0-FRC):/dev/foobar. Nov 27 2014. 'help' to list commands.
[/] $ ls
dev     etc     scripts
[/] $
```

Figure 1: RTEMS running on TMS570 HDK

References

[1] Texas Instruments, *TMS570 Data sheet*, `www.ti.com/lit/ds/symlink/tms570ls20216.pdf`

[2] M. M. Ghahroodi, E. Ozer and D. Bull, *SEU and SET-tolerant ARM Cortex-R4 CPU for Space and Avionics Applications*, `www.median-project.eu/wp-content/uploads/median2013_submission_5.pdf`

[3] ARM, *CortexTM-R4 and Cortex-R4F Revision: r1p3 Technical Reference Manual*, `infocenter.arm.com`

[4] On-Line Applications Research Corporation (OAR), *RTEMS C User's Guide*, `docs.rtems.org/doc-current/share/rtems/pdf/c_user.pdf`

[5] RTEMS Database, *TMS570 RTEMS BSP*, `devel.rtems.org/wiki/TBR/BSP/Tms570`

Implementation and test of a flash-free configuration upset mitigation strategy for the CBM ToF ROB FPGA[*]

A. Oancea, C. Stüllein, J. Gebelein, S. Manz, and U. Kebschull
IRI, Goethe-Universität, Frankfurt, Germany

The Read-Out Board (ROB) for the CBM ToF readout chain is the connection between the front-end electronics (FEE) and data acquisition (DAQ) and processing further downstream. As such, unlike the rest of the devices in the DAQ chain, it is situated fairly close to the FEE and is therefore exposed to radiation. The ROB requires an FPGA for simple data pre-filtering and compression, the radiation-caused configuration memory upsets of which need to be mitigated. So far, mitigation approaches always included a local memory storing the golden copy of the configuration memory and a respective controller, e.g. a local Flash memory and Actel FPGA in the SysCore v.2.x and SysCore v3.x [1, 2]. On the one hand, Flash technology has a considerably lower Total Ionizing Dose limit than SRAM based FPGAs, and on the other hand, precautions for upsets in the user logic of the Actel FPGA still need to be taken. Therefore, a new approach without a local memory or controller exposed to radiation was developed for the ROB.

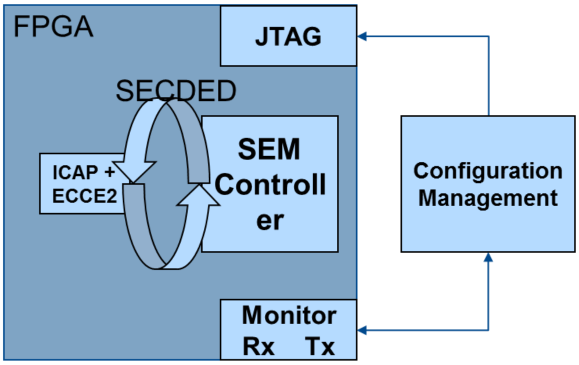

Figure 1: Conceptual overview of the mitigation approach. The SEM Controller is capable of correcting single frame upsets and reporting dobule frame upsets (SECDED), as well as reporting a need for a complete reset in case of multiple upsets per frame.

The developed approach uses the Soft Error Mitigation Xilinx IP Core (SEM Controller), which is able to autonomously detect and correct Single-Bit Upsets (SBUs), and report on Multiple-Bit Upsets (MBUs) (Fig. 1). If a configuration frame has two upsets, the affected frame is reported to a configuration management entity that can be on another level of the DAQ chain. From there, the affected frame can be dynamically overwritten via JTAG without resetting the FPGA. A reset is only necessary when more than two upsets occur in the same frame, since the SEM Controller cannot identify the location of the upsets anymore. The radiation-hardened GBTx, which will be used in the final setup, provides remote JTAG and GPIO connections through the GBT-SCA, and therefore a local controller is no longer required. An AC701 development board is currently running the SEM controller, while the configuration entity is running on a PC, which also monitors events.

The setup has been tested in two beam times at COSY, Jülich in August and December 2014. An overview of the event distribution can be seen in Fig. 2. For the low-rate event distribution, which is closer to realistic event rates in the final setup, it would take roughly 10 min to an SBU, and 71 min to an MBU. A full reprogram was needed every 14 hours.

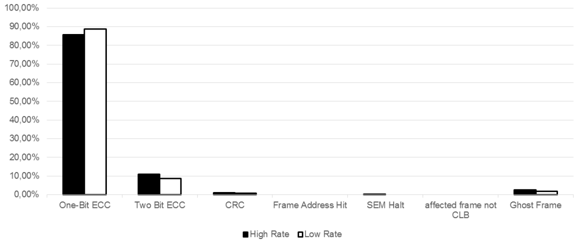

Figure 2: Distribution of different error types for high (2.5E7 protons/second) and low (4.2E6 protons/second) rates. Roughly 90% of all events are SBUs and do not require intervention from outside. Most other errors (8%) are two-bit upsets and are handled by the configuration management entity. In rare cases, a full reset was required (CRC).

References

[1] A. Oancea *et al.*, CBM Progress Report 2013, Darmstadt 2014, p. 89

[2] J. Gebelein, G. May and U. Kebschull, CBM Progress Report 2013, Darmstadt 2014, p. 88

---

[*] Work supported by HGS-HIRe

Design, assembly and test of a positioning system for beam tests*

C. Stüllein, A. Oancea, J. Gebelein, S. Manz, and U. Kebschull
IRI, Goethe-Universität, Frankfurt, Germany

Motivation

The correct alignment of devices under test (DUT) according to the beam is an important and time-consuming task in the setup of beam tests. It can be difficult to adjust the position of a DUT, especially if it is mounted in a simple rigid frame structure, since the structure has to be manually loosened. Particularly during an ongoing test, it is not possible to correct the position. But this may be necessary if the initial alignment was bad or the beam moved since the setup. Another problem could be the (re)programming of FPGAs. In addition, even if the design is made to be fault-tolerant (e.g., using TMR), the programming interfaces are not. So it would be desirable to move the DUT out of the beam for reprogramming.

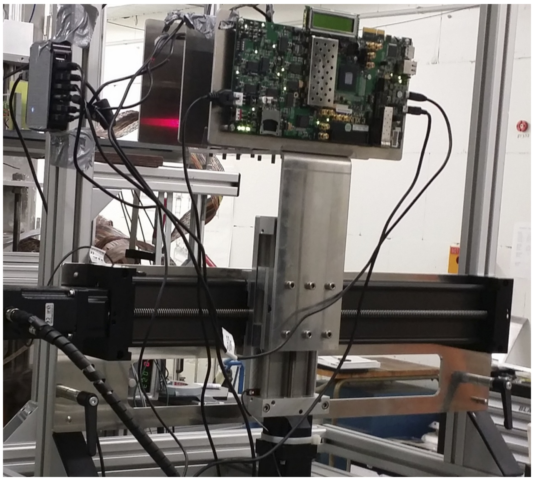

Figure 1: Photo of the stage assembled with a Xilinx eval board used in the setup for a SEM-Controller test [1]

Approach

For that purpose a remote-controlled Two-Axis positioning system (Fig. 1) was developed. It consists of a 100 mm z axis attached to the moveable carriage of a 500 mm x axis. The whole x axis can be in addition manually adjusted in height to meet the actual requirements. The z axis carriage holds the carrier for several board-specific (or general-purpose) frames. The axes are driven by two stepper motors (NEMA23 with up to 4 A continuous current). The stepper drivers and the pulse controller are connected over cables which are long enough to be placed away from the stage. In the current version, the pulse controller provides a CAN interface and is capable to handle two stepper drivers and the limit switches (hall sensors) of the axes. The whole system is controlled by a Windows application with support for PS3/XBox wireless controllers as a simple interface for coarse and fine positioning.

Results

The setup was tested at COSY, Jülich in December 2014. During a stress test with repetitive homing movements, the current and different temperatures were measured and recorded. Moreover, the required steps until reaching the limit switches were observed to check for step losses. The temperatures are shown in Fig. 2. The combined overall current was around 1.8 A with slow movement speeds and 2.5 A at higher speed.

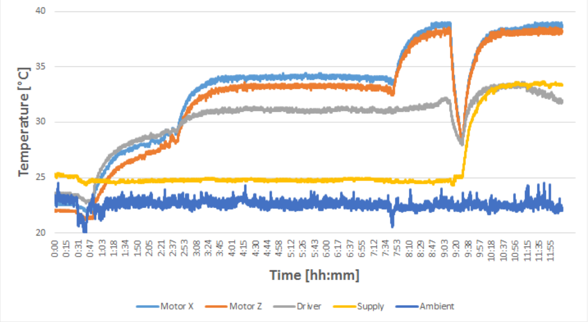

Figure 2: Temperatures during different stress tests. With permanent high-speed movement, the motor temperatures are just below 40°C at 22°C ambient temperature. The internal power supply was not used in the beginning.

Next Steps

One big functional improvement will be the design of an optional beam detector which allows for auto-tracking. An SRAM-based beam detector with this functionality is currently under development.

References

[1] A. Oancea *et al.*, *Implementation and test of a flash-free configuration upset mitigation strategy for the CBM ToF ROB FPGA*, this report

---

* Work supported by igus® YES program

Evaluation of FRAM for use in radiation environments*

J. Gebelein, C. Stüllein, and U. Kebschull
IRI, Goethe-Universität, Frankfurt, Germany

Ferroelectric Random Access Memory (FRAM) is a non-volatile, low power memory with high read/write speed and high endurance. It stores bit information in semi-permanent electric dipoles formed within a dielectric crystal cell by reversible spontaneous electrical polarization [1]. Each storage cell is composed of either two transistors and two capacitors (2T2C) as shown in Fig. 1, or one transistor and one capacitor (1T1C). The MOSFET is built in a conventional CMOS process, while the capacitor typically uses ferroelectric PZT ($\mathrm{Pb(Zr,Ti)O_3}$) material. PZT can easily be added to a conventional CMOS process by insertion of two mask layers between substrate contact and metal layers [1].

Table 1: Comparison of FRAM, Flash and SRAM

Specification	FRAM	Flash	SRAM
read time	110 ns	<120 ns	1 ns
write time	180 ns	1s/sector	<1 ns
standby curr.	5 μA	5 μA	7 μA
r/w current	4 mA	12-24 mA	40 mA
single bit r/w	yes	no	yes
endurance	10^8-10^{12}	100.000	∞

Since the FRAM's ferroelectric storage cells are promoted to be unsusceptible against magnetic fields as well as radiation, FRAM is a prominent candidate to replace current technologies in particle accelerators – a comparison is given in Table 1. But the surrounding CMOS transistors are still susceptible to radiation effects. To investigate this assumption, a beam test was performed at COSY, Jülich in August 2014, using 2 GeV protons and a total flux of $6 \cdot 10^8\,\mathrm{s}^{-1}$. Two COTS FRAM chips placed on development boards were selected for irradiation: Fujitsu MB85RS256B FRAM chip on mikroElektronika MIKROE-1486 break-out board (32 KB plain FRAM array) as well as Texas Instruments MSP430FR5739 FRAM chip on MSP-EXP430FR5739 Experimenter Board (16 MHz 16-Bit RISC Microcontroller with 16 KB FRAM storage). Two boards of each type were irradiated in parallel. The first ones were powered and read out continuously in beam while the second ones were hold completely passive and unpowered. All chips were initialized with a logical 0/1 pattern.

Throughout the beam test, no upset could be detected in the Fujitsu devices, neither in active read-back mode nor in passive mode at the end. Unfortunately, the constantly powered device broke down because of a leakage failure after about 160 krad. The current drain raised gradually from an initial operation value of 0.0007 A up to a final value of 0.100 A. After an unpowered annealing period of multiple hours at room temperature, the device was fully functional again, and the stored FRAM configuration was still unchanged.

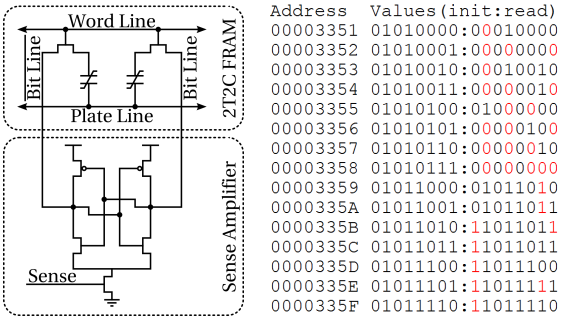

```
Address   Values(init:read)
00003351 01010000:00010000
00003352 01010001:00000000
00003353 01010010:00010010
00003354 01010011:00000010
00003355 01010100:01000000
00003356 01010101:00000100
00003357 01010110:00000010
00003358 01010111:00000000
00003359 01011000:01011010
0000335A 01011001:01011011
0000335B 01011010:11011011
0000335C 01011011:11011011
0000335D 01011100:11011100
0000335E 01011101:11011111
0000335F 01011110:11011110
```

Figure 1: Left: FRAM 2T2C cell circuit according to [2]; right: MSP430FR5739 bit errors during read-back.

While the passively irradiated Texas Instruments FRAM chip showed no errors, the actively operated one observed a single failure throughout the test. It lead to an upset of multiple stored bit values in a single continuous chain as shown in Fig. 1. All values remained statically stored within the FRAM cell. A possible causer is the utilized sense amplifier (AMP). Sense AMPs in CMOS are usually realized as 4-transistor latch-type circuits as depicted in Fig. 1. In consequence, a Single Event Transient (SET) in the AMP transistor's cross-coupled inverters the pulse width of which overlaps with the sensing interval can lead to incorrect cell *read* results. Reading an FRAM cell is a destructive process – every cell *read* results in a subsequent cell *write*. This may have caused the SET's *latching* into a permanent Single Event Upset (SEU), even in the radiation-tolerant FRAM cells. The characteristic structure of the observed upsets furthermore clearly allows to draw conclusions about the internal memory structure: AMPs are arranged in parallel to the memory rows, which enables their reuse across the memory columns. If a single AMP is upset, a single bit position within multiple words is affected.

References

[1] V. C. Kumar and B. Underdahl, *Texas Instruments FRAM MCUs for Dummies*, John Wiley & Sons Inc., Hoboken, New Jersey 2012

[2] Fujitsu Semiconductor, *Application Note AN-21377 about: FRAM MCU Key Strengths and Applications*, 2012

---

* Work supported by BMBF (05P12RFFCM)

A CBMNet bridge for the TRB3[*]

M. Penschuck[1], *J. Michel*[1], *J. Stroth*[1,2], *and the TRB3 collaboration*
[1]Goethe-Universität, Frankfurt, Germany; [2]GSI, Darmstadt, Germany

The TRB3 is a flexible and modular FPGA-based data acquisition platform originating from the HADES detector at GSI. Unifying all base functionality on a universal main board, connectivity to the experimental setup is established using up to five application-specific add-on boards. The platform is used by a number of detectors, amongst them prototypes for CBM-MVD and CBM-RICH.

The board features five inexpensive Lattice ECP3 FPGAs optimised for a high IO count rather than for computational power, which is typically not required for early DAQ stages: one central chip primarily executes management- and network-related tasks while the remaining FPGAs together with their respective add-ons form four independent sub-systems. Applications include FPGA-based TDC- (up to 264 channels/board with a precision of 7.2 ps RMS [1]) and ADC-measurements as well as the read-out of high-speed digital signals, e.g. for the MAPS in case of CBM-MVD. The TRB3 can be operated in a stand-alone fashion only requiring an external power supply and a PC capable of Gigabit Ethernet (GbE); however, large systems are inherently supported by its internal network protocol, TrbNet, which was originally developed for HADES.

In order to bring forward the integration of TRB3-based experiments into the CBM DAQ, uplink- and synchronisation capabilities were added to the platform. As most TRB3 applications are intricately built around the TrbNet infrastructure, it was decided not to replace TrbNet but to develop a bridge between both networks. The adoption included the implementation of CBMNet's physical layer, the migration of its high-level functions onto a new FPGA platform as well as the design of protocols to bridge the semantically different network types.

Since TrbNet features a central trigger and read-out scheme, CBM's streaming data transport is emulated using a free-running mode of operation based on periodic pulsers. These cause the front ends to deliver their zero-suppressed data in packets with a temporal binning comparable to FlesNet time-slices. To reduce data overhead, load-adaptive trigger frequencies based on external signals, such as an spill-indicator, are supported.

As shown in Fig. 1, current network topologies foresee a single CBMNet bridge for (possibly) multiple interconnected TRB3s since TrbNet hubs are easily available; in case of bandwidth limitation multiple uplink modules are provisioned in the firmware. An unpacker software building on top of the FlesDAQ infrastructure [2] is available in CBMRoot. Additionally, a dual-stack uplink with CBMNet and GbE is feasible.

Synchronisation with native CBMNet front ends is possible by means of freely configurable DLMs. Several approaches suitable for one to many DLMs are supported and exhibit an event-to-event jitter of < 50 ps RMS after converting TrbNet timestamps into the CBMNet domain.

Graphical user interfaces to configure, monitor and debug the new firmware were developed and enable non-experts to operate the system. The network bridge was successfully used in conjunction with the current CBM-RICH prototype during a beam time in November 2014 at CERN-PS.

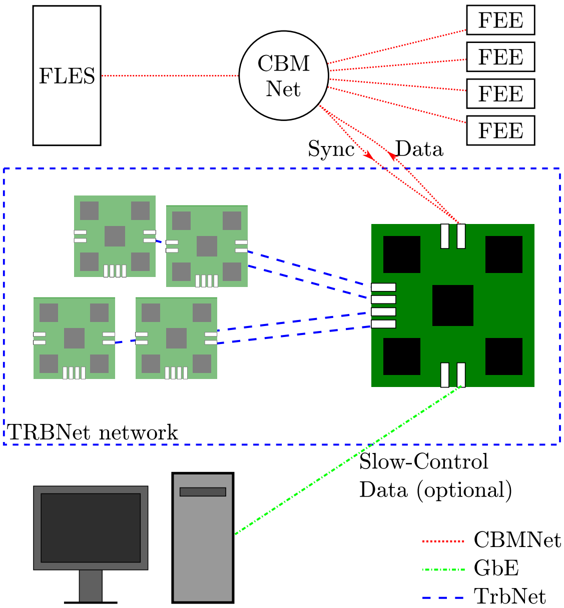

Figure 1: A typical TRB3 set-up with CBMNet bridge. If multiple boards are used, they can share a common CBMNet link. Slow-Control is available only via GbE.

References

[1] C. Ugur and the TRB3 collaboration, *264 Channel TDC Platform applying 65 channel high precision (7.2 psRMS) FPGA based TDCs*, IEEE NoMe TDC, October 2013

[2] D. Hutter, *CBM FLES Input Interface Developments*, this report

---

[*] This work has been supported by BMBF (05P12RFFC7), EU-FP7 HadronPhysics3, HGS-HIRe, GSI and HIC for FAIR.

Status of CBMnet readout and the prototype ASIC*

S. Schatral[1,2], *F. Lemke*[1], *I. Som*[3], *T. K. Bhattacharyya*[3], *and U. Bruening*[1]

[1]ZITI, Universität Heidelberg, Mannheim, Germany; [2]GSI, Darmstadt, Germany; [3]Indian Institute of Technology, Kharagpur, India

The CBMnet protocol is currently present in all stages of the CBM data acquisition (DAQ) network for the TRD and STS readout. Beside the two FEE ASICs using CBMnet links over HDMI cable, the cores are also integrated in the Read-Out Controller (ROC), the FLES Interface Board (FLIB) and further FPGA to FPGA interconnects. For these links Xilinx Gigabit Transceiver over SFPs are used. A typical setup is depicted in Fig. 1. To improve the link stability under influence of radiation, a reworked CBMnet Version 3.0 was developed and implemented, containing a link layer, various physical layer implementations and more network related building blocks to deliver generally required features in CBM network devices. The implementations were optimized for FPGA and ASIC use. The logic is built in such a way that a malfunction triggered by a single event effect is detected and the corresponding functional blocks are reset. In this manner, data acquisition over a long time is possible without any interruption. Larger test beam read-outs with up to three SPADICs per ROC were tested in laboratory and in beam. The FLIB physical layer implementation was intensively tested to work reliably under all conditions. The design can handle up to eight links now.

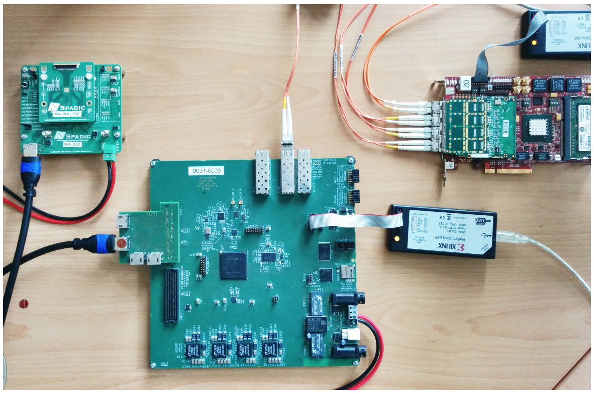

Figure 1: Read-out with FLIB, Syscore3 and SPADIC

A prototype of the readout and aggregation ASIC was designed together with the Indian Institue of Technology Kharagpur (IITKGP). Therefore, an internship student from IITKGP was visiting the University of Heidelberg for half a year in 2014. This was possible because of successfully raised additional funding from the Heidelberg Center South Asia. This mixed-signal ASIC consists of a full-custom 5 Gb/s serializer/deserializer designed by IITKGP, including design elements such as phase-locked loop, bandgap reference, and clock data recovery, and a digital designed network communication and aggregation part designed by the computer architecture group of the University of Heidelberg.

In addition, there are test structures and an I2C readout integrated to ease bringing up and monitoring. A specialty of this test ASIC is the aggregation of links featuring different data rates, running with bundles of 500 Mb/s LVDS [1]. This enables flexible readout setups of mixed detectors respectively read out by various chips. There are 1x, 2x, or 4x LVDS connections available enabling up to 2 Gb/s for a front-end connection. The prototype will be able to run in a mixed configuration, e.g., one 1x, two 2x, and one 4x. A prototype structure diagram depicting the link configuration possibilities is presented in Fig. 2. As communication protocol for the prototype, a unified link protocol is used including control messages, data messages, and synchronization messages on an identical lane. The design was successfully simulated, verified, and hardware-emulated using Spartan 6 FPGAs. The miniASIC mixed-signal design was prepared and simulated together with the collaboration partners from IITKGP. The first chance in 2015 for a submission using the TSMC 65nm LP Europractice process will be taken.

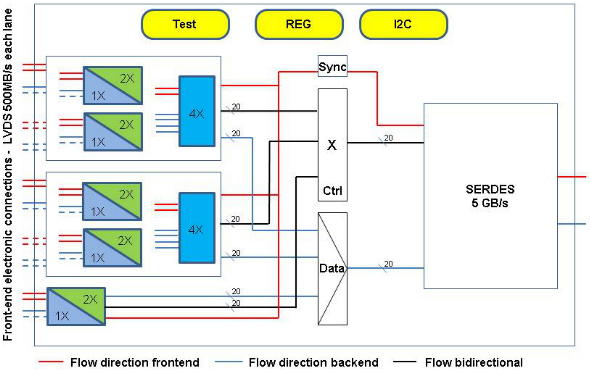

Figure 2: Link connection diagram for the HUB ASIC

References

[1] S. Schatral, F. Lemke and U. Brüning, JINST **9** (2014) C03022

---

* Work supported by GSI and BMBF (FAIR-CBM 05P12VHFCE)

Ready to tape-out of 5Gbps 4:1 serializer and deserializer in TSMC 65 nm LP technology

I. Som, S. Sarangi, A. Das, and T. K. Bhattacharyya
Indian Institute of Technology, Kharagpur, India

In mid 2014, there were some significant changes at architectural as well as design level for the ASIC HUB core analog IP. Accordingly, most of the sub-components are redesigned for the two way design methodology (bottom-up and top-down approach). The complete design, both from front and back end at pre-tape out level was rebuilt in just little more than half a year (Fig. 1). Some of the major changes are described below.

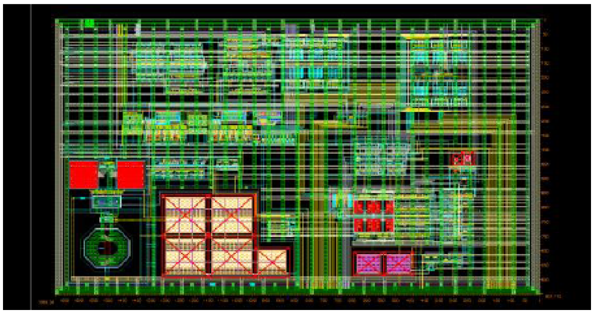

Figure 1: Top level view of the ASIC with power grid structure ($1650\,\mu\mathrm{m} \times 950\,\mu\mathrm{m}$)

Each HUB ASIC digital interface consists of four CMOS voltage channels each with a 1.25 Gbps data stream. There is a 4:1 CML level data multiplexer which serializes four input CMOS to CML converted data streams to a single 5 Gbps serial data sequence in association of Tx PLL. This PLL can generate a 5 GHz clock from the 125 MHz input reference clock. Though 2.5 GHz PLL is sufficient to retime the serialized output data stream with double-edge sampling, the 5.0 GHz design was set for future upgrades to 10 Gbps capabilities and as well for test and measurement purposes. The serial data stream then passes through a three TAP Decision Feedback Equalizer (DFE) with output having capabilities to drive 50 Ω through specified channels in order to prevent signal reflection and mismatch losses (Fig. 2). In addition, a 50 Ω output LVDS driver was also incorporated to drive the measuring equipment of high speed signaling. Several (eight) signals can be channeled through this driver through a measurement selection signal multiplexer. One of the major challenges for a 50 Ω resistive driver design is the process corner variation, which is more than $\pm 16\,\%$ relative to the nominal one. To reduce this variation down to less than $\pm 2\,\%$, the distribution of process resistance in association with corner correction switches was implemented. The right half of Fig. 2 shows this implementation.

On the receiver side, the signal is resistively (50 Ω) terminated at the input of an adaptable Continuous Time Linear Equalizer (CTLE), which essentially boosts the high-frequency component of the signal to re-energize it after passing through a lossy channel. The clock and retimed data are generated in the Clock and Data Recovery (CDR) module which essentially has its own reference 2.5 GHz clock generator. The VCO used in the CDR has a four-stage ring architecture. Each stage consists of a CML delay to reduce the layout area. One of the most notorious features of the delay cell is process corner variation of the output frequency spectrum as well as tuning ranges. The variation of the frequency band across the corner is found to be non-overlapping. So we needed to introduce several low silicon area solutions such as voltage DAC, current tuning etc. to adjust corner deviations. The complete analog ASIC consumes 176 mW of peak transient power.

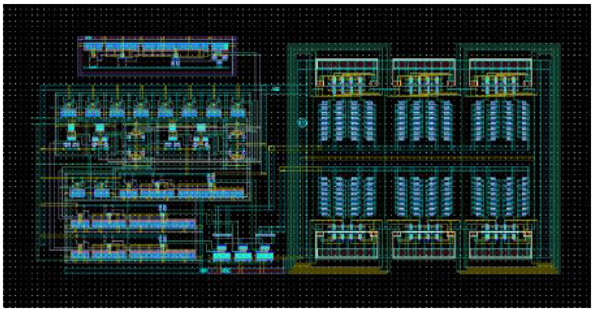

Figure 2: Top level view 3-TAP FIR structure (Equalizer) with 50 Ω matching termination to mitigate nonlinear effect of the transmission cable

The physical implementation of the analog IP was completed with careful layout techniques to reduce the effect of cross talk/coupling at the high-frequency path, and the necessary post-layout simulations were performed to validate the physical design.

References

[1] F. Lemke, S. Schatral and U. Brüning, CBM Progress Report 2013, Darmstadt 2014, p. 86

[2] N. Krishnapura *et al.*, IEEE ISSCC (2005) 60

[3] J. Savoj and B. Razavi, IEEE DAC (2001) 121

Computing

CBM component database

E. P. Akishina[1], *E. I. Alexandrov*[1], *I. N. Alexandrov*[1], *I. A. Filozova*[1], *and V. V. Ivanov*[1,2]
[1]LIT JINR, Dubna; [2]National Research Nuclear University ”MEPhi”, Moscow, Russia

The CBM Component Database (DB) is designed and implemented as a part of the CBM Databases project [1] according to the User Requirements Document [2]. The Component DB is used to store and manage the properties of the detector hardware and electronic components. It contains characteristics, statuses, test results, certificates and other parameters both numeric/strings and images. The current relational DB structure allows to use it for any CBM detector performing minor adjustments. The components of different detectors (STS, Magnet, PSD, RICH, ToF, MUCH, MVD, TRD, ECAL) will be stored in different databases. Data is accessed through the common authorization service. The Component DB has a tree structure. The root of the tree has the name of the CBM facility part such as Magnet, MVD, STS etc. The list of the detector components is stored in the tree. The tree leaf is connected to a table with according names and values. The tests, certificates and statuses are stored in the DB as the references. Test of the components are images. Certificate details depend on the component and can be implemented for each detector. The catalog of different statuses can be defined for each detector separately.

Authorization for each detector is needed. The responsible person can work only with the data of the corresponding detector. Web access is organized for viewing, inserting and editing data. The implementation is realized on the basis of client-server interaction. The same schema for all subdetectors was produced. Scripts and their usage in according html pages were implemented. Figure 1 presents an example of the Magnet main page. The details of the Magnet component are shown on the right. Figure 2 shows the page for editing Magnet details.

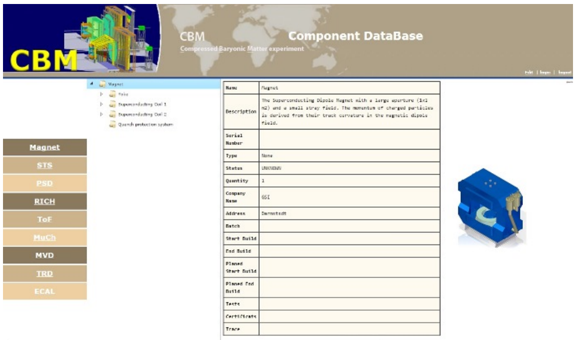

Name	Magnet
Description	The Superconducting Dipole Magnet with a large aperture (1x1 m2) and a small stray field. The momentum of charged particles is derived from their track curvature in the magnetic dipole field.
Serial Number	
Type	None
Status	UNKNOWN
Quantity	1
Company Name	GSI
Address	Darmstadt
Batch	
Start Build	
End Build	
Planed Start Build	
Planed End Build	
Tests	
Certificats	
Trace	

Figure 1: View mode GUI example for Magnet

The system implementation is based on the software DBMS PostgreSQL v8.4.20. Basic services are supported:

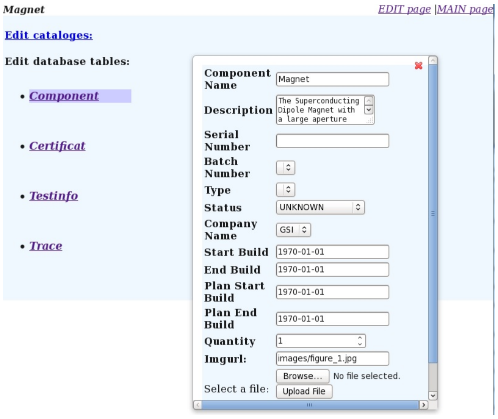

Component Name: Magnet
Description: The Superconducting Dipole Magnet with a large aperture
Serial Number:
Batch Number:
Type:
Status: UNKNOWN
Company Name: GSI
Start Build: 1970-01-01
End Build: 1970-01-01
Plan Start Build: 1970-01-01
Plan End Build: 1970-01-01
Quantity: 1
Imgurl: images/figure_1.jpg
Select a file: No file selected.

Figure 2: Edit mode GUI example for Magnet

data viewing for detector components, search in navigation mode, inserting and editing data for the detector component, support of the catalogs, authorization services for system access. The authorization is based on affiliation to the detectors group. There are several catalogs such as Manufacturer Companies, Component Categories, Batches Details, Quality Measurement Units, and Quality Criteria.

The web interface allows to work with the system from any place with internet access, to reach data from mobile device on according speed level. The current Magnet Component DB is completely implemented, filled with data and available through the link: http://cbmdb.jinr.ru/magnet.main.php. STS and MVD tree structures are defined. They are going to be filled in with data after some specification. The Users Guide for the Component DB support is developed and ready for use [3].

References

[1] E. P. Akishina *et al.*, *Conceptual Considerations for CBM Databases*, E10-2014-103 JINR Communication, Dubna

[2] E. P. Akishina *et al.*, *User Requirements Document for CBM Component Database*, http://lt-jds.jinr.ru/record/67403?ln=en

[3] E. P. Akishina *et al.*, *Users Guide for CBM Component Database*, http://lt-jds.jinr.ru/record/67404?ln=en

Status of the CBM MVD simulation model*

S. Amar-Youcef[1]*, M. Deveaux*[1]*, E. Krebs*[1]*, B. Linnik*[1]*, B. Milanovic*[1]*, Ph. Sitzmann*[1]*, T. Tischler*[1]*, and J. Stroth*[1,2]

[1]Goethe-Universität, Frankfurt, Germany; [2]GSI, Darmstadt, Germany

The MVD simulation model is subject to a major revision, and considerable progress has been achieved. In the following its motivation and status are discussed.

Motivation. Because of its proximity to the target and its excellent spatial resolution, the MVD is the dedicated detector to resolve secondary vertices. In addition, its capability to clean-up background in di-electron spectra is subject of a dedicated study [1]. However, the primal implementation in simulation lacked in a realistic description (with respect to e.g. the material budget or peculiar sensor features) for advanced studies. These studies are needed to develop strategies to achieve best performances, to analyze critical points and to finalize the concept of the MVD and its tools.

The revision of the MVD model, to be incorporated into the CbmRoot simulation framework, aims at a more realistic description of the current understanding of the MVD. Before, in the standard scenario, the MVD was simplified as two homogeneous discs at 5 cm and 10 cm downstream the target, with an outer (inner) radius of 2.5 cm (0.5 cm) and 5 cm (0.5 cm), respectively. As no representation of individual sensors was included, this simplification possesses many limitations. These limitations involve mainly sensor properties beyond the hit response as e.g. the data parallelism of sensors, the rolling-shutter frame read-out, bandwidth limitations, busy circuits, a definition of a fake hit rate, time stamping and the data format.

The new approach [2] addresses these issues and is based on a segmented geometry with four stations (at 5 cm, 10 cm, 15 cm and 20 cm downstream the target) including all relevant features. Its underlying sensor characteristics are borrowed from MIMOSIS. The detailed geometry was elaborated in CAD. The conversion from the respective description into the ROOT geometry format was conducted by a dedicated tool. In this way we are able to respond very quickly to changes in the detector design.

Along with the proper representation of the gradual material budget, there is the possibility to incorporate the missing features mentioned above, as hits are assigned to sensors now. The data parallelism is incorporated by restructuring the data processing through the three process steps called digitizer, cluster finder and hit finder. Here, the corresponding data representations called Monte Carlo (MC) hits, digis (firing pixels) and clusters, which serve as input for the respective process step, are assigned to the respective sensors. All further properties of the sensors are incorporated within the digitizer. The previously mentioned digis are particularly important, as they describe the response of the sensor to impinging hits mimicked by the digitizer. Apart from the generated pattern of single hits the interference among hits is important to consider. This is implemented in the digitizer by creating the signal amplitudes and distributions of all hits before jointly discriminating to generate the binary charge measurement. Hits from consecutive events might pile-up and/or neighboring hits merge. This is particularly true because of the long integration time of one frame of $\sim 30\ \mu s$. The respective output is dependent upon the included features as listed above. These features require a definition of the temporal sequence of the recorded MC hits accordingly. Its considerations are relevant especially for the time-based track reconstruction of CBM. The time-based consideration is a necessary condition to use the reconstruction software with real data, too.

In order to verify the performance in the reconstruction (e.g. tracking), matching of all data states to MC truth is incorporated. All geometry information are accessible via the 'GeoHandler'-Class. For the tracking a simplified representation of the material budget is provided in the form of a map in dedicated files provided together with the digitizer.

In order to study the impact of misalignment, the position of the individual sensors can be modified within the simulation.

Status. The new MVD geometry and data processing has been incorporated into CbmRoot. All previous functionality has been re-established and can be used within the event-based reconstruction. Time-based reconstruction is not yet fully established in CbmRoot. Likewise the MVD model does not yet comprise all the details. However, all necessary preparations have been provided. Event pile-up can be studied via background events. Moreover, further details related to the performance of the sensor (as e.g. aging with the integrated radiation dose, noisy pixels, different pixel geometries) have not yet been treated.

The current representation of the MVD in simulation is the prerequisite for realistic simulations on the performance of the MVD in secondary vertexing and background rejection in di-electron spectroscopy.

References

[1] E. Krebs, *Background rejection in the dilepton analysis with the CBM-Micro Vertex Detector*, this report

[2] P. Sitzmann, *Integration eines sensorbasierten Detektorresponsemodells*, Master Thesis, Universität Frankfurt, 2015

---

* Work supported by BMBF (05P12RFFC7), HIC for FAIR and GSI

Event-building process from free-streaming data

V. Singhal[1], *S. Chattopadhyay*[1], *and V. Friese*[2]
[1]Variable Energy Cyclotron Centre, Kolkata, India; [2]GSI, Darmstadt, Germany

Up to now most High-Energy physics experiments are based on a hardware triggered approach, which means a specific set of hardware signaling the entire electronics to collect data. The trigger signal defines the event boundary; therefore the available simulation and reconstruction software work on an event-by-event basis. In contrast, because of the unprecedented interaction rates and complex trigger signatures, the CBM experiment will not employ conventional triggered electronics. Instead, self-triggered will deliver data to the DAQ system on detection. In this scenario, the event boundary will not be defined by any hardware. This implies a novel read-out and data acquisition concept which will generate free-streaming data. To perform analysis of this time stamped, free-steaming data, event association must be performed in software. To simulate the data stream, the CbmRoot framework was extended to simulate and process time-stamped data, the smallest unit of which is called ”digi” [1].

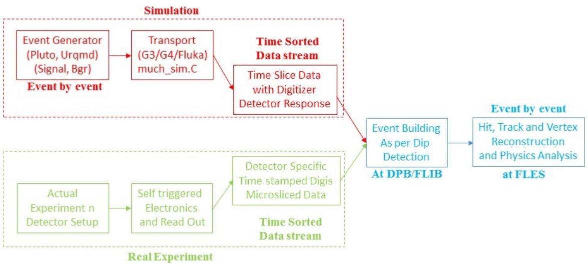

Figure 1: Simulation and analysis process chain

The simplest approach to the problem of event definition from free-streaming data acts directly on the time stamp of the digis, prior to any reconstruction step. Thus, an event association package has to be introduced at the appropriate place in the simulation, reconstruction and analysis chain which will separate the data stream into events, which should cater to the actual experiment data processing. Figure 1 shows the proposed process chain for both simulation and real experiment. The data flow shows that all the available hit, track, vertex reconstruction and physics analysis packages can be used if a new process named event building is introduced which will convert the timestamped data stream into an event-by-event data stream. In the following we describe a procedure to address this issue.

A time-stamped raw data stream is generated by simulation, and each detector generates a separate raw data stream like STS data stream, MUCH data stream etc, which all will be stored in a ROOT TTree. As a first step towards the reconstruction of such free-streaming data, we introduced an event-building process which tags physical events based on the time information of the raw data. The process counts the digis in each nanosecond and put these values in a vector. Then the process identifies and analyzes dips in the continuous vector. Data between two dips indicates probable event candidates, which are then further analysed with respect to a number of parameters like minimum and maximum number of digis per event, average event duration, etc. Fig. 2 shows the flowchart for the event building process. In this process a vector indexed nanosecond is created, which contains the number of digis in the nanoslice and the index of first digi of this nanoslice. Presently our sample set contains free-streaming data only for the muon detector system (MUCH).

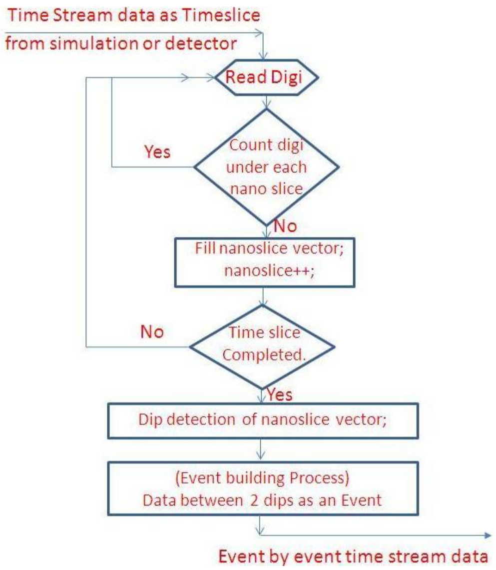

Figure 2: Flowchart for the proposed event building

Fine tuning of the event-building process was performed with respect to MUCH on the basis of different parameters. A similar procedure will be developed for the other detector systems. Once events can be defined with respect to all the detector systems, all available reconstruction algorithms, working on an event-by-event basis, could be used without any modification for processing time-stamped, free-streaming data.

References

[1] V. Friese, J. Phys. Conf. Ser. **331** (2011) 032008

4-Dimensional Cellular Automaton track finder for the CBM Experiment[*]

V. Akishina[1,2,3] *and I. Kisel*[1,2,4]

[1]Goethe-Universität, Frankfurt, Germany; [2]GSI, Darmstadt, Germany; [3]JINR, Dubna, Russia; [4]FIAS, Frankfurt, Germany

The CBM experiment at FAIR will focus on the measurement of rare probes at interaction rates up to 10 MHz. The beam will provide free stream of particles, such that some events may overlap in time. This requires full online event reconstruction not only in space, but also in time, the so-called 4D (4-dimensional) event reconstruction. A time-slice is reconstructed in parallel between cores within a CPU, thus minimising communication between CPUs. This is a task of the First-Level Event Selection (FLES) package.

The FLES reconstruction package consists of several modules: track finding, track fitting, short-lived particle finding, event building and event selection. The Cellular Automaton (CA) track finder is fast and robust and thereby will be used for the online track reconstruction. This method benefits from enumeration suppression by introducing a phase of building short track segments at an early stage before going into the main combinatorial search. The reconstruction efficiency for the primary tracks with momentum higher than 1 GeV/c in case of event-based analysis (see 3D column of Table 1) is 96.1%.

Table 1: Track reconstruction performance for 3D event-by-event analysis, super-event (3+1)D and time-based 4D reconstruction for 100 mbias Au+Au collisions at 25A GeV

Efficiency, %	3D	(3+1)D	4D
All tracks	83.8	80.4	83
Primary high-p	96.1	94.3	92.8
Primary low-p	79.8	76.2	83.1
Secondary high-p	76.6	65.1	73.2
Secondary low-p	40.9	34.9	36.8
Clone level	0.4	2.5	1.7
Ghost level	0.1	8.2	0.3
Time/event/core	8.2 ms	31.5 ms	8.5 ms

As a special study of the CA track finder stability the algorithm behavior was investigated with respect to the track multiplicity. For this study, a super-event, which includes a number of minimum bias events, was reconstructed with no time information taken into account. In a super-event we combine space coordinates of hits from a number of minimum-bias Au+Au events at 25A GeV and give it to the CA track finder as an input to reconstruct with the regular procedure. The reconstruction efficiency dependence is stable: the efficiency for all tracks changes by 4% only for the extreme case of 100 minimum bias events in the super-event (see (3+1)D column of Table 1), compared to the case of event-based analysis.

In a next step, the time information was included to the algorithm. This results in a higher reconstruction efficiency (see 4D column in table 1). In particular the time information drastically decreased ghost tracks and made the reconstruction 3.7 times faster than without the time information ((3+1)D column of Table 1). The speed now is 8.5 ms and comparable with the event-based analysis. The CA track finder was fully parallelised inside the time-slice. The parallel version shows the same efficiency as the sequential one and achieves a speed-up factor of 10.6 while parallelising between 10 Intel Xeon physical cores with hyper-threading.

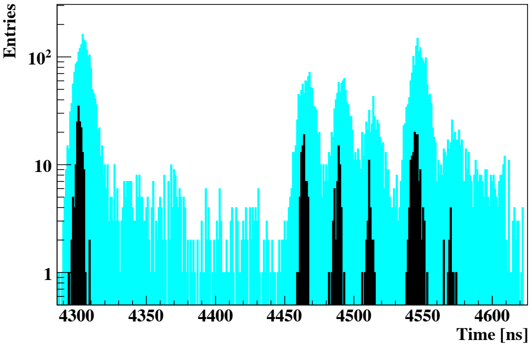

Figure 1: Distribution of time measurements in a part of a time-slice at the interaction rate of 10^7 Hz. The hit time measurements are shown in light blue, the track times in black.

A first version of event building based on the 4D track finder was implemented. The hit time distribution illustrating the complexity of defining event borders in a time-slice is shown Figure 1 with blue color, the resulting distribution of reconstructed track time with black. Reconstructed tracks clearly represent event-corresponding groups. The FLES package is ready for the 4D reconstruction of time-slices in CBM.

References

[1] I. Kisel, I. Kulakov, and M. Zyzak, IEEE Trans. Nucl. Science **60** (2013) 3703

[2] V. Akishina and I. Kisel, *Online 4-Dimensional Reconstruction of Time-Slices in the CBM Experiment*, submitted to IEEE Trans. Nucl. Science

---

[*] Work supported by HICforFAIR, FIAS and HGS-HIRe for FAIR

A “vector finding” approach to track reconstruction in CBM MUCH

A. Zinchenko, V. Myalkovskiy, D. Peshekhonov, and V. Peshekhonov
LHEP JINR, Dubna, Russia

The existing track reconstruction method in CBM MUCH is based on the track following approach. It consists in the STS track propagation through the MUCH subsystem using the Kalman filter procedure. Although quite straightforward, this method has some deficiencies such as a necessity to run a prior STS reconstruction or the effect of the absorbers, which blows up the track covariance matrix and makes hit selection right behind them rather difficult in a high hit density environment (in the first stations) or for one-coordinate detectors (straw tubes - Fig. 1).

Here, an alternative approach to the track reconstruction task in MUCH is described based on a so-called “vector reconstruction” procedure [1]. The idea is to build track segments (vectors) for each MUCH station and merge them with each other (and finally with STS tracks) through the absorbers. This approach offers some advantages (besides being alternative): the vector finder can be run for all stations in parallel, and the procedure is rather simple (straight line fit of a few measurements), there is a possibility to trigger on di-muons, the damaging effect of absorbers is excluded at the first stage of reconstruction allowing to fully exploit coordinate reconstruction accuracy for handling hit combinatorics.

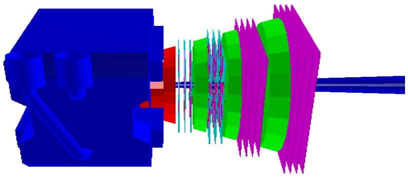

Figure 1: SIS100 CBM muon system configuration with straw tubes comprising two last detector stations

The vector finder in the magnetic field-free region can be realized very efficiently using the solution of the linear equation system from the Least Squares Method (LSM). It consists in finding the minimum value of the χ^2 - functional (for 2-D detectors):

$$\chi^2 = \sum_{i=1}^{N_{planes}} \left[\frac{(x(z)-x_i)^2}{\sigma_{x_i}^2} + \frac{(y(z)-y_i)^2}{\sigma_{y_i}^2}\right],$$

where $x(z) = x_0 + T_x \cdot z$ and $y(z) = y_0 + T_y \cdot z$ are the vector equations in two planes with track parameters (x_0, y_0, T_x, T_y) and the sum is taken over the number of planes in the detector station (i.e. the number of points with coordinates (x_i, y_i) and errors $(\sigma_{x_i}, \sigma_{y_i})$). A similar expression can be written for one-dimensional detectors (straw tubes).

The minimum value of χ^2 is found by taking its partial derivatives with respect to the track parameters and setting them to 0. As a result, the following system of equations is obtained (for 2-D detectors - GEMs):

$$\sum_i \begin{pmatrix} 1 & 0 & z_i & 0 \\ 0 & 1 & 0 & z_i \\ z_i & 0 & z_i^2 & 0 \\ 0 & z_i & 0 & z_i^2 \end{pmatrix} \begin{pmatrix} x_0 \\ y_0 \\ T_x \\ T_y \end{pmatrix} = \sum_i \begin{pmatrix} x_i \\ y_i \\ x_i \cdot z_i \\ y_i \cdot z_i \end{pmatrix}.$$

Here it is assumed that the measurement errors are the same for all hits in a station, which is a reasonable approximation for MUCH. One can see that the left matrix does not depend on individual hit measurements and can be called a configuration matrix $\mathbf{A}$. As such, it can be computed at the initialization stage and kept in memory for the whole processing. The configuraton matrices also define the covariance matrices of the fitted vector parameters $\mathbf{V} = \sigma^2 \cdot \mathbf{A}^{-1}$.

The above formalism is used as follows: for each detector station, different hit combinations are fitted by straight lines. Combinations with high χ^2-value are rejected. To reduce hit combinatorics, some a priori constraints can be applied (e.g., vector angles). At the next step, vectors from sequential stations are merged through the absorbes, taking into account multiple scattering in the absorber material and covariance matrices of vectors. Again, only vector pairs with low enough matching χ^2 are accepted. At the end, matching with STS tracks is done.

Some results on vector matching in two last stations are presented in Table 1. Here the signal muon pair efficiency (from ω decays) is shown along with the average number of background tracks in central Au+Au collisions at $8A$ GeV. The background tracks include the ”real” tracks, i.e. the ones from real particles (punch-through hadrons or decay muons) and ”ghosts”, i.e. combinations of two vectors from different particles. Although the results are very preliminary, one can see that the MUCH configuration with straw tubes demonstrates somewhat better performance (because of the higher coordinate resolution).

Table 1: Tracking efficiency for the dimuon signal and background track rate

Geometry	Efficiency,%	⟨ Bkg. tracks / event⟩	
		”real”	”ghost”
GEM	4.3±0.3	1.23±0.02	0.50±0.01
Straws	4.9±0.3	1.22±0.02	0.30±0.01

References

[1] A. Zinchenko *et al.*, CBM Progress Report 2010, Darmstadt, 2011, p.38

Cellular automaton track finding algorithm in MUCH

T. O. Ablyazimov[1] *and V. V. Ivanov*[1,2]
[1]JINR, Dubna, Russia; [2]National Research Nuclear University "MEPhI", Moscow, Russia

In [1] we proposed a system of criteria for quick selection of $J/\psi \to \mu^+\mu^-$ events, registered by the MUCH detector, in nucleus-nucleus collisions at high energies. These criteria are based only on information about the parameters of the tracks found in the MUCH, and provide a background suppression of $\sim$1,000. For their implementation we need to quickly and reliably reconstruct the tracks registered by the MUCH detector layers. The presently used `littrack` algorithm [2] does not provide enough speed. In addition, its initialization requires information on the tracks previously reconstructed in the STS detector. In this connection, we developed a fast track search algorithm in MUCH, using information of hits from this detector only.

The algorithm is built on the model of Cellular Automaton and is aimed at the reconstruction of tracks passing the entire MUCH system. This means that we demand that the reconstructed tracks have hits on all MUCH stations. As the magnetic field is weak even in the region of the first MUCH station, and the muons able to pass through the absorbers if they have momenta not less than 3 GeV/c, we use a linear track model. In this model, the elements of the track are straight line segments, the ends of which are hits on the middle layers of adjacent stations. Since the reconstructed tracks meet the decays of short-lived particles, it is possible to impose limitations on the angles of the segments of the track – they have to be close to the slope of the line drawn through the target center and one of the ends of the segment. Given the efficiency of detection layers, we also demand that the track have hits in at least two detection layers of each station.

The algorithm comprises three steps:

1. Middle point calculation: a) a hit in the middle layer of a station is rejected if there is not at least one corresponding hit in one of the edge layers of this station; b) if two hits which lay on the opposite outermost layers of a station can belong to the same decay muon track, but there is no suitable hit on the middle layer, we create a hit there by linear interpolation of the outermost hits coordinates, supposing the middle hit was lost because of hardware malfunction.

2. Segment set construction (which are track building blocks): for later calculations we store all the segments having ends laying on adjacent stations which have geometrical properties appropriate for the tracks of decay muons (determined by Monte Carlo simulation in advance).

3. Segment linking and final track reconstruction: starting from the segments having ends on the last station, segment chains are built by connecting neighbouring segments. Two segments are considered neighbours if the right end of one and the left end of another is the same hit, and if the angle between them does not exceed the limits determined by Monte Carlo simulation. The chain of connected segments is considered a reconstructed track if it connects the last station with the first one. If a given rightmost segment can be connected with the first station by several chains, the chain having the least χ^2 value is chosen among them.

In order to evaluate the track reconstruction efficiency, model data generated with PLUTO ($J/\psi \to \mu^+\mu^-$ decay, signal) and UrQMD (central Au+Au collisions at 25A GeV, background) were used. The reconstruction efficiency depending on the muon momentum is presented in Fig. 1.

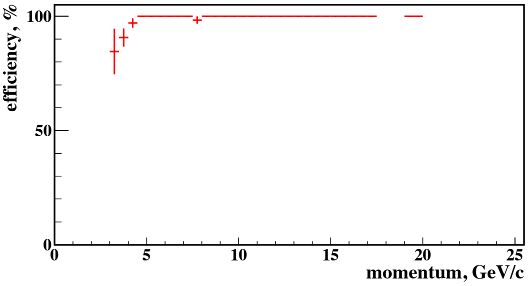

Figure 1: Reconstruction efficiency for decay muons as function of momentum

The average efficiency over the entire momentum range is 99 %. The computation time of a scalar version of the algorithm is 10 ms, which is several orders of magnitude smaller than for `littrack`.

References

[1] T. O. Ablyazimov and V. V. Ivanov, $J/\psi \to \mu^+\mu^-$ *decay selection criteria with MUCH*, this report

[2] A. Lebedev, PhD thesis, Dubna 2010

On the performance of $\mathrm{J}/\psi \to e^+e^-$ reconstruction algorithms

O. Yu. Derenovskaya[1] *and V. V. Ivanov*[1,2]
[1]LIT JINR, Dubna, Russia; [2]National Research Nuclear University "MEPhi", Moscow, Russia

The measurement of J/ψ decays is one of the key goals of the CBM experiment. The procedure of the J/ψ registration in its di-electron decay channel includes a chain of methods and corresponding algorithms for the reconstruction of trajectories and momenta of charged particles with STS, electron/positron identification with RICH, TRD and TOF, as well as construction of the J/ψ candidates and their characteristics using the KFParticle package [1]. Taking into account that selection and reconstruction decays of J/$\psi \to e^+e^-$ are planned to be carried out in real time of the CBM experiment, the used methods and algorithms should be not only effective but also fast.

In this paper the time-consuming estimation of the existing algorithms based on their acceleration via code vectorization by means of SIMD instructions and parallelization between the processor cores that are implemented using different software environments is carried out. Details can be found in [2]. Table 1 presents the speed-up factors of the algorithms (Cellular Automaton and Kalman Filter in the STS, ring reconstruction with RICH, electron identification in the TRD applying the ω_n^k criterion, KFParticle package) obtained with using SIMD instructions.

Table 1: Speedup factors of the algorithms obtained with using SIMD instructions

STS: CA	STS: KF	RICH: ring reconst.	TRD:el.id. with ω_n^k	KFParticle
2	4	2	3.5	2.5

It should be noted that there is a certain reserve to accelerate the computing in this way, because some algorithms, such as the track reconstruction of the charged particle with the TRD, are not subjected to vectorization, and others, for example the KFParticle package, is not fully vectorized. In the case of the maximum possible optimization and vectorization of all algorithms, the total acceleration factor may be considerably higher.

According to preliminary estimates, the share of central collisions in the real experiment should not exceed 1%. In this regard, we used events corresponding to a mixture of central (1%) and minimum bias (99%) Au+Au-collisions at $25A$ GeV to determine the performance of the algorithms. Furthermore, to avoid dependence of the algorithms to the particle multiplicity, we calculate the average time Δt which a specific algorithm takes for processing a single trajectory. To do this, the following formula is used:

$$\Delta t = \frac{t_{\mathrm{mbias}}}{N_{\mathrm{mbias}}} \cdot 0,01 + \frac{t_{\mathrm{centr}}}{N_{\mathrm{centr}}} \cdot 0,99, \qquad (1)$$

where t_{mbias} is the average time spent by the algorithm on one minimum-bias event and t_{centr} is the same value for one central event; N_{mbias} and N_{centr} are the average numbers of reconstructed tracks in minimum-bias and central events, respectively.

Table 2 presents the average time Δt (in μs/track or μs/ring) which $\mathrm{J}/\psi \to e^+e^-$ reconstruction algorithms spend on data processing. Note that the presented results refer to the SIMD-algorithms (except the track reconstruction with the TRD) and were obtained using one logical CPU core.

Table 2: Average time Δt (in μs/track or μs/ring) which the SIMD-algorithms spend on data processing

STS: CA	STS: KF	RICH: ring reconst.	TRD: track reconst.	TRD: el.id. with ω_n^k	KFParticle
164.5	0.5	49	1390	0.5	9.15

The results shows that the time spent by the algorithm of track reconstruction of charged particles in the TRD exceeds the summed time of all other algorithms by factors. It should be noted that an alternative approach to track finding in the TRD, based on a Cellular Automatonm is now under development. It is expected that the new algorithm will not be inferior in efficiency to the existing method but more reliable and productive.

All of the above algorithms were adapted in software environments (OpenMP, OpenCL and TBB) for parallel computation on high performance hybrid servers constructed on the basis of multi-core CPU and GPU. All algorithms shows a good linear scalability with the number of the cores included in the processing.

The scalability analysis of the algorithms allowed us to estimate the acceleration of data processing using the technologies for high-performance computing and identified "weak" spots in the chain of the methods for J/ψ reconstruction (track reconstruction in TRD), which is under further investigation.

References

[1] O. Yu. Derenovskaya and V. V. Ivanov, PEPAN, Letters, T.11, No.4 (188), 2014, pp. 862-885

[2] O. Yu. Derenovskaya and V. V. Ivanov, Bulletin of PFUR, Series Matematics. Information Sciences. Physics. No. 4, 2014, pp. 50-67

$J/\psi \to \mu^+\mu^-$ decay selection criteria with MUCH

T. O. Ablyazimov[1] *and V. V. Ivanov*[1,2]
[1]JINR, Dubna, Russia; [2]National Research Nuclear University "MEPhI", Moscow, Russia

The measurement of J/ψ production in collisions of heavy nuclei stands among the main objectives of the CBM experiment. One of the ways of J/ψ detection is the identification of muon pairs from $J/\psi \to \mu^+\mu^-$ decays. As the interaction rate in CBM is planned to be up to 10 MHz, whereas the DAQ recording ability is expected to be in the range of 10 kHz – 25 kHz [1, 2, 3], fast and efficient algorithms are needed to filter the stream of raw experimental data. A trigger of signal events with a suppression ratio of 400 – 1000 is needed.

For fast selection of $J/\psi \to \mu^+\mu^-$ events, a system of criteria which uses only geometric properties of muon tracks in the MUCH detector was designed. To make it applicable in practice, a cellular automaton (CA) based algorithm for fast searching tracks in MUCH was developed. This algorithm uses only information of the MUCH hits and is optimized to find tracks passing through the MUCH system. The description of the CA track-finder algorithm can be found elsewhere [4].

To decide whether a pair of reconstructed tracks corresponds to a muon pair from a J/ψ decay, the two following criteria are applied: 1) the tracks must correspond to particles with opposite electric charges, and 2) the distance between points where these tracks cross the middle layer of the first MUCH station must not be less than 50 cm (Fig. 1).

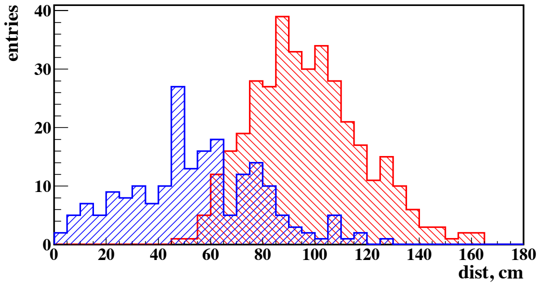

Figure 1: Distributions of distances between points of crossing the first MUCH station by signal (red) and background (blue) track pairs

As it turned out, the electric charge sign of a particle can be determined with a high degree of certainty ($\sim$ 93 %) by the angle in the $x - z$ projection between the two following lines: 1) the tangent to the reconstructed track in the point where it crosses the first MUCH station, and 2) the line connecting the above mentioned point on the first MUCH station and the center of the target. For positively charged particles this angle is positive, and for negatively charged ones it is negative (Fig. 2).

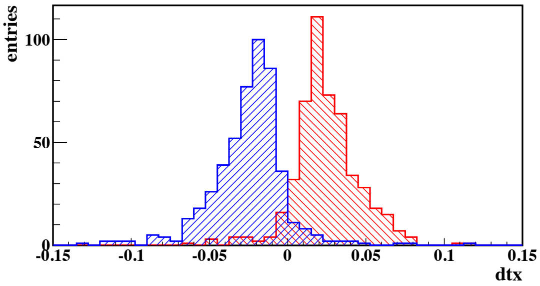

Figure 2: Distributions of angles between the tangent to the reconstructed track in the point of its intersection with the first MUCH station and the line connecting the intersection point and the center of target for positively (red) and negatively (blue) charged particles

To assess the efficiency of the procedure for the selection of signal events $J/\psi \to \mu^+\mu^-$, two sets of model data were used: 1) 10^5 background events generated with the UrQMD model for minimum-bias Au+Au collisions at $25A$ GeV, 2) 10^3 "signal" events, in which several $J/\psi \to \mu^+\mu^-$ decays, generated using the package PLUTO, were added to a background event corresponding to a central Au+Au collision at $25A$ GeV.

The testing of the developed criteria on model data demonstrated both a suppression ratio of 1,000 for background events and a selection efficiency of 87.5 % for muon pairs from J/ψ decay.

References

[1] A. Kiseleva *et al.*, CBM Progress Report 2008, Darmstadt 2009, p. 69

[2] P. P. Bhaduri *et al.*, CBM Progress Report 2008, Darmstadt 2009, p. 70

[3] V. Friese, Lect. Notes Comp. Sc. **7125** (2012) 17

[4] T. O. Ablyazimov and V. V. Ivanov, *Cellular Automaton algorithm for finding tracks in MUCH*, this report

Event-by-event extraction of kinetic and chemical freeze-out properties in the CBM experiment*

V. Vovchenko[1,2,3,4], *I. Kisel*[1,2,3], *and D. Anchishkin*[4,5]

[1]Goethe-Universität, Frankfurt, Germany; [2]GSI, Darmstadt, Germany; [3]FIAS, Frankfurt, Germany; [4]Taras Shevchenko University, Kiev, Ukraine; [5]Bogolyubov Institute for Theoretical Physics, Kiev, Ukraine

The future CBM experiment at FAIR is designed to study properties of strongly interacting matter produced in heavy-ion collisions at high baryon densities. It will employ high intensity beams and large acceptance detectors. One important task is to extract the thermal parameters of matter at stages of kinetic and chemical freeze-out from the observed data. The extraction of thermal parameters is implemented as a package within the CbmRoot framework.

The kinetic freeze-out temperature of charged pions is extracted from their measured momentum spectrum. In the simplest scenario the particles are assumed to have a Boltzmann momentum distribution with no collective flow. To test the method, 1000 Monte Carlo (MC) events with thermally distributed pions ($T = 128$ MeV) were generated and then processed in CbmRoot. Reconstructed STS Tracks, as well as the initial MC Tracks, were used to calculate the average transverse mass of pions $\langle m_T \rangle$, which was then used to estimate the temperature. Because of the limited detector acceptanc and imperfect reconstruction efficiency, the mean transverse mass of STS tracks differs from the MC one. Therefore, an appropriate correction was performed using the known momentum dependence of acceptance and reconstruction efficiency. Figure 1 depicts the extracted Boltzmann temperature on the event-by-event level. It is seen that the extracted temperature has a Gaussian-like distribution around the theoretical value of 128 MeV when one uses MC Tracks (blue line) or STS Tracks with proper correction on acceptance (red line). If this correction on acceptance is neglected, one gets essentially different (incorrect) values of temperature (green line). The procedure, developed for this model, can be used as a basis for analysis in the framework of more complex and more realistic models.

The parameters of the chemical freeze-out are extracted by fitting the measured particle ratios in the framework of the Hadron Resonance Gas model. All strange and non-strange hadrons which are listed in the Particle Data Tables are included. The model is implemented in CbmRoot and works similarly to the THERMUS package [1]. The grand canonical ensemble formulation is used, and excluded-volume corrections are included in the framework of the thermodynamic mean-field approach [2]. The fit can be performed on event-by-event level and also on the inclusive spectra level. Figure 2 shows the extracted temperature and baryonic chemical potential from MC events generated in the thermal model with $T = 100$ MeV and $\mu_B = 550$ MeV. For each parameter extraction a set of 10 events was used, and the fit error estimates were calculated and depicted as well. The extracted values are consistent with the theoretical input.

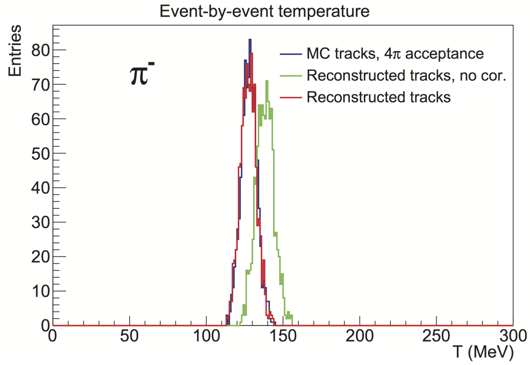

Figure 1: The temperature of pions extracted on event-by-event level using the MC tracks (blue line), STS tracks without acceptance correction (green line), and STS tracks with correction for acceptance (red line).

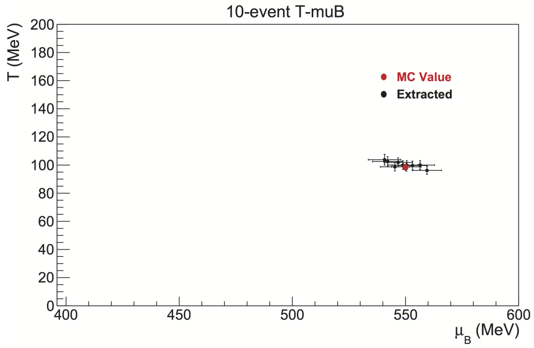

Figure 2: The temperature and the baryonic chemical potential extracted from the 10-event sets in the framework of the Hadron Resonance Gas model. The theoretical MC value is shown by the red dot.

References

[1] S. Wheaton, J. Cleymans and M. Hauer, Comput. Phys. Commun. **180** (2009) 84

[2] D. Anchishkin and V. Vovchenko, arXiv:1411.1444 [nucl-th]

---

* Work supported by the Hessian LOEWE initiative through the Helmholtz International Center for FAIR (HIC for FAIR)

Physics Performance

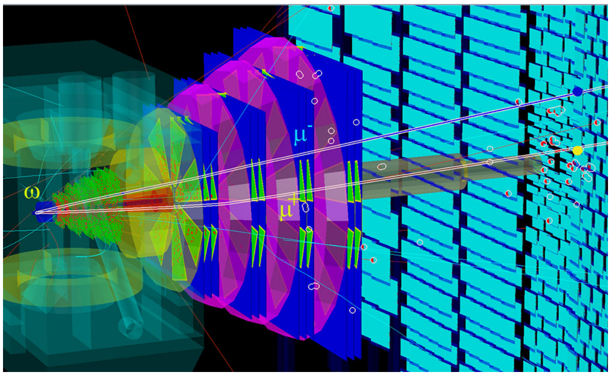

Nuclear fragments with CBM at SIS100

V. P. Ladygin[1], *K K. Gudima*[1,2], *N. B. Ladygina*[1], *and A. A. Lebedev*[1,3]
[1]LHEP-JINR, Dubna, Russia; [2]IAP, ASM, Kishinev, Moldova; [3]GSI, Darmstadt, Germany

Light nuclear fragments are formed from nucleons at the latest stage of the evolution of the fireball, called the stage of freeze-out. Simple coalescence models [1] predict that the invariant yield of light nuclei with mass A is proportional to the A-th power of the nucleon yield and coalescence factor B_A, which characterizes the coalescence probability. This factor depends on the fireball size, it can be measured in the experiment and used to estimate the reaction volume in which the composite particles are created.

Simulations were performed for 100k minimum-bias Au+Au events at $4A$ GeV using the Dubna Cascade Model [2] for the hadron setup of the CBM detector at SIS100. Secondary particles were selected using the m^2-p/Z correlation, where momentum and time-of-flight were reconstructed from STS and TOF information, respectively. This method leads to some contamination of misidentified protons, especially at high momentum values [3].

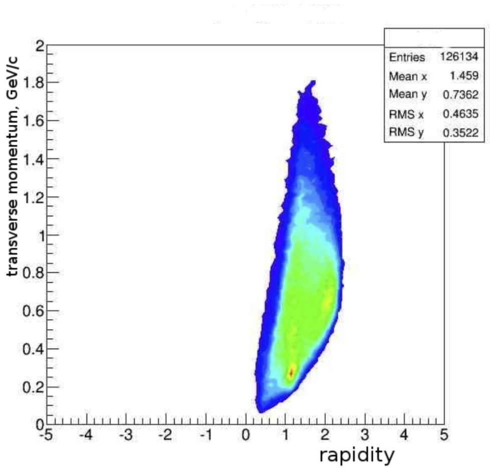

Figure 1: $y - p_T$ distribution for deuterons from minimum-bias Au+Au collisions at $4A$ GeV [2]

The transverse momentum-rapidity ($y - p_T$) distribution for deuterons from minimum-bias Au+Au collisions at $4A$ GeV [2] is presented in Figure 1. The yield is ~1.2 deuteron/event with ~97% of purity selection. The dominant reaction mechanisms are coalescence and projectile fragmentation. Deuterons with rapidity values $\sim$ 1.2 and typical transverse momenta $p_T \sim 0.3$ GeV/c are produced via coalescence, while deuterons with the rapidity values ~ 2.02 come from the fragmentation process.

The $y - p_T$ distribution for tritons from minimum-bias Au+Au collisions at $4A$ GeV [2] is presented in Figure 2. The yield is $\sim$ 0.046 tritons/event with $\sim$ 90% of purity selection. Here, the dominant mechanism is coalescence. The purity selection for ^{3}He using the m^2-p/Z correlation is much worse ($\sim 40\%$) because of the large contamination of the background protons and deuterons. Additional information on the charge of the nuclear fragments is required to improve the purity.

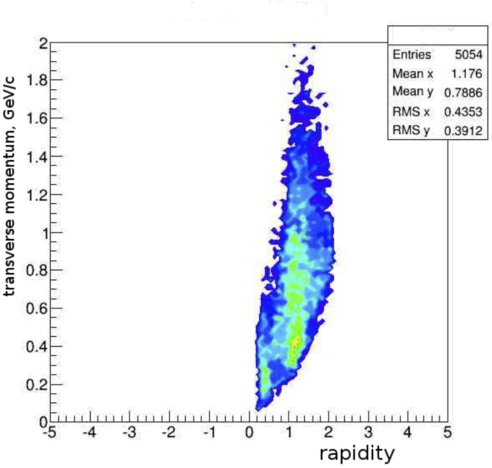

Figure 2: $y - p_T$ distribution for tritons from minimum-bias Au+Au collisions at $4A$ GeV [2]

The yields for deuterons and tritons obtained from the simulation of 100k central Au+Au collisions at 4 A·GeV [2] are $\sim$ 4.1 and $\sim$ 0.24, respectively. The purities of the selection are found to be the same as for the minimum bias events. The dominant reaction mechanism is coalescence for the both nuclei.

In summary, The CBM setup at SIS100 allows to obtain data on the light nuclei production in the mid- and forward rapidity regions. Systematic studies of the light nuclear fragments and hyper-nuclei production with CBM could distinguish different approaches in the description of the relativistic heavy ion collisions [4].

References

[1] L. P. Csernai and J. I. Kapusta, Phys. Rep **131** (1986) 223

[2] V. D. Toneev *et al.*, Nucl. Phys. **A 519** (1990) 463C

[3] V. P. Ladygin, A I. Malakhov and T. A. Vasiliev, CBM Progress Report 2010, Darmstadt 2011, p. 58

[4] J. Steinheimer *et al.*, Phys. Rev. **B 714** (2012) 85

TOF PID

S. M. Kiselev
ITEP, Moscow, Russia

10^6 Au+Au UrQMD events at $4A$, $10A$ GeV (for the setups A, B and C), $25A$ and $35A$ GeV (for the setup C) simulated and reconstructed in the frame of the CbmRoot package were used for this analysis. Setups A: SIS100 with TOF at 6m, B: SIS100 with TOF at 10m, C: SIS300 with TOF at 10m. The TOF resolution σ_{TOF}=80 ps was taken in the TOF hit producer. For global track matching with TOF hits the "nearest hit" mode was selected.

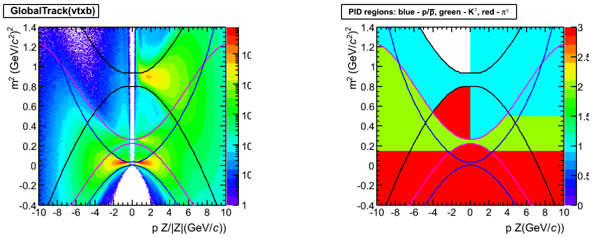

Figure 1: Setup A. Central Au+Au events at $10A$ GeV. Left: distribution of global tracks with the vertex cut on the plane (p, m^2); right: PID regions for different species. $\pm 3\sigma_p(p)$, $\pm 3\sigma_K(p)$ and $\pm 3\sigma_\pi(p)$ boundaries are shown by the solid lines.

Figure 1 (left) shows the distribution of global tracks after a vertex cut for selecting primaries. For different species the PID regions on the plane (p, m^2) are defined in Fig. 1 (right). To increase the purity for anti-protonsm the tracks from the "white" region (mostly includes protons) are excluded from the PID analysis. The PID efficiency is defined as the ratio of the correctly identified tracks to all global tracks, the PID purity is a ratio of the correctly identified tracks to all tracks from the PID region.

Figures 2 and 3 present PID efficiency and purity for $4A$ and $10A$ GeV, respectively. At $4A$ GeV the multiplicity of anti-protons is very low, 3×10^{-5} per event, and the statistic is not sufficient. At $10A$ GeV the multiplicity of anti-protons is 10^{-2} per event. In spite of high PID efficiency for anti-protons, its PID purity is low ($\sim 0.1 - 0.2$) because of the large contribution of tracks from protons. The PID results are weakly sensitive to beam energy (4/$10A$ GeV) and TRD (with/without TRD). In the momentum region $1 < p < 3 - 4$ GeV/c PID efficiency is high, $\sim 0.9 - 1$, PID purity > 0.8, except for anti-protons.

Figure 4 presents PID efficiency and purity at $10A$, $25A$ and $35A$ GeV with the setup C. The PID efficiency is weakly sensitive to the beam energy. PID purity is most sensitive for anti-protons, it increases with the energy up to ~ 0.4 at $35A$ GeV. For other species PID purity changes within $5 - 10\%$.

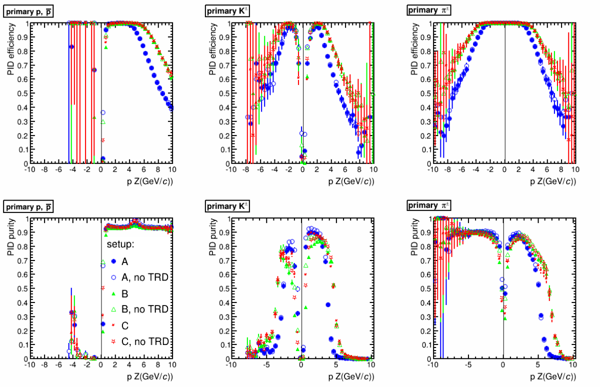

Figure 2: PID efficiency and purity for minimum bias Au+Au events at $4A$ GeV with the setups A, B and C

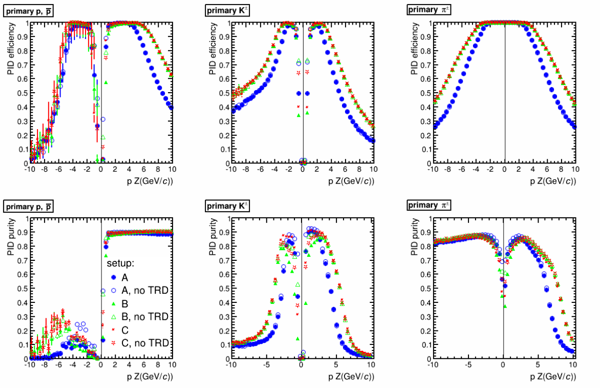

Figure 3: PID efficiency and purity for central Au+Au events at $10A$ GeV with the setups A, B and C

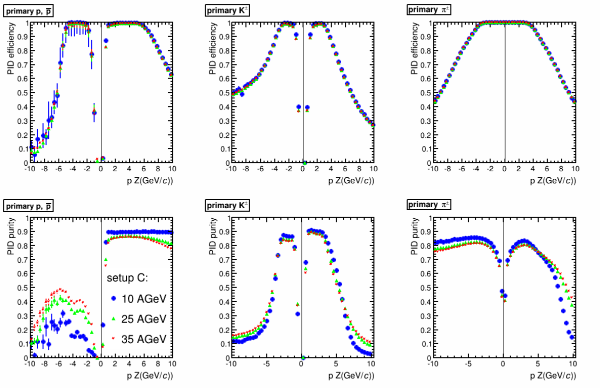

Figure 4: Setup C. PID efficiency and purity for central Au+Au events at $10A$, $25A$ and $35A$ GeV

ϕ meson production in Au+Au collisions and its reconstruction feasibility in the CBM experiment

V. Vovchenko[1,2,3,4], *I. Vassiliev*[1], *I. Kisel*[1,2,3], *and M. Zyzak*[1,2,3]
[1]GSI, Darmstadt, Germany; [2]FIAS, Frankfurt, Germany; [3]Goethe-Universität, Frankfurt, Germany; [4]Taras Shevchenko University, Kiev, Ukraine

The CBM experiment at FAIR aims at studying properties of the QCD diagram at high baryon densities and moderate temperatures. One of the most interesting particles among other rare probes is the ϕ meson, which consists of $s\bar{s}$ pair and can decay inside the fireball. In that case it carries direct information about the production of $s\bar{s}$ pairs. ϕ production of in heavy-ion collisions has earlier been studied in other experiments, such as HADES [1] and NA49 [2]; however, the up to now existing data are rather scarce in the CBM energy range.

To study the production of ϕ mesons at CBM energies and above, and the feasibility of its reconstruction, minimum-bias Au+Au events were generated with the UrQMD-3.4 model at $4A$–$160A$ GeV energies. For each energy 1 million events were generated (see Fig. 1). Among these events only 10% of the most central were considered. The centrality was determined in accordance with the charged multiplicity in the rapidity window of $|y_{\rm c.m.}/y_{\rm beam}| < 0.5$. Additionally, 10^4 central (impact parameter $b = 0$ fm) events generated with the PHSD-3.0 model [3] were analyzed for comparison.

The ϕ meson has a relatively small lifetime ($c\tau \simeq$ 45 fm), and there is a certain probability for it to decay inside the fireball. For this reason, the ϕ meson is not considered a stable particle in transport models such as UrQMD and PHSD by default. Therefore, in order to calculate the ϕ multiplicity they are forced to be stable with respect to decays in UrQMD and PHSD by adjusting the corresponding flag.

The precise measurement of the ϕ/K^- ratio allows to extract the fraction of K^- coming from ϕ decay [1]. The results of calculations for this quantity within UrQMD and PHSD are depicted in Fig. 1. Additionally, experimental data of HADES and NA49 collaborations are shown by symbols with error bars. We note that NA49 data is for Pb+Pb collisions. The data shows a plateau in energy dependence at higher collision energies. This effect is qualitatively well reproduced in UrQMD and PHSD. At low energies ($p_{\rm lab} \lesssim 7$ AGeV), however, a decrease of the ratio with collision energy is shown by the available data but not by the models. Taking into account that available data in this energy range are rather scarce, future measurements with CBM may help to clarify the presence of such an effect.

In order to study the feasibility of ϕ meson reconstruction with CBM, 5 millions central Au+Au events at $6A$ GeV were simulated. K^+ and K^- identified in the TOF detector are combined to pairs by the KF Particle Finder package. The resulting invariant-mass distribution for the K^+K^- pairs is shown in Fig. 2 where the ϕ signal is clearly visible.

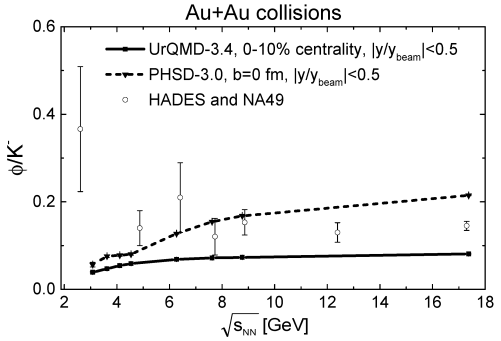

Figure 1: Energy dependence of the ϕ/K^- ratio, calculated in UrQMD and PHSD. Experimental data of the HADES and NA49 collaborations are depicted by the symbols with error bars.

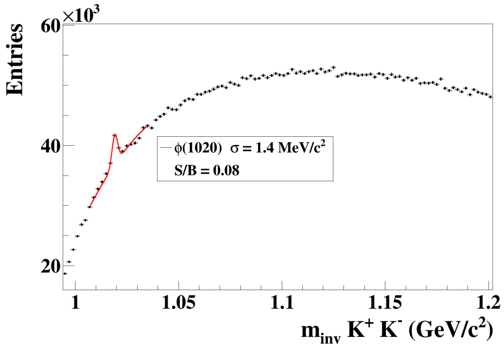

Figure 2: Invariant-mass distribution of K^+K^- pairs for 5 million central Au+Au events at $6A$ GeV. The shape of the combinatorial background is estimated by the mixed-event technique.

References

[1] G. Agakishiev *et al.* [HADES Collaboration], Phys. Rev. **C 80** (2009) 025209

[2] C. Alt *et al.* [NA49 Collaboration], Phys. Rev. **C 78** (2008) 044907

[3] E.L. Bratkovskaya, W. Cassing, V.P. Konchakovski, O. Linnyk, Nucl. Phys. **A 856** (2011) 162

Multi-strange (anti)baryon enhanced production at FAIR energies

I. Vassiliev[1], *I. Kisel*[1,2,3], *M. Zyzak*[1,2,3], *and the CBM Collaboration*

[1]GSI, Darmstadt, Germany; [2]FIAS, Frankfurt, Germany; [3]Goethe-Universität, Frankfurt, Germany

One of the predicted signatures of the phase transition from nuclear matter to a deconfined phase is the enhanced production of multi-strange particles. Additionally the yield of particles carrying strange (anti)quarks is expected to be sensitive to the fireball evolution and formation of the Quark Gluon Plasma (QGP). In order to estimate the effect of QGP creation in the heavy ion collisions we used PHSD 3.0 model [1] — a microscopic off-shell transport approach that consistently describes the full evolution of a relativistic heavy-ion collision from the initial hard scatterings and string formation through the dynamical deconfinement phase transition to the QGP, as well as hadronization, and to the subsequent interactions in the hadronic phase. The yield of Ω^+ hyperon ($\bar{s}\bar{s}\bar{s}$) seems to be very sensitive to the production mechanism at the FAIR energies. The results of our calculations are shown in Fig. 1, where the red points correspond to the partonic phase mechanism and the blue ones — to subsequent interactions in the hadronic phase. Each point is calculated for 5M central Au+Au PHSD (HSD) events. According to the PHSD 3.0 model, most of the Ω^+ particles are produced in the QGP phase.

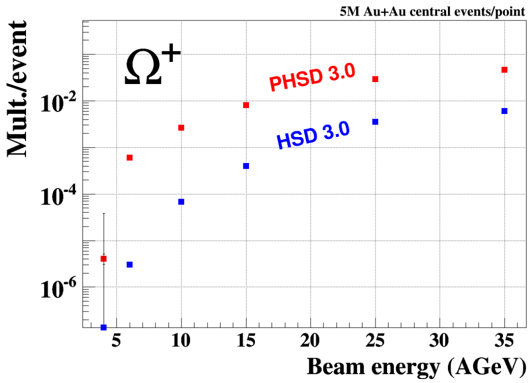

Figure 1: Yields of Ω^+ as a function of the beam energy calculated in the PHSD and HSD models. Each point corresponds to $5 \cdot 10^6$ central Au+Au PHSD (red) or HSD (blue) events.

Multi-strange hyperons will be identified in the CBM experiment by their decays into charged hadrons, which are than detected in the Silicon Tracking System (STS) and the Time-of-Flight (TOF) detector.

To study the performance of multi-strange hyperon reconstruction in the CBM experiment, several sets of $5 \cdot 10^6$ central Au+Au PHSD and HSD events at $4A$, $6A$ and10A GeV for the SIS-100 case and at $15A$, $25A$ and $35A$ GeV for the SIS-300 energy range were simulated. The high statistics allows to calculate also the $\Omega^\pm$ reconstruction efficiency directly, avoiding signal embedding into the PHSD events. Together with the wide range of the beam energies, it allows to investigate the systematic behavior of different physics observables, e.g. direct and elliptic flow, excitation function and antihyperon-to-hyperon ratios.

The Ω^+ hyperon decays into $\bar{\Lambda}K^+$ with the branching ratio of 67.8% and $c\tau$ = 2.46 cm. The STS v13d geometry with 8 double-sided segmented strip detectors, cables and support frames was used for the event reconstruction. Particle identification with the realistic "umbrella" shaped TOF v13a geometry for the SIS-100 energies and v13b for the SIS-300 energies were applied. The KF Particle Finder [2] package was used to reconstruct Ω^+. A typical reconstructed invariant-mass spectrum is shown in Fig. 2. The red line indicates the fit the signal and background by a polynomial plus Gaussian function.

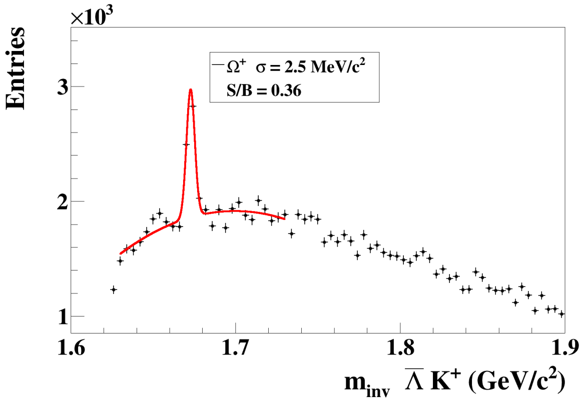

Figure 2: Reconstructed invariant-mass distribution of $\bar{\Lambda}K^+$ pairs in central Au+Au collisions at $25A$ GeV. The red line indicates the signal plus background fit by a polynomial plus Gaussian function.

The Ω^+ reconstruction efficiency results in about 6.2% for central PHSD events. A good signal to background ratio of about 0.36 is observed due to the TOF antiproton particle identification procedure and KF Particle $\bar{\Lambda}$ reconstruction.

References

[1] E.L. Bratkovskaya, W. Cassing, V.P. Konchakovski and O. Linnyk, Nucl. Phys. **A 856** (2011) 162

[2] I. Kisel, I. Kulakov and M. Zyzak, IEEE Trans. Nucl. Science **60** (2013) 3703

Reconstruction of Σ hyperons with ECAL at SIS100

S. M. Kiselev
ITEP, Moscow, Russia

The feasibility of the reconstruction of Σ hyperons using the ECAL was studied on samples of UrQMD events at the SIS100 energies: 10^7 p+C and 10^6 p+Cu minimum bias events at 10 GeV, 10^6 minimum bias and 10^6 head-on p+C events at 30 GeV. The set-up consists of MVD, STS, TOF and ECAL wall of the size X×Y=5.76 × 8.64 m^2 with the beam gap $|Y| < 0.48$ m distanced from a target at 12 m. Reconstructed photons with $p > 0.3$ GeV/c and $\chi^2_{\mathrm{cluster}} < 1000$ have been taken for the analysis. We analyzed the decays $\Sigma^0 \to \Lambda\gamma$ and $\Sigma^+ \to p\pi^0$.

1. $\Sigma^0 \to \Lambda\gamma$. For the reconstruction of $\Lambda \to p\pi^-$ PID information was not exploited. Λ is named by "accepted" if each of its decay products has MC points in at least 4 STS stations, and by "reconstructed" if each decay product has a reconstructed track (≥ 70 % of track hits belong to the same MC track). Single track cut: impact parameter in the target plane for positive and negative tracks (in σ) > 4. Vertex quality cuts: χ^2 of the fitted vertex < 2, distance of closest approach < 0.2 cm. Additional topological cuts: impact parameter of the reconstructed mother track < 0.15 cm, position of the fitted decay vertex along the beam axis in the range 3 - 25 cm. The reconstructed Λ within the range $m_\Lambda \pm 25$ MeV and reconstructed γ were chosen as candidates for Σ^0 analysis. Figure 1 (top) shows an example of the invariant mass distributions of signal and background $\Lambda\gamma$ pairs. Table 1 summarizes characteristics of the analysis: signal yield, acceptance, reconstruction and cut efficiencies, signal-to-background ratios $S/B_{\pm 2\sigma}$ and significances.

Table 1: $\Sigma^0 \to \Lambda\gamma$

system	yield /event	acc. eff.	rec. eff.	cut eff.	S/B /sign.
pC@10	0.004	0.027	0.45	0.12	0.11/2.2
pCu@10	0.017	0.015	0.45	0.13	0.11/1.2
pC@30	0.009	0.042	0.61	0.26	0.08/2.1
pC@30,b=0	0.029	0.042	0.59	0.30	0.08/3.9

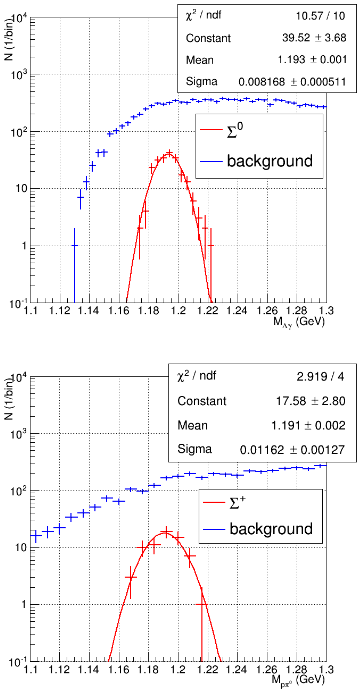

Figure 1: Invariant mass spectra of signal and background $\Lambda\gamma$ (top panel) and $p\pi^0$ (bottom panel) pairs for head-on p+C events at 30 GeV

Table 2: $\Sigma^+ \to p\pi^0$

system	yield /event	acc. eff.	rec. eff.	cut eff.	S/B /sign.
pC@10	0.008	0.011	0.46	0.03	0.08/1
pCu@10	0.018	0.007	0.47	0.02	-
pC@30	0.010	0.022	0.50	0.14	0.04/1
pC@30,b=0	0.030	0.019	0.56	0.19	0.07/2.1

2. $\Sigma^+ \to p\pi^0$. For π^0 candidates the pairs with 0.124$< M_{\gamma\gamma} < 0.144$ GeV/c were selected. No PID was used to select the proton candidates. The positive tracts with the impact parameter in the target plane (in σ) > 5 have been used to reject the positive primaries. Figure 1 (bottom) shows an example of the invariant mass distributions of signal and background $p\pi^0$ pairs of selected candidates.

Table 2 summarizes characteristics of the analysis. Because of the lower efficiencies we have ~ 5 times less signal pairs than for the channel $\Sigma^0 \to \Lambda\gamma$. To estimate S/B for the p+Cu system, the current statistics is not sufficient.

Results for head-on p+C events at 30 GeV agree with those obtained with light ECAL in [1]. In order to achieve a reasonable significance level of about 10, two orders of magnitude more event statistics is required.

References

[1] S. M. Kiselev, CBM Progress Report 2012, Darmstadt 2013, p. 105

Reconstruction of $\eta'(958)$ with ECAL at SIS100

S. M. Kiselev
ITEP, Moscow, Russia

The feasibility of $\eta'(958)$ reconstruction using the ECAL was studied on samples of UrQMD events at the SIS100 energies: 10^7 p+C and 10^6 p+Cu minimum bias events at 10 GeV, 10^6 minimum bias and 10^6 head-on p+C events at 30 GeV. The set-up consists of MVD, STS, TOF and ECAL wall of the size X×Y=5.76 $\times$ 8.64 m^2 with the beam gap $|Y| < 0.48$ m distanced from a target at 12 m. Reconstructed photons with $p > 0.5$ GeV/c and $\chi^2_{cluster} < 1000$ have been taken for the analysis. We analyzed the decay $\eta'(958) \rightarrow \pi^+\pi^-\eta$ (BR=43%).

In the invariant mass spectrum of MC primaries there is a peak at $m_{\eta'(958)}$. Figure 1 demonstrates an example for p+Cu at 10 GeV. We assume that triples of primaries in the range $0.960 < M_{\pi^+\pi^-\eta} < 0.964$ GeV are from "primary" $\eta'(958)$. There is large background; the part of the "primary" $\eta'(958)$ corresponding to the signal is ~60 %.

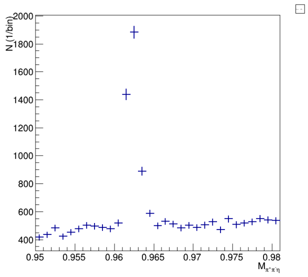

Figure 1: Invariant mass spectrum of $\pi^+\pi^-\eta$ triplets of primaries for p+Cu at 10 GeV

An example of invariant mass distributions for $\gamma\gamma$ pairs around η mass is shown in Fig. 2. The peak from η has σ ~20 MeV. For η candidates the pairs with $0.530\,\mathrm{GeV/c^2} < \mathrm{M}_{\gamma\gamma} < 0.560\,\mathrm{GeV/c^2}$ were selected.

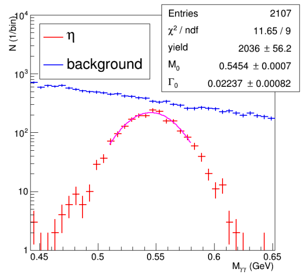

Figure 2: Invariant mass spectra of $\gamma\gamma$ pairs with $p_T^{\gamma\gamma} >$ 0.2 GeV/c for p+C at 10 GeV

PID information was not used to select π^+ and π^- candidates. The impact parameter cut < 4 (in σ) was used to reject secondary charged tracks. Figure 3 shows an example of invariant mass distributions for selected $\pi^+\pi^-\eta$ triples. Table 1 summarizes characteristics of the analysis: signal yield, acceptance, reconstruction and cut efficiencies, signal-to-background ratios $S/B_{\pm 2\sigma}$ and significances.

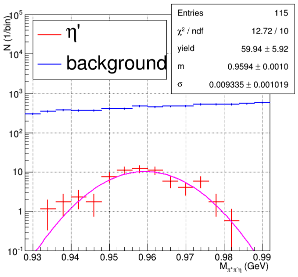

Figure 3: Invariant mass spectra of selected $\pi^+\pi^-\eta$ triplets for head-on p+C collisions at 30 GeV

Table 1: $\eta'(958) \rightarrow \pi^+\pi^-\eta$

system	yield x100	acc. eff.	rec. eff.	cut eff.	S/B /sign.
pC@10	0.09	0.011	0.98	0.29	0.061/1.0
pCu@10	0.45	0.057	0.96	0.12	-
pC@30	0.3	0.035	0.99	0.45	0.014/0.6
pC@30,b=0	1.1	0.030	0.99	0.37	0.014/1.0

To estimate S/B for the p+Cu system, the employed statistics is not sufficient. In order to achieve a reasonable significance level of about 10, two orders of magnitude more event statistics is required. The channel $\eta' \rightarrow \pi^0\pi^0\eta$ (BR=22%) has one order of magnitude lower total detection efficiency and needs even more statistics. Because of the small branching ratio, the channel $\eta' \rightarrow \gamma\gamma$ (BR=2%) also requires higher statistics.

Results for head-on p+C events at 30 GeV agree with those obtained with light ECAL at 6 m presented earlier [1].

References

[1] S. M. Kiselev, CBM Progress Report 2012, Darmstadt 2013, p. 104

Low-mass di-electron reconstruction in the CBM experiment*

E. Lebedeva and C. Höhne
Justus-Liebig-Universität, Gießen, Germany

One of the main purposes of the CBM experiment at the upcoming FAIR facility is the reconstruction of low-mass vector mesons. The CBM experiment will be capable to reconstruct low-mass vector mesons in both leptonic decay channels: muons and electrons. The current status of low-mass di-electron simulations at 3.5A GeV, 8A GeV (SIS-100) and 25A GeV (SIS-300) will be presented in this report.

The simulations were performed with the latest version of the CBMROOT software (February 2015). UrQMD v3.3 was used to generate the event background. Signals were implemented using the PLUTO decayer with multiplicities from HSD. The following geometries were used in the simulations: STS - $v13d$, RICH - $v14a\_1e$ (8AGev) or $v14a\_3e$ (25AGeV), TRD - $v14a\_1e$ (8A GeV) or $v14a\_3e$ (25A GeV), TOF - $v13b$. The RICH geometry implemented here is based on a CAD design and includes realistic material budgets for all components [1]. The smearing algorithm was used for the TRD detector response simulation. In order to avoid additional background from gamma-conversions in the target, a 25μm Au target was used.

Electron identification was performed using the RICH, TRD and ToF detectors. The identification methods in the RICH and TRD detectors are based on an Artificial Neural Networks with specified input parameters for each detector.

The dominant background in e^+e^- pairs are random combinations of electrons and positrons from π^0-Dalitz decay and γ conversion. The aim of the background suppression strategy is to reject those pairs even if they were only partially reconstructed. The first cut is a pair cut in which all e^+ e^- pairs with invariant mass below 25 MeV are removed assuming that they originate from γ conversion. In the next two cuts fully reconstructed and identified electrons are combined with potential electron candidates that have momentum information only either because they left the acceptance after/within the STS or they escaped the electron identification because of inefficiencies. The last cut on p_t must be applied very gently, as it can reject the signal as well. In addition another topology cut can be used, which allows to suppress background pairs if one track was not fully identified in all detectors.

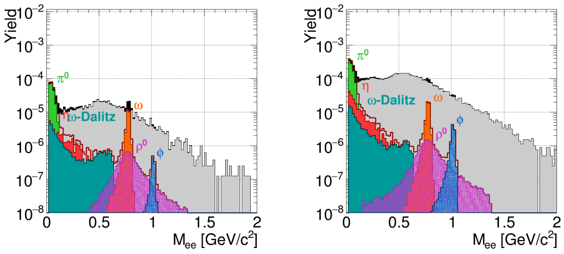

Figure 1: Invariant mass spectra for 2M central Au+Au collisions at a beam energy of 8A GeV (left) and 25A GeV (right) after applying all cuts

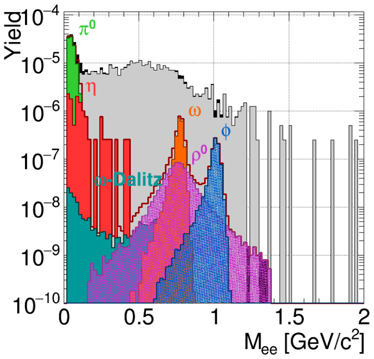

Figure 2: Invariant mass spectra for 1M central Au+Au collisions at 3.5A GeV beam energy after applying all cuts

For the first time a low-mass di-electron simulation was obtained for central Au+Au collisions at 3.5A GeV beam energy. Electron identification for this simulation was performed with RICH and ToF information only. The magnetic field was scaled down by 50 % in order to account for the lower momenta. Invariant mass distributions after applying all background rejection cuts are presented in Figs. 1 and 2. The S/B ratios and efficiencies for low-mass mesons are summarized in Table 1.

Table 1: S/B ratios and efficiencies after applying all cuts

	3.5AGeV		8AGeV		25AGeV	
	S/B	Eff.[%]	S/B	Eff.[%]	S/B	Eff.[%]
ρ	-	1.97	-	1.70	-	1.58
ω	0.090	2.31	0.74	1.89	0.17	1.68
ϕ	0.096	2.92	0.07	2.61	0.10	2.40

References

[1] S. Lebedev and C. Höhne, CBM Progress Report 2013, Darmstadt 2014, p. 98

---

* This work was supported by HIC for FAIR, by the GSI F&E-Cooperation with Giessen, and by BMBF grant 05P12RGFCG.

Background rejection in the dilepton analysis with the CBM-Micro Vertex Detector*

E. Krebs[1], *T. Galatyuk*[2,3], *and J. Stroth*[1,3] *for the CBM collaboration*
[1]Goethe-Universität, Frankfurt, Germany; [2]Technische Universität, Darmstadt, Germany; [3]GSI Darmstadt, Germany

The light vector mesons ρ, ω and ϕ are excellent probes of the strongly interacting matter under extreme conditions. Their leptonic decay channels are of interest as leptons leave the hot and dense fireball without strong interaction and may reveal information on the characteristics of the matter created in the collisions. Single electron or positron tracks from incompletely detected γ conversions and Dalitz decays of π^0 mesons are the most abundant source contributing to the significant combinatorial background. This study aims at exploring the use of the topology of MVD hits to reduce this background, despite of the fact that additional background is produced because of the material budget of the MVD.

To do so, electron pairs from meson decays were simulated from a thermal source for central Au+Au reactions at SIS-100 energies such that the meson spectra are consistent with p_T and rapidity distributions measured by NA49 [1]. The decays of various sources simulated with the Pluto event generator [2] are embedded into the hadronic environment obtained from UrQMD transport model calculations. The magnetic field was set to 100% strength and δ electrons with energies above 1 MeV were added equivalent to a 10 kHz interaction rate.

The strategy of background rejection comprises several steps. In order to identify leptons from photon conversions that were produced outside of the target region, each reconstructed track is extrapolated to the primary decay vertex and removed from the analysis depending on its deviation from the vertex. One characteristic for conversion pairs is their small opening angle. A wedge cut is applied taking into account the opening angle of an identified electron to its closest neighbor with particle identification and product of the momenta of the two tracks. As lepton tracks from background sources can predominantly be found at low transverse momenta, such tracks are rejected as well [3].

The MVD of the CBM experiment can further contribute to reduce this background by including hits from the MVD into the track reconstruction. An improved rejection of pairs originating from the target region could be observed. Previous studies have shown that the MVD stations are also a source for γ conversions which can not be effectively rejected by the vertex extrapolation cut, especially in the first two stations closest to the target. Extrapolating tracks to the first MVD station and requiring that they are in its acceptance helped to better suppress off-vertex tracks from γ conversions and resulted in an improved signal-to-background ratio for the low mass vector mesons ρ, ω and ϕ as depicted in Tab. 1. The invariant mass spectrum of the full cocktail after all analysis steps is presented in Fig. 1.

Table 1: Signal-to-background ratios and significance for dilepton decays in different mass regions

Mass Range $\left[\frac{\mathrm{GeV}}{\mathrm{c}^2}\right]$	MVD Stations	S/B	$\mathrm{S}/\sqrt{\mathrm{S}+\mathrm{B}}$
$0-0.15$	0 4	6.56 8.27	31.3 29.4
$0.15-0.6$	0 4	0.10 0.14	3.7 3.7
$0.6-1.2$	0 4	0.15 0.21	4.9 5.4
$\omega \to e^+e^-$	0 4	0.67 0.96	7.4 8.0
$\phi \to e^+e^-$	0 4	0.13 0.19	0.74 0.86

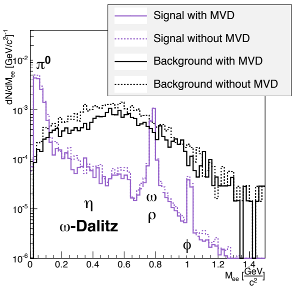

Figure 1: Invariant mass spectrum after all cuts are applied for central Au+Au collisions at $8A$ GeV

Lately, there have been major updates to the CBM software with more realistic digitization and geometries for the CBM detectors, including the MVD [4]. Their effects on the dielectron reconstruction are under investigation.

References

[1] C. Alt *et al.* (NA49 Collaboration), Phys. Rev. **C 78** (2008) 044907

[2] I. Froehlich *et al.*, PoS(ACAT2007)076 (2007)

[3] T. Galatyuk, PhD Thesis, Goethe-Universität, Frankfurt am Main 2009

[4] S. Amar-Youcef *et al.*, *Status of the CBM MVD simulation model*, this report

---

* This work has been supported by BMBF (05P12RFFC7), HIC for FAIR, HGS-HIRe, H-QM, and GSI.

Towards a realistic event generator for in-medium and QGP dileptons

F. Seck[1], *I. Fröhlich*[2], *T. Galatyuk*[1,3], *J. Markert*[2], *and J. Stroth*[2,3]
[1]Technische Universität, Darmstadt, Germany; [2]Goethe-Universität, Frankfurt, Germany; [3]GSI, Darmstadt, Germany

Until now the hadronic cocktails produced with the event generator Pluto [1] for the HADES and CBM experiments included only a contribution from freeze-out sources.

However as dileptons are radiated from the fireball during the whole space-time evolution, medium effects like the broadening of the ρ should also be included in the simulations. Calculations of the in-medium ρ spectral function by R. Rapp and J. Wambach [2] demonstrate that a large part of the in-medium ρ mesons feed into the mass region below the ρ/ω pole mass down to zero masses.

The basic idea behind the event generator under development is to simulate an ensemble of events with a transport model like UrQMD [3]. The space-time evolution of these events is then divided into four-dimensional cells (similar approaches were conducted in [4, 5]). Afterwards the quantities needed as input for the Rapp - Wambach spectral function, i.e. temperature T, the baryon chemical potential μ_B (or density ϱ_B) and the collective flow velocity $\vec{v}_{coll}$, can be extracted locally for each cell.

The observation that the momentum distributions start to resemble Gaussians after ∼5 fm/c suggests a thermalization of the system. We have thus used a Maxwell-Boltzmann fit to determine the temperature of the cell. The net baryon as well as the energy density can be obtained with the four-current method [6].

The temperature and baryon density evolution results in the trajectory of the cell. Figure 1 shows this trajectory followed by the cell at the center of the collision.

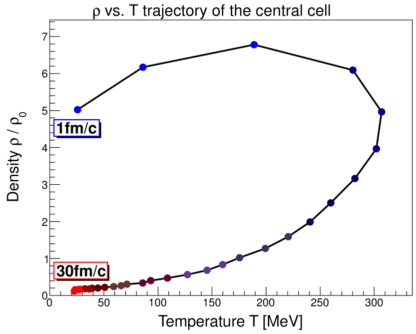

Figure 1: Phase-space trajectory of the central cell in Au+Au at $20A$ GeV as extracted from UrQMD tranport model calculations. A marker is indicating the time evolution in 1 fm/c steps.

The modular structure of Pluto makes it feasible to customize the event generator and incorporate models of in-medium physics, like the Rapp - Wambach spectral function, as well as the emission due to multi-pion annihilation and QGP radiation as plug-ins.

If the input parameters to the thermal emission rates exceed a certain threshold we will use the in-medium spectral function for the dileptons emitted from this cell. Otherwise the vacuum spectral functions will be utilized.

Figure 2 shows the hadronic cocktail produced with Pluto for Au+Au collisions at a beam energy of $25A$ GeV with the in-medium ρ and ω contributions provided by R. Rapp. In addition the dileptons stemming from QGP radiation are included in the cocktail.

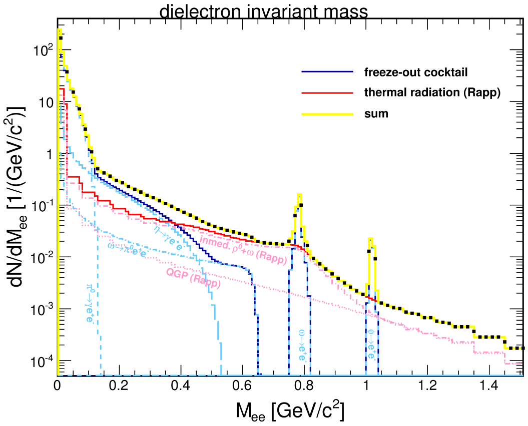

Figure 2: Dilepton cocktail for Au+Au collisions at 25 AGeV produced with Pluto including also in-medium and QGP contributions

In the upcoming months the focus will lie on the calculation of the dilepton emission rates for different collision systems at FAIR energies with a spectral function package from R. Rapp. Consistency checks will be done as well.

The main objective of this work is then the implementation of this concept into Pluto in such a way as to enable users to pick the collision system of their choice and simulate a realistic dilepton mass spectrum for their analyses.

We thank Ralf Rapp for providing m-p_T-distributions of the in-medium spectral function.

References

[1] I. Fröhlich *et al.*, PoS(ACAT2007)076 (2007)
[2] R. Rapp and J. Wambach, Adv. Nucl. Phys. **25** (2000) 1
[3] S. Bass *et al.*, Prog. Part. Nucl. Phys. **41** (1998) 255
[4] J. Kapusta, Nucl. Phys. **A 715** (2003) 709
[5] S. Endres *et al.*, arXiv:1412.1965
[6] S. Vogel *et al.*, Phys. Rev. **C 78** (2008) 044909

Towards e^+e^- conversion*

S. Reinecke and K.-H. Kampert
Bergische Universität, Wuppertal, Germany

Dalitz decays of π^0 and η ($\pi^0/\eta \rightarrow e^+e^-\gamma$) typically are, after all analysis steps, the dominant part of the background in the dilepton decay analysis of rare vector mesons, even in view of the good particle ID capabilities of CBM. In order to precisely estimate the amount of Dalitz contributions in the final event sample, one has to measure the multiplicity of π^0 and η; the branching ratio into Dalitz decays is then well known. For counting π^0 and η the main decay channel $\pi^0/\eta \rightarrow \gamma\gamma$ is best suited. The detection of the two photons can be done via conversion ($\gamma \rightarrow e^+e^-$) in the detector material or in the target itself and a subsequent reconstruction of the conversion electrons with the STS and the RICH detector. This idea was successfully applied for example by HADES [1] and is now under investigation for CBM as well. So far only an exploratory study is available [2]. In the report presented here first steps towards a realistic study will be shown using all CbmRoot developments since then.

As a starting point for the understanding of the simulation framework we performed so-called detector tomography studies. These studies consist of photons (generated with the box generator) converting somewhere in the detector material. With a graphical visualisation of the conversion coordinates from MC-true data, a cross-check of the implemented geometries is possible as well as the identification of parts with high material budget. The conversion points in the whole CBM detector (top view) are shown in Fig. 1, where the different subdetectors of CBM can be clearly recognized.

The next step towards a full conversion analysis is the reconstruction of π^0 reconstructing the two decay photons via $\gamma \rightarrow e^+e^-$ conversion in the target. In the simulation reconstructed tracks from the GlobalTrack array are matched to MCtracks, thus invariant mass spectra using the four true decay electrons can be calculated. Using MC-true momenta the results fit the theoretical mass for the π^0. If the invariant mass is calculated based on reconstructed quantities, the result shown in Fig. 2 is obtained (for 20k central Au+Au collisions at $25A$ GeV).

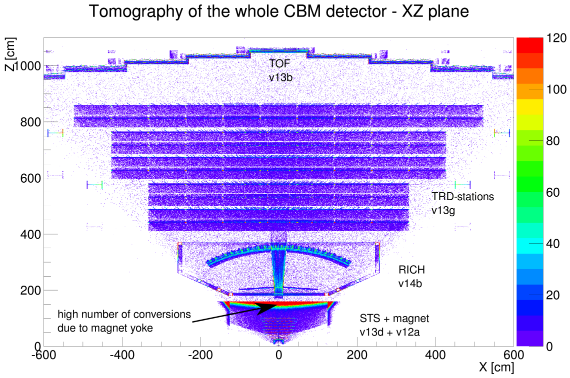

Figure 1: Tomography picture of the whole CBM detector in the XZ-plane (top view). The color scale marks the number of conversions and is therefore an indicator for the material budget.

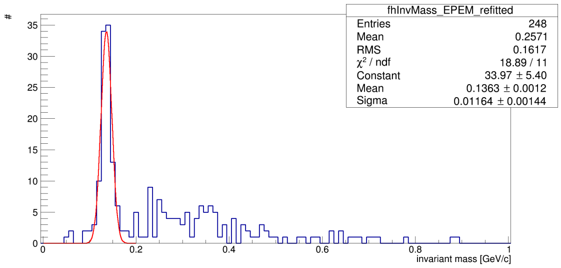

Figure 2: Invariant mass spectra of π^0 (identified via MC-truth) with refitted momenta (at the primary vertex) of the e^+/e^-. The fit of the π^0 peak considered the range up to 0.2 GeV/c^2 only.

The π^0 peak is clearly visible. A Gaussian fit of the peak-region gives a mean value of $\sim$ 136 MeV/c^2 and a sigma of $\sim$ 11 MeV/c^2. However, roughly half of the entries result in a wrong, broadly distributed mass. This broadened mass distribution has to be related to wrong momentum reconstruction or multiple scattering of the electrons. More detailed understanding of this finding is necessary as it would be an important efficiency loss in the π^0 reconstruction.

The KFParticle package provides the reconstruction of a large variety of particles, including the π^0. Results can be compared to the direct reconstruction as described above once the full π^0 reconstruction using all identified electrons is established.

References

[1] G. Agakishiev *et al.*, Phys. Rev. **C 88** (2013) 024904

[2] M. Klein-Bösing, *Development of a Transition Radiation Detector and Reconstruction of Photon Conversions in the CBM Experiment*, dissertation thesis, Münster 2009

---

* Work supported by BMBF 05P12PXFCE

π^0 reconstruction through a γ-conversion method with KF Particle Finder in the CBM experiment*

M. Zyzak[1,2,3], *I. Kisel*[1,2,3], *and I. Vassiliev*[1]

[1]GSI, Darmstadt, Germany; [2]Goethe-Universität, Frankfurt, Germany; [3]FIAS, Frankfurt, Germany

The CBM experiment is being designed to study heavy-ion collisions at extremely high interaction rates and track densities. One of the main observables for CBM are light vector mesons decaying through dilepton channels, which are of the particular importance for the physics program of the experiment. Because of the low branching ratio the key issue for reconstruction of light vector mesons is background suppression. Being a major source of this background, π^0 and γ-conversion have to be carefully studied.

The main decay channel of π^0 is the $\pi^0 \rightarrow \gamma\gamma$ channel with a branching ratio of 98.8%. The γ can be reconstructed in the Silicon Tracking System (STS) when it was converted into an electron-positron pair in the material or support structures of the detector: $\gamma \rightarrow e^+e^-$. To study this decay, π^0 reconstruction through a γ-conversion method was implemented in the KF Particle Finder package for short-lived particle reconstruction.

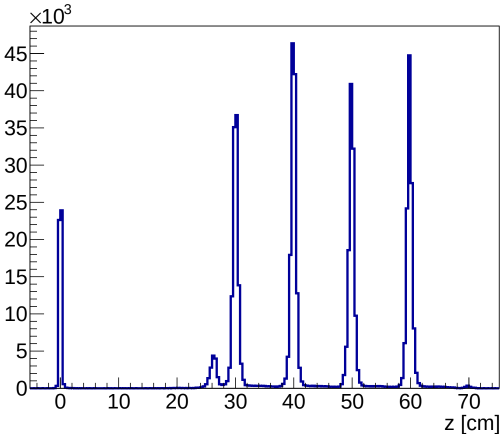

Figure 1: Distribution of the z-position of reconstructed γ particles. The obtained histogram represents the positions of the target, the beam pipe window and four stations of the STS detector.

At the first stage tracks from electrons and positrons registered in STS are selected using particle identification (PID) information from the Ring Image Cherenkov Detector (RICH), Transition Radiation Detector (TRD) and Time of Flight (ToF) detector. Selected tracks are combined into γ candidates. Based on the Kalman filter mathematics, the KF Particle Finder package allows to achieve a high reconstruction quality of the particles. For example, the distribution of the reconstructed z-position nicely represents the structure of the detector: the target at 0 cm, the beam pipe window at 26 cm and four stations of the STS detector at 30, 40, 50 and 60 cm (see Fig. 1). Then the γ-candidates within a 3σ region around the peak position ($0\ \mathrm{MeV}/c^2$) are selected and combined with each other. The high quality of the γ candidates allows reconstruction of π^0 with a width of $1.7\ \mathrm{MeV}/c^2$ and signal to background ratio of 0.77 already for 5 million central Au+Au events at $25A$ GeV (see Fig. 2).

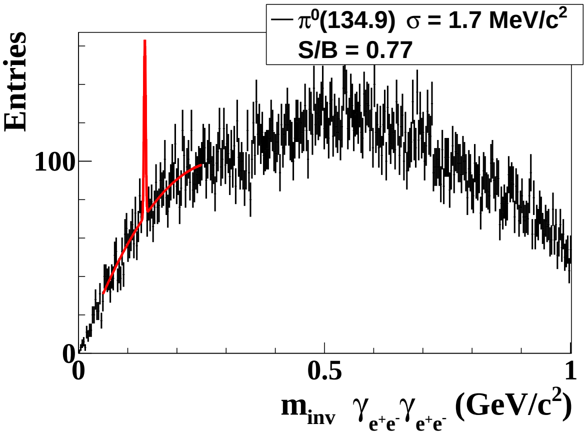

Figure 2: Mass distribution of $\gamma\gamma$ pairs for 5 million central Au+Au events at $25A$ GeV using PID information form the RICH, TRD and ToF detectors. The peak from π^0 is nicely seen with a width of $1.7\ \mathrm{MeV}/c^2$ and a signal to background ratio of 0.77.

The average gamma conversion factor within the STS detector is about 6.5%. This gives a probability of $4 \cdot 10^{-3}$ for both γ daughters to produce tracks. Tacking into account the efficiency of the track finding, PID detector and particle construction, the overall π^0 reconstruction efficiency is about 10^{-6}. However, the big advantage of the method is high resolution and signal to background ratio.

Summarizing, π^0 reconstruction was implemented in the KF Particle Finder package. A high quality of the obtained π^0 particles allows to study the background for dielectronic decays of rare probes.

---

* Work supported by HICforFAIR, FIAS and HGS-HIRe for FAIR.

Thermal di-muons at FAIR energy

S. Samanta[1]*, S. Chattopadhyay*[2]*, S. Das*[1]*, and S. K. Ghosh*[1]
[1]Bose Institute, Kolkata, India; [2]Variable Energy Cyclotron Centre, Kolkata, India

Lepton pairs are expected to serve as a probe of the QGP because they are electromagnetically interacting particles. So the mean free path of the leptons exceed the size of the system formed after the heavy ion collisions and hence the leptons leave the system undisturbed after their production, carrying the information about the initial state of the system. Furthermore, thermal di-leptons are important as they carry the information of temperature and chemical potential of the system and they are expected to dominate in the intermediate invariant mass region. Here we have estimated thermal di-muon production in the QGP phase at FAIR energy and applied them to MUCH simulations for the CBM experiment at FAIR, Germany.

We assume that, in heavy-ion collisions, large initial temperature T_i or large chemical potential μ_i lead to the formation of thermally a equilibrated quark-gluon plasma (QGP). The system then evolves in space and time. With decreasing T and μ, there is a first-order phase transition from QGP to the hadronic phase. In the QGP phase, dileptons are produced dominantly from quark-antiquark annihilation. In this process, a quark interacts with an antiquark to form a virtual photon which subsequently decays into a lepton pair. In case of massless quark and antiquark, the number of dileptons produced per unit dilepton invariant mass squared M^2, per unit four-volume, is given by [1]

$$\frac{dN_{\mu^+\mu^-}}{dM^2 d^4x} = N\frac{\sigma(M)}{2(2\pi)^4}M^2 f_1(\epsilon)F_2(\frac{M^2}{4\epsilon})(\frac{2\pi}{w(\epsilon)})^{1/2}, \quad (1)$$

with $N = N_c N_s^2 \sum_{f=1}^{N_f}(e_f/e)^2$ (= 20/3 for 2 flavour) where N_c, N_s are color and spin degeneracy factors respectively, N_f is the number of flavour, e_f is the electric charge of a quark with flavour f, $\sigma(M) = \frac{4\pi}{3}\frac{\alpha^2}{M^2}\sqrt{(1-\frac{4m_l^2}{M^2})}(1+\frac{2m_l^2}{M^2})$, α is the fine structure constant, m_l is the mass of the lepton (in our present analysis m_l is the mass of muons), $F_2(E) = -\int_\infty^E f_2(E')dE'$, f_1 (f_2) is the quark (antiquark) distribution function, $\epsilon(M)$ is the root of the equation $\frac{d}{dE}[lnf_1(E) + lnF_2(\frac{M^2}{4E})]_{E=\epsilon} = 0$, $w(\epsilon) = -[\frac{d^2}{dE^2}(lnf_1(E) + lnF_2(\frac{M^2}{4E}))]_{E=\epsilon}$.

Eq. 1 is valid for a static plasma in which T and μ are held fixed. But in heavy-ion collisions, the system will expand with time, and as a result T and μ will decrease. For simplicity we assume one dimensional Bjorken expansion [2] for which $d^4x = \pi R_A^2 \tau d\tau dy$, where R_A is the radii of the colliding nuclei, y is the fluid rapidity and τ is proper time. For Au+Au collisions at $\sqrt{s_{NN}} = 8$ GeV, the initial time of the thermalized fireball is taken as 1 fm. One can estimate T_i and μ_i applying conservation laws of net-baryon number and entropy. If we assume that the entire evolution of the fireball from the initial time until the freeze-out time is strictly adiabatic, we can relate the initial entropy density and net-baryon density with freeze-out observables by the relations $s_i \simeq \frac{1}{\pi R^2 \tau_i}(\frac{ds}{dn}\frac{dn}{dy})_f$ and $n_{b_i} \simeq \frac{1}{\pi R^2 \tau_i}(\frac{dn_b}{dy})_f$, where $s_i = c_s^2((148/30)\pi^2 T_i^3 + 6\mu_i^2 T_i)$, $(\frac{ds}{dn})_f = c_s^2/2.04(37\pi^4/15 + \mu_f^2\pi^2/T_f^2) + 4c_s^2 T_f/\mu_f$ and $n_{bi} = 2/3(\mu_i T_i^2 + \mu_i^3/\pi^2)$. c_s is the speed of sound. Using the available experimental data near $\sqrt{s_{NN}} = 8$ GeV, we have estimated T_i and μ_i as 190 MeV and 1060 MeV, respectively. To obtain the time evolutions of T and μ we have used the equations $n_b\tau = \text{const.}$ and $\epsilon\tau^{1+c_s^2} = \text{const.}$ assuming $P = c_s^2\epsilon$ ($c_s^2 = \text{const.}$) where P is the pressure and ϵ is the energy density given by $\epsilon = 37\pi^2 T^4/30 + 3\mu^2 T^2 + 3\mu^4/(2\pi^2)$.

With the above mentioned formalism we estimated invariant mass and transverse-momentum spectra of thermal di-muons. Using those theoretical calculations we generated four-momenta of μ^+ and μ^- and used them in simulations with CbmRoot, employing the FairAsciiGenerator as our primary event generator. The geometry used in this simulation is the CBM muon setup for SIS300. After passing through absorbers and detectors, we reconstructed the invariant mass of muon pairs. We applied several cuts like hits in MUCH detectors ≥ 14, hits in STS detectors ≥ 4 and $\chi^2 < 3$. We compared the reconstructed invariant mass to that of muon pairs from the decay of low-mass vector mesons (ρ and ω). The latter were simulated using the PLUTO event generator. Figure 1 shows the reconstructed di-muon invariant mass spectrum. In the low-mass region the thermal contribution is buried inside low-mass vector mesons. However, they are important in the intermediate-mass region.

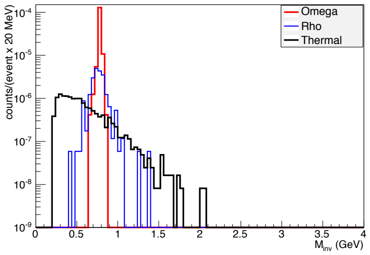

Figure 1: Reconstructed invariant mass of di-muons

References

[1] C. Y. Wong, Phys. Rev. **C48** (1993) 902

[2] J. D. Bjorken, Phys. Rev. **D 27** (1983) 140

Sensitivity of MUCH for the extraction of the fireball temperature from di-lepton spectra*

K. Dey[1,2], *P. P. Bhaduri*[3], *S. Chattopadhyay*[3], *and B. Bhattacharjee*[1]

[1]Department of Physics, Gauhati University, Guwahati, India; [2]Department of Physics, Bodoland University, Kokrajhar, India; [3]Variable Energy Cyclotron Centre, Kolkata, India

The NA60 collaboration reported an excess of muon pairs with respect to the predicted yield at the intermediate mass region $1\,\mathrm{GeV}/c^2 < M < 2.5\,\mathrm{GeV}/c^2$ in In+In collisions at $158A$ GeV [1]. The transverse mass distribution of these excess dimuons can well be described by an exponential function and thus has a thermal origin. In the low mass region, the effective temperature increases with invariant mass because of the development of strong radial flow in the late phase of the collision, whereas in the intermediate mass range, the effective temperature drops significantly. This suggests that above 1 GeV/c^2, the emission source of thermal dimuons is largely partonic in origin, when radial flow has not yet built up [1]. The CBM experiment at FAIR will also address the above issue by scanning the dilepton spectra starting from low mass vector meson (LMVM) up to charmonia at both SIS100 and SIS300. The MUCH (Muon Chamber) detector consisting of a segmented absorber system and detector layers (sector-shaped gaseous chambers) will be responsible for the muon detection. It is therefore important to study the feasibility of a precise determination of the effective temperature with the MUCH setup. In this report an attempt has therefore been made to study the sensitivity of MUCH for the extraction of the fireball temperature from the transverse mass distribution.

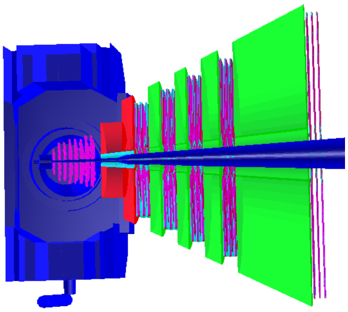

Figure 1: Schematic view of MUCH (SIS-100b) with STS and dipole magnet. The first absorber is made of carbon (60 cm), the others of iron (20 cm + 20 cm + 30 cm + 135 cm).

The simulation was performed for central Au+Au collisions at E_{lab} = $8A$ GeV within the CBMROOT framework (JULY14) for standard the SIS-100b (5 absorbers) geometry (Fig. 1). Background particles and signal muons (from ϕ decay) were generated using the UrQMD and PLUTO [2] event generators, respectively. GEANT3 was used to transport the generated particles through the detector set-up. To account for a realistic detector geometry, the readout modules are segmented in pads for obtaining the final response. For the present study, a 1° segmentation scheme was implemented. Furthermore, *local maxima finder* were incorporated to the simulation as cluster deconvolution algorithms to reconstruct hits. The hits thus generated are used for the tracking. The invariant-mass technique was used to reconstruct ϕ mesons (Fig. 2).

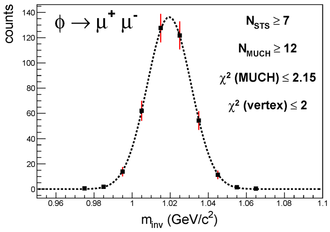

Figure 2: Reconstructed invariant mass spectrum of $\phi \rightarrow \mu^+\mu^-$

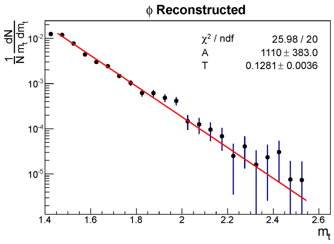

Figure 3: Transverse mass spectra of ϕ mesons for central Au+Au collisions at $8A$ GeV

The reconstructed transverse mass spectra were fitted with a simple exponential $1/m_T dN/dm_T \sim \exp(-m_T/T_{\mathrm{eff}})$ as shown in Fig. 3. The resulting inverse slope known as effective temperature (T_{eff}) is found to be (128.1 ± 3.6) MeV, which is in agreement with the input temperature $T = 125$ MeV within the uncertainty. We thus conclude that with the SIS-100b geometry the determination of temperature of the fireball is a possibility.

References

[1] R. Arnaldi (NA60 collaboration), Eur. Phys. J. **C 59** (2009) 607

[2] `http://www-hades.gsi.de/computing/pluto`

---

* Work supported by DST, Govt. of India

Reconstruction of Drell-Yan di-muons with CBM

P. P. Bhaduri and S. Chattopadhyay
Variable Energy Cyclotron Centre, Kolkata, India

The generation of muon pairs originating from the Drell-Yan (DY) process at FAIR energies is described elsewhere [1]. In this report we describe the full simulation and reconstruction of the DY di-muon spectra, using the CBM muon detector system optimized for Au+Au collisions at 25A GeV. The SIS-300 configuration of the muon detection system, aimed for J/ψ measurements, comprises of 6 absorbers and 6 tracking stations located between the absorber segments. The first absorber is made of 60 cm graphite; all others are of iron [2].

The DY event generator creates a Drell-Yan di-muon, decays it into two oppositely charged muons in the mother rest frame and finally boosts the two muons into the lab frame. The four-momenta of the two muons are stored in a ROOT file on an event-by-event basis. We have developed the FairDYMuonGenerator class which essentially reads the ROOT file and adds these two DY muon tracks to the FairStack via the FairPrimaryGenerator class. The track vertices are all chosen to be zero ($v_x = v_y = v_z = 0$). In order to optimize the computations, events are then simulated by embedding one DY muon pair into the background particles generated by UrQMD for Au+Au collisions at 25A GeV. Particles are passed through the CBM detector system using the GEANT3 transport engine. Tracks are reconstructed using the standard reconstruction routines provided by the CbmRoot package. For analysis, tracks having (i) more than 6 STS hits, (ii) more than 17 muon hits, (iii) track $\chi^2_{\mathrm{STS}} \leq 1.5$, (iv) track $\chi^2_{\mathrm{MUCH}} \leq 1.5$ and (v) $\chi^2_{\mathrm{vertex}} \leq 2$ are selected. The cut parameters are optimized based on previous studies for J/ψ detection in the di-muon channel.

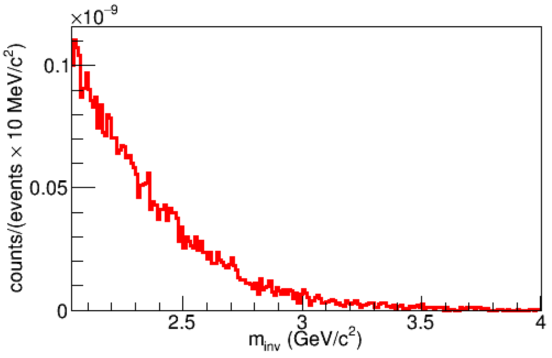

Figure 1: Invariant mass distribution of muon pairs from the Drell-Yan process, reconstructed in Au+Au collisions at 25A GeV

The invariant mass spectrum for reconstructed DY di-muons in the mass range $2\,\mathrm{GeV/c^2} \leq m_{\mathrm{inv}} \leq 4\,\mathrm{GeV/c^2}$ is shown in Fig. 1. In total, 500,000 embedded events are simulated to generate this spectrum. The pair reconstruction efficiency (including the geometrical acceptance of the detector) is extracted using Monte-Carlo information of the simulated tracks and comes out to be 2.4%, which is about a factor of three smaller than the J/ψ reconstruction efficiency, for the same experimental configuration. This can be assigned to the lower momentum of the single muon tracks coming from the DY process. Figure 2 shows a comparison of the normalized DY mass spectrum to the combinatorial background spectrum. The DY spectrum is normalized by the multiplicity of the DY pairs, which comes out to be $N_{\mathrm{DY}} = 1.5 \cdot 10^{-6}$ in central Au+Au collisions at 25A GeV. The combinatorial background is found to be two order of magnitudes higher than the contribution of the DY process.

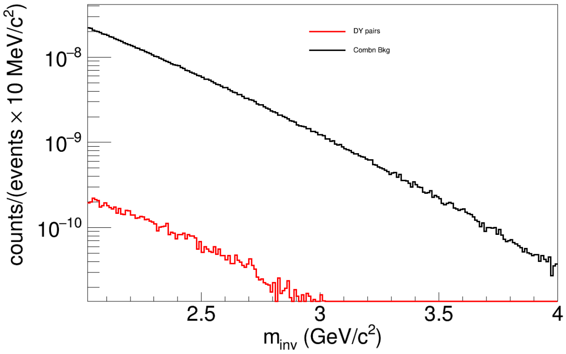

Figure 2: Comparison of the di-muon invariant mass spectrum from the Drell-Yan process to the uncorrelated background from random combinations

As a next step we would like to parametrize the reconstructed mass shape, which will be required for the extraction of the Drell-Yan yield from the raw di-muon data.

References

[1] P. P. Bhaduri and S. Chattopadhyay, *Generation of Drell-Yan di-muons at FAIR*, this report

[2] P. P. Bhaduri and S. Chattopadhyay, CBM Progress Report 2013, Darmstadt 2014, p. 117

Collision centrality determination in the CBM experiment*

S. Seddiki[1], M. Golubeva[2], I. Selyuzhenkov[1], V. Mikhaylov[3,4], A. Kugler[3], and P. Tlusty[3]

[1]GSI, Darmstadt, Germany; [2]INR RAS, Troitsk, Russia; [3]NPI of ASCR, Řež, Czech Republic; [4]CTU, Prague, Czech Republic

The magnitude of the impact parameter b in a heavy-ion collision is not known experimentally. Estimating b is important for the study by CBM of many physics observables, e.g., the event-by-event fluctuations of conserved quantities at mid-rapidity or collective flow. The multiplicity of produced particles in the overlap zone of the nuclei can be used as an experimental proxy of the b value. All events are sorted in centrality classes, the most central one being the collisions with highest multiplicity ($b \approx 0$) of produced particles and the most peripheral one with lowest multiplicity (when the b value is about the sum of the radii of the two nuclei). Since the b value and the particle multiplicity are correlated only on average, for a given multiplicity (centrality) class of events only an average value $\bar{b}$ and its spread σ_b can be estimated.

The Projectile Spectator Detector (PSD) of the CBM experiment is designed to register forward spectator nucleons and fragments emitted in nucleus-nucleus collisions at very small polar angles. The multiplicity of spectators can also be used as an independent way to determine centrality. In the case of spectator measurements, the most central events correspond to a low spectator multiplicity (small energy deposition in the PSD), while peripheral events result in a large amount of spectators (large energy deposition in the PSD).

The performance of the centrality determination was studied using the DCM-QGSM heavy-ion collision event generator [1]. The PSD was either used as a standalone detector utilizing correlations between the energy deposited in different PSD subevents (segments), or in combination with the CBM Silicon Tracking System (STS) which measures the multiplicity of produced particles. In the case of the PSD standalone analysis, it was required to have at least 40 GeV of energy in the PSD1 subevent or a total energy in two PSD2 and PSD3 subevents above 15 GeV to exclude very peripheral collisions.

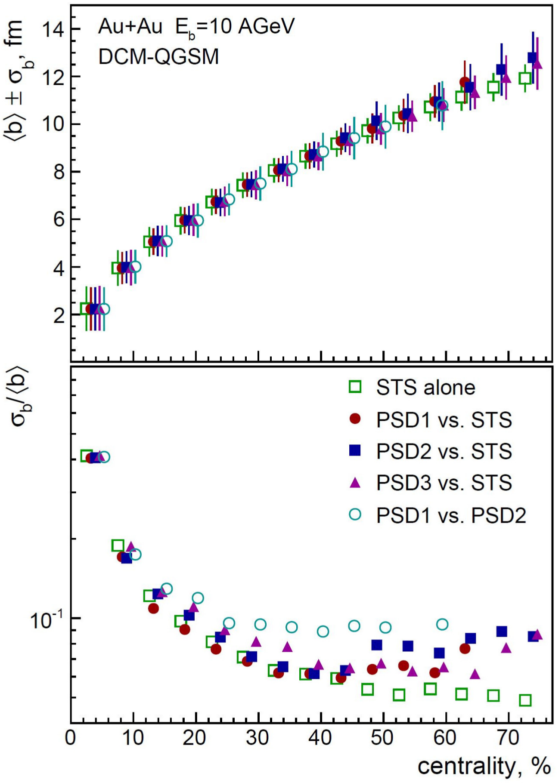

Figure 1: Average $\bar{b}$ and width σ_b of the impact parameter distribution (top); impact parameter resolution ($\sigma_b/\bar{b}$) (bottom).

Figure 1 shows the performance of the centrality determination for Au+Au collisions at $E_{\mathrm{beam}} = 10A$ GeV. The PSD is positioned at 8 m from the target. Centrality classes are defined by using various detector subevent combinations. The top panel shows the average impact parameter value $\bar{b}$ (central value) and σ_b (as the error bars) versus the centrality estimate from different subevent correlations. The bottom panel presents the same information in terms of impact parameter resolution $\sigma_b/\bar{b}$ of different centrality estimators. The $\bar{b}$ and σ_b were determined from Gaussian fits of the impact parameter distribution for a given centrality class.

The results in Fig. 1 demonstrate that the PSD can be used standalone for the centrality determination and, depending on the collision energy, has a comparable impact parameter resolution $\sigma_b/\bar{b}$ to that of the STS. This provides an independent method in the CBM experiment for the centrality determination with detected spectator fragments. When used together with the STS detector, the PSD helps to improve the overall centrality determination in the centrality range of 0-40% and allows for centrality determination in narrow classes with a width of at least 5%.

References

[1] The SHIELD code, `www.inr.ru/shield/index.html`

---

* Work supported by the European Community FP7 - Capacities, contract HadronPhysics3 n°283286.

Anisotropic flow and reaction plane reconstruction with the CBM experiment*

V. Mikhaylov[1,2], *M. Golubeva*[3], *A. Kugler*[1], *V. Kushpil*[1], *S. Seddiki*[4], *I. Selyuzhenkov*[4], *and P. Tlusty*[1]
[1]NPI of ASCR, Řež, Czech Republic; [2]CTU, Prague, Czech Republic; [3]INR RAS, Troitsk, Russia; [4]GSI, Darmstadt, Germany

The projectile Spectator Detector (PSD) of the CBM experiment is designed to register forward spectator nucleons and fragments emitted in nucleus-nucleus collisions at very low polar angles. It will be used to determine the orientation of the collision reaction plane. The accuracy of the reaction plane determination with the PSD depends on the multiplicity and energy distributions of spectators and the magnitude of their directed flow v_1.

The PSD performance is studied with simulated Au+Au collisions in the beam energy range $2A$-$30A$ GeV, which corresponds to that of future accelerator rings SIS100/SIS300 at FAIR. To identify the most suitable heavy-ion event generator for the performance study, the simulated directed flow with the UrQMD [1], DCM-QGSM [2], LA-QGSM [2], and HSD [3] heavy-ion event generators is compared to experimental data from the E895 [4] and STAR [5] collaborations. Figure 1 shows this comparison in terms of the slope of the proton directed flow at mid-rapidity dv_1/dy. Protons are used for the directed flow comparison because they are the most abundant particles in this kinematic region. The magnitude of the directed flow generated with different collision generators varies significantly, while DCM-QGSM seems to be the most consistent model in describing the data over the whole energy range. The possibility of collision fragment generation in the spectator region and the qualitative agreement with the experimental data for directed flow justifies the use of DCM-QGSM for the PSD performance study.

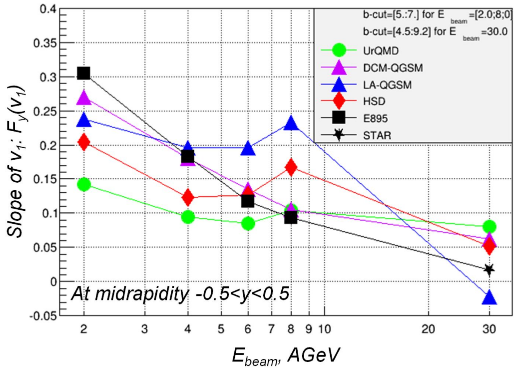

Figure 1: The slope of proton directed flow at midrapidity simulated with different collision generators in comparison to experimental data from E895 [4] and STAR [5]

The CBM detector response is simulated with the GEANT4 Monte-Carlo package for three different configurations: (1) "PSD-accept.", where the simulated azimuthal distributions of the particles within the geometrical acceptance of the PSD ($0.215° < \theta < 5.0°$ for $E_{\text{beam}} = 2A - 8A$ GeV and $0.115° < \theta < 2.7°$ for $\text{E}_{\text{beam}} = 30A$ GeV) were used without simulating the actual PSD response; (2) "PSD-geom., B=0", where PSD response is simulated without the CBM magnetic field (this allows to study the bias due to the finite PSD segmentation); (3) "PSD-geom., B>0", the same as configuration (2) but with magnetic field on.

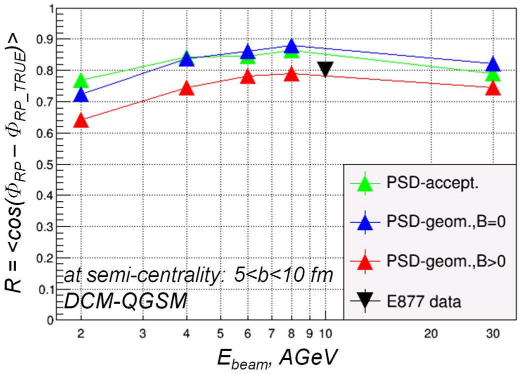

Figure 2: Reaction plane resolution correction factor for v_1. Results are from the DCM-QGSM model and E877 [6]

The reaction plane resolution, quantified in terms of correction factor used in the directed flow measurement, is shown in Fig. 2. The resolution simulated with the DCM-QGSM generator is similar to that of the E877 experiment [6]. The transverse segmentation of the PSD seems to have a small effect. While the CBM magnetic field introduces a significant bias, the reaction plane resolution is still high even in presence of the magnetic field.

References

[1] The UrQMD model, `urqmd.org`

[2] The SHIELD code, `www.inr.ru/shield/index.html`

[3] The HSD model,
`fias.uni-frankfurt.de/ brat/HSD/index1.html`

[4] H. Liu *et al.* (E895), Phys. Rev. Lett. **84** (2000) 5488

[5] L. Adamczyk *et al.* (STAR), Phys. Rev. Lett. **112** (2014) 164301

[6] J. Barrette *et al.* (E877), Phys. Rev. **C 55** (1997) 1420

---

* Work supported by the European Community FP7 - Capacities, contract HadronPhysics3 n°283286 and grant LG12007 of the Ministry of Education of the Czech Republic

CBM Physics

$$\frac{\chi_q}{T^2} = \sum_{i\in baryons} 9F(T, m_i) \cosh \frac{3\mu_q}{T}$$

$$\begin{aligned} \frac{I}{2} &= \sum_{i\in mesons} (2I_i^{(3)})^2 F(T, m_i) + \sum_{i\in bary} \\ &= \frac{8}{3} G^{(3)} + (F^{(2)} + 5F^{(4)}) \cosh \frac{3\mu_q}{T} \end{aligned}$$

Rapidity dependent strangeness enhancement of the produced particles at FAIR energies*

K. Dey[1,2] *and B. Bhattacharjee*[1]

[1]Department of Physics, Gauhati Univ., Guwahati, India; [2]Department of Physics, Bodoland Univ., Kokrajhar, India

It has now been understood that the width of the rapidity distribution of various produced particles, in addition to kinematic effects, has got a non-trivial baryon density effect as well [1]. The heavy ion collision at FAIR energies, where the baryon density could be something of the order of 5-10 times the normal nuclear matter density, might play a vital role in understanding the role of rapidity distribution of net-baryon density on the width of the rapidity distribution of hadrons containing leading quarks. Furthermore, strangeness enhancement which has been considered as one of the traditional signatures of QGP is studied quite extensively considering strangeness to be conserved both globally and locally. However, Steinheimer *et al.* [2] predicted from UrQMD calculations that although strangeness is conserved globally, it is not uniformly distributed over rapidity space leading to a local violation of strangeness conservation. Because of the limitation of the detector acceptance, most past and ongoing heavy ion experiments could measure the strangeness enhancement at mid-rapidity only. A number of strange particles do contain leading quark(s) and thus a study of the rapidity dependent strangeness enhancement is of considerable importance. In this work, by generating 93 million UrQMD events, an attempt has therefore been made to study the rapidity dependent strangeness enhancement at FAIR energies.

Following Ref. [3], the strangeness enhancement factor is defined as

$$E_S = \left[\frac{(Yield)_{AA}}{< N_{\pi^-} >}\right]_{central} / \left[\frac{(Yield)_{AA}}{< N_{\pi^-} >}\right]_{peripheral}.$$

In Fig. 1, E_S is shown as a function of rapidity for various identified particles for Au+Au collisions at 30A GeV. It is interesting that E_S depends strongly on rapidity, and this dependence follows two distinctive patterns. While the enhancement factor at mid-rapidity is found to be maximum for the particles containing leading quarks (filled circle), the same is observed to be minimum at mid-rapidity for the particles containing produced quarks only (open circle). Even though $\Omega^-(sss)$, consisting of three produced quarks, is observed to be behaving differently than those hadrons with all its constituents as produced quarks, a slight decrease in the enhancement at mid-rapidity is clearly visible. This apparent anomalous behavior could be due to the contribution of Ξ^- (containing one leading quark), in the production of Ω^- via the $\Xi K^- \rightarrow \Omega\pi$ channel.

To understand the underlying dynamics of such rapidity dependent strangeness enhancement, Fig. 2 shows the widths of the rapidity distribution of identified particles as a function of centrality. Evidently, the different patterns of rapidity dependence of E_S reflect in the dependence of rapidity width on centrality. The width of the rapidity distribution increases when going from central to peripheral collisions for the particles containing leading quarks, a feature that might be attributed to the variation of net-baryon density with impact parameter. Fig.2 also shows that for all particles containing produced quarks only, except Ω^-, the rapidity width follows a decreasing pattern with decreasing centrality for the particles. This observation may be attributed to the fact that the size of the central fireball and hence the scattering effect decreases with the decreasing centrality.

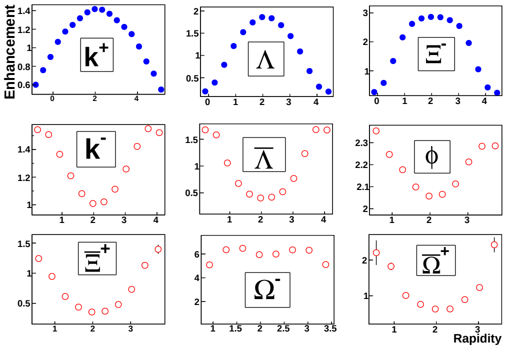

Figure 1: Strangeness enhancement factor as a function of rapidity for particles containing at least one leading quark (filled circle) and particles containing only produced quarks (open circle) for $Au + Au$ collision at 30A GeV.

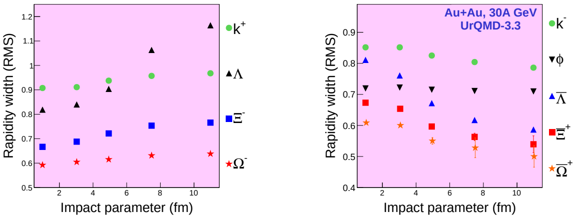

Figure 2: Rapidity width as a function of impact parameter for identified particles for $Au + Au$ collision at 30A GeV.

References

[1] K. Dey and B. Bhattacharjee, Phys. Rev. **C 89** (2014) 054910 (2014)

[2] J. Steinheimer *et al.*, Phys. Lett. **B 676** (2009) 126

[3] S. Soff *et al.*, Phys. Lett. **B 471** (1999) 89

---

* Work supported by DST Govt. of India

Production of Omega hyperons at FAIR energies

H. Jahan[1], *S. Chattopadhyay*[2], *and N. Ahmad*[1]
[1]Aligarh Muslim University, Aligarh, India; [2]Variable Energy Cyclotron Center, Kolkata, India

The main objective of relativistic heavy-ion collisions is to study strongly interacting matter at extreme conditions in terms of temperature and energy density. At high temperature and/or baryon density, nuclear matter is expected to undergo a transition to free quarks and gluons known as the quark-gluon plasma (QGP) [1]. A baryon-rich QGP will affect the flavor composition of the produced medium and thus the production of K^+, K^-, Λ, $\bar{\Lambda}$ etc. [2]. The effect is more noticeable for multi-strange baryons (and anti-baryons), thus making them a sensitive probe for the QGP phase. Therefore, the investigation of the enhancement in the production of Ω^-(sss) in heavy-ion collisions compared to pp or pA collisions becomes an interesting area of studies [3]. In the present work, we have therefore performed a systematic model-based study of the production of Ω^-(sss) and $\bar{\Omega}^+(\bar{s}\bar{s}\bar{s})$ in central Au+Au collisions at $E_{\rm lab}$ from 5-90 GeV/A. We have studied the energy dependence of Ω^- and $\bar{\Omega}^+$ and the strangeness enhancement estimated by taking the ratio to the corresponding yields in pp collisions at the same energy. We employed two types of models: the microscopic transport models UrQMD and AMPT (the latter in both hadronic and partonic mode) and the statistical hadronization model THERMINATOR. We have studied 1 million events with a rapidity cut $|y|<0.5$ arround mid-rapidity.

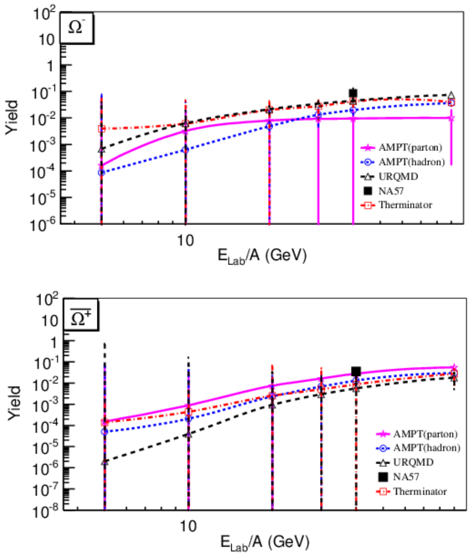

Figure 1: Excitation function of the yields of Ω^- and $\bar{\Omega}^+$ in central Au+Au collisions

Fig. 1 shows the average multiplicity of Ω^- and its antiparticle as function of lab energy $E_{\rm lab}$. In these figures, yields from various models are compared to the available NA57 data [4]. All models predict a steep excitation function up to $E_{\rm lab}/A \approx 20$ GeV, from when on the increase is more moderate. The experimental data are under-predicted by all models, showing that the latter are not able to incorporate all mechanisms of strange particle productions. However, for $\bar{\Omega}^+$ AMPT in partonic mode comes closest to the measurement. As the study is confined to the midrapidity region, it can not be concluded whether the enhanced production in the partonic mode of AMPT is due to enhanced production by coalescence compared to the associated production in the hadronic mode or to a change in the rapidity distribution. However, the observation of enhanced production of multi-strange particles in the partonic mode of AMPT at these energies suggests this observable to be sensitive to the formation of a partonic medium.

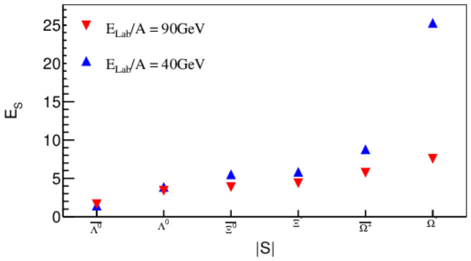

Figure 2: Variation of the enhancement factor with strangeness number

The variation of the enhancement factor as the function of strangeness number is shown in Fig. 2 for $E_{\rm lab}/A = 90$ and 40 GeV respectively for the partonic mode of AMPT. The enhancement factor is higher at the lower energy and increases with increasing strange quark number. This suggests that strangeness production increases faster in pp collisions than in A+A collisions.

In summary, our study of model predictions show that multi-strange hyperons are key probes for the upcoming heavy-ion programme at FAIR.

References

[1] S. A. Bass *et al.*, J. Phys. **G 25** (1999) R1
[2] S. Uddin *et al.*, Phys. Lett. **B 278** (1992) 357
[3] E. Anderson *et al.*, Phys. Lett. **B 449** (1999) 401
[4] F. Antinori *et al.*, Phys. Lett. **B 595** (2004) 68

Strange meson-baryon interaction in hot and dense nuclear matter: from hadronic models to transport simulations*

D. Cabrera† [1,2], *A. Ilner* [1,2], *L. Tolós* [1,3], *J. Aichelin* [4], *E. Bratkovskaya* [1,2], *and W. Cassing* [5]
[1]FIAS, Frankfurt, Germany; [2]ITP, Frankfurt, Germany; [3]ICE (IEEC/CSIC), Bellaterra, Spain; [4]Subatech, Nantes, France; [5]ITP, Giessen, Germany

Introduction

We study the dynamics of strange pseudoscalar and vector mesons in hot and dense nuclear matter within a self-consistent coupled-channel approach based on the meson-baryon chiral Lagrangian. Our results set up the starting point for implementations in microscopic transport approaches of heavy-ion collisions, particularly at the conditions to be met in the future experiments at GSI/FAIR and NICA@Dubna. Such developments are in progress, exploiting the successful collaboration between the transport groups of Nantes and FIAS-Frankfurt.

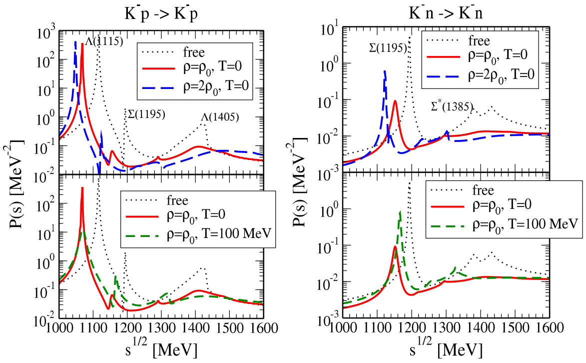

Figure 1: In-medium transition probability $\mathcal{P}$ for the elastic K^-p (left) and K^-n (right) reactions. The peaks associated to the $\Lambda(1115)$, $\Sigma(1195)$ and $\Lambda(1405)$ resonances are clearly visible in the vacuum case.

$\bar{K}N$ interaction in hot and dense matter

In the $\bar{K}N$ sector we focus on the calculation of in-medium (off-shell) transition rates for the most relevant binary reactions involved in strangeness production close to threshold energies (e.g. $\bar{K}N \to \pi\Sigma$), with special attention to the role of sub-threshold hyperon resonances ($\Lambda(1405)$, $\Lambda(1115)$, $\Sigma(1195)$ and $\Sigma^*(1385)$), isospin effects (e.g. $\bar{K}p$ vs $\bar{K}n$, cf. Fig. 1) and the angular dependence of the scattering amplitudes and cross sections (s and p waves are accounted for). Together with the spectral function and the nuclear optical potential of strange mesons and hyperons, our results permit a systematic accounting of medium effects in the $S = -1$ sector regarding the production, propagation and rescattering of light strange hadrons.

Strange vector mesons: K^*, $\bar{K}^*$ and ϕ

We have also pursued recent theoretical developments regarding the dynamics of strange vector mesons (K^*, $\bar{K}^*$ and ϕ) in the nuclear medium, in connection with experimental activity from heavy-ion collisions and nuclear production reactions. Our work focuses on the extension to finite temperatures of previous chiral hadronic models for the vector meson self-energy in dense matter (cf. Fig. 2), where the key mechanisms for medium modification are: (i) the excitation of strange baryon resonances in quasi-elastic scattering (e.g. $\bar{K}^*N \to \bar{K}^*N$), which translates into resonance-hole modes that mix with the vector-meson quasiparticle peak; and (ii) the decay into hadronic modes (e.g. $\bar{K}^* \to \bar{K}\pi$), where the daughter particles are also dressed and low-energy modes are Bose-enhanced.

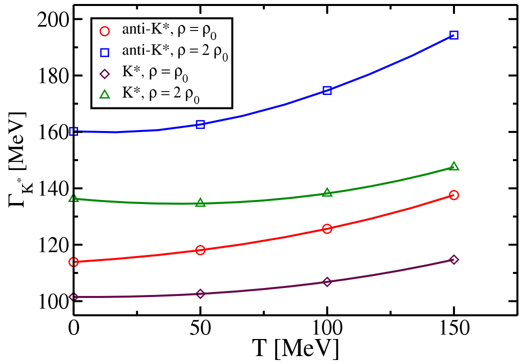

Figure 2: Temperature evolution of the $\bar{K}^*(K^*)$ width – or self-energy – due to $\bar{K}(K)\pi$ in-medium decays

References

[1] D. Cabrera, L. Tolos, J. Aichelin and E. Bratkovskaya, Phys. Rev. **C 90** (2014) 055207

[2] A. Ilner, D. Cabrera, P. Srisawad and E. Bratkovskaya, Nucl. Phys. A **A 927** (2014) 249

[3] L. Tolos *et al.*, J. Phys. Conf. Ser. **562** (2014) 012010

[4] D. Cabrera *et al.*, J. Phys. Conf. Ser. **503** (2014) 012017

---

* Work supported by the HIC for FAIR framework of the LOEWE program and BMBF (Germany) under project No. 05P12RFFCQ.

† cabrera@fias.uni-frankfurt.de

K^* dynamics in a nuclear medium*

A. Ilner[† 1,2], *D. Cabrera*[‡ 1,2], *and E. Bratkovskaya*[§ 1,2]
[1]FIAS, Frankfurt, Germany; [2]Institut für theoretische Physik, Goethe-Universität, Frankfurt, Germany

The K^* and the $\bar{K}^*$ are vector mesons that are composed of a light and a strange quark, i.e. the K^* is composed of a u and a $\bar{s}$ quark and the $\bar{K}^*$ is composed of a u and a s quark. We study the in-medium properties of these mesons in a dense and hot nuclear medium. The in-medium properties are based on chirally motivated models and these in-medium effects are parametrised as density or temperature dependent effective masses and widths. For broad in-medium particles we adopt the relativistic Breit-Wigner prescription, i.e. the spectral function

$$A_i(M,\rho_N) = \frac{\frac{2}{\pi} \cdot C_1 \cdot M^2 \cdot \Gamma_i^*(M,\rho_N)}{\left(M^2 - M_i^{*2}(\rho_N)\right)^2 + \left(M\Gamma_i^*(M,\rho_N)\right)^2}\ , \tag{1}$$

where C_1 stands for a normalisation constant, which is determined as the spectral function must fulfil the sum rule $\int_0^\infty A_i(M,\rho_N)dM = 1$, and $i = K/\bar{K}, K^*/\bar{K}^*$.

The in-medium effects are based on the complex self-energy obtained by solving the strange meson (off-shell) dispersion relation $E^2 - |\vec{p}^2| - M_i^2 - \Pi_i = 0$, i.e. the width of the spectral function is related to the imaginary part of the self-energy as

$$\mathrm{Im}\,\Pi_i(M,\rho_N) = -\Gamma_i^*(M,\rho_N) \cdot M \tag{2}$$

and the mass shift is related to the real part of the self-energy as

$$\mathrm{Re}\,\Pi_i(M_i^*,\rho_N) = M_i^2 - (M_i^*)^2 \tag{3}$$

(with M_i being the nominal mass in vacuum, i.e. $M_{K^*} = 0.892$ GeV). A vacuum width of $\Gamma_V^0 = 42$ MeV has been used throughout all of our calculations for the vector mesons.

We distinguish two scenarios for energies where the medium is dense and is filled with baryonic particles (FAIR; $\mu_B \neq 0, T \approx 0$) and when the medium is hot and filled with pionic particles (RHIC, LHC; $\mu_B \approx 0, T \neq 0$). The behaviour of strange vector mesons is different for these two media. Additionally the behaviour of a strange particle is different from the behaviour of a strange antiparticle in a dense nuclear medium, whereas it is the same in a hot nuclear medium (we are dealing with an isotopically symmetric pionic medium).

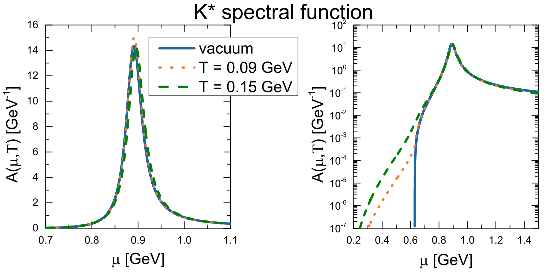

Figure 1: The K^* spectral function is shown as a function of the invariant K^* mass μ for different temperatures T. The blue solid line is for the vacuum case, the orange dotted line is for a temperature of $T = 0.09$ GeV and the green dashed line is for a temperature of $T = 0.15$ GeV. The same results are shown on a linear (left plot) and on a logarithmic (right plot) scale.

In figure 1 one can see spectral function for the K^* (and consequently the $\bar{K}^*$) in a hot, pionic medium. The effects of the medium are negligible, there is only a small mass shift and a very small broadening. However, when looking at the logarithmic plot one can see that the K^* gains some enhancement in the low mass region at temperatures $T > 0$.

For the K^* in a dense nuclear medium the width of the K^* decreases with increasing density since the kaon becomes slightly heavier as a result of the repulsive KN interaction. However, this is compensated by the repulsive self-energy from the K^*N interaction. The resulting K^* self-energy in a $t\rho$ approximation leads to a mildly repulsive K^* mass shift of about 5% (30 MeV) at a density of $\rho_N = \rho_0$. The change in the shape of the spectral function is negligible.

The major effects for the $\bar{K}^*$ in a dense nuclear medium come mainly from both the $\bar{K}\pi$ decay channel and from the highly inelastic $\bar{K}^*N$ interaction, leading to decay widths as large as 200 MeV at normal nuclear matter density $\rho_N = \rho_0$.

References

[1] A. Ilner, D. Cabrera, P. Srisawad and E. Bratkovskaya, Nucl. Phys. **A 927** (2014) 249

---

[*] Work supported by the Helmholtz International Center for FAIR within the framework of the LOEWE program, HGS-HIRe for FAIR, H-QM and the BMBF (Germany) under project no. 05P12RFFCQ.

[†] ilner@fias.uni-frankfurt.de

[‡] cabrera@fias.uni-frankfurt.de

[§] Elena.Bratkovskaya@th.physik.uni-frankfurt.de

Creation and annihilation of antimatter at FAIR energies*

P. Moreau[1], *J. Aichelin*[2], *and E. Bratkovskaya*[1]
[1]FIAS, Goethe Universität, Frankfurt, Germany; [2]Subatech, Université de Nantes, Nantes, France

The 'Big Bang' scenario implies that in the first microseconds of the universe the entire state has emerged from a partonic system of quarks, antiquarks and gluons – a quark-gluon plasma (QGP) – to color neutral hadronic matter consisting of interacting hadronic states (and resonances) in which the partonic degrees of freedom are confined. Nowadays this early phase can be reproduced in relativistic heavy ion collisions. They show indeed that such a QGP can exists and that it interacts more strongly than hadronic matter. Consequently the concept of a weakly interacting system described by perturbative QCD (pQCD) has to be questioned.

The dynamics of partons, hadrons and strings in relativistic nucleus-nucleus collisions can be analyzed within the Parton-Hadron-String Dynamics approach [1, 2]. In this transport approach the partonic dynamics is based on Kadanoff-Baym equations for Green functions with self-energies from the Dynamical QuasiParticle Model (DQPM) which describes QCD properties in terms of 're-summed' single-particle Green functions [3]. The lattice QCD results, of which the parameters of DQPM are fitted on, lead to a critical temperature $T_c \approx 160$ MeV which corresponds to a critical energy density of $\epsilon_c \approx 0.5\ \mathrm{GeV/fm^3}$.

The aim of this project is to study, with the help of PHSD, the creation and annihilation of anti-matter at the FAIR facility in the future CBM and PANDA experiments. Since anti-matter (or antiparticles) does not exist in our world it has to be created first by strong interactions before its dynamics can be studied in different hadronic or partonic environments. These experiments aim at the exploration of the QCD phase diagram, especially to find out the order of the phase transition between hadrons and partons at high baryonic densities. In addition we will study the optical potential of different hadrons and the in-medium properties of hadrons in the strange and the charm sector. To verify that our approach is adequate for this study we start out with the calculation of the measured spectra of particles and anti-particles at RHIC energies. We have found a good agreement with the PHENIX data for single particle spectra in Au+Au (figure 1) and p+p (figure 2) collisions at mid-rapidity. One can see that the production of particles and anti-particles in pp collisions is very similar while in Au+Au collisions we observe the effects of anti-baryon absorption at low p_T as well as rescattering on the partonic and hadronic levels.

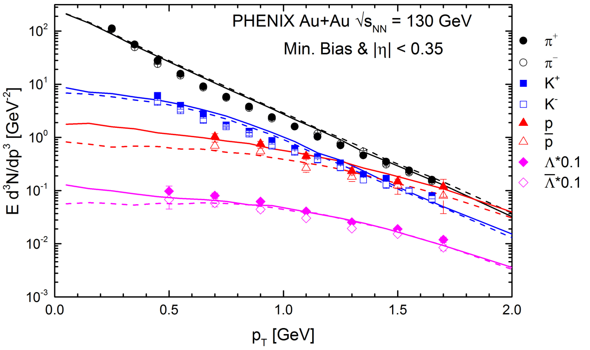

Figure 1: Invariant p_T spectra in Au+Au collisions at $\sqrt{s_{NN}} = 130$ GeV for π^+, π^-, K^+, K^-, p, $\bar{p}$, Λ and $\bar{\Lambda}$ obtained with PHSD, in comparison with the experimental data from the PHENIX collaboration [4, 5]

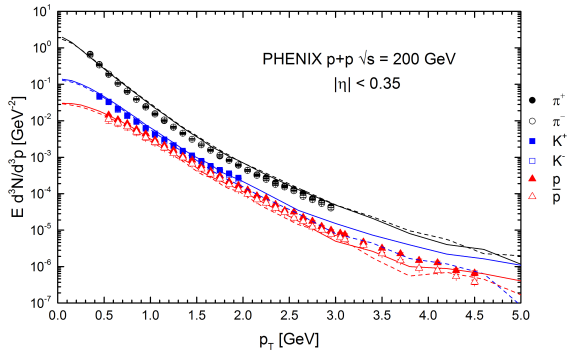

Figure 2: Invariant p_T spectra in p+p collisions at $\sqrt{s} = 200$ GeV for π^+, π^-, K^+, K^-, p and $\bar{p}$ obtained with PHSD in comparison with the experimental data from the PHENIX collaboration [6]

References

[1] W. Cassing and E. L. Bratkovskaya, Nucl. Phys. **A 831** (2009) 215

[2] E. L. Bratkovskaya, W. Cassing, V. P. Konchakovski and O. Linnyk, Nucl. Phys. **A 856** (2011) 162

[3] W. Cassing, Eur. Phys. J. ST **168** (2009) 3

[4] K. Adcox *et al.* [PHENIX Collaboration], Phys. Rev. **C 69** (2004) 024904

[5] K. Adcox *et al.* [PHENIX Collaboration], Phys. Rev. Lett. **89** (2002) 092302

[6] A. Adare *et al.* [PHENIX Collaboration], Phys. Rev. **C 83** (2011) 064903

---

[*] Work supported by HIC4FAIR/HGS-HIRe.

Simulation results on elliptic flow at FAIR energies

S. Sarkar, S. Ghosh, P. Mali, and A. Mukhopadhyay
Department of Physics, North Bengal University, Siliguri, India

In high-energy heavy-ion collisions elliptic flow refers to a preferential emission of particles with respect to a given azimuthal angle [1]. The magnitude of this effect is characterized by an elliptic flow parameter, defined as [2]:

$$v_2 = \langle \cos 2(\phi - \psi) \rangle$$

where ϕ is the azimuthal angle of an outgoing particle, ψ is the azimuthal angle of the impact parameter, and the angular brackets denote averaging over many particles and many events. In this preliminary investigation we report some aspects of the elliptic flow in Au–Au collision at $E_{lab} = 20$A GeV and 40A GeV, using the UrQMD [3] and the AMPT model (both default and string melting versions) [4]. The results are based on a statistics of 2×10^5 events for each simulation. The initial spatial anisotropy of the created system is quantified by the eccentricity [5]:

$$e_{std} = \left(\sigma_y^2 - \sigma_x^2\right) / \left(\sigma_y^2 + \sigma_x^2\right)$$

where σ_x, σ_y denote the standard deviations of the x, y coordinates of the participating nucleons in the transverse plane. However, even at fixed impact parameter the number of participating nucleons (N_{part}) and their positions can fluctuate from event to event. To address this issue the eccentricity is redefined [5]:

$$e_{part} = \sqrt{(\sigma_y^2 - \sigma_x^2)^2 + 4(\sigma_{xy})^2} / \left(\sigma_y^2 + \sigma_x^2\right)$$

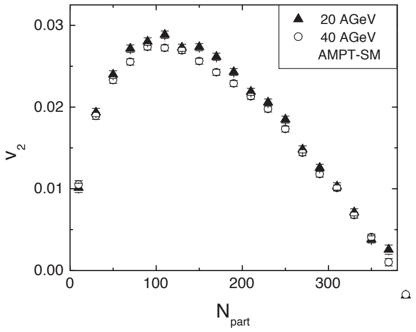

Figure 1: v_2 versus N_{part} from AMPT-SM for $20A$ and $40A$ GeV

In Fig. 1 we plot v_2 as a function of N_{part} for both incident energies using the AMPT code. We see that the nature of variation of v_2 is almost independent of the incident energy at this energy scale. This also holds for results from UrQMD and AMPT without string melting. Figure 2 compares model results on v_2 at $E_{lab} = 20$A GeV. Results of all models nearly follow the same pattern, the UrQMD plot being slightly more symmetric than the AMPT plots. Because of the strong asymmetry of the nuclear overlap region in the mid-central collisions, v_2 is large. For the AMPT-string melting model v_2 values of peripheral and mid-central events are found to be the largest.

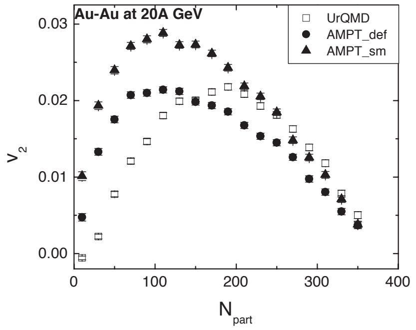

Figure 2: v_2 versus N_{part} for different models at $20A$ GeV

In Fig. 3 we have plotted v_2/e_{std} and v_2/e_{part} against N_{part} for all three models at $E_{lab} = 20$A GeV. Within errors v_2/e appears to scale with N_{part}. Several other aspects of elliptic flow like variation of v_2 with transverse momentum and pseudo-rapidity (not shown here) were also examined.

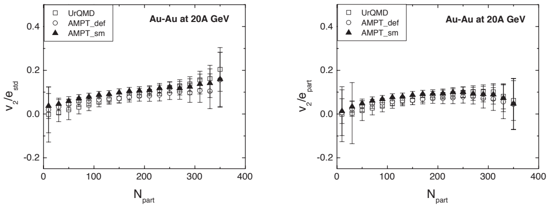

Figure 3: v_2/e_{std} (left) and v_2/e_{part} (right) versus N_{part}

References

[1] J. Y. Ollitrault, Phys. Rev. **D 46** (1992) 229
[2] A. M. Poskanzer *et al.*, Phys. Rev. **C 58** (1998) 1678
[3] S. A. Bass *et al.*, Prog. Nucl. Part. Phys. **41** (1998) 255
[4] Z. Lin *et al.*, Phys. Rev. C **72** (2005) 064901
[5] B. Alver *et al.* (PHOBOS collaboration), Phys. Rev. Lett, **98** (2007) 242302.

Evolution of strangeness fluctuations at FAIR energies

S. Ahmad[1], *S. Chattopadhyay*[2], *and M. Farooq*[1]
[1]University of Kashmir, Srinagar, India; [2]Variable Energy Cyclotron Center, Kolkata, India

Fluctuations of conserved quantities are considered to be sensitive indicators of the phase transition and the critical point [1]. For heavy-ion collisions at relatively low energy, likely to be accessible at FAIR, the extreme density region created in the collision might result in large fluctuations of specific quantities. It is interesting to study the propagation of these fluctuations especially in terms of their survival at freeze-out.

We used UrQMD3.4 to study the space-time evolution of the fluctuations in central Au+Au collisions at E_{lab} from 10-90 GeV/A. In the default, pure hadronic transport mode of UrQMD, time scans were performed from t = 1 fm/c to t = 30 fm/c. We used 5 million events with a rapidity cut $|y| < 1$ arround $\mathrm{y}_{\mathrm{mid}}$. The observable ν_{dyn} [2], which is not subject to volume, detector acceptance and ineffeciency effects, was used as fluctuation measure.

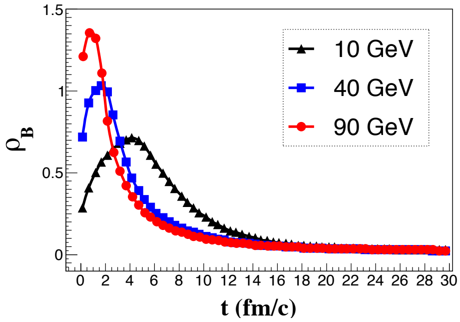

Figure 1: Evolution of baryon density with time elapsed after collision

Fig. 1 shows the variation of net baryon density with time at different collision energies, which demonstrates the importance of heavy-ion collisions at FAIR. As expected from the time required for two nuclei to pass each other, the peak density is achieved faster at higher beam energy but the high-density stage is longer lived at lower energies.

ν_{dyn} for K/π essentially represents the fluctuations in strangeness production. Figure 2 shows that this observable starts with a large value and subsequently reduces to saturated values. The reduction is faster for the case of 10A GeV where multiple interactions play a dominant role. Production of strangeness at lower energy also leads to larger fluctuations.

We calculated ν_{dyn} of K/π at freeze-out as shown in Fig. 3 for three scenarios, namely the pure hadronic transport case with no hydrodynamic expansion, with hydrodynamic expansion using the "hadronic gas" equation of state, and with the "chiral" equation of state. The red triangles in the plot can be compared with the end points of Fig. 2. It is seen that ν_{dyn} is positive for K/π showing the dilution of the correlation between kaons and pions at later times after the collision. In case of hydrodynamic evolution, it is seen that at lower collision energies, fluctuations in the K/π ratio after hydro expansion with both types of equations of state are higher than for the pure transport results. The chiral equation of state (which includes a phase transition as well) shows more enhancement in fluctuation for K/π at lower beam energies. This makes the measurement of fluctuations at lower beam energy an interesting topic.

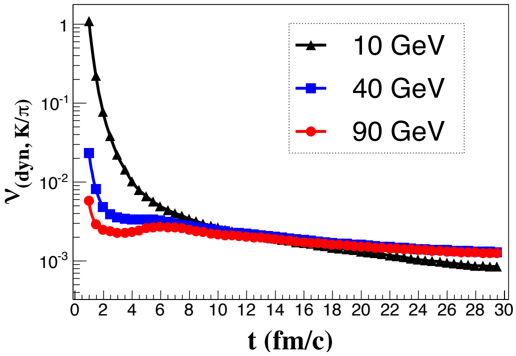

Figure 2: Evolution of ν_{dyn} of K/π at different collision energies (pure transport case)

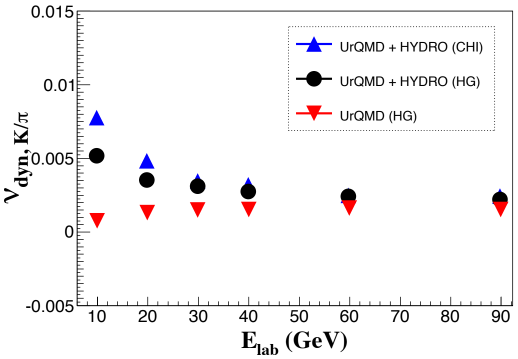

Figure 3: Beam energy dependence of ν_{dyn} for K/π at freeze-out with pure transport and with hydro evolution using two equations of state

References

[1] V. Koch, arXiv:0810.2520

[2] C. Pruneau *et al.*, Phys. Rev. **C 66** (2002) 044904

Generation of Drell-Yan di-muons at FAIR

P. P. Bhaduri[*1] and S. Chattopadhyay*[1]

[1]Variable Energy Cyclotron Centre, 1/AF Bidhan Nagar, Kolkata-700 064, India

The measured di-muon invariant mass spectrum, in relativistic heavy-ion collision experiments, is a superposition of different sources coming from various origins. In order to disentangle different sources and to estimate their respective experimental acceptances, each process needs to be studied independently using a Monte Carlo (MC) simulation method within the given experimental conditions. In this report we describe our recent efforts to develop a MC code to generate muon pairs from the Drell-Yan (DY) process in the FAIR energy regime. Our approach closely follows the methods developed by the NA50 Collaboration for di-muon simulations [1]. For a complete kinematic description of a particle, one needs to know its charge, mass and momentum. Thus when studying pairs, there are ten independent parameters. The DY process is the electromagnetic annihilation of a quark and anti-quark of the same flavor, with the creation of a virtual photon that decays into a lepton pair. In this case some of the ten parameters are constrained by charge and four-momentum conservation. For complete characterization of the DY pair four independent variables namely, pair mass ($M_{2\mu}$), rapidity in the centre of mass frame (y^*), transverse momentum p_T and di-muon azimuthal angle are required. Decay of a di-muon into two single muons introduces two additional degrees of freedom which can conveniently chosen to be the polar (θ_{cs}) and azimuthal (ϕ_{cs}) angle of one of the two muons in the Collins-Soper reference frame. For calculation of the DY distributions, we adopt the following parametrization of the kinematic variables in our code. The pair mass and rapidity distributions can be parametrized following the double differential cross section from leading order perturbation theory:

$$
\begin{aligned}
&\frac{d^2\sigma(AB \to \mu^+\mu^-)}{dy^* dM} = \qquad (1)\\
&K_{DY}\frac{8\pi\alpha^2}{9M^3}\sum_q e_q^2[F_q^1(x_1, M^2) \times F_{\bar{q}}^2(x_2, M^2)\\
&+F_{\bar{q}}^1(x_1, M^2) \times F_q^2(x_2, M^2)]
\end{aligned}
$$

where M is invariant mass of the produced dilepton, $\alpha = e^2/4\pi$ is the fine structure constant and x_1, x_2 respectively represent the projectile and target nucleons momentum fractions carried by partons with charge e_q in a collision of centre of mass energy $\sqrt{s}$ and can be written as $x_{1,2} = \frac{M}{\sqrt{s}} exp(\pm y^*)$. $F_q(F_{\bar{q}})$ denotes the parton distribution function for quarks (anti-quarks). $K_{DY} \sim 2$ takes care of higher order contributions. Integrating the above equation over pair mass or rapidity, one gets single differential distributions in pair rapidity or mass. The differential p_T distributions are generated using a Bessel function of the transverse mass m_T as $\frac{dN}{dp_T} \propto p_T m_T K_1(m_T/T)$, where K_1 is the first order modified Bessel function, and $T = 170$ MeV, consistent with the modeling of p_T distribution in J/ψ simulations. DY pairs are then decayed into two muons in the pair rest frame which are then boosted to the laboratory frame. The distributions of the decay angles are generated with the following parametrization. A uniform distribution is chosen for ϕ_{cs}, and for the polar angle distribution we have used $\frac{dN}{dcos(\theta_{cs})} \propto 1 + \lambda cos^2(\theta_{cs})$, where $\lambda = 1$ as measured by the NA10 experiment.

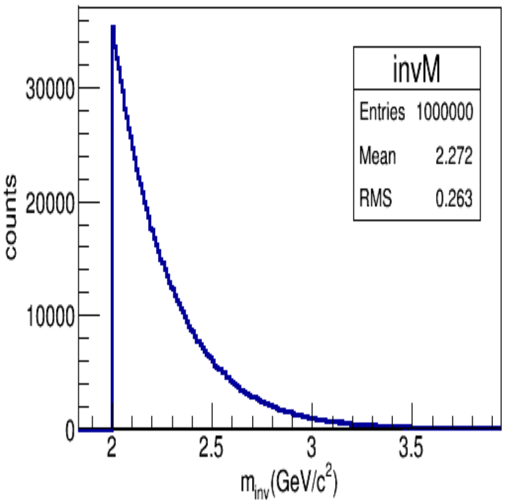

Figure 1: Invariant mass distrbution of the di-muons from the Drell-Yan process, generated over the full phase space

The result of our calculations is displayed in Fig. 1. It shows the invariant mass dsitribution of the DY muon pairs for $25A$ GeV Au+Au collisions, generated over the full phase space (4π). The invariant mass is calculated from the four momentum of the two single muons in the lab frame and in the pair mass region $2 \leq m_{DY} \leq 4$ GeV/c^2.

References

[1] P. Cortese, *J/ψ, ψ' and Drell-Yan production in proton-nucleus collisions at 450 GeV incident energy at the CERN SPS*, Tesi di Dottorato di Ricerca, Università Degli Studi Di Torino, December 2000

---

[*] partha.bhaduri@vecc.gov.in

Heavy-quark dynamics in a hot and dense medium*

H. Berrehrah[1], *E. Bratkovskaya*[1], *W. Cassing*[2], *P. B. Gossiaux*[3], *and J. Aichelin*[3]
[1]Frankfurt Institute for Advanced Studies, Frankfurt, Germany; [2]Institut für Theoretische Physik, Universität Giessen, Germany; [3]Subatech, Nantes, France

Introduction

We study the dynamics of on- and off-shell heavy quarks Q in the quark-gluon plasma (QGP) as produced in relativistic nucleus-nucleus collisions. The interactions of heavy quarks with the partonic environment at finite temperature T and finite quark chemical potential μ_q are investigated in terms of transport coefficients within the dynamical quasiparticle model (DQPM) designed to reproduce the lattice-QCD (lQCD) results (including the partonic equation of state) in thermodynamic equilibrium. The collisional scattering cross sections σ^{Q}_{elas} are evaluated for perturbative partons (massless on-shell particles) and for dynamical quasi-particles (massive on or off-shell particles) using the leading order Born diagrams [2, 3].

Charm spatial diffusion coefficient

Based on σ^{Q}_{elas} in a finite T and μ_q medium [1, 2, 3, 4], the on- and off-shell heavy quark dynamical collisional energy loss and transport coefficients are computed [1, 3, 4]. As an example, the charm spatial diffusion coefficient D_s is shown in Fig. 1 at finite T (top) and finite T and μ_q (bottom) where our non-perturbative DpQCD model (Dressed pQCD using DQPM pole masses for the partons) is confronted with nuclear many-body calculations below and close to the critical temperature T_c from Ref. [5].

The hadronic and partonic D_s join smoothly and show a pronounced minimum close to T_c at $\mu_q = 0$ as well as at finite μ_q. Close to and above T_c its absolute value matches the lQCD calculations for $\mu_q = 0$. The smooth transition of the heavy-quark transport coefficients from the hadronic to the partonic medium corresponds to a crossover transition in line with lattice calculations, and differs substantially from perturbative-QCD calculations (Moore & Teaney) which show a large discontinuity at T_c. This indicates that in the vicinity of T_c dynamically dressed massive partons should be the effective degrees of freedom in the quark-gluon plasma.

The heavy quark scattering cross sections and transport properties [1, 2, 3, 4] form the basis of a consistent study of the heavy quark dynamics in heavy-ion collisions at FAIR, SPS, RHIC and LHC energies where the partonic processes are implemented into the Parton-Hadron-String-Dynamics (PHSD) transport approach.

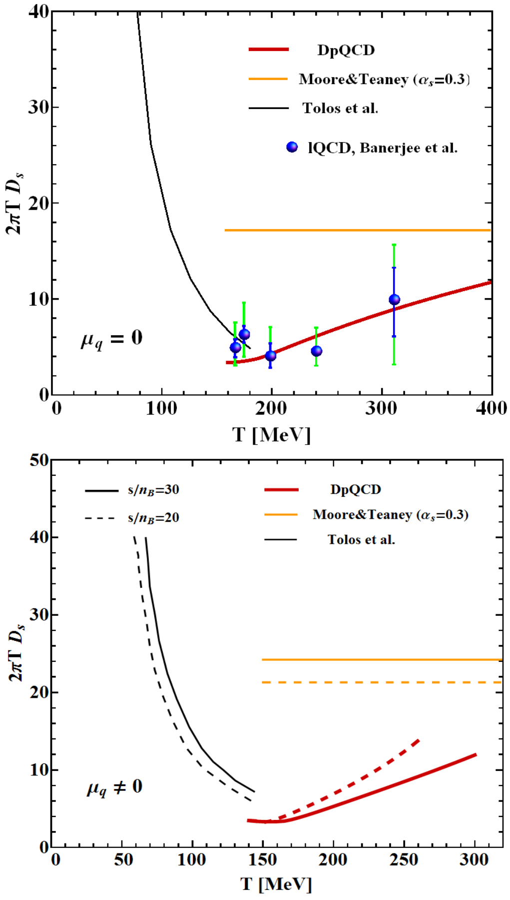

Figure 1: Spatial diffusion coefficient for heavy quarks, D_s, as a function of T for $\mu_q = 0$ (top) and $\mu_q \neq 0$ (bottom). The hadronic diffusion coefficient is taken from [5]. For partonic environment the result from the DpQCD model is compared to pQCD [6], and lattice calculations from Ref. [7]

References

[1] H. Berrehrah *et al.*, Phys. Rev. **C 90** (2014) 051901

[2] H. Berrehrah *et al.*, Phys. Rev. **C 89** (2014) 054901

[3] H. Berrehrah *et al.*, Phys.Rev. C90 (2014) 064906

[4] H. Berrehrah *et al.*, arXiv:1412.1017 [hep-ph]

[5] L. Tolos and J. M. Torres-Rincon, Phys. Rev. **D 88** (2013) 074019

[6] G. D. Moore and D. Teaney, Phys. Rev. **C 71** (2005) 064904

[7] D. Banerjee *et al.*, Phys. Rev. **D 85** (2012) 014510

---

* Work supported by DFG and "HIC for FAIR" framework of the "LOEWE" program. The computational resources were provided by the LOEWE-CSC.

CBM Publications 2014

- J. Adamczewski *et al.*:
  The CBM RICH project
  Nucl. Instrum. Methods **A 766** (2014) 101
  doi:10.1016/j.nima.2014.05.071

- J. Adamczewski *et al.*:
  Wavelength shifting films on multianode PMTs with UV-extended window for the CBM RICH detector
  Nucl. Instrum. Methods **A 766** (2014) 180
  doi:10.1016/j.nima.2014.05.011

- J. Adamczewski *et al.*:
  Determination of tolerances of mirror displacement and radiator gas impurity for the CBM RICH detector
  Nucl. Instrum. Methods **A 766** (2014) 250
  doi:10.1016/j.nima.2014.04.074

- J. Adamczewski *et al.*:
  Event reconstruction in the RICH detector of the CBM experiment at FAIR
  Nucl. Instrum. Methods **A 766** (2014) 250
  doi:10.1016/j.nima.2014.04.082

- J. Adamczewski *et al.*:
  The CBM-RICH detector
  JINST **9** (2014) C06002
  doi:10.1088/1748-0221/9/06/C06002

- M. Al-Turany *et al.*:
  Extending the FairRoot framework to allow for simulation and reconstruction of free streaming data
  J. Phys. Conf. Ser. **513** (2014) 022001
  doi:10.1088/1742-6596/513/2/022001

- T. Balog:
  Overview of the CBM detector system
  J. Phys. Conf. Ser. **503** (2014) 012019
  doi:10.1088/1742-6596/503/1/012019

- S. Belogurov *et al.*:
  Development and application of CATIA-GDML geometry builder
  J. Phys. Conf. Ser. **513** (2014) 022003
  doi:10.1088/1742-6596/513/2/022003

- M. Ciobanu *et al.*:
  ADI, an Ultrafast Preamplifier - Discriminator ASIC for Time-of-Flight Measurements
  IEEE Trans. Nucl. Sci. **61** (2014) 1015
  doi:10.1109/TNS.2014.2305999

- I. Deppner *et al.*:
  The CBM Time-of-Flight wall - a conceptual design
  JINST **9** (2014) C10014
  doi:10.1088/1748-0221/9/10/C10014

- M. Deveaux and J. Heuser:
  The silicon detector systems of the Compressed Baryonic Matter experiment
  PoS(Vertex 2013)009 (2014)
  http://pos.sissa.it/archive/conferences/198/009/Vertex2013_009.pdf

- D. Doering *et al.*:
  Noise performance and ionizing radiation tolerance of CMOS Monolithic Active Pixel Sensors using the 0.18μm CMOS process
  JINST **9** (2014) C05051
  doi:10.1088/1748-0221/9/05/C05051

- P. Ghosh *et al.*:
  Systematic characterization and quality assurance of silicon micro-strip sensors for the Silicon Tracking System of the CBM experiment
  JINST **9** (2014) C07001
  doi:10.1088/1748-0221/9/07/C07001

- P. Ghosh:
  Track measurement in the high multiplicity environment at the CBM Experiment
  J. Phys. Conf. Ser. **503** (2014) 012028
  doi:10.1088/1742-6596/503/1/012028

- J. Heuser and V. Friese:
  Measurement of rare probes with the silicon tracking system of the CBM experiment at FAIR
  Nucl. Phys. **A 931** (2014) 1136
  doi:10.1016/j.nuclphysa.2014.08.076

- C. Höhne:
  Measurement of dileptons with the CBM experiment at FAIR
  Nucl. Phys. **A 931** (2014) 735
  doi:10.1016/j.nuclphysa.2014.09.106

- K. Kasinski, W. Zabolotny and R. Szczygiel:
  Interface and protocol development for STS read-out ASIC in the CBM experiment at FAIR
  Proc. SPIE **9290** (2014) 929028
  doi:10.1117/12.2074883

- S. Lebedev:
  Selected event reconstruction algorithms for the CBM experiment at FAIR
  J. Phys. Conf. Ser. **513** (2014) 022019
  doi:10.1088/1742-6596/513/2/022019

- E. Lebedeva and C. Höhne:
  Investigation of surface homogeneity of mirrors for the CBM-RICH detector and low-mass di-electron feasibility studies
  J. Phys. Conf. Ser. **503** (2014) 012002
  doi:10.1088/1742-6596/503/1/012002

- Q. Li *et al.*:
  A FPGA-based Cluster Finder for CMOS Monolithic Active Pixel Sensors of the MIMOSA-26 Family
  J. Phys. Conf. Ser. **513** (2014) 022021
  doi:10.1088/1742-6596/513/2/022021

- B. Milanovic *et al.*:
  A prototype for the data acquisition of the CBM Micro-Vertex Detector
  PoS(TIPP2014)404
  http://pos.sissa.it/archive/conferences/213/404/TIPP2014_404.pdf

- L. Naumann *et al.*:
  Precision measurement of timing RPC gas mixtures with laser-beam induced electrons
  JINST **9** (2014) C10009
  doi:10.1088/1748-0221/9/10/C10009

- M. Petriş and M. Petrovici:
  Development of a time resolution and position sensitive Multi-Gap, Multi-Strip RPC for high counting rate experiments
  J. Phys. Conf. Ser. **533** (2014) 012009
  doi:10.1088/1742-6596/533/1/012009

- S. Seddiki:
  The Compressed Baryonic Matter experiment
  J. Phys. Conf. Ser. **503** (2014) 012027
  doi:10.1088/1742-6596/503/1/012027

- S. Seddiki:
  The Compressed Baryonic Matter experiment
  EPJ Web Conf. **71** (2014) 00120
  doi:10.1051/epjconf/20147100120

- P. Sitzmann *et al.*:
  A data parallel digitizer for a time-based simulation of CMOS Monolithic Active Pixel Sensors with FairRoot
  J. Phys. Conf. Ser. **513** (2014) 022007
  doi:10.1088/1742-6596/513/2/022007

- Y. Wang *et al.*:
  Study on high rate MRPC for high luminosity experiments
  JINST **9** (2014) C08003
  doi:10.1088/1748-0221/9/8/C08003

- W. Zabolotny and G. Kasprowicz:
  Data processing boards design for CBM experiment
  Proc. SPIE **9290** (2014) 929023
  doi:10.1117/12.2073377

- W. Zhu *et al.*:
  A thin float glass MRPC for the outer region of CBM-TOF wall
  Nucl. Instrum. Methods **A 735** (2014) 277
  doi:10.1016/j.nima.2013.09.044

- W Zhu *et al.*:
  A new design of MRPC to reduce noise and crosstalk
  JINST **9** (2014) C07007
  doi:10.1088/1748-0221/9/7/C07007

CBM presentations 2014

http://cbm-wiki.gsi.de/cgi-bin/view/Public/PublicPresentations2014

Doctoral, diploma, master and bachelor theses 2014

http://cbm-wiki.gsi.de/cgi-bin/view/Public/Thesis2014

Workshops and Meetings 2014

Workshop on module assembly for the CBM Silicon Tracking System

15 – 16 January 2014, Kharkiv, Ukraine

At the beginning of 2014, members of the CBM Silicon Tracking System Project met in Kharkiv, Ukraine, to address technology developments and the planning of the pre-series production of STS detector modules. The meeting was hosted by the company *LED Technologies of Ukraine Ltd* (`http://ltu.ua`) to which our technology partners previously affiliated with the Ukrainian *State Enterprise for Scientific Research Technological Institute of Instrument Engineering (SE SRTIIE)* had recently moved. The company's main business is modern lighting technology for the ukrainian market. It also comprises an international division, headed by Prof. V. Borshchov, that engages in instrumentation for international scientific research projects.

The concrete outcome of the meeting was a task list and schedule for technology developments needed on module assembly for the CBM STS project. The work could be supported lateron by GSI with funds and assembly machinery through mediation by an STCU project. During the meeting, also work aspects of current and forthcoming participation in the European Projects HadronPhysics3 (work package ULISINT) and HadronPhysicsHorizon (work package NOVITEC, planned) were discussed.

`https://indico.gsi.de/conferenceDisplay.py?confId=2588`

23st CBM Collaboration Meeting

7 – 11 April 2014, GSI, Darmstadt, Germany

`https://indico.gsi.de/conferenceDisplay.py?confId=2184`

Workshop on the Silicon Tracking System of CBM at FAIR: Towards production readiness

16 – 18 June 2014, Heiligkreuztal, Germany

The CBM Silicon Tracking System Project held a comprehensive workshop in June 2014, focused on achieving production readiness, the start signal for series construction of the detector components. The meeting was locally organized at Monastery Heiligkreuztal near Tübingen, Germany, by the CBM team of the University of Tübingen (H.-R. Schmidt et al.), offering a pleasant and quiet environment stimulating the project's discussions. The 33 participants comprised physicists and engineers from the STS institutes in Germany, Poland, Russia and Ukraine.

During dedicated expert work group sessions, detailed assessment of the current development status and concrete planning of the upcoming tasks on the silicon sensors, the read-out electronics, module and ladder assembly, system integration and cooling emerged. The meeting concluded with detailed input to the project plan, with timeline of tasks, work teams, and milestones to monitor for the STS project's progress.

https://indico.gsi.de/conferenceDisplay.py?confId=2610

24^{nd} CBM Collaboration Meeting

8 – 12 September 2014, Krakow, Poland

CBM week: 24th Collaboration Meeting and Physics Symposium

Kraków, 8-12 September, 2014

Auditorium Maximum, Jagiellonian University

Local Organizers:

Paweł Staszel
Janusz Brzychczyk
Roman Płaneta
Andrzej Wieloch

https://indico.gsi.de/event/cbm-week-2014-09

https://indico.gsi.de/conferenceDisplay.py?confId=2218

The CBM Collaboration

- **Aligarh, India, Department of Physics, Aligarh Muslim University**

  N. Ahmad, M.D. Azmi, M. Irfan, H. Jahan, M.M. Khan

- **Beijing, China, Department of Engineering Physics, Tsinghua University**

  Jianping Cheng, Zhi Deng, Dong Han, Xinjie Huang, Jin Li, Yuanjing Li, Yulan Li, Pengfei Lyu, Yi Wang, Xianglei Zhu

- **Bhubaneswar, India, Institute of Physics**

  D.P. Mahapatra, N.R. Panda, P.K. Sahu

- **Bucharest, Romania, Horia Hulubei National Institute of Physics and Nuclear Engineering (IFIN-HH)**

  C. Andrei, D. Bartoş, I. Berceanu, A. Bercuci, G. Caragheorgheopol, V. Cătănescu, F. Constantin, A. Herghelegiu, M. Petriş, A. Petrovici, M. Petrovici, A. Pop, L. Radulescu, C. Schiaua, M.-G. Târzilă

- **Bucharest, Romania, Atomic and Nuclear Physics Department, University of Bucharest**

  D. Argintaru, V. Baban, C. Beşliu, M. Cãlin, V. Covlea, T. Eşanu, A. Jipa, I. Lazanu, C. Ristea, O. Ristea, A. Scurtu, N.G. Tuturas

- **Budapest, Hungary, Eötvös Loránd University (ELTE)**

  M. Csanád, Á. Fülöp, A. Kiss, A. Szabó

- **Budapest, Hungary, Institute for Particle and Nuclear Physics, Wigner Research Centre for Physics, Hungarian Academy of Sciences**

  T. Kiss, T. Tölyhi, D. Varga, Gy. Wolf

- **Chandigarh, India, Department of Physics, Panjab University**

  M.M. Aggarwal, A.K. Bhati, M. Kaur

- **Darmstadt, Germany, Facility for Antiproton and Ion Research in Europe GmbH (FAIR)**

  J. Eschke[1], W.F.J. Müller[1]

- **Darmstadt, Germany, GSI Helmholtzzentrum für Schwerionenforschung GmbH (GSI)**

  A. Abuhoza[13,2], M. Al-Turany, A. Andronic, R. Averbeck, E. Badura, T. Balog, D. Bertini, O. Bertini, S. Chatterji, M.I. Ciobanu[14], H. Deppe, D. Emschermann, H. Flemming, U. Frankenfeld, V. Friese, J. Frühauf, J. Hehner, J.M. Heuser, R. Holzmann, M. Ivanov, R. Karabowicz, M. Kiš, V. Kleipa, K. Koch, P. Koczoń, W. König, B.W. Kolb, D. Kresan, I. Kulakov, J. Kunkel, A. Lebedev[3], J. Lehnert, Y. Leifels, S. Löchner, P.-A. Loizeau, A.M. Marin Garcia, S. Masciocchi, D. Miskowiec, I. Momot[4], T. Morhardt, W. Niebur, J. Pietraszko, J. Sánchez Rosado, S. Schatral[5], C.J. Schmidt, K. Schweda, S. Seddiki, I. Selyuzhenkov, A. Senger, P. Senger[2], C. Simons, M. Singla, I. Sorokin[4], D. Soyk, C. Sturm, A. Toia[2], F. Uhlig, I. Vassiliev, R. Visinka, C. Wendisch, N. Winckler, P. Zumbruch, M. Zyzak

- **Darmstadt, Germany, Institut für Kernphysik, Technische Universität Darmstadt**

  T. Galatyuk[1], A. Rost, F. Seck

- **Dresden, Germany, Institut für Strahlenphysik, Helmholtz-Zentrum Dresden-Rossendorf (HZDR)**

  Xingming Fan, K. Heidel, B. Kämpfer[15], R. Kotte, A. Laso Garcia[15], L. Naumann, J. Wüstenfeld

- **Dubna, Russia, Laboratory of Information Technologies, Joint Institute for Nuclear Research (JINR-LIT)**

  T. Ablyazimov, P. Akishin, E. Akishina, T. Akishina, E. Alexandrov, I. Alexandrov, D. Belyakov, O. Derenovskaya, I. Filozova, Valery Ivanov, Victor Ivanov, G. Ososkov, A. Raportirenko, P. Zrelov

- **Dubna, Russia, Veksler and Baldin Laboratory of High Energy Physics, Joint Institute for Nuclear Research (JINR-VBLHEP)**

  Yu. Anisimov, S. Avdeev, M. Baznat, A. Bychkov, V. Chepurnov, S. Chernenko, K. Davkov, V. Davkov, D. Dementiev, S. Dubnichka, Z. Dubnichkova, O. Fateev, V. Golovatyuk, K. Gudima, Yu. Gusakov, A. Ierusalimov, E.-M. Ilgenfritz, V. Karnaukhov, G. Kekelidze, A. Khvorostukhin, V. Kirakosyan, V. Kramarenko, A. Kurilkin, P. Kurilkin, S. Kuznetsov, V. Ladygin, A. Malakhov, V. Mialkovski, Yu. Murin, S. Parzhitskiy, D. Peshekhonov, V. Peshekhonov, E. Plekhanov, S. Rabtsun, S. Razin, A. Shabunov, N. Shumeiko, I. Tsakov, T. Vasiliev, B. Yuldashev, Yu. Zanevsky, A. Zinchenko, V. Zryuev

- **Frankfurt, Germany, Frankfurt Institute for Advanced Studies, Goethe-Universität Frankfurt (FIAS)**

  V. Akishina[3,1], M. Bach, J. de Cuveland, D. Eschweiler, S. Gorbunov, H. Hartmann, D. Hutter, E. Iakovleva, S. Kalcher, I. Kisel, G. Kozlov[3], M. Kretz, V. Kucher, V. Lindenstruth[1], M. Pugach[1,4], V. Vovchenko

- **Frankfurt, Germany, Institut für Kernphysik, Goethe-Universität Frankfurt**

  S. Amar-Youcef, H. Appelshäuser, A. Arend, T. Balle, C. Blume, J. Book, H. Büsching, H. Cherif[1], M. Deveaux, P. Dillenseger, D. Doering, I. Fröhlich, P. Ghosh[1], S. Gläßel, E. Hellbär, P. Kisel[1,3], P. Klaus, A. Kotynia[1], M. Koziel, E. Krebs, G. Kretschmar, P. Larionov[1], Qiyan Li[7], B. Linnik, H. Malygina[1,4], J. Markert, J. Michel, B. Milanović, C. Müntz, M. Penschuck, J. Pieper, P. Reichelt, F. Roether, J. Scholten, P. Sitzmann, S. Strohauer, J. Stroth[1], M. Tanha, T. Tischler, M. Wiebusch

- **Frankfurt, Germany, Institute for Computer Science, Goethe-Universität Frankfurt**

  S. Böttger, T. Breitner, H. Engel, C. García Chávez, J. Gebelein, A. Gómez Ramírez, T. Janson, U. Kebschull, C. Lara, J. Lehrbach, J.A. Lucio Martínez, S. Manz, A. Oancea

- **Gatchina, Russia, National Research Center "Kurchatov Institute", Petersburg Nuclear Physics Institute (PNPI)**

  V. Baublis, V. Dobyrn, V. Golovtsov, D. Ivanischev, Vladimir Ivanov, A. Khanzadeev, L. Kochenda, B. Komkov, V. Kozlov, P. Kravtsov, E. Kryshen, L. Kudin, N. Miftakhov, V. Nikulin, E. Rostchin, Yu. Ryabov, V. Samsonov[8,9], O. Tarassenkova, S. Volkov, E. Vznuzdaev, M. Vznuzdaev, M. Zhalov

- **Gießen, Germany, Justus-Liebig-Universität Gießen**

  J. Bendarouach, C.A. Deveaux, M. Dürr, C. Höhne, J.M. Kopfer[10], S. Lebedev[3], E. Lebedeva, T. Mahmoud

- **Guwahati, India, Department of Physics, Gauhati University**

  B. Bhattacharjee, B. Debnath, K. Dey, R. Talukdar

- **Hefei, China, Department of Modern Physics, University of Science & Technology of China (USTC)**

  Ping Cao, Hongfang Chen, Huanhuan Fan[11], Cheng Li, Ming Shao, Yongjie Sun, Zebo Tang, Junfeng Yang, Yifei Zhang, Lei Zhao

- **Heidelberg, Germany, Physikalisches Institut, Universität Heidelberg**

  I. Deppner, D. Gottschalk, N. Herrmann, Tae Im Kang, C. Simon, Ya Peng Zhang

- **Heidelberg, Germany, Zentrales Institut für Technische Informatik, Universität Heidelberg, Standort Mannheim**

  U. Brüning, P. Fischer, C. Kreidl, M. Krieger, F. Lemke, I. Peric, D. Wohlfeld

- **Indore, India, Indian Institute of Technology Indore**

  R. Sahoo

- **Jaipur, India, Physics Department, University of Rajasthan**

  R. Raniwala, S. Raniwala

- **Jammu, India, Department of Physics, University of Jammu**

  A. Bhasin, A. Gupta, S. Mahajan, B.V.K.S. Potukuchi, S.S. Sambyal, M.K. Sharma

- **Karlsruhe, Germany, Karlsruhe Institute of Technology (KIT)**
  S. Bähr, M. Balzer, J. Becker, T. Blank, M. Dreschmann, L. Meder, J. Meyer, O. Sander, M. Weber
- **Katowice, Poland, Institute of Physics, University of Silesia**
  A. Bubak, A. Grzeszczuk, E. Kaptur, S. Kowalski, K. Schmidt, E. Stephan, W. Zipper
- **Kharagpur, India, Indian Institute of Technology Kharagpur**
  P. Banerjee, T.K. Bhattacharyya, A. Haldar, S. Haldar, S. Sarangi, A.K. Singh, I. Som
- **Kolkata, India, Department of Physics, Bose Institute**
  R.P. Adak, S. Das, S.K. Ghosh, S. Raha, R. Ray, S. Samanta
- **Kolkata, India, Department of Physics and Department of Electronic Science, University of Calcutta**
  S. Bandyopadhyay, A. Bhattacharyya, A. Chakrabarti, Sanatan Chattopadhyay, G. Gangopadhyay, S. Sau
- **Kolkata, India, Variable Energy Cyclotron Centre (VECC)**
  Z. Ahammed, P.P. Bhaduri, Subhasis Chattopadhyay, M. Dey, A.K. Dubey, V. Jain, S.A. Khan, S. Mandal, E. Nandy, T. Nayak, S. Pal, A. Roy, J. Saini, R.N. Singaraju, V. Singhal, Y.P. Viyogi
- **Kraków, Poland, AGH University of Science and Technology (AGH)**
  M. Baszczyk, A. Drozd, J. Gajda, P. Gryboś, K. Kasiński, R. Kłeczek, P. Kmon, W. Kucewicz, P. Maj, P. Otfinowski, J. Rauza, T. Satława, R. Szczygieł, M. Żoładź
- **Kraków, Poland, Marian Smoluchowski Institute of Physics, Jagiellonian University**
  M. Adamczyk, T. Barczyk, J. Brzychczyk, L. Dutka, Z. Majka, R. Najman, R. Płaneta, Z. Sosin, P. Staszel, A. Wieloch
- **Kyiv, Ukraine, High Energy Physics Department, Kiev Institute for Nuclear Research (KINR)**
  M. Borysova, A. Chaus, A. Kovalchuk, V. Kyva, V. Militsija, V. Pugatch, D. Storozhyk, M. Teklishyn
- **Kyiv, Ukraine, Department of Nuclear Physics, National Taras Shevchenko University of Kyiv**
  O. Bezshyyko, L. Golinka-Bezshyyko, I. Kadenko, Yu. Onishchuk, V. Plujko, A. Volochniuk
- **Moscow, Russia, Institute for Nuclear Research (INR)**
  O. Andreeva, D. Finogeev, M. Golubeva, F. Guber, A. Ivashkin, O. Karavichev, T. Karavicheva, E. Karpechev, A. Kurepin, A. Maevskaya, S. Morozov, O. Petukhov, I. Pshenichnov, A. Reshetin, A. Sadovsky, A. Shabanov, N. Topil'skaya, E. Usenko
- **Moscow, Russia, Institute for Theoretical and Experimental Physics (ITEP)**
  A. Akindinov, S. Belogurov, A. Chernogorov, D. Golubkov, F. Khasanov, S. Kiselev, A. Kolosova, I. Korolko, D. Malkevich, K. Mikhailov, A. Nedosekin, E. Ovcharenko[3], V. Plotnikov, M. Prokudin, I. Rostovtseva, A. Semennikov, R. Sultanov, Yu. Zaitsev
- **Moscow, Russia, National Research Nuclear University MEPhI**
  E. Atkin, Yu. Bocharov, V. Butuzov, P. Ivanov, E. Malankin, O. Malyatina, D. Normanov, D. Osipov, A. Petrovskiy, V. Shumikhin, A. Simakov, M. Strikhanov, Yu. Volkov
- **Moscow, Russia, National Research Centre "Kurchatov Institute"**
  D. Blau, A. Kazantsev, V. Manko, I. Yushmanov
- **Moscow, Russia, Skobeltsyn Institute of Nuclear Phyiscs, Lomonosov Moscow State University (SINP-MSU)**
  N. Baranova, D. Karmanov, M. Korolev, M. Merkin, V. Popov, A. Voronin
- **Münster, Germany, Institut für Kernphysik, Westfälische Wilhelms-Universität Münster**
  R. Berendes, C. Bergmann, N. Heine, Ch. Klein-Bösing, M. Kohn, W. Verhoeven, J.P. Wessels

- **Obninsk, Russia, National Research Nuclear University**

  N. D'Ascenzo, A. Galkin, V. Galkin, D. Ossetski, V. Saveliev

- **Prague, Czech Republic, Czech Technical University (CTU)**

  V. Petráček, V. Pospisil, L. Škoda

- **Protvino, Russia, Institute for High Energy Physics (IHEP)**

  S. Golovnya, S. Gorokhov, A. Kiryakov, I. Lobanov, E. Lobanova, V. Rykalin, S. Sadovsky, Yu. Tsyupa, A. Vorobiev

- **Pusan, Korea, Pusan National University (PNU)**

  Kyung-Eon Choi, Jongsik Eum, Kunsu Oh, Jihye Song, Sanguk Won, In-Kwon Yoo

- **Řež, Czech Republic, Nuclear Physics Institute, Academy of Sciences of the Czech Republic**

  A. Kugler, V. Kushpil, V. Mikhaylov, O. Svoboda, P. Tlustý

- **Split, Croatia, University of Split**

  M. Anđelić, I. Carević, M. Dželalija

- **Srinagar, India, Department of Physics, University of Kashmir**

  F. Ahmad, S. Ahmad, S. Bashir, M.F. Mir, W. Raja

- **St. Petersburg, Russia, Ioffe Physico-Technical Institute, Russian Academy of Sciences**

  V. Eremin, E. Verbitskaya

- **St. Petersburg, Russia, V.G. Khlopin Radium Institute (KRI)**

  O. Batenkov, V. Jakovlev, V. Kalinin, A. Veshikov

- **St. Petersburg, Russia, St. Petersburg State Polytechnic University (SPbSPU)**

  A. Berdnikov, Y. Berdnikov

- **Strasbourg, France, Institut Pluridisciplinaire Hubert Curien (IPHC), IN2P3-CNRS and Université de Strasbourg**

  G. Claus, A. Dorokhov, W. Dulinski, M. Goffe, A. Himmi, K. Jaaskelainen, F. Rami, I. Valin, M. Winter

- **Tübingen, Germany, Physikalisches Institut, Eberhard Karls Universität Tübingen**

  E. Friske, B. Heß, E. Lavrik, A. Lymanets[4], I. Panasenko[4], H.R. Schmidt, J. Wiechula

- **Varanasi, India, Department of Physics, Banaras Hindu University**

  A. Chauhan, A. Prakash, B.K. Singh, C.P. Singh

- **Warsaw, Poland, Institute of Electronic Systems, Warsaw University of Technology**

  A. Byszuk, M. Gumiński, G. Kasprowicz, J. Pluta, K. Poźniak[12], R. Romaniuk, D. Wielanek, W. Zabołotny[12]

- **Warsaw, Poland, Institute of Experimental Physics, University of Warsaw**

  M. Kirejczyk, T. Matulewicz, K. Piasecki, J. Rożynek, B. Sikora, K. Siwek-Wilczyńska, I. Skwira-Chalot, J. Tarasiuk, A. Turowiecki, K. Wiśniewski

- **Wuhan, China, College of Physical Science and Technology, Central China Normal University (CCNU)**

  Xu Cai, Guangming Huang, Feng Liu, Dong Wang, Yaping Wang, Changzhou Xiang, Nu Xu, Zhongbao Yin, Daicui Zhou

- **Wuppertal, Germany, Fachbereich Physik, Bergische Universität Wuppertal**

  K.-H. Becker, J. Förtsch, K.-H. Kampert, C. Pauly, D. Pfeifer, J. Pouryamout, S. Querchfeld, J. Rautenberg, S. Reinecke

Additional affiliations:
[1] GSI Helmholtzzentrum für Schwerionenforschung GmbH (GSI), Darmstadt, Germany
[2] Institut für Kernphysik, Goethe Universität Frankfurt, Frankfurt, Germany
[3] Laboratory of Information Technologies, Joint Institute for Nuclear Research (JINR-LIT), Dubna, Russia
[4] High Energy Physics Department, Kiev Institute for Nuclear Research (KINR), Kyiv, Ukraine
[5] Zentrales Institut für Technische Informatik, Universität Heidelberg, Standort Mannheim, Heidelberg, Germany
[6] Institute for Theoretical and Experimental Physics (ITEP), Moscow, Russia
[7] College of Physical Science and Technology, Central China Normal University (CCNU), Wuhan, China
[8] National Research Nuclear University MEPhI, Moscow, Russia
[9] St. Petersburg State Polytechnic University (SPbSPU), St. Petersburg, Russia
[10] Fachbereich Physik, Bergische Universität Wuppertal, Wuppertal, Germany
[11] Physikalisches Institut, Universität Heidelberg, Heidelberg, Germany
[12] Institute of Experimental Physics, University of Warsaw, Warsaw, Poland
[13] also: King Abdulaziz City for Science and Technology (KACST), Riyadh, Saudi Arabia
[14] also: Institute of Space Science, Bucharest, Romania
[15] also: Technische Universität Dresden, Dresden, Germany

Contacts

Chairman of the Collaboration Board
Yogendra P. Viyogi
viyogi@veccal.ernet.in

Spokesman
Peter Senger
p.senger@gsi.de

Deputy Spokesman
Yuri Zaitsev
zaitsev@itep.ru

Deputy Spokesman
Subhasis Chattopadhyay
sub@veccal.ernet.in

Technical Coordinator
Walter Müller
w.f.j.mueller@gsi.de

Physics Coordinator
Volker Friese
v.friese@gsi.de

Ressource Coordinator
Jürgen Eschke
j.eschke@gsi.de

Management Board
S. Chattopadhyay, N. Herrmann, M Petrovici, F. Rami, J. Stroth, Y. Zaitsev

`http://www.fair-center.eu/for-users/experiments/cbm.html`

CBM

FAIR

HELMHOLTZ
GEMEINSCHAFT

GSI

Bundesministerium
für Bildung
und Forschung

HIC for FAIR
Helmholtz International Center

CRISP
The Cluster of Research Infrastructures
for Synergies in Physics

Study of Strongly Interacting Matter
HadronPhysics3